An Investigation of a Structural Phase Transition: The R-Point Instability in $KMnF_3$

Thesis submitted by

Ursula Joy Nicholls

for the degree of
Doctor of Philosophy

University of Edinburgh

September 1987

To the memory of my father, William Owen Nicholls

Declaration

The work in chapter 3 was done in collaboration with Chris Lucas. All other work is my own, except where otherwise stated.

Acknowledgements

I would like to thank my supervisor Professor R.A. Cowley for introducing the projects considered in this thesis, and for all his helpful advice and encouragement over the last three years. I would also like to thank my second supervisor Dr. R.J. Nelmes and Dr. Simon Bates for many helpful discussions and useful tips.

I am grateful to the Institut Laue-Langevin for the use of the neutron scattering facilities, and especially thank Dr. Leo Cussen for his invaluable help both in setting up and running the experiments there. I would like to thank René for his technical assistance on IN3, and also Dr. Tom Ryan and Mr. Hugh Vass for their assistance in the x-ray scattering experiments based in Edinburgh.

I acknowledge the award of a Science and Engineering Research Council grant and the support of the Edinburgh Regional Computing Centre. The analysis of the experimental data in chapters 4 and 5 was performed on the distributed array processor (DAP) at the University of Edinburgh, and I am grateful to Dr. Peter Mitchell for the use of his fitting program Shamgar's Oxgoad.

The two crystals $KMn_{0.99}Mg_{0.01}F_3$ and $KMn_{0.9}Mg_{0.1}F_3$ were grown by Dr. Roger Ward at the University of Oxford for which I am grateful.

Finally, I would like to thank my future husband Ian for all his help, and really for just being Ian.

Abstract

This thesis is primarily an experimental study of the R-point structural instability which occurs in $KMnF_3$ at a temperature of 186 K.

A series of x-ray scattering experiments were performed on a nearly-perfect sample crystal of $KMnF_3$ in order to investigate the static critical behaviour close to the transition temperature. The critical exponents β, ν and γ describing the temperature dependence of the order parameter, the static susceptibility and the correlation length were determined. An anomalous second component (of very narrow wavevector width) was observed in the scattering cross section close to the transition temperature, in addition to the anisotropic diffuse scattering from the softening R_{25} normal mode. The anomalous component was well described by an isotropic Lorentzian-squared lineshape.

The dynamic critical behaviour of the type of phase transition which occurs in $KMnF_3$ has been extensively studied, and there is evidence for the presence of a central resolution limited component in the spectral response. This central peak may or may not be analogous to the anomalous component observed in the x-ray scattering cross section. In an attempt to correlate the two phenomena, and also to clarify the role of defects in a displacive structural phase transition, x-ray and neutron scattering experiments have been performed on samples of $KMnF_3$ with known impurity content. Our results indicate that the two effects occur over differing temperature ranges and are to this extent distinct, and, moreover, that neither is significantly enhanced by the presence of point defects.

CONTENTS

CHAPTER 1

INTRODUCTION

A phase transition occurs in a thermodynamic system where there is a discontinuous or singular behaviour with a continuous change in a control parameter. The essential characteristic of many phase transitions is the spontaneous breaking, at the transition temperature, of some of the symmetry operations of the high symmetry phase (usually the high temperature phase). A phase transition can also be described as corresponding to a divergence of the correlation between a fluctuating quantity at two different points (giving long range order). The primary observables for many phase transitions, and those considered here, are the order parameter (which measures the difference between the coexisting phases), the susceptibility (the response of the order parameter to a conjugate field) and the correlation length (the dimension of the largest correlated volume). These exhibit power law behaviour as functions of $t = (T/T_c - 1)$, described by the critical exponents β, γ and ν. It has been found that any critical regime can be associated with two basic features, firstly, that the critical indices are not independent of each other but are related via certain scaling properties, and secondly, that the critical exponents are insensitive to the microscopic details of the interaction and only depend upon certain essential features of the system (universality).

The application of mean field theories in the characterization of phase transitions has been very successful, providing reliable qualitative descriptions. The essential principle is to reduce the many body problem to a tractable single body problem which can be solved self consistently, which necessitates the neglect of critical fluctuations. In particular, Landau theory (1937) describes a phase transition in terms of relatively few phenomenological parameters. Landau assumes that the free energy, G, of a system can be expanded analytically as a power series in the order parameter, the coefficients being temperature dependent: The physical value of the order parameter is that which minimizes G. Although it provides a generalized theory applicable to several different types of phase transitions, Landau theory neglects many of the subtleties of universality, and predicts critical exponents which are invalid close to the transition temperature where critical fluctuations cannot be ignored. It is necessary to turn to the renormalisation group theory for a correct evaluation.

The essential idea of the renormalisation group method introduced by Wilson (1971), and further developed by Wilson and Kogut (1974), in order to extrapolate the critical behaviour of a system is to relate the physical properties of a system close to its critical point to properties of a similar system that is far from criticality. The development of the theory in modelling very complex systems by very simple hamiltonians is justified by the universality hypothesis (Kadanoff 1971). In essence, all systems with the same qualitative features (for example, the spatial dimension, the number of components of the order parameter) are said to belong to the same universality class, and to exhibit critical behaviour characterized by the same set of universal quantities. The aim is therefore to relate the properties of a system with a large effective correlation length $\hat{\xi} = \xi/a$ (where a is the lattice spacing) to one with $\hat{\xi}$ small. The renormalisation group (RG) operation in Fourier space consists of a two part operation to construct an 'effective' hamiltonian $H(b)$ from the initial, physical hamiltonian H_o

$$H(b) = \mathbb{R}(b)\, H_o \qquad (1)$$

The first part is a configurational integral over the modes with larger wavevector $|k| > \Lambda/b$ where Λ is some cut-off wavevector and b a scale factor, and the second is a rescaling of the vectors in reciprocal space so they again cover the range between zero and Λ. The effective hamiltonian $H(b)$ obtained is 'less critical' than H_o since the system produced has a lattice spacing larger by a factor of b, and $\hat{\xi}(b) = \hat{\xi}/b$.

It is evident that a repeated application of the RG operation will generate a sequence of effective hamiltonians which trace out a trajectory or 'flow line' in parameter space, each being less critical than its predecessor and each containing the information that determines the critical (small wavevector) properties of the hamiltonian H_o. The flow line terminates in a fixed point of the RG operation such that

$$H^* = \mathbb{R}(b)\, H^* \qquad (2)$$

which has a correlation length which is infinite or zero, corresponding to critical or non-critical fixed points respectively. Since the flow lines are of decreasing correlation length, the flow line will only terminate in a critical fixed point if H_o is itself critical. Consequently the iterative procedure must begin on the critical

surface in parameter space in order to reach the critical fixed point. The universality concept implies that all systems belonging to one universality class will tend to the same critical fixed point, and the scaling hypothesis is justified in that the two quantities (t and the field conjugate to the order parameter) which are adjusted in order for a phase transition to occur control two 'scaling fields' which must vanish at the fixed point.

The analytic techniques employed in the theory of critical phenomena exploit the use of 'small' parameters. (For example, $\varepsilon = d_c - d$ where $d_c = 4$ is the critical borderline dimension, above which fluctuations are so weak that mean field predictions for universal quantities become exact). These techniques involve either direct perturbation expansion methods via Feynman diagrams (Wilson 1972), or a perturbative treatment of the RG transformation involving the solution of the differential equations of hamiltonian flow (Wegner and Houghton 1973).

This thesis is primarily concerned with experimental investigations of structural phase transitions, at which a material changes its crystallographic structure. Most phase transitions of this kind belong to one of two types, displacive (when some or all of the atoms in the unit cell are shifted from their high temperature positions at the transition temperature), and order-disorder (which, as the name implies, is associated with an ordering of some misplaced variable at T_c). Two examples of displacive phase transitions are, firstly, that of $BaTiO_3$ at 393 K, in which the static displacement of the atoms is the same in every unit cell (see, for example, Megaw 1947, Kanzig 1951, Shirane et al 1955 and Harada et al 1970), and secondly, that of $SrTiO_3$ at 110 K. In this example, the high temperature perovskite phase is distorted by an anti-phase rotation of neighbouring octahedra (see figure 1.1), and the unit cell in the distorted phase consists of two unit cells of the high temperature phase (Unoki and Sakudo 1967, Shirane and Yamada 1969).

Measurements had shown that, at least for the displacive type of transition, the atoms in the distorted phase are only slightly displaced from the equilibrium positions of the high temperature phase, and the displacements have a definite relationship from one unit cell to another. This led to the suggestion by Cochran (1960)

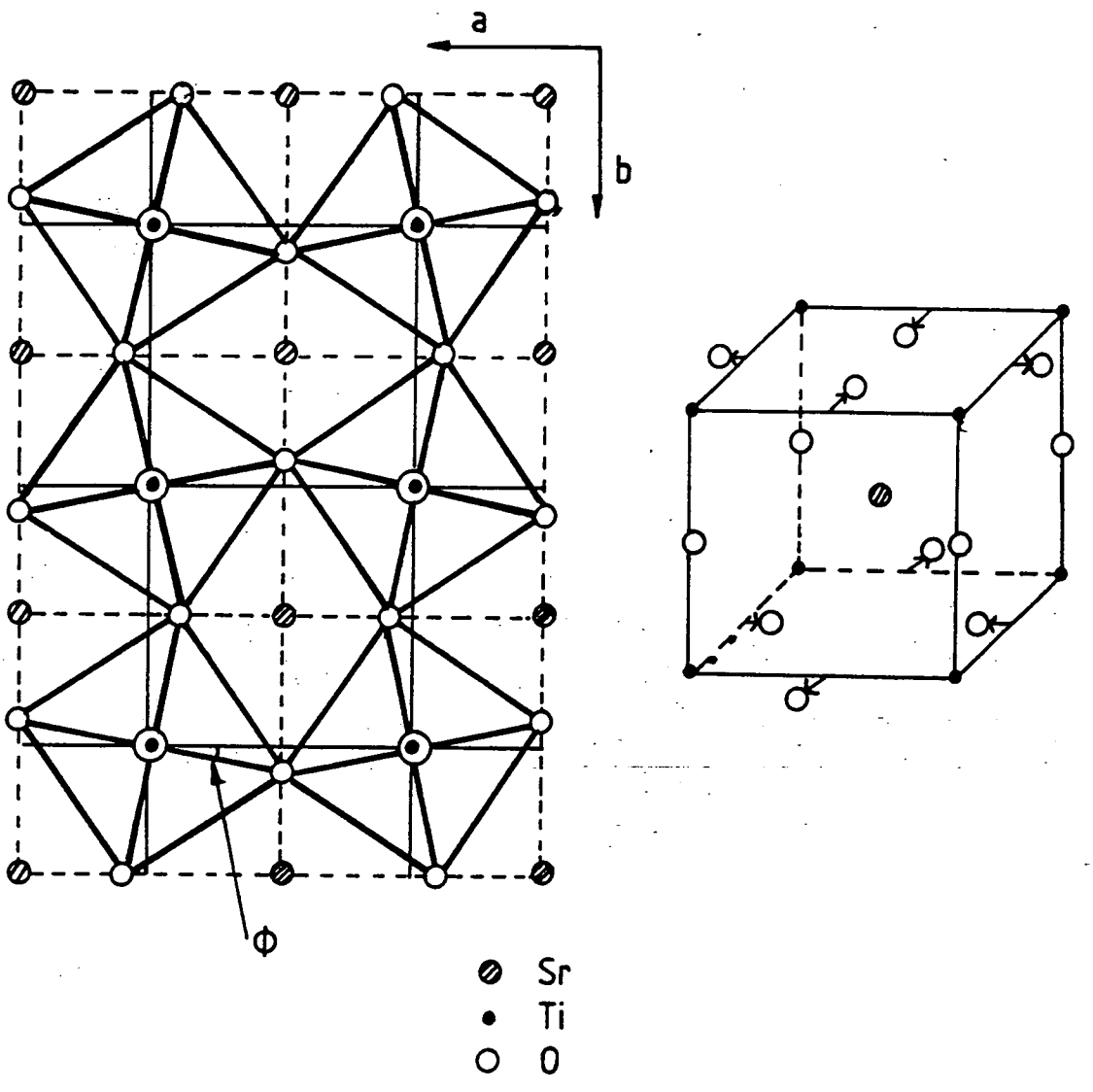

Figure 1.1

A projection along a cubic axis of the distorted phase of $SrTiO_3$ as deduced by Unoki and Sakudo (1967). (After Shirane and Yamada 1969).

and Anderson (1960) that such a phase transition might be the result of an instability of the crystal against some normal mode of vibration of the high temperature phase. This hypothesis has been successfully borne out in principle by many experiments as reviewed by Scott (1974) and Shirane (1974), but has been found to be inadequate in detail, as will be discussed below. The order parameter of a displacive phase transition is the amplitude of the normal mode which describes the distortion; in general the description involves a linear combination of n normal mode coordinates and the order parameter has n components. In $SrTiO_3$ the order parameter has three components (since the oxygen octahedra can rotate about any of three cubic axes) and wavevector $q_s = 2\pi/a_o(\frac{1}{2}, \frac{1}{2}, \frac{1}{2})$ for all three components. The term secondary order parameter as applied to a structural phase transition is used to describe distortions which arise at the phase transition which do not break as many symmetry operations as are broken by the primary ordering. In $SrTiO_3$ there is a macroscopic strain below T_c in addition to the primary distortion which has a temperature dependence described by an exponent $\tilde{\beta}$, where one expects $\tilde{\beta} > 2\beta$.

In the soft-mode approach to the dynamics of a structural phase transition, the frequency of the relevant unstable normal mode decreases to zero at T_c, below which temperature the crystal distorts so as to stabilize the mode; the distortion is described as the 'frozen in' amplitude of the normal mode. This concept, based on the harmonic oscillator form of the static susceptibility, is strictly inconsistent since the frequencies of the normal mode in a harmonic crystal are not temperature dependent. The conjecture becomes acceptable if the frequencies are interpreted as effective or renormalised frequencies obtained from the weakly anharmonic crystal model (reviewed by Cowley 1963 and discussed briefly below). It is also necessary to include a phenomenological damping term in the model for the dynamic susceptibility since many soft-modes are found to be damped or even overdamped above the transition temperature. The soft-mode frequencies then define the poles of the dynamic susceptibility in complex frequency space. The movement of these poles towards the origin corresponds to an impending divergence of the static susceptibility and hence signals the approach to a continuous phase transition.

Landau theory, extended by Ginsburg to include the fluctuations in the leading terms, can be used to describe the behaviour of a harmonic crystal with short range interactions, to a first approximation. The free energy for a multi-component order parameter is

$$G = G_s + \frac{1}{2N} \sum_{pq} \sum_{\mathbf{k}} R_{pq}(\mathbf{k})\, Q_p(\mathbf{k})\, Q_q(-\mathbf{k}) + \ldots . \qquad (3)$$

where

$$\mathbf{k} = \mathbf{q} - \mathbf{q}_s \qquad (4)$$

and

$$R_{pq}(\mathbf{k}) = a\,(T - T_c)\,\delta_{pq} + \sum_{\alpha\beta} f_{\alpha\beta}(pq)\, k_\alpha k_\beta \qquad (5)$$

and G_s is the static part of the free energy, N is the number of unit cells in the crystal and $Q_p(\mathbf{k})$ is the amplitude of the normal mode. There are no linear terms in $\mathbf{k}$ if $\mathbf{q}_s$ is a high symmetry wavevector. This model assumes that the coefficients $f_{\alpha\beta}$ are temperature independent and predicts that the critical exponent for the correlation function is $\nu = 0.5$, and that the lineshape of the scattering is Lorentzian in wavevector for a given temperature, with the width of the Lorentzian depending on the direction of the wavevector.

Landau theory can be applied to a weakly anharmonic crystal such as $SrTiO_3$ if the harmonic frequencies $\omega_p(\mathbf{k})$ are replaced by

$$\tilde{\omega}_p(\mathbf{k},\omega)^2 = \omega_p(\mathbf{k})^2 + \Sigma_p(\mathbf{k},\omega) \qquad (6)$$

where Σ is the anharmonic part of the self-energy and depends on the frequency used in an experiment. It is assumed to be well behaved at T_c. The parameters of Landau theory and the various contributions to the self-energy of the soft-mode can be calculated in terms of the anharmonic interactions and normal modes of a material by the use of weakly anharmonic perturbation theory. This has been carried out quantitatively for $SrTiO_3$ by Bruce and Cowley (1973), who find that the anharmonic effects are not large when compared with results for alkali halides at the same temperatures, but that the harmonic frequencies of the soft-mode are very small. This possibly occurs because one of the atoms is a loose fit in its site in the lattice and is easily displaced from its high symmetry position.

As discussed previously, Landau theory is inappropriate close to a transition temperature where the critical fluctuations must be included in a self consistent

way. In order to correctly predict the critical behaviour of a displacive structural phase transition such as that occurring in $SrTiO_3$, the RG methods introduced by Wilson must be employed. The basic hamiltonian appropriate for a structural phase transition associated with an n-fold degenerate soft-mode is that of the n-component Landau - Ginzburg - Wilson model, which has a stable fixed point referred to as the (isotropic) n-component Heisenberg fixed point, since it belongs to the same universality class as the Heisenberg model of ferromagnetism. However, since $n>1$, the order parameter symmetry will generally permit various additional interactions which are not isotropic and it is possible for these to cause a change in universality class (crossover behaviour). The most important perturbations are those of cubic symmetry, as reviewed in detail by Aharony (1976). The consensus of opinion is that in the case $d=n=3$ the stable fixed point of the effective hamiltonian including the perturbations remains the isotropic fixed point as above: asymptotically the cubic interactions are renormalised to zero fixed point values by the critical fluctuations, and the appropriate critical exponents are those of the $n=3$ component Heisenberg model.

When the anisotropy is large, the observed critical behaviour will be characterized not by the isotropic exponents, but by effective critical exponents which reflect the anisotropy. Calculations to leading order in ϵ (Natterman and Trimper 1975) suggest that in situations where the α^{th} branch is flat along the α^{th} cubic axis, the effective exponents β_{eff} and γ_{eff} will be somewhat larger than their asymptotic counterparts. Furthermore, a system with very large anisotropy actually lies outside the domain of attraction of the stable Heisenberg fixed point and may promote a first order phase transition (Bruce 1974 and Natterman 1976).

The classical soft-mode approach to the dynamical behaviour of a system undergoing a structural phase transition, and also some more detailed theories, suggest that the response should be characterised by a single softening resonance with an associated timescale. However, the inelastic neutron scattering measurements of Riste et al (1971) and Shapiro et al (1972) show that this is not the case for the displacive phase transition in $SrTiO_3$ at $T_c=110K$ (for which the soft-mode phenomenology is particularly appropriate). They observed a central resolution limited component in the scattering profile in addition to the phonon-like response. The damped

phonon peak initially softened in accord with the classical soft-mode theory but saturated a few degrees above T_c, while the narrow component centered on zero frequency first appeared at ~50K above T_c and exhibited an intensity which diverged as T_c was approached. These results mean that the near critical behaviour of the order parameter degrees of freedom in displacive phase transitions must be characterised by two distinct timescales. The first is a short timescale whose magnitude is set by the soft-mode side-band and the second a longer timescale associated with the narrow central peak.

Shapiro et al analysed their results in terms of a phenomenological model which supposed that the response function was that of a damped simple harmonic oscillator coupled, with a constant δ, to some unspecified internal degree of freedom with relaxation time τ_o, to provide an additional channel for decay. The form for the susceptibility was (see Feder 1976 for a simple derivation)

$$\begin{aligned}\chi^{-1}(q_p,\omega) &= \omega_o(q_p)^2 - \omega^2 - 2i\omega\Gamma_o - i\omega\tau_o\delta^2/(1-i\omega\tau_o) \\ &= \omega_\infty(q_p)^2 - \omega^2 - 2i\omega\Gamma_o + \Sigma(q_p,\omega)\end{aligned} \qquad (7)$$

where

$$\omega_\infty(q_p)^2 = \omega_o(q_p)^2 + \delta^2 \qquad (8)$$

and

$$\Sigma(q_p,\omega) = -\delta^2/(1-i\omega\tau_o) \qquad (9)$$

is a contribution to the anharmonic self-energy. If the damping constant Γ_o is small the response function can be separated into two components, a damped harmonic oscillator with resonances at $\pm\omega_\infty(q_p,T) \equiv \pm\omega_\infty(q_p)$ and a narrow Lorentzian of width $\omega_L = (\omega_o^2/\omega_\infty^2)/\tau_o$ centered on zero frequency. This model, convolved with the instrumental resolution function, adequately described the measured scattering profiles at the R-point in $SrTiO_3$ at various temperatures above T_c. The model also predicts that, since the lattice instability occurs when $\omega_o(0,T_c)$ tends to zero and not when $\omega_\infty(0,T_c)$ tends to zero, at T_c we have that $\omega_\infty(0,T_c) = \delta(T_c)$ which is non zero provided $\delta(T_c)$ is non zero. The analysis clearly showed this to be the case for $SrTiO_3$.

Further high resolution studies of the central peak in $SrTiO_3$ were made by Mezei and Heyter (1974) using a spin-echo spectrometer and Töpler et al (1975, 1977)

using a back-scattering spectrometer in an attempt to resolve the frequency width, but these measurements only yielded an upper limit of 2×10^{7} Hz. The role of crystal defects has been investigated by Hastings et al (1978) who measured the central peak intensity in hydrogen reduced $SrTiO_3$ as a function of free carrier concentration, and found the intensity of the central peak at a given value of $T-T_c$ did increase with carrier concentration, though only slightly. A measurement of the critical scattering using x-rays reported by Darlington and O'Connor (1976) showed the intensity of the central peak to increase as the x-ray energy was decreased. This was interpreted by the authors as evidence for a 'surface layer' which assumed the distorted low temperature structure at a temperature above that of the bulk, so giving rise to Bragg scattering with an intensity inversely proportional to the x-ray penetration depth (and hence energy). This interpretation would provide a simple explanation for the observed quasi-elastic scattering: The increase in intensity of the central peak as T_c is approached corresponds to a growing thickness of the 'surface layer'. Cowley and Shirane (1978) further investigated this idea by using neutron scattering with a masking technique in order to control the portion of the crystal illuminated. They found that, although the volume of the surface layer could be sufficient to account for the intensity of the central peak observed, the scattering from the whole crystal and that from the interior alone are nominally the same.

Measurements of the dynamic response function at R-point instabilities in other members of the perovskite family have been made. A central peak has been observed in $KMnF_3$ at the phase transition at 186 K (Shapiro et al 1972), in $RbCaF_3$ at the phase transition at 193 K (Almairac et al 1977) and in $LaAlO_3$ at the phase transition at 767 K (Kjems et al 1973). However, the temperature dependence of the parameter δ extrapolated from the data analysis varies from material to material, which suggests that the phenomenology is unable to account for the different experimental conditions. In each case the behaviour of the soft-phonon side-band is qualitatively consistent with that of $SrTiO_3$ and approximately sample independent, converging to a non-zero value at T_c.

There is also evidence for the presence of quasi-elastic scattering in the dynamical response function of many other structural phase transitions. The observation of a central peak in the order-disorder type, such as occur in $NaNO_2$, is well established (Hoshino and Motegi 1967). The two measured timescales are presumed to arise from two different excitations in the system, firstly, the large oscillations of the NO_2 groups

between two possible low temperature positions and secondly, the small collective oscillations of the atoms within the NO_2 groups about the positions of equilibrium set by the instantaneous configuration of the NO_2 groups; the former sets a relatively long timescale and gives rise to the quasi-elastic scattering. Early neutron scattering measurements at the structural phase transition associated with the softening of the elastic constant in Nb_3Sn by Axe and Shirane (1974) showed a reolution limited component at zero frequency, and this was also observed for a similar phase transition in $PrAlO_3$ (Birgeneau et al 1974). The central peak has been seen in the critical scattering above the ferroelectric phase transition in $Pb_5Ge_3O_{11}$ at 451K where, unlike in $SrTiO_3$, it was found to exist for a range of wavevectors around each reciprocal lattice point (Cowley et al 1976). Other occurences of the central peak include the commensurate-incommensurate phase transition in $BaMnF_4$ (Cox et al 1979), the ω-phase transition exhibited by bcc Zr-Nb alloys (Moss et al 1973, Axe et al 1975) and the structural instability associated with the M-point zone boundary mode in $KMnF_3$ and $NaNbO_3$ (Shapiro et al 1974, Darlington and O'Connor 1978). There is at present no evidence for a central peak above the 'near classical' ferroelectric phase transition in KH_2PO_4, where critical fluctuations are reduced by piezoelectric coupling to shear modes. However, molecular dynamical simulations of simple models undergoing structural phase transitions provide clear evidence for quasi-elastic scattering above the transition temperature (Schneider and Stoll 1973, 1975, 1976, Aubry 1975, 1976 a, b).

There have been many attempts to understand and explain the origin of the anomalous frequency response in a displacive phase transition near the critical point, as reviewed in detail by Bruce and Cowley (1980). Several theories are based on an anharmonic perturbation analysis in which the calculation of the phonon self-energy is extended to higher orders (Silberglitt 1972, Cowley and Coombs 1973, Murata 1975, Bausch and Halperin 1978). Such theories are primarily concerned with calculating the contribution to the self-energy made by phonon-density fluctuations (that is, by the fluctuation in the numbers of other phonons) which can couple to the soft-mode if the symmetry is correct. In such a calculation, since unphysical singular behaviour can only be suppressed if correct account is taken of the finite lifetime of the intermediate phonons, the perturbation theory must include all possible scattering processes (see figure 1.2) and hence be carried to infinite order. With certain simplifying assumptions this can lead to a self-energy of the form given by equation (9) and a central peak with a critically diverging intensity (Bruce and Cowley 1980). In general, there will be a linear coupling between the soft-mode and the phonon-density fluctuations

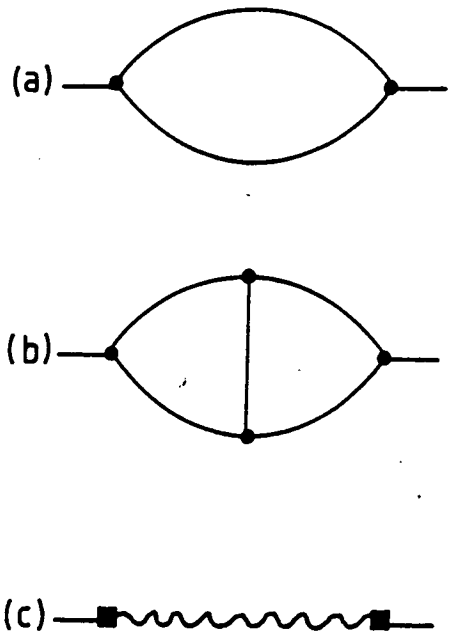

Figure 1.2

Diagrammatic representation of processes contributing to the soft-mode self-energy:

a) The leading order frequency dependent contribution.

b) One of the infinite sequence of additional processes which must be included when the soft-mode can couple to pairs of modes $(\mathbf{q}_1 j_1)$ and $(-\mathbf{q}_1 j_1)$.

c) A schematic representation of the sum of processes b).

(After Bruce and Cowley 1980).

only if both transform according to the same representation of the space group, that is, if $q_s = 0$. Consequently, in the case of $SrTiO_3$, a central peak is predicted in the low temperature phase where the zone-boundary above T_c becomes a zone-centre due to the unit cell doubling. In addition, the difference between the adiabatic and isothermal response of the soft-mode below the transition temperature will give rise to a thermally diffusive contribution to the central peak. This contribution always reflects thermal fluctuations in some coordinate with macroscopic order, and as such can only appear in conjunction with a Bragg peak (Heller 1970, Schulhof et al 1971).

The theory considered thus far considers the non-critical regime and ignores critical fluctuations. This may be why it fails to account for the presence of a quasi-elastic component in the $T > T_c$ soft-mode spectral response function in systems such as $SrTiO_3$. One approach to extending the theory into the critical region is to assume that close to T_c critical fluctuations produce microdomains of distorted crystal (corresponding to the low temperature structure) within which coupling between the soft-coordinate and the phonon-density fluctuations is allowed. This idea led to the prediction by Feder (1971) that a thermally diffusive central peak exists above T_c, and also to the phonon perturbation calculations of Silberglitt (1972) who proposed that certain 'precursor' contributions to the phonon self-energy should be included close to T_c (figure 1.3a). Silberglitt concluded that a narrow central peak should be observed in the frequency reponse function of $SrTiO_3$ above T_c. Murata (1975) and Ohnari and Takada (1979) suggested that other precursor contributions should also be included in the calculation (figure 1.3b), but unfortunately the predicted characteristics of the central peak are not consistent with experimental observations.

A more systematic attempt at extending the theory to the critical domain lies in the treatment of critical fluctuations via dynamic renormalisation group theory. This was principally developed by Halperin et al (1972, 1974, 1976) in an extension of the static renormalisation group theory discussed briefly above. The essential element is an equation of motion which replaces the effective hamiltonian of the static case; the dynamic behaviour near a critical point is found to be characterized by certain 'universal quantities': See Hohenberg and Halperin (1977) for a review. However, a universality class is not defined solely by a few 'essential qualitative features' as in the static instance, but is also found to reflect the fundamental conservation laws characterizing the motion. This is manifested in results which predict that the spectral response is dominated, asymptotically as T tends to T_c^+, by a central component with

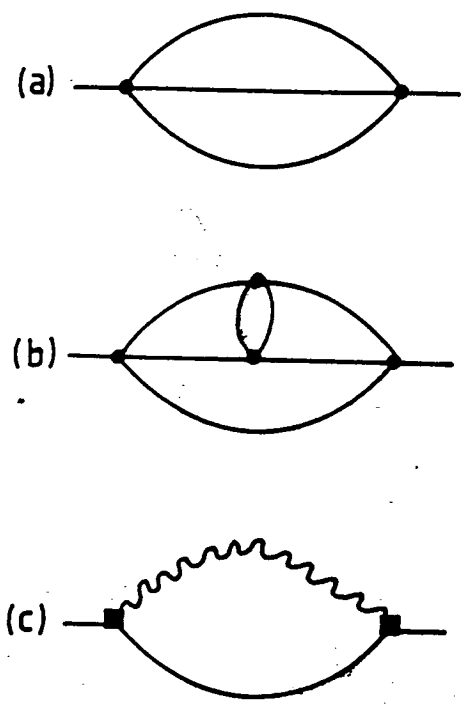

Figure 1.3

Diagrammatic representation of important processes contributing to the soft-mode self-energy in the critical region above T_c:

a) The leading frequency dependent contribution carrying critical singularities. This process is the dynamic precursor of that depicted in figure 1.2a.

b) The dynamic precursor of the process shown in figure 1.2b.

c) The dynamic precusor of the sum of processes represented by figure 1.2c.

(After Bruce and Cowley 1980).

a width whose **q** and t dependence is non-universal. When the specific heat is divergent the central peak is due to the non-linear interaction between the soft-coordinate and the thermal phonon-density fluctuations, as conjectured by Feder (1971) and Murata (1975). When the specific heat remains finite, this coupling can be neglected and the central peak (which may not be distinguishable from the phonon side-band) arises from non-linear coupling to non-thermal fluctuations: The process singled out by Silberglitt (1972), figure 1.3a, represents the leading contribution to the self-energy within an ε expansion for that particular class of system.

The renormalisation group analysis fails to establish the magnitude of the central peak width, or to predict the range of reduced temperature over which it should be visible. The very narrow central feature observed by Shapiro et al in the neutron scattering cross section of the phonon response function of $SrTiO_3$ is not consistent with renormalisation group estimates, which suggest that for a displacive system the width of the critical scattering should not be very different from that expected for an overdamped soft-mode (Bausch and Halperin 1978). This intimates that a discussion based on a concept of two distinct timescale may be invalid.

The above theories are linked by a common scheme, the use of perturbation theory within a reciprocal space basis of harmonic phonon coordinates. This is a consistent way to approach the dilemma of the central peak, given that a system such as $SrTiO_3$ is expected to be described by a weakly anharmonic crystal model (Cowley 1963). However, in practice the calculation of the soft-mode self-energy is not a trivial question and the results obtained do not present a clear picture of the two timescales observed in a displacive phase transition. A second approach provides a more conceptually appealing explanation of the longer timescale but is not analytically explicit: It associates the central peak with the existence of precursor clusters of local order (Schneider and Stoll 1973), which introduce an order-disorder component into the collective motion (Krumhansl and Schrieffer 1975, Aubry 1975, 1976 a, b, Varma 1976). The concept of precursor microdomains was introduced within the framework of anharmonic perturbation theory by Silberglitt (1972), but here it plays a more crucial role as displayed in molecular-dynamics studies on a model system undergoing a structural phase transition (Schneider and Stoll 1973, 1976). The critical behaviour is described as follows: The critical growth in correlation length with reducing temperature is expressed in the appearance and growth of clusters (a group of adjacent atoms, all of which at a given instant are displaced to the same side of the high symmetry site),

each cluster persisting in a relatively well defined form for some typical lifetime τ during which its boundaries may diffuse (or propagate) through the system. The two timescales can thus be visualized; firstly, each atom exhibits a relatively fast motion about a quasi-equilibrium position displaced from the high symmetry site and secondly, the quasi-equilibrium position itself evolves at a relatively slow rate determined by the time for which the cluster encompasses the atom in question. This explanation is clearly reminiscent of that of the order-disorder type of structural phase transition discussed earlier in the chapter. The central peak is analogous to that associated with the order-disorder system's 'collective inter-well mode', and is best regarded as the precursor of the superlattice Bragg peak which appears below T_c. The central peak must have a non-zero, critically narrowing, width in $\mathbf{q}$ and ω, reflecting the finite, but growing, range and lifetime of the order associated with the precursor clusters. These results reveal a unity in the critical behaviour of order-disorder and displacive systems. At a characteristic temperature $T_{ch} > T_c$ the growing coherence of the motion drives a displacive/order-disorder crossover. In the displacive regime ($T > T_{ch}$), the atoms oscillate predominantly about their high symmetry sites and the excitation spectrum is dominated by a softening high temperature phonon. In the order-disorder regime ($T_{ch} > T > T_c$), the atoms oscillate about quasi-equilibrium positions displaced from the high symmetry sites to form clusters of dynamic precursor order: Under the stabilising influence of the clusters the high temperature phonon evolves into its low temperature counterpart without exhibiting a complete softening, while the critical slowing down is transferred to a cluster induced quasi-Bragg central component. The clusters are regarded as direct space manifestations of critical fluctuations and are associated with a precursor order parameter (Bruce et al 1980). The region $T_{ch} > T > T_c$ is therefore the range of temperature over which non-classical critical behaviour is evident. Consequently, the stronger critical fluctuations, the greater the deviations from classical critical behaviour, the more pronounced is the order-disorder character of the system and the more crucial the role of the cluster boundary. This idea has been developed by Bruce et al (1979).

There have been several attempts to formulate analytic theories in one dimension for the cluster picture and the characteristic temperature T_{ch} at which the central peak appears has been specified in various ways (Krumhansl and Schrieffer 1975, Aubry 1975, 1976 a, b, Bishop and Krumhansl 1975, Varma 1976, Bruce and Schneider 1977, Bruce 1978). These enjoy some limited success but, as yet, they have not been extended to systems of higher dimensionality. It may thus be seen that although the cluster picture

has an intuitive appeal, analytic expressions of this idea are of dubious merit with regard to the three dimensional systems of primary interest.

A third approach, described in detail by Halperin and Varma (1976), considers the influence of crystal imperfections upon the static and dynamic critical response at a displacive structural phase transition. It is found that the predicted behaviour varies according to the symmetry and dynamics of a defect cell. In particular, an impurity frozen at a site which properly breaks the symmetry of the high temperature phase will couple linearly to the order parameter. This will induce a non-zero value of the order parameter in the neighbourhood of the impurity, even above the transition temperature, which will give rise to an elastic scattering peak whose magnitude increases as T tends to T_c. The problem of the extreme narrowness in frequency of the experimentally observed central peak is therefore resolved: The strain field surrounding an impurity stabilizes the low temperature structure (Axe et al 1974) and introduces a Bragg-like component into the scattering. The role of defects at a structural phase transition is thus of crucial importance and should always be considered in the analysis of any experimental results. It is a major aim of this thesis to attempt to quantify the effects of impurities at the displacive phase transition in $KMnF_3$ at $T = 186\,K$ by using x-ray and neutron scattering techniques.

This thesis is subdivided as follows. Chapter 2 reviews some background theory for x-ray and neutron scattering and describes the experimental arrangements and major resolution degrading effects in both cases. Chapter 3 reports work requiring a high resolution x-ray scattering technique: The effects of dry etching on semiconductor surfaces was investigated by the use of two different x-ray scattering procedures. Chapter 4 contains the results of x-ray scattering measurements of the critical behaviour at the R-point instability in pure $KMnF_3$. The critical exponents β, γ and ν describing the temperature dependence of the order parameter, the static susceptibility and the correlation length were determined. A second anomalous component was observed in the scattering cross section close to the transition temperature, which may or may not be analogous to the central peak discussed extensively above: The central peak has been observed in the dynamic response function in $KMnF_3$ by Shapiro et al (1972). In an attempt to correlate the two phenomena, and also to pursue the role of defects at a displacive structural phase transition, x-ray and

neutron scattering experiments have been performed on samples of $KMnF_3$ with known impurity content. Chapter 5 describes the results of experiments on the two samples $KMn_{0.99}Mg_{0.01}F_3$ and $KMn_{0.90}Mg_{0.10}F_3$.

CHAPTER 2

THE RESOLUTION OF TRIPLE AXIS SPECTROMETERS

2.1 Introduction

Traditionally, experimental studies of the microscopic character of structural phase transitions have been made by neutron scattering measurements of the order parameter and dynamic susceptibility. However, if accurate values of the critical exponents γ and ν are required, x-ray scattering is a more obvious technique since it automatically measures the static susceptibility, and has a considerably improved wavevector resolution over the best neutron triple axis spectrometers. The two scattering methods can therefore provide complementary information about the details of a structural phase transition. Furthermore, both techniques have applications which are distinct.

X-rays have a wavelength comparable with the lattice spacing of a crystal, but an energy considerably greater than that of the lattice excitations (phonons). Consequently, the measured scattering cross section automatically integrates over the energy, to give the differential cross section

$$\frac{d\sigma}{d\Omega} = \int_0^\infty \frac{d^2\sigma}{d\Omega\, d\omega}\, d\omega \qquad (1)$$

The major use of x-rays is in structural crystallography, since the differential cross section is proportional to the structure factors of the Bragg reflections for elastic scattering

$$\left(\frac{d\sigma}{d\Omega}\right)_{elastic} = S_o(\mathbf{Q}) = \sum_{\tau_h} |F(\mathbf{Q})|^2 \delta(\mathbf{Q}-\tau_h) \qquad (2)$$

where τ_h is a reciprocal lattice vector, and

$$F(\mathbf{Q}) = \sum_k f(k) \exp(+i\mathbf{Q}.\mathbf{R}_k) \exp(-W_k) \qquad (3)$$

The sum runs over all atomic sites $\mathbf{R}_k$ in the unit cell, $f(k)$ being the form factor

and $\exp(-W_k)$ the Debye-Waller factor for the k^{th} atom in the unit cell. The Debye-Waller factor is the contribution to the scattering from all single site non-interacting normal modes of the lattice vibrations. The total scattering cross section is an integral over the resolution broadened peak.

X-rays also enable the static dielectric susceptibility to be determined since, in the one-phonon approximation for wavevector transfer **Q**,

$$\left(\frac{d\sigma}{d\Omega}\right)_{\text{one-phonon}} = S_j(\mathbf{Q}) = \sum_{\tau_h} |F_j(\mathbf{Q})|^2 \mathcal{P}_j(\mathbf{q}) \delta(\mathbf{Q}+\mathbf{q}-\boldsymbol{\tau}_h) \qquad (4)$$

where

$$F_j(\mathbf{Q}) = \sum_k f(k)\, \mathbf{Q}.\mathbf{e}(k,\mathbf{q}_j) \exp(+i(\mathbf{Q}+\mathbf{q}).\mathbf{R}_k) \exp(-W_k) \qquad (5)$$

is the structure factor of the normal mode j, with eigenvector $\mathbf{e}(k,\mathbf{q}_j)$. $\mathcal{P}_j(\mathbf{q})$ is the static displacement-displacement correlation function, related in the classical approximation to the static dielectric susceptibility $\chi_j(\mathbf{q})$ by a factor $1/k_B T$. It is assumed that only the normal mode is temperature dependent and that all other modes contribute to a constant background. This temperature dependence is described by the critical exponents γ and ν where

$$\chi_j(0) = C_+ t^{-\gamma} \qquad \xi_\alpha = f_+(\alpha)\, t^{-\nu} \qquad (6)$$

where $t = (T/T_c - 1)$ and ξ_α is the correlation length in a direction α.

X-ray scattering is also a powerful non-invasive technique in the study of surfaces and interfaces, and has an immediate application in the characterization of heteroepitaxial semiconducting structures. The two methods employed are total external x-ray reflectivity, and glancing incident angle x-ray rocking curve and surface scattering analyses. It is possible to determine the electron density profile as a function of depth, the individual layer thicknesses, the interfacial roughness parameters and any lattice strain.

Thermal neutrons have a wavelength which is comparable with the lattice spacing, as well as an incident energy of the same order of magnitude of that of

the collective excitations (phonons and magnons). It is possible to determine the total scattering cross section by using a two axis spectrometer, where the neutrons scattered in a particular direction are recorded irrespective of their energy. However in this case, since neutrons with different energy transfers $\hbar\omega$ will have different wavevector transfers $\mathbf{Q}$, the integrated intensity becomes an integral along a particular path in $(\mathbf{Q},\omega)$ space rather than simply an integral over ω. In order to recover the latter, the variation in $\mathbf{Q}$ must be negligible for all frequency transfers that occur. This can be achieved with an incident beam of energy much larger than $\hbar\omega$.

Neutron scattering provides an accurate measure of the dynamic dielectric susceptibility providing the scattering from the fluctuations in the order parameter are well separated in frequency from the other modes of the same symmetry.

$$\left(\frac{d^2\sigma}{d\Omega\, d\omega}\right)_{\text{one-phonon}} = \frac{k_f}{k_i} S_j(\mathbf{Q},\omega) = \frac{k_f}{k_i} \sum_{\tau_h} \left|F_j(\mathbf{Q})\right|^2 \mathcal{P}_j(\mathbf{q},\omega)\, \delta(\mathbf{Q}+\mathbf{q}-\tau_h) \qquad (7)$$

The dynamic displacement-displacement correlation function $\mathcal{P}_j(\mathbf{q},\omega)$ is related to the imaginary part of the dynamic susceptibility by the following relation

$$\mathcal{P}_j(\mathbf{q},\omega) = \frac{\hbar}{\pi}\left(n(\omega)+1\right)\chi_j^{Im}(\mathbf{q},\omega) \qquad (8)$$

where $n(\omega)$ is the phonon occupation number. The dynamic susceptibility can be approximated to that of a classically damped harmonic oscillator, provided the soft-mode frequency $\omega_j(\mathbf{q})$ is interpreted as an effective or renormalized frequency

$$\chi_j^{-1}(\mathbf{q},\omega) = \omega_j^2(\mathbf{q}) - \omega^2 - 2i\omega\Gamma_o \qquad (9)$$

where Γ_o is the damping coefficient.

Neutrons have a third property which can be exploited in the experimental study of phase transitions, a magnetic moment μ_n. The magnetic interaction between this moment and the electronic magnetic moment of a magnetic atom leads to scattering lengths of a similar order of magnitude as the nuclear scattering considered above. The equations which govern the scattering are identical in outline to those of the nuclear interaction, and enable the spin-spin correlation function at

a magnetic phase transition to be determined, as well as the magnetic structure above and below a transition temperature.

2.2 Description of Triple Axis Spectrometers

2.2.1 X-ray spectrometer

The essential elements of a triple crystal x-ray spectrometer are shown in figure 2.1 in the [+M,-S,+A] configuration. Here M, S and A refer to the monochromator, sample and analyser crystals respectively, and the signs to the scattering sense at each crystal. The angles ϑ_m and ϑ_a are determined by the crystallographic reflections at the monochromator and analyser crystals which collimate the incident and scattered radiation. They are normally equal, and are held constant in an experiment. The two angles which can be varied in any experiment are ψ (the sample crystal setting angle) and $\varphi = 2\vartheta_s$ (the analyser/detector setting angle).

The x-ray source for all experiments considered in this thesis was a rotating anode generator with a copper target. The spectral distribution of this target excited by 30 keV electrons is shown in figure 2.2. The CuK_α doublet at ~8 keV is of primary importance, the wavelengths are

$$K_{\alpha 1} = (1.54051 \pm 0.00058)\ \text{Å}$$
$$K_{\alpha 2} = (1.54455 \pm 0.00058)\ \text{Å}$$

It can be seen that the ratio of the intensities of the $K_{\alpha 1}$ to $K_{\alpha 2}$ lines is approximately two to one; the intensity of the $K_{\alpha 1}$ characteristic line is considerably greater than that of the Bremsstrahlung continuum.

The monochromator and analyser crystals used were either mosaic (pyrolitic graphite) or 'perfect' (silicon or germanium) flat crystals. The different resolution properties of these arrangements are considered later. It is possible for the monochromator to be curved (Johann monochromator (Johann 1931)) or to involve multiple reflections from the same sample (Bonse-Hart monochromator (Bonse and Hart 1965)) in order to vary these properties. The monochromator and pre-sample slit system control the

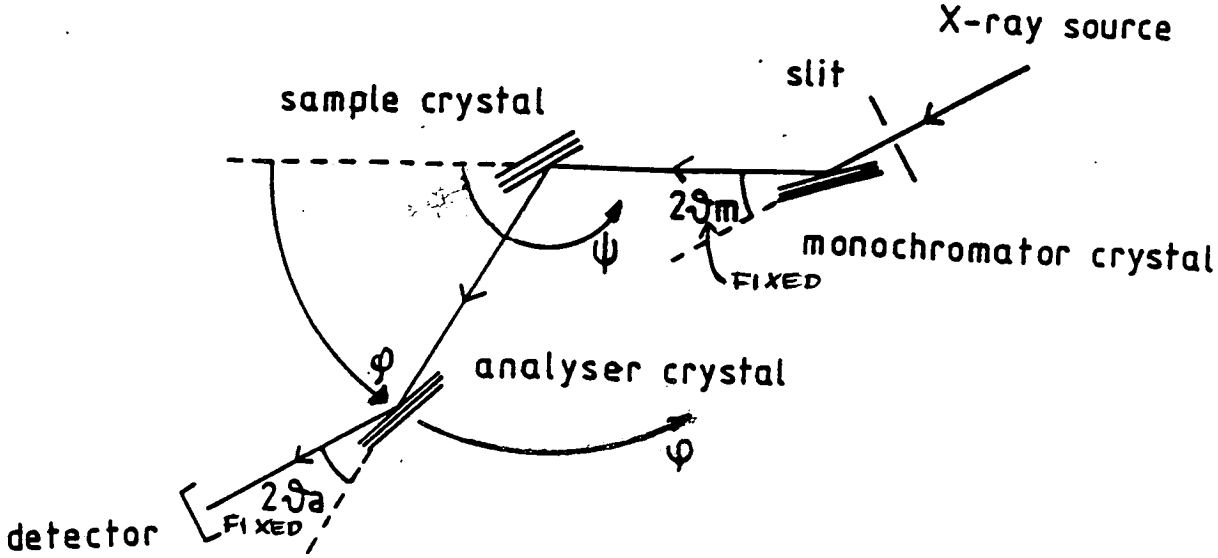

Figure 2.1

The essential elements of a triple crystal X-ray spectrometer in the [+M,-S,+A] configuration.

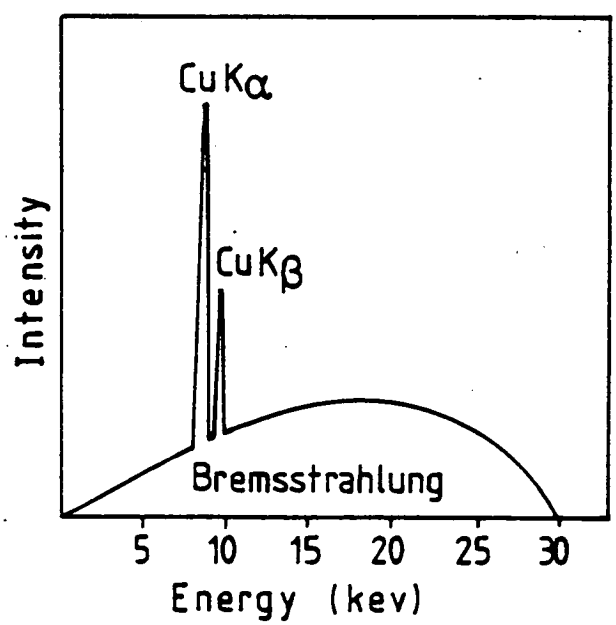

Figure 2.2

The spectral distribution of a copper target excited by 30keV electrons.

angular divergence of the beam incident upon the sample and the range of monochromatisation (error in the wavelength).

The detector was a NaI (Tl) scintillation counter with an energy resolution window of 4 keV FWHM at 8 keV. This means that higher harmonics of the frequency (chiefly $\lambda/2 = 16$ keV) which may be passed by the spectrometer will not be counted.

The use of the third analyser crystal in an x-ray spectrometer considerably simplifies the resolution properties of the instrument. This is because it probes reciprocal space only, and is independent of the position in real space of the scattered beam. Consequently such direct space effects as

- finite source size
- intensity distribution within the source
- beam path lengths
- x-ray beam penetration in the monochromator and analyser crystals
- sample size and shape

can be neglected when using a triple axis x-ray spectrometer.

2.2.2 Neutron Spectrometer

A triple axis neutron spectrometer consists of the same essential elements as the x-ray instrument described above, and is shown in figure 2.3. The monochromator angle ϑ_m determines the nominal incident wavevector amplitude $|\mathbf{k}_i|$ for the neutrons incident on the sample crystal, and the analyser angle ϑ_a defines the scattered wavevector amplitude $|\mathbf{k}_f|$. Unlike the x-ray spectrometer, the two angles ϑ_m and ϑ_a are not necessarily equal, and normally only one is held constant in an experiment. The sample crystal setting angle ψ and Bragg angle ϑ_s are also varied.

The neutron experiments described here were carried out at the thermal neutron source at the Institut Laue-Langevin, Grenoble, France. The nuclear reactor core produces high energy neutrons which are then slowed down by collisional

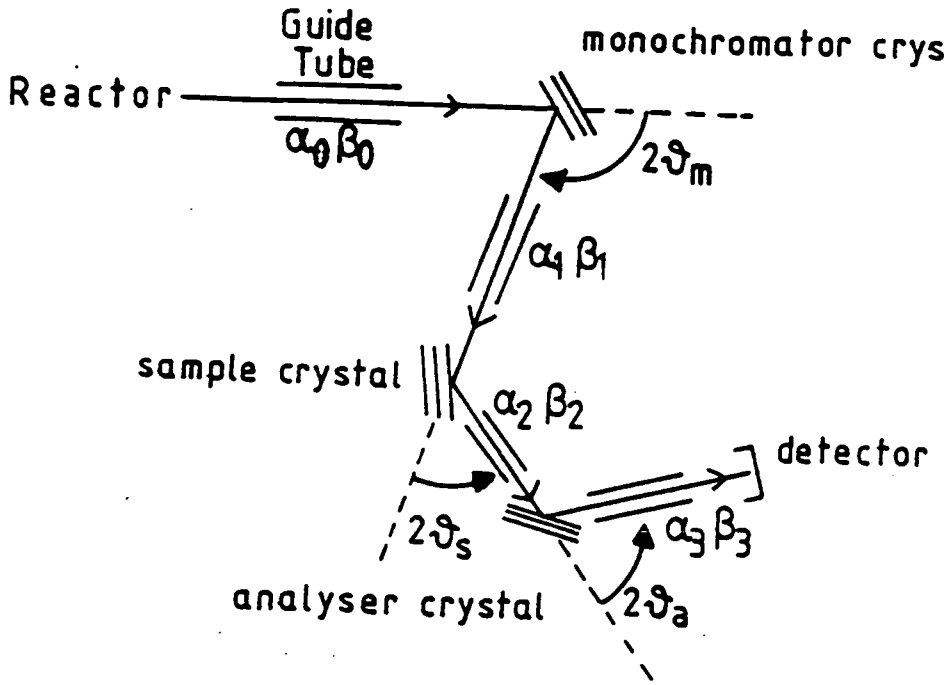

Figure 2.3

The essential elements of a triple axis neutron spectrometer in the [+M,-S,-A] configuration.

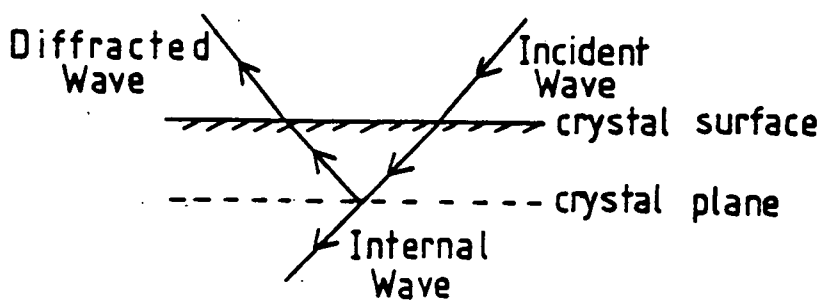

Figure 2.4

The 'Bragg case' of X-ray diffraction from plane parallel crystal plates.

processes as they pass through a moderating material (eg. D_2O). The outgoing neutrons have a spread of energies which is approximately a Maxwell-Boltzmann distribution with a peak corresponding to a neutron wavelength of $\lambda = 1.2$ Å. It is possible to shift this peak by including a hot or cold source, to give the wavelength limits $0.4 < \lambda < 0.8$ Å (hot source) or $\lambda > 4.0$ Å (cold source).

The monochromator crystal used in all experiments was a flat pyrolitic graphite crystal, and the analyser was either flat pyrolitic graphite or germanium. When pyrolitic graphite crystals are used higher harmonics of the frequency must be eliminated by inserting a filter (on arm 1 for fixed $|\mathbf{k}_i|$), which lowers the probability of transmission of those harmonics. The filters employed were either pyrolitic graphite ($|\mathbf{k}_i| = 2.662 \text{Å}^{-1}$) or cooled beryllium ($|\mathbf{k}_i| = 1.5 \text{Å}^{-1}$) . However, if the beam is diffracted by a germanium (111) reflection at the analyser crystal, the systematic absence of the (2 2 2) reflection means that the $\lambda/2$ component can be completely eliminated.

The neutron beam is passed through collimators on all three arms of the spectrometer in order to restrict the horizontal and vertical divergence of the transmitted neutrons. A monitor is placed on arm 1 which counts the number of neutrons incident on the sample. Consequently in a scan the number of neutrons reaching the detector is counted for a fixed monitor count. This compensates for inevitable fluctuations in the incident neutron flux.

2.3 The Wave Dynamical Theory of X-ray Diffraction for an Ideal Crystal

In a crystal which has negligible mosaicity and a perfect lattice, the wave dynamical theory of x-ray scattering provides a general theory of diffraction, in which normal absorption as well as the interaction between incident and scattered radiation are taken into account (Zachariasen 1945). Normal absorption occurs for all directions of incidence, but extinction is an additional absorption that arises when the Bragg equation is exactly or nearly satisfied. The wave kinematical theory of diffraction neglects both normal absorption and extinction since it assumes that the incident x-ray wave suffers no change as it enters the crystal medium. In other words, the contribution to the electric field inside the crystal which comes from the diffracted waves is neglected. In fact the incident and diffracted waves form a coupled system and the general theory

of x-ray diffraction becomes a problem in dispersion theory. The wave kinematical theory is a first approximation to the wave dynamical theory in the limit of small crystals, and as will be shown, can adequately predict the direction of diffraction maxima in the case of larger crystals as well.

The solution to the dynamical theory which is of interest is that for the Bragg case, where the diffracted wave leaves the crystal via the same boundary as it entered (figure 2.4). In the limit of a thick crystal, with negligible normal absorption, the intensity of the diffracted wave is found in terms of a function y (rotating crystal method)

$$y = 1 - (\vartheta - \vartheta_b) \sin 2\vartheta_b \; / \; K \, |\alpha_h| \qquad (10)$$

where K=1 for normal and $K = |\cos 2\vartheta_b|$ for parallel polarization, ϑ_b is the Bragg glancing angle, and ϑ the actual glancing angle, and with

$$\alpha_h = - e^2 F_h \; / \; m \omega_o^2 V \varepsilon_o \qquad (11)$$

where V is the crystal unit cell volume, ω_o is the x-ray angular frequency and F_h is the structure factor for the reciprocal lattice vector $\boldsymbol{\tau}_h$

$$F_h = \sum_k f(k) \exp(+i \boldsymbol{\tau}_h . \mathbf{R}_k) \exp(-W_k) \qquad (12)$$

for atoms of type k in the unit cell.

The solution for the ratio of diffracted intensity I_d to the incident intensity I_o is

$$\begin{aligned} I_d / I_o &= 1 && |y| < 1 \\ I_d / I_o &= 1 - \sqrt{\left(1 - {}^1/_{y^2}\right)} && |y| > 1 \end{aligned} \qquad (13)$$

giving the curve shown in figure 2.5 (the 'Darwin curve' see Darwin 1914). The region $|y| < 1$ corresponds to $2\vartheta_b > \pi$ that is, to total external reflection. The centre of the diffraction pattern is $y = 0$ or

$$\vartheta - \vartheta_b = K |\alpha_h| \; / \; \sin 2\vartheta_b \qquad (14)$$

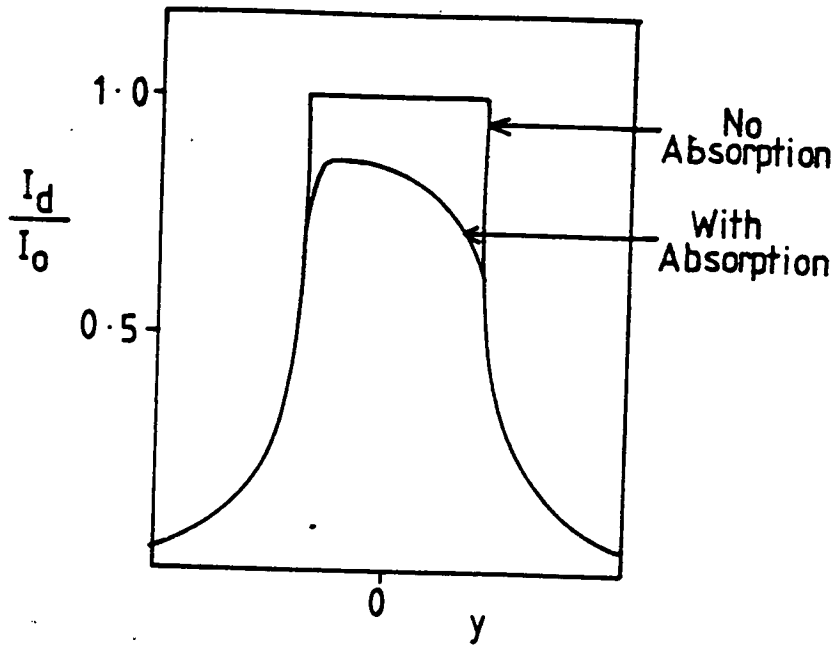

Figure 2.5

The solution to the wave dynamical theory of X-ray diffraction for a perfect crystal, commonly called the Darwin curve, which effectively gives the spectral reflectivity from a sample as a function of incident angle.

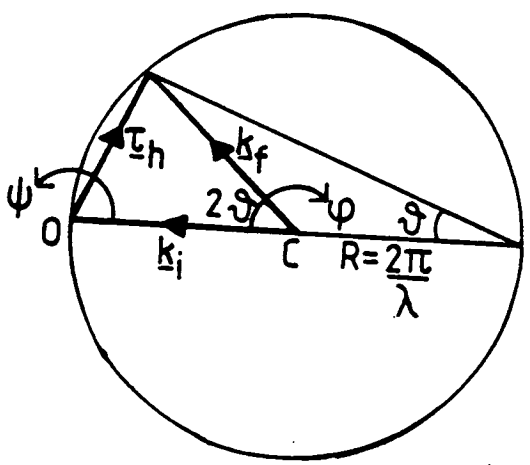

Figure 2.6

The Ewald sphere construction for elastic (Bragg) scattering. $\mathbf{k}_f$ and $\mathbf{k}_i$ are the incident and scattered wavevectors and $\boldsymbol{\tau}_h$ the reciprocal lattice vector.

In practice, this deviation from the Bragg glancing angle is negligibly small. These results show that the intensity of the diffracted beam decreases with an increase in the structure factor of the Bragg reflection; consequently extinction causes a larger reduction in intensity for a strong reflection than for a weak reflection.

The 'tails' in intensity corresponding to large |y| arise because the crystal is semi-infinite in extent perpendicular to its surface (ie. because there is a step function in electron density at the surface). Consequently the scattering in reciprocal space is resolution limited in the crystal plane, but extended in a direction normal to the surface. This has been discussed using a kinematical approach by Andrews and Cowley (1985) and independently by Robinson (1986), and will be considered in more detail later.

Normal Absorption

The penetration depth of the x-ray beam is limited by photoelectric absorption (the transfer of energy to ejected electrons). It can be described by a linear absorption coefficient μ, which is defined as the fractional intensity decrease per unit length of path through the medium. The penetration depth is typically tens to hundreds of microns. The qualitative effect of normal absorption on the diffracted intensity for a thick crystal is shown in figure 2.5.

Real Crystals

In the majority of real crystals the total integrated intensities of the x-ray reflections are found to be stronger by a factor of ten or more than predicted by the wave dynamical theory and the experimental measurement of the half width of the diffraction maxima amounts to minutes of arc instead of the few seconds of arc which theory predicts. Furthermore, experiments show that the diffraction pattern for a given reflection of a given crystal species varies within wide limits from one specimen to another. The other scattering mechanisms which should be taken into account, incoherent (Compton) scattering which occurs everywhere in space (see Compton and Allison 1935), and thermal diffuse scattering (disorder due to heat motion) which is isotropically distributed about a Bragg reflection, cannot explain this difference. Therefore the crystal must consist of 'mosaic blocks', each being in itself an ideal crystal but

adjacent blocks being misoriented with respect to each other (Darwin 1914, 1922). The extinction within any one block is thus as described above, and is called primary extinction, whereas the power loss due to the beam path through previous mosaic blocks is called secondary extinction.

In a real crystal the width of a diffraction maximum is limited by the mosaic spread (angular variation between blocks) of the sample, while the intensity varies according to the size of the mosaic blocks; the Darwin curve is usually approximated to a gaussian or error function so that the tails in intensity may not be visible.

2.4 X-ray Experiments: Resolution Effects

The geometrical arguments which determine the direction of a scattered x-ray beam can be summarized by the Ewald sphere construction in reciprocal space, shown in figure 2.6. The Bragg condition is satisfied when a reciprocal lattice point lies on the surface of the Ewald sphere and

$$\mathbf{k}_f = \mathbf{k}_i + \boldsymbol{\tau}_h \tag{15}$$

for elastic scattering. Here $\mathbf{k}_i$ and $\mathbf{k}_f$ are the incident and scattered wavevectors, $\boldsymbol{\tau}_h$ is a reciprocal lattice vector, and

$$|\mathbf{k}_f| = |\mathbf{k}_i| = k_o = 2\pi/\lambda \tag{16}$$

$$|\boldsymbol{\tau}_h| = 2k_o \sin\varphi/2 \tag{17}$$

The major resolution degrading effects of a triple axis x-ray spectrometer are now considered. In reciprocal space, each effect causes an uncertainty in the position of a reciprocal lattice point in a specific direction. As implied above, the diffraction pattern shown in figure 2.5 will only be realised in practice if a crystal has a small mosaic spread. For the moment, it is assumed that this is the case for all three crystals in a triple crystal x-ray spectrometer. Consequently there will be two degrading effects associated with each crystal, the Darwin 'tails' (or surface streak) due to the finite extent of the crystal in one direction and the small but non-zero mosaic spread. The monochromator crystal has only one variable associated with it and so these two effects are superimposed along the same direction in reciprocal space; for the analyser crystal (which also has only one associated variable) they are aligned along a different direction. These two directions vary according to the reciprocal lattice

point under investigation. NB. in the following simplified discussion the difference in uncertainty (that is, the difference in amplitude) between the two effects is not considered (the reader is referred to Cowley (1987) for a more precise treatment). In the case of the sample crystal, the surface streak remains perpendicular to the sample crystal surface at all reciprocal lattice points, while the direction of the uncertainty associated with the sample mosaic spread varies depending on the reciprocal lattice point under investigation.

The resolution degrading effects can be summarised as follows

$\Delta\vartheta_m$ the angular uncertainty due to the monochromator mosaic spread (in reciprocal space this also corresponds to the monochromator surface streak)

$\Delta\vartheta_s$ the angular uncertainty due to the sample mosaic spread

$\Delta\vartheta_{sur}$ the angular uncertainty corresponding to the sample surface streak in reciprocal space

$\Delta\vartheta_a$ the angular uncertainty due to the analyser mosaic spread (in reciprocal space this also corresponds to the analyser surface streak)

$\Delta\vartheta_v$ the vertical divergence of the incident and scattered beams

$\Delta\lambda$ the wavelength spread of the incident beam

Each of these degrading effects causes an uncertainty in either the angle ψ or in φ or in both. The corresponding reciprocal space uncertainty or uncertainties can be evaluated from the diagram in figure 2.6. Any uncertainty $\Delta\psi$ in ψ causes a small rotation of the vector triangle about the origin of reciprocal space, and the associated spread in wavevector is in a direction perpendicular to $\boldsymbol{\tau}_h$

$$\Delta \mathbf{q}_\psi = 2 k_o \Delta\psi \sin\varphi/2 \, \hat{\mathbf{q}}_\perp \qquad (18)$$

where $\hat{\mathbf{q}}_\perp$ is a unit vector in the direction perpendicular to $\boldsymbol{\tau}_h$. Similarly, any uncertainty $\Delta\varphi$ in φ causes a small rotation of the Ewald sphere about its centre and the associated spread in wavevector is in a direction perpendicular to $\mathbf{k}_f$

$$\Delta q_{\varphi} = k_o \Delta\varphi \, (\cos\varphi/2 \, \hat{q}_{\parallel} - \sin\varphi/2 \, \hat{q}_{\perp}) \qquad (19)$$

where $\hat{q}_{\parallel}$ is a unit vector in the direction parallel to τ_h.

The corresponding behaviour of the major resolution degrading effects in reciprocal space can be calculated in terms of Δq_{ψ} and Δq_{φ}.

$\Delta\vartheta_m$: The error due to the monochromator causes ψ and φ to rotate through $\Delta\vartheta_m$, which implies that in reciprocal space

$$\Delta q_{\vartheta_m} = \Delta q_{\psi} + \Delta q_{\varphi} = k_o \Delta\vartheta_m \, (\cos\varphi/2 \, \hat{q}_{\parallel} + \sin\varphi/2 \, \hat{q}_{\perp}) \qquad (20)$$

which is a streak at an angle $\varphi/2$ to τ_h and hence perpendicular to k_i.

$\Delta\vartheta_s$: The sample mosaic spread causes ψ to rotate through $\Delta\vartheta_s$ while φ is constant and well defined. Hence in reciprocal space

$$\Delta q_{\vartheta_s} = \Delta q_{\psi} = 2 k_o \Delta\vartheta_s \sin\varphi/2 \, \hat{q}_{\perp} \qquad (21)$$

which is a streak perpendicular to τ_h.

$\Delta\vartheta_{ss}$: In reciprocal space the sample surface streak lies in a direction perpendicular to the sample crystal surface at all reciprocal lattice points.

$\Delta\vartheta_a$: The analyser mosaic spread causes φ to rotate through $\Delta\vartheta_a$, and defines the range of angle which the detector system will accept. In reciprocal space

$$\Delta q_{\vartheta_a} = \Delta q_{\varphi} = k_o \Delta\vartheta_a \, (\cos\varphi/2 \, q_{\parallel} - \sin\varphi/2 \, q_{\perp}) \qquad (22)$$

which is a streak at an angle $-\varphi/2$ to τ_h and hence perpendicular to k_f.

$\Delta\vartheta_v$: The vertical divergence of the beam is not observed in the plane of reciprocal space which is defined by the spectrometer. It is normally limited to $\sim 0.5^\circ$ by a horizontal slit.

$\Delta\lambda$: The wavelength spread of the incident beam also has a specific locus in reciprocal space which must be calculated via Bragg's law.

$$\begin{aligned} \lambda &= 2d \sin\vartheta \\ d\lambda &= 2d \cos\vartheta \, d\vartheta \\ \Delta\vartheta &\sim \Delta\lambda/\lambda \tan\vartheta \end{aligned} \qquad (23)$$

The monochromator rotates by an angle $\Delta\vartheta_m^\lambda$ where

$$\Delta\vartheta_m^\lambda = \Delta\lambda/\lambda \tan\vartheta_m \qquad (24)$$

the sample by an angle $\Delta\vartheta_s^\lambda$

$$\Delta\vartheta_s^\lambda = \Delta\lambda/\lambda \, (\tan\vartheta_m - \tan\vartheta_s) \qquad (25)$$

(the negative sign arises because the scattering sense is [+M,-S,+A]), and the analyser by an angle $\Delta\vartheta_a^\lambda$

$$\begin{aligned} \Delta\vartheta_a^\lambda &= \Delta\lambda/\lambda \, (\tan\vartheta_a - \tan\vartheta_s) + \Delta\vartheta_s \\ &= \Delta\lambda/\lambda \, (\tan\vartheta_m - 2\tan\vartheta_s + \tan\vartheta_a) \end{aligned} \qquad (26)$$

In practice, $\vartheta_m = \vartheta_a$ so that

$$\begin{aligned} \Delta\vartheta_a^\lambda = \Delta\varphi^\lambda &= 2\,\Delta\lambda/\lambda \, (\tan\vartheta_m - \tan\vartheta_s) \\ \Delta\vartheta_s^\lambda = \Delta\psi^\lambda &= \Delta\lambda/\lambda \, (\tan\vartheta_m - \tan\vartheta_s) \end{aligned} \qquad (27)$$

and the ratio of $\Delta\varphi^\lambda$ to $\Delta\psi^\lambda$ is two to one. The corresponding uncertainty in reciprocal space is

$$\Delta q_\lambda = \Delta q_\psi + 2\Delta q_\varphi = 2k_o \Delta\psi^\lambda \cos\varphi/2 \, \hat{\mathbf{q}}_{\parallel} \qquad (28)$$

which is a streak parallel to $\boldsymbol{\tau}_h$.

The loci of these major resolution degrading effects combine to form a 'star-like' pattern in reciprocal space for a triple crystal (+1,-S,+1) x-ray spectrometer

when the mosaic spreads of the three crystals are small (see figure 2.7). If this is not the case, the diffraction curve for each crystal is that of a gaussian function with a width determined by the mosaic spread, and the expected resolution pattern in reciprocal space is an ellipse. The predictions will be compared later with experimental measurements.

The Accessible Region in Reciprocal Space

All x-ray diffraction experiments were carried out on extended face crystals in reflection geometry (Bragg case) as shown in figure 2.4. This maximises the signal amplitude, but considerably restricts the available region in reciprocal space since if the beam is diffracted back into the sample it cannot be observed. Figure 2.8 shows the available area for the (+1,-S,+1) spectrometer configuration.

Absorption Correction

The use of extended face crystals in reflection geometry means that the absorption of the x-ray beam is dependent upon the angle between the incident beam and the sample crystal face, ψ. Specifically, the correction term for the integrated intensity (and peak intensity) of the diffracted beam at a Bragg reflection is

$$I_{out} / I_{in} = 1 / \mu (1 + \sin \psi / \sin (\varphi - \psi)) \qquad (29)$$

where μ is the coefficient of linear absorption. Consequently the two reflections (h k 0) and (h -k 0) which have the same Bragg angle, will have different intensities since their sample angles ψ differ. The geometrical construction for diffraction at these two reflections is shown in figure 2.8.

Lorentz Correction

The Lorentz factor is a geometrical term which corrects the measured intensity of a Bragg reflection for the different rates at which a reciprocal lattice point sweeps through the diffraction sphere. The correction term for the integrated intensity of a Bragg reflection is

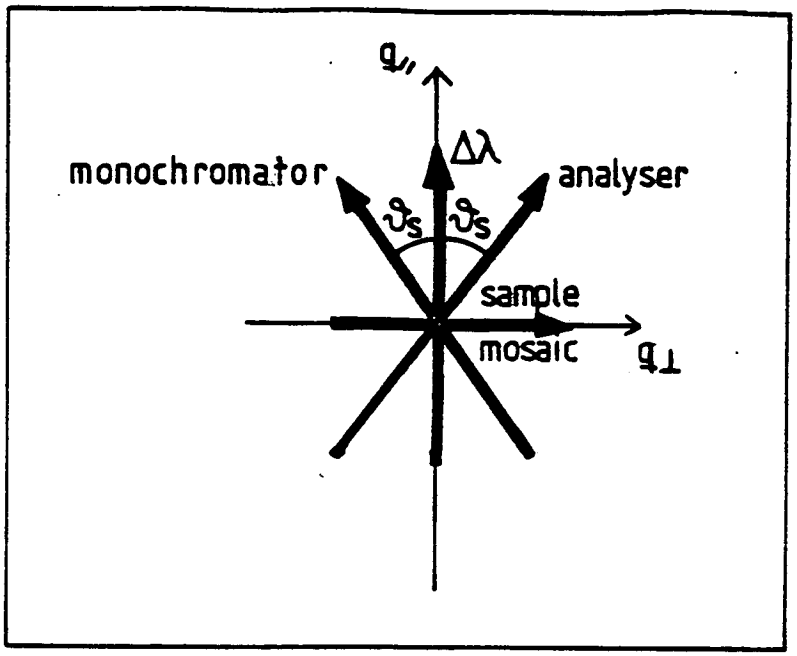

Figure 2.7

The combined loci in reciprocal space of the major resolution degrading effects for a triple crystal X-ray spectrometer in the [+M,-S,+A] configuration.

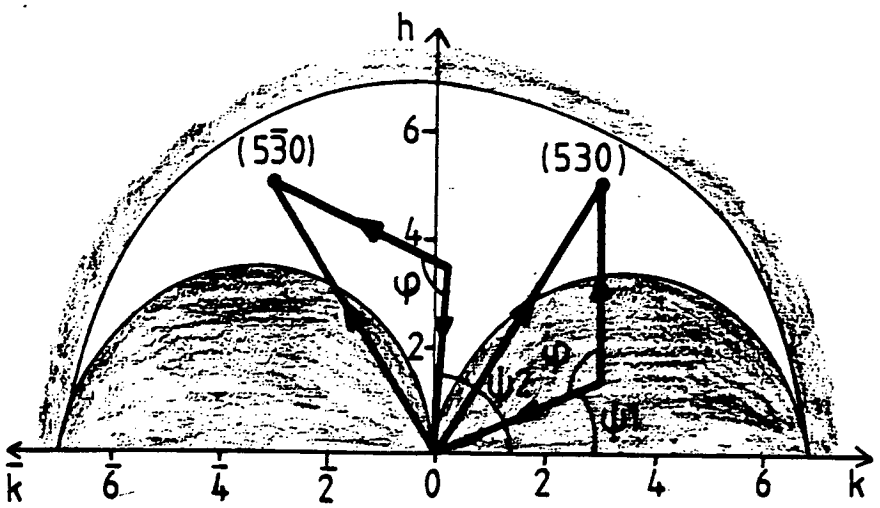

Figure 2.8

The accessible region in reciprocal space for an X-ray [+M,-S,+A] experiment on an extended face crystal in reflection geometry. The geometrical construction for diffraction from the (530) and (5-30) Bragg reflections is also shown.

$$I_{out}/I_{in} = 1/\sin\varphi \qquad (30)$$

There is some doubt if this correction term is always valid for a triple crystal x-ray spectrometer (see Cowley 1987).

2.5 X-ray Experiments: Actual Resolution Measurements

2.5.1 Low Resolution: Flat pyrolitic graphite monochromator and analyser crystals, silicon sample crystal.

The pyrolitic graphite crystals are disordered within the hexagonal basal plane but have a mosaic structure around the hexagonal **c** axis [0 0 0 1]; the distribution of orientations of the mosaic blocks can be approximated by a gaussian function as discussed above.

Some measurements of the resolution function at the Bragg reflections (4 0 0) and (4 -4 0) are shown in figure 2.9 (pre-monochromator slit width 0.5 mm). In the case of a mosaic crystal this slit effectively controls the mosaic spread of the monochromator $\Delta\vartheta_m$ since it restricts the area of crystal illuminated. It can be seen that the resolution is dominated by $\Delta\vartheta_m$ and $\Delta\vartheta_a$, and that to approximate $\Delta\vartheta_m$ by a gaussian function may be inappropriate.

The reciprocal space resolution is therefore fixed to be $\sim 2\times10^{-3}$ Å^{-1} in one direction by the analyser crystal, and can be varied between 2×10^{-3} Å^{-1} and 2×10^{-2} Å^{-1} in the perpendicular direction depending upon the pre-monochromator slit.

2.5.2 High Resolution: Flat germanium monochromator and analyser crystals, GaAs sample crystal.

The germanium crystals have a very small mosaic spread and can be considered perfect crystals. All major resolution degrading effects can be observed in an experiment, as shown in figure 2.10 for the (4 0 0) and (4 2 2) Bragg reflections.

The silicon monochromator and analyser crystals fix the reciprocal space resolution to be $\sim 5\times10^{-4}$ Å^{-1}, a factor of 10^{-2} smaller than that of pyrolitic

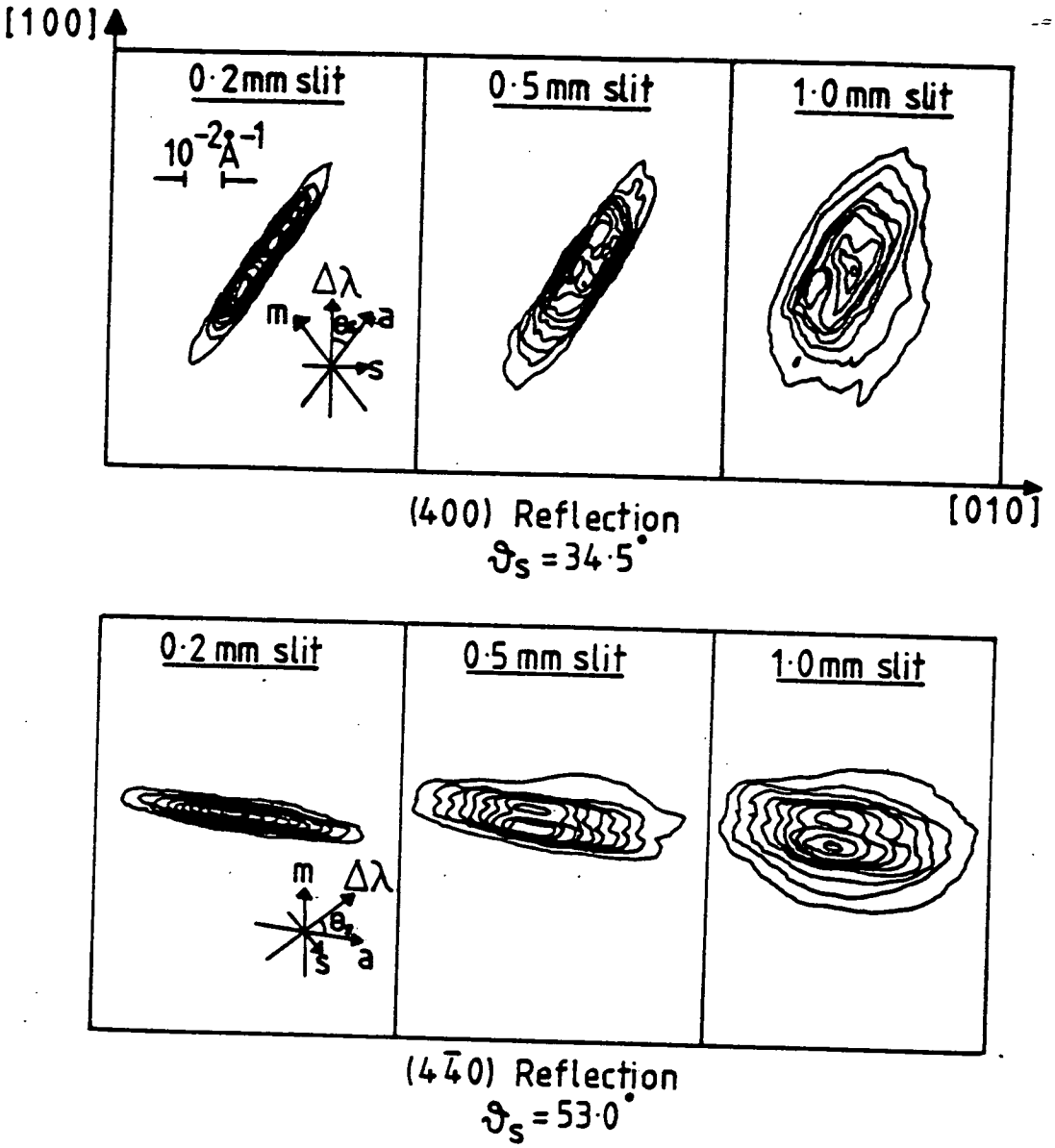

Figure 2.9

The resolution of a triple crystal X-ray spectrometer with pyrolitic graphite monochromator and analyser crystals; silicon sample crystal and various different pre-monochromator slits, for the (400) and (4-40) Bragg reflections.

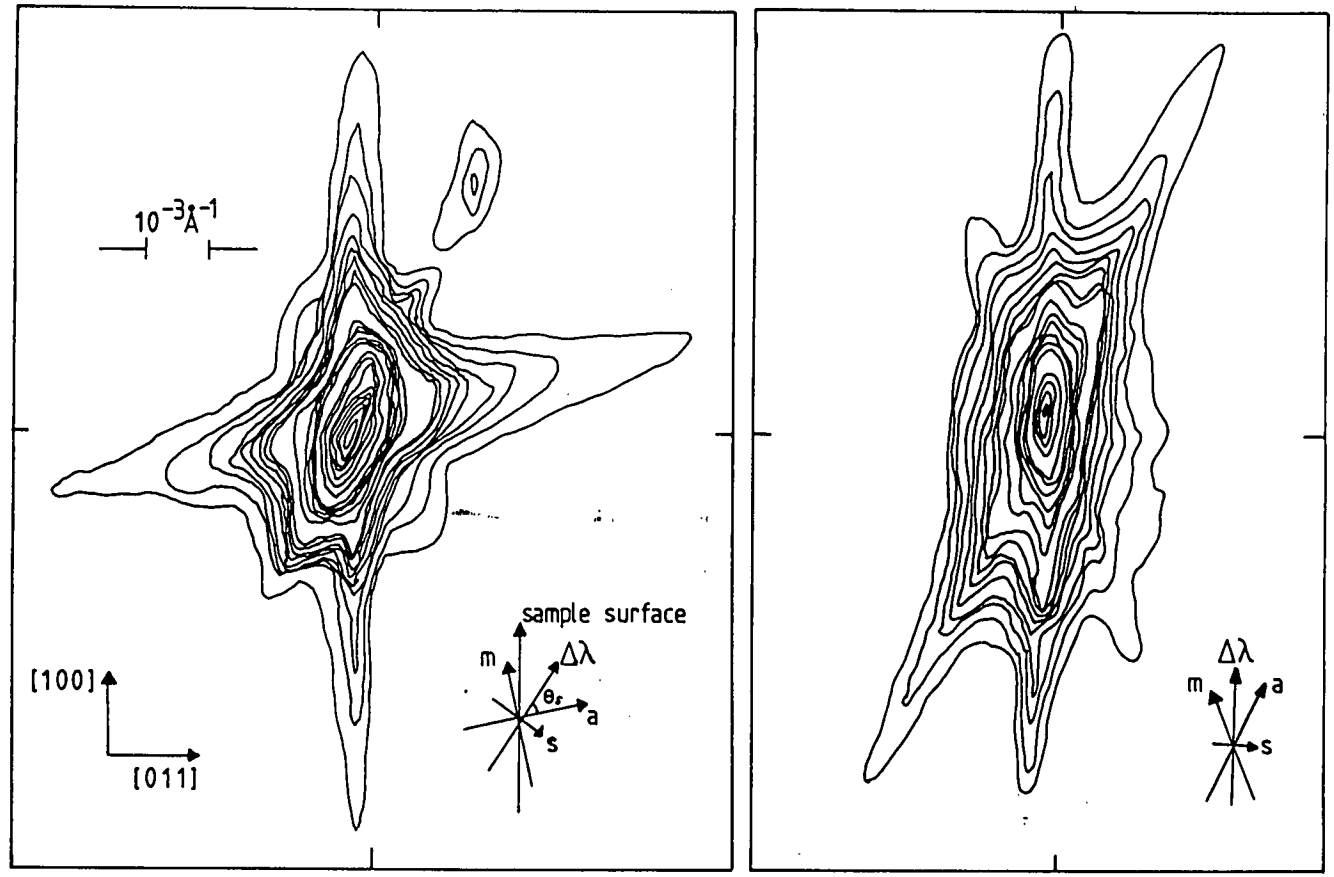

Figure 2.10

The resolution of a triple crystal X-ray spectrometer with germanium monochromator and analyser crystals and GaAs sample crystal, for the (400) and (422) Bragg reflections. The contours refer to the levels 0.1%—1%, 1%—10% and 10%—100%.

graphite. However the higher resolution means that the $K_{\alpha 2}$ component from the copper K_{α} source must be specifically eliminated. This is achieved by introducing a knife edge or narrow slit after the monochromator where the $K_{\alpha 1}$ and $K_{\alpha 2}$ are spatially separated.

2.6 Neutron Experiments: Resolution Effects

The neutron wavevector and energy transfers to the sample are defined as

$$\mathbf{Q} = \mathbf{k}_i - \mathbf{k}_f \qquad \hbar\omega = \hbar^2/2m\,(k_i^2 - k_f^2) \tag{31}$$

Hence the sample must be set at an angle ϑ_s to the direction of $\mathbf{k}_i$ where

$$\vartheta_s = \tfrac{1}{2}\cos^{-1}(\mathbf{k}_i.\mathbf{k}_f/k_i k_f) \tag{32}$$

Elastic scans correspond to $\hbar\omega = 0$, that is, $|\mathbf{k}_i| = |\mathbf{k}_f|$ (as for x-ray diffraction), but inelastic scans ($\hbar\omega \neq 0$) mean that either $|\mathbf{k}_i|$ or $|\mathbf{k}_f|$ must be fixed in order to determine $\mathbf{Q}$ and $\hbar\omega$ uniquely.

The major resolution degrading effects of a triple axis neutron spectrometer are the following

- mosaic spreads of the monochromator, analyser and sample crystals
- finite vertical and horizontal collimation on the spectrometer arms

As mentioned previously, the distribution of orientations of the mosaic blocks of a crystal can be approximated by a gaussian function. In addition, assuming gaussian transmission functions for the collimators, a general formulation of the resolution function of a triple axis neutron spectrometer has been derived by Cooper and Nathans (1967). The resolution function is shown to be

$$R(\mathbf{X}) = R_o \exp(-\tfrac{1}{2}\,\mathbf{X}\,\underline{\underline{M}}\,\mathbf{X}) \tag{33}$$

where

$$\mathbf{X} = (\delta\mathbf{Q}, \delta(\hbar\omega)) \tag{34}$$

and $\delta\mathbf{Q}$ and $\delta(\hbar\omega)$ are errors in the wavevector and energy transfers respectively. R_o and the elements M_{kl} of the matrix $\underline{\underline{M}}$ are functions of $|\mathbf{k}_i|$, $\mathbf{Q}$, ω, the monochromator and analyser mosaic spreads and the horizontal and vertical collimations.

For any straight line through the coordinates $\mathbf{Q}$ and ω, the resolution function is a gaussian function of $\delta\mathbf{Q}$ and $\delta\omega$. The resolution ellipsoid is defined by

$$\sum_{k=1}^{k=4} \sum_{l=1}^{l=4} M_{kl} X_k X_l = 1.386 \qquad (35)$$

when the resolution function assumes the value $\frac{1}{2} R_o$.

The Cooper and Nathans formulation has been extended by Werner and Pynn (1971) to include the effect of the sample mosaic spread, and considerable work concerning the normalization factor been completed by Dorner (1972) and by Chesser and Axe (1973).

Other resolution effects such as extinction, normal absorption, and the Lorentz correction will affect the intensity of a Bragg reflection as for x-ray diffraction, although the experimental configuration of a small crystal bathed in a beam means that normal absorption is just a function of the crystal thickness and is independent of the angle of incidence. Incoherent scattering arises from the presence of different nuclear isotopes of the scattering atoms, and also from different directions of the nuclear spin relative to the spin direction of the incident particle, and is isotropic in space. Multiple scattering (scattering of neutrons by Bragg reflection many times within a single block of crystal) can also be important.

2.7 Neutron Experiments: Actual Resolution Measurements

2.7.1 Low Resolution: Pyrolitic graphite monochromator crystal, germanium analyser crystal, pyrolitic graphite filter, $KMn_{0.99}Mg_{0.01}F_3$ sample crystal. Collimator angles 0.66°, 0.5°, and 0.33°.

The resolution function of the Bragg reflection (200) is shown in figure 2.11, as seen in transverse $[0\zeta\zeta]$ and longitudinal $[\zeta 00]$ directions and also as an

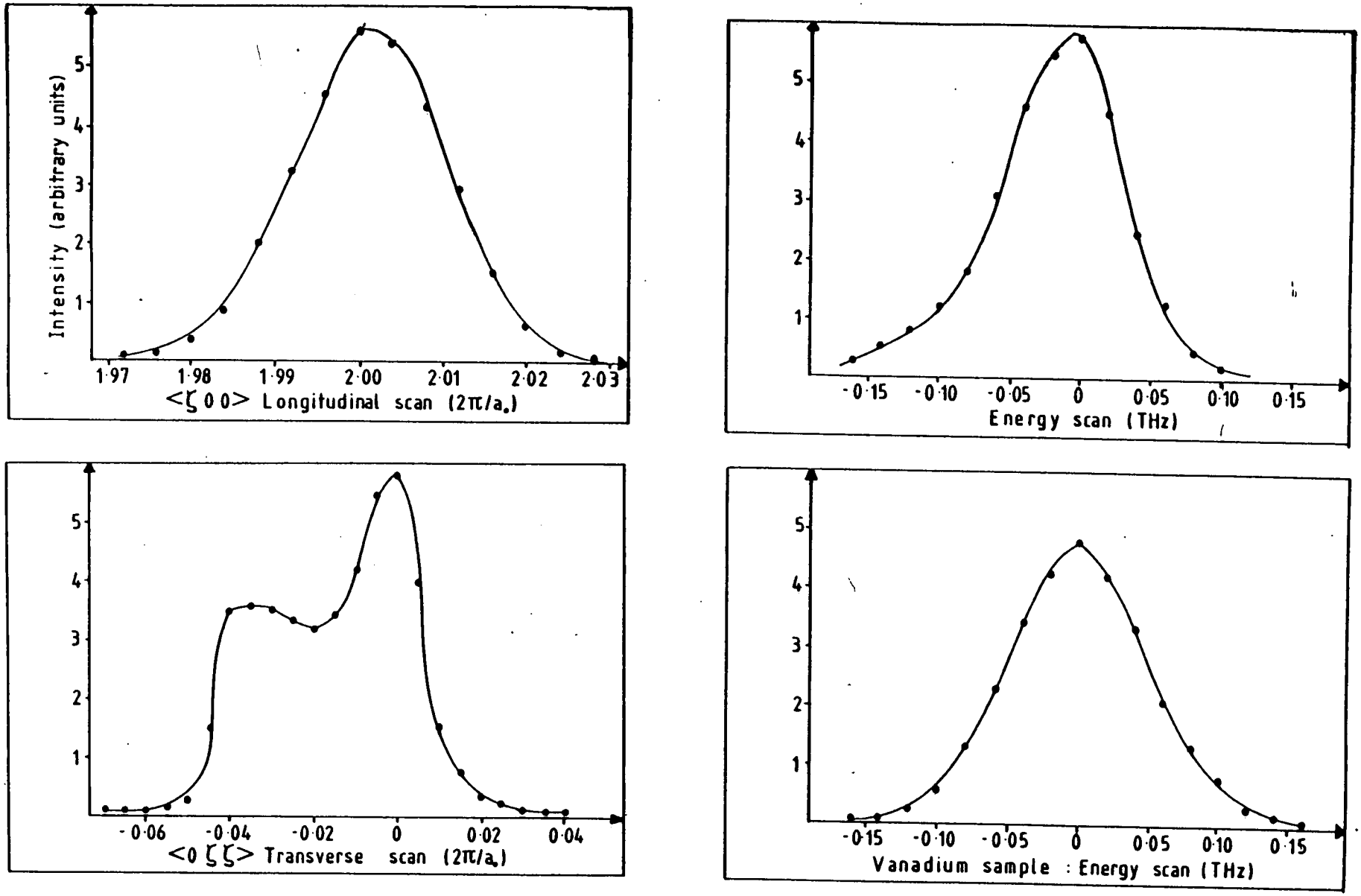

Figure 2.11

The resolution of a triple axis neutron spectrometer with pyrolitic graphite monochromator crystal, germanium analyser crystal, pyrolitic graphite filter, 0.66°, 0.5°, 0.33° collimators. The reflection is the (2 0 0) reciprocal lattice point for a $KMn_{0.99}Mg_{0.01}F_3$ sample crystal at T=190K.

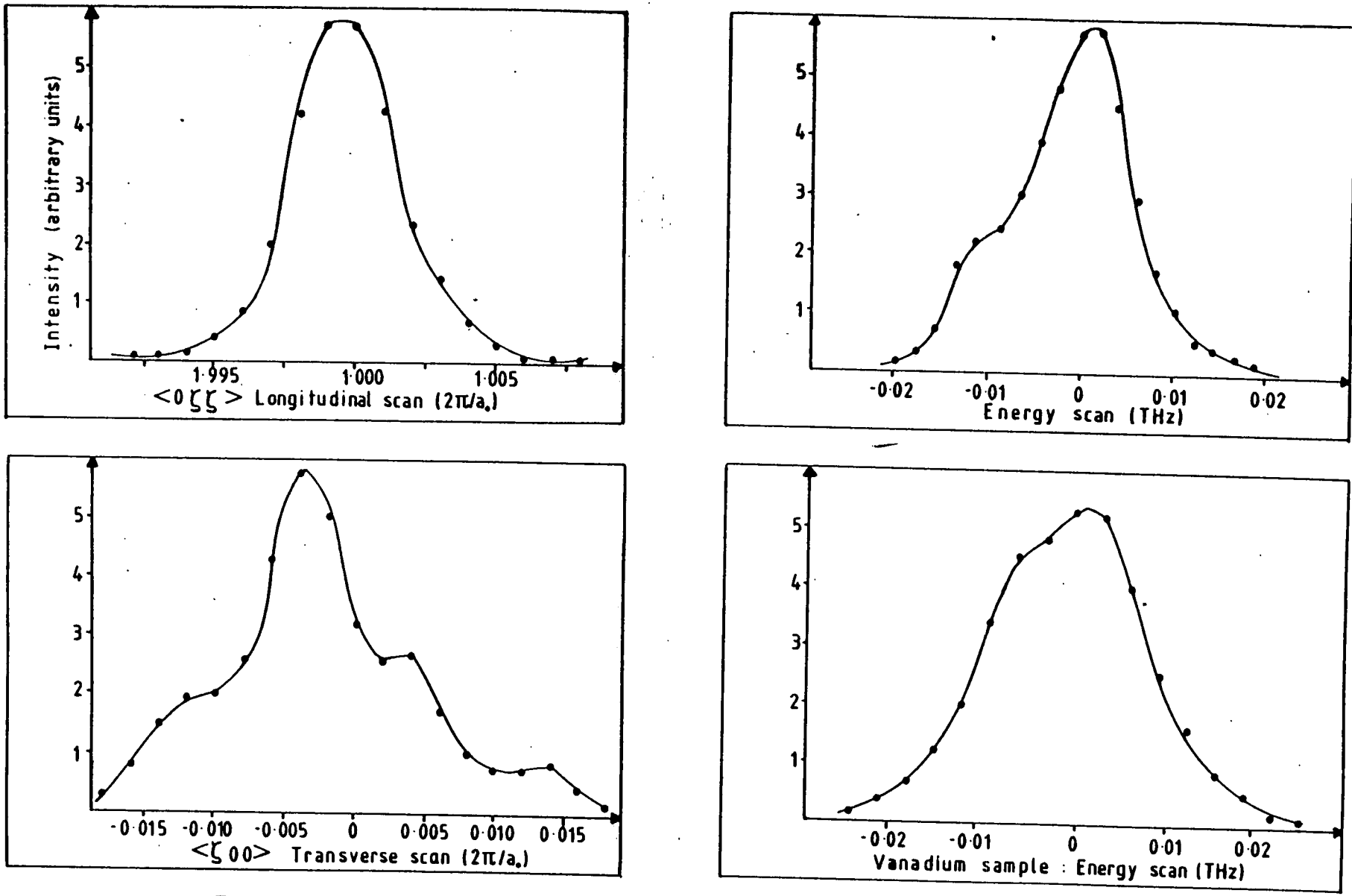

Figure 2.12

The resolution of a triple axis neutron spectrometer with pyrolitic graphite monochromator crystal, germanium analyser crystal, cooled beryllium filter, 0.66° , 0.5° , 0.33° collimators. The reflection is the (0 1 1) reciprocal lattice point for a $KMn_{0.99}Mg_{0.01}F_3$ sample crystal at T=200K.

energy scan. It can be seen that to approximate the resolution function as a gaussian in all directions and energy may be inappropriate. In particular, the mosaic spread of a sample (as seen in a transverse scan) is rarely gaussian in shape. The maximum energy width of the resolution function is found by scanning the energy with a Vanadium sample, since this scatters isotropically in space.

The resolution in wavevector is $\sim 0.07\,\text{Å}^{-1}$ (FWHM) in the transverse direction, $\sim 0.032\,\text{Å}^{-1}$ in the longitudinal direction, and ~ 0.10 THz (Bragg width) and ~ 0.12 THz (Vanadium sample width) in energy. The vertical divergence, determined by the natural collimator heights and the size of the crystal, was approximately 3.0°.

2.7.2 High Resolution: Pyrolitic graphite monochromator crystal, germanium analyser crystal, cooled beryllium filter, $KMn_{0.99}Mg_{0.01}F_3$ sample crystal. Collimator angles are 0.66°, 0.5° and 0.33°.

The resolution function of the Bragg reflection (011) when a cooled Beryllium filter is included, is shown in figure 2.12. The widths (FWHM) are $\sim 0.023\,\text{Å}^{-1}$ in the transverse direction, $\sim 0.0063\,\text{Å}^{-1}$ in the longitudinal direction, and ~ 0.014 THz (Bragg width) and ~ 0.02 THz (Vanadium sample width) in energy. The vertical divergence was again ~3.0°.

CHAPTER 3

AN EXAMPLE OF HIGH RESOLUTION X-RAY SCATTERING: INVESTIGATION OF THE EFFECTS OF DRY ETCHING ON GaAs SURFACES

3.1 Introduction

Two different x-ray scattering methods have been used to study the effects of the dry etching technique upon the surface of GaAs wafers. The first uses total external reflection of x-rays, which occurs for sufficiently small angles of incidence (Cowley and Ryan 1987 and references therein). A measurement of the reflectivity as a function of angle of incidence provides information about the refractive index, and hence electron density, as a function of depth. A complementary technique, applicable only to crystalline materials, is to measure the surface scattering close to a Bragg reflection. This scattering arises from the abrupt termination of the crystal lattice and has been described in detail by Andrews and Cowley (1985). It provides information about the roughness of the crystal interface only.

3.2 Dry Etching Technique

The dry etching was performed by R. Cheung of the Department of Electrical and Electronic Engineering, Glasgow University.

Many devices based on gallium arsenide and other III-V compound semiconductors are in production or development for various electronic systems. These systems include digital and optoelectronic integrated circuits (high-speed signal processing and fibre-optic communications), monolithic microwave circuits (e.g. radar) and optoelectronic equipment such as lasers and photodetectors. Also, devices based on quantum effects (which require structures on a length scale of 50nm) are being developed on these materials (Thoms et al 1986). Etching is an essential part of the fabrication of such devices, and dry etching is a particularly useful technique since it can produce near step function profiles on the surface of the device.

The dry etching method assessed in the x-ray experiments was one of reactive ion bombardment using $SiCl_4$ molecules. The gas enters a plasma between two parallel aluminium electrodes, supplied by a 13.56 MHz radio frequency, where it is ionised. The GaAs wafer is placed on the lower electrode, which is at a temperature of $\sim 40^{\circ}C$ and to which is applied a DC bias. The gas flow through the region is controlled at ~ 30 cc / min and the pressure constrained to be 30 - 40 mtorr. The etching is primarily achieved by means of a reaction between the freed chlorine ions and the gallium and arsenic atoms of the wafer, which produces $GaCl_2$ and $AsCl_2$. These products are thought to be volatile at the temperature and pressure concerned, which means they will be swept away. However, there will also be damage to the etched region caused by the following

- collisional processes resulting from direct ion bombardment
- deposition of compounds produced in the plasma
- deposition of material from the vacuum chamber and electrodes
- redisposition of sputtered substrate material in polycrystalline form
- diffusion into the surface of the reaction products

Assessment of the extent of this damage in terms of the deterioration of the performance of electronic devices has been made by Doughty et al (1985, 1986) by measuring the 'ideality factor' of Schottky diodes. Photoluminescence measurements were also made for diodes which had been irradiated with 633 nm HeNe laser light. All of these results only provide information about the deterioration with dry etching of electrical conductivity and semiconducting properties. X-ray techniques contribute additional information since they probe the structure of a material.

3.3 Experimental Results

The incident and scattered x-rays were collimated by reflection from the (111) planes of germanium crystals.

3.3.1 Reflectivity Measurements

The measurements were performed by choosing some scattering angle φ, and scanning the angle of incidence ψ (which is less than ψ_c the critical angle)

to find the integrated intensity of the specularly reflected beam from all parts of the surface. This is analogous to a 'rocking-curve' measurement of a Bragg reflection to find the mosaic spread of a sample. The profile of the curve reflects the macroscopic flatness of the surface, on a millimetre or centimetre scale. The reflectivity R is this integrated intensity, which is found as a function of scattering angle φ. It is convenient to describe the results in terms of a function $T = R\varphi^4$, for reasons discussed in the next section. Shown below are the reflectivity results for the control GaAs wafer (figure 3.1) and the dry etched sample (figure 3.2). The effect of wet etching the second sample is to drastically change the results (figure 3.3).

3.3.2 Surface Scattering Measurements

The GaAs crystals were aligned with the [110] and [001] directions in the horizontal plane of the diffractometer. The mosaic spread of the GaAs control wafer was found to be $\sim 0.008^\circ$. The surface scattering at a Bragg reflection has the form of resolution limited streaks with wavevectors perpendicular to the surface (Andrews and Cowley 1985). The measurements were made near the (113) Bragg reflection which means that the surface streak is easily resolved from other resolution degrading effects. Also, since the reflection has a small incidence angle $\psi \sim 1.5^\circ$, a greater proportion of the scattering will originate in the surface layer.

The intensity was measured by scanning the wavevector $\mathbf{q}_x = (\zeta\zeta 0)$ through the streak at various positions of the wavevector offset $\mathbf{q}_y = (00\zeta)$ (that is, centered at $\mathbf{Q} = \boldsymbol{\tau}_h \pm \mathbf{q}_y$) and integrating over the scan. The intensity is corrected for absorption, the Lorentz factor and thermal diffuse scattering. The result for the second (dry etched) sample is shown in figure 3.4a, together with the same measurements after wet etching (3.4b).

3.4 Analysis of Results

3.4.1 Reflectivity Measurements

The specular reflectivity of a system consisting of a layer of thickness d, followed by an infinitely thick bulk is given by

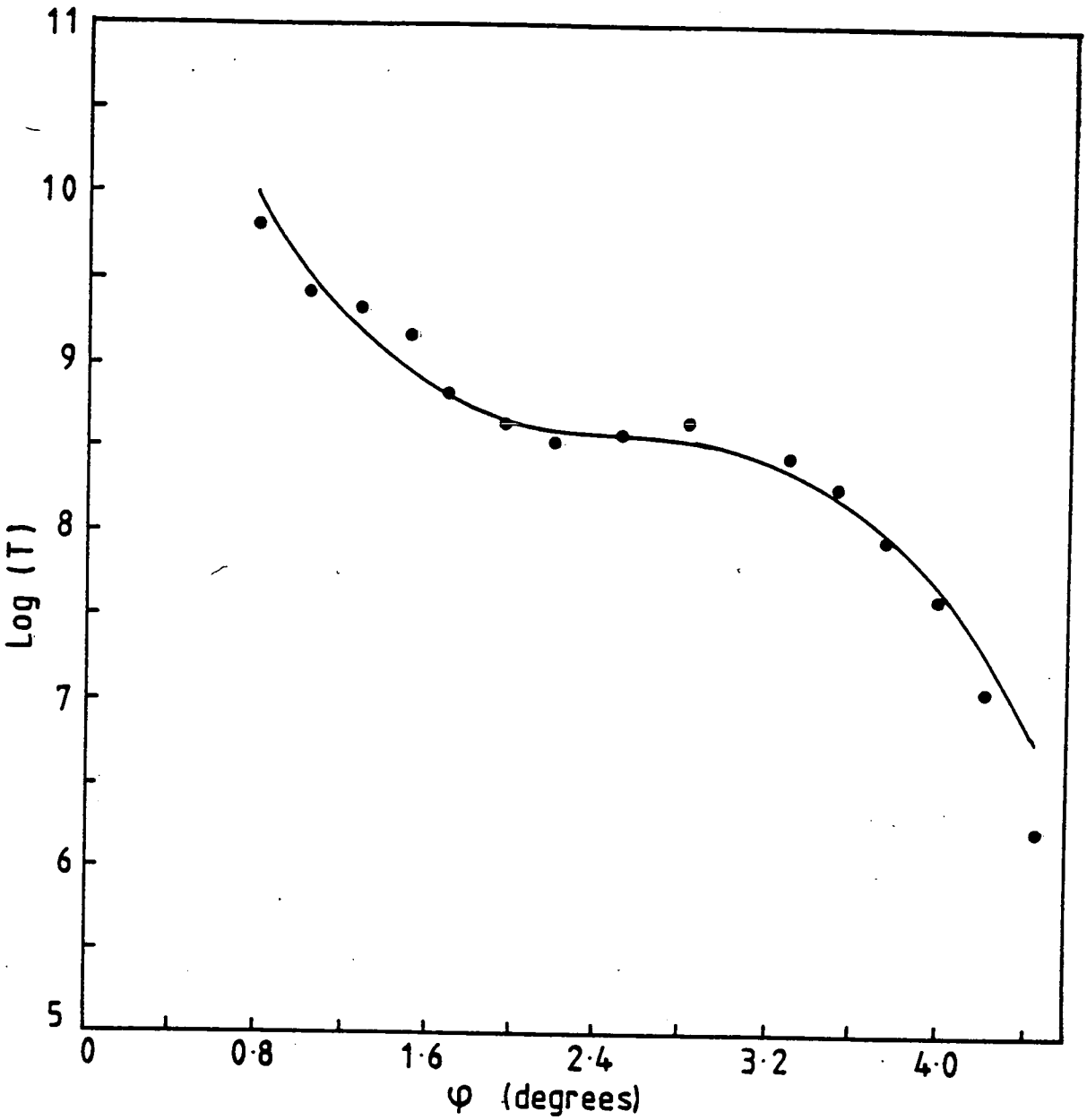

Figure 3.1

Spectral reflectivity result for the control GaAs sample. The solid line is a least squares fit to the model described in the text, and gives a surface layer of 26Å with an electron density differing by 9% from the substrate.

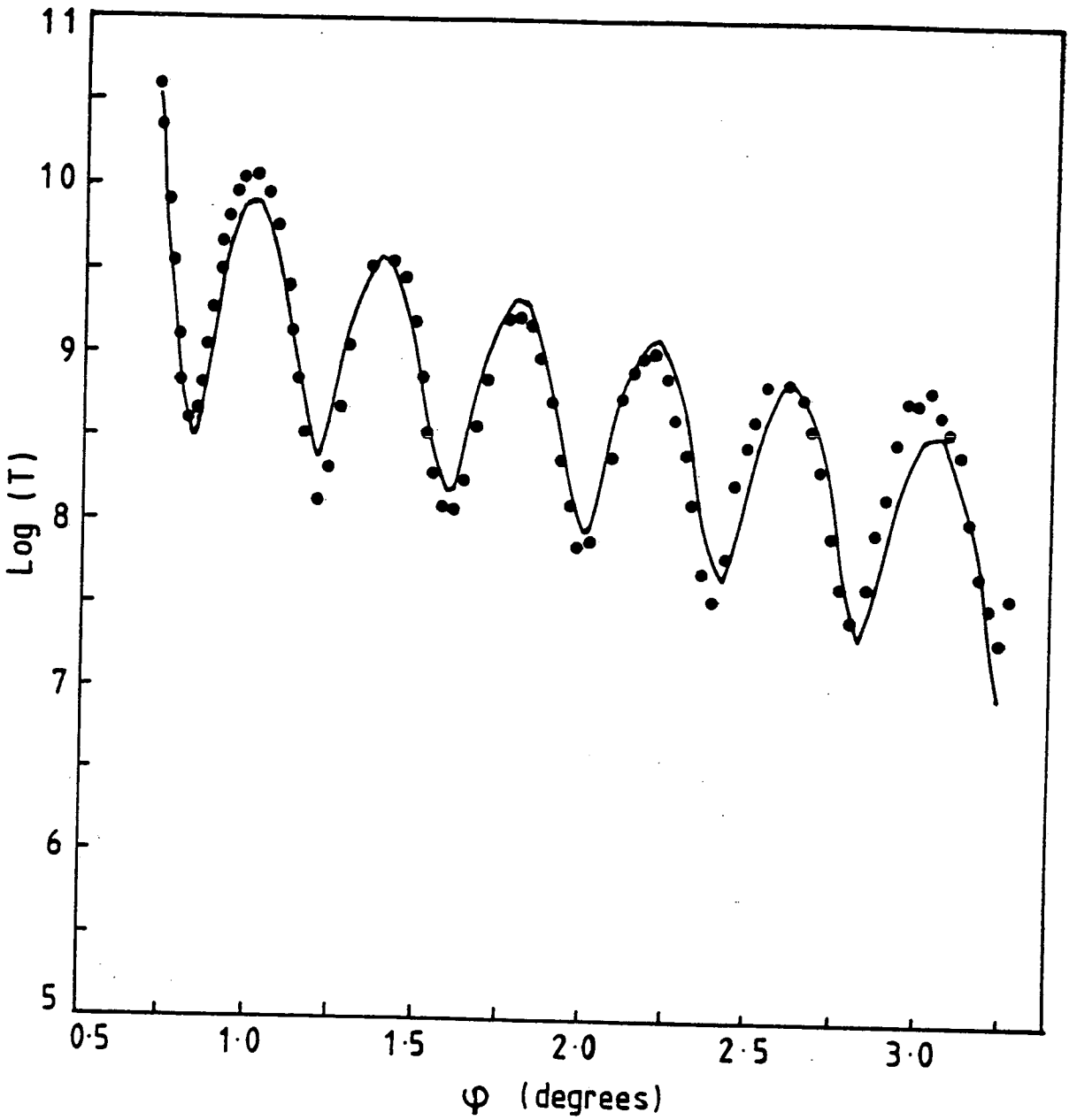

Figure 3.2

Spectral reflectivity result for the dry etched (100W, 30V DC bias) GaAs sample. The solid line is a least squares fit to the model described in the text, and gives a surface layer of ~200Å with an electron density differing by 22% from the substrate.

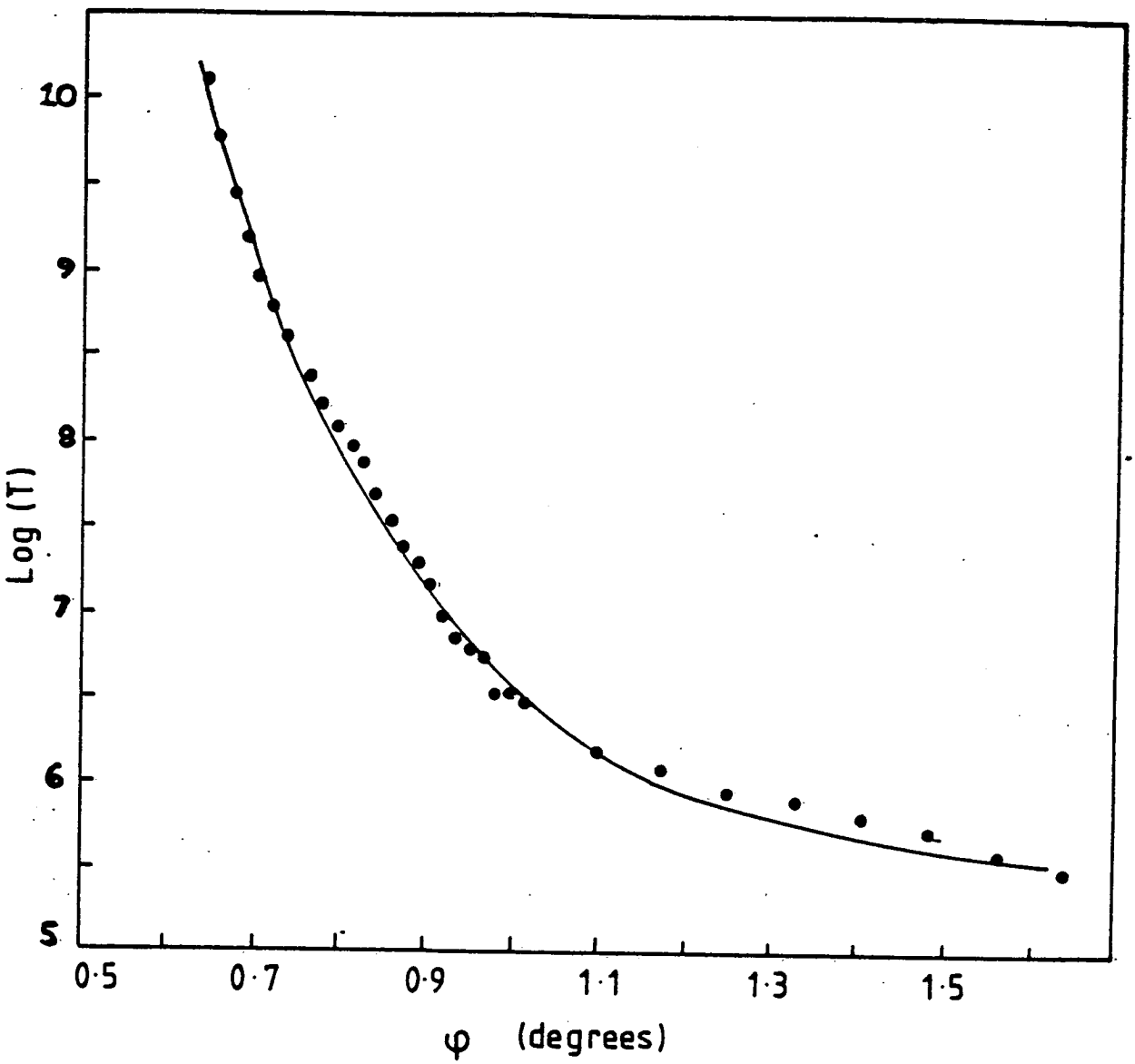

Figure 3.3

Spectral reflectivity result for the second sample after boiling in HCl for thirty minutes. The solid line is a least squares fit to the model described in the text, and shows the surface layer to be completely removed leaving a surface roughness of ~38 Å.

$$R = \frac{r_{12}^2 + r_{12} r_{23} a + r_{23}^2}{1 + a r_{12} r_{23} + r_{12}^2 r_{23}^2} \qquad (1)$$

where

$$a = 2\cos(4\pi f_2 d/\lambda) \qquad (2)$$

and the amplitude reflectivities at the interfaces are

$$r_{12} = \frac{f_1 - f_2}{f_1 + f_2} \qquad r_{23} = \frac{f_2 - f_3}{f_2 + f_3} \qquad (3)$$

while

$$f_1 = \psi^2 - \psi_c^2(i) \qquad (4)$$

where $\psi_c(i)$ is the critical angle for layer i. For $\psi \gg \psi_c$, the interface reflectivities can be written

$$r_{12} = \frac{\psi_c^2(2)}{4\psi^2} \qquad r_{23} = \frac{\psi_c^2(3) - \psi_c^2(2)}{4\psi^2} \qquad (5)$$

Consequently the denominator in the expression for R contains a term ψ^4, and the data is represented in the form $T = R\varphi^4$ where $\varphi = 2\psi$. The roughness of the interfaces is incorporated by assuming a gaussian roughness when the interface reflectivities become

$$r_{12} = \left(\frac{f_1 - f_2}{f_1 + f_2}\right) \exp\left(-\tfrac{1}{2}\left(4\pi\sigma_1 \sin(\psi/\lambda)\right)^2\right) \qquad (6)$$

where σ_1 is the root-mean-square value of the 1-2 interface, with a similar expression for the reflection coefficient r_{23} which depends on a surface roughness σ_2. As can be seen in figures 3.1, 3.2 and 3.3 this model adequately describes the results. The steady decrease of T with increasing φ is due to the surface roughness; the oscillations arise from the interference between waves reflected from the first and second interfaces, and the period of oscillation gives an

accurate measure of the layer thickness d. The amplitude of the oscillations is a measure of the difference in electron density between the layer and bulk, the increase in the relative amplitude of the oscillations with φ describes the interface roughness σ_2.

The parameters were fitted using a least squares fit to the experimental results and are listed in table 3.1 below. As can be seen in the results for the GaAs control wafer, a 26 Å layer is observed on the surface of the sample. This layer has an electron density difference of ~9 % from the bulk, and is probably an oxide layer. It is generally known that GaAs when exposed to air grows an oxide layer over a period of time. We find this layer stabilizes at a thickness of 26 Å.

A surprising result is found in the dry etched GaAs sample. A layer of ~200 Å with an electron density differing by ~22 % from that of the bulk GaAs is clearly observed (figure 3.2). This layer has to be of nearly constant thickness over a length scale of tens of millimetres to produce regular oscillations in the reflectivity curve. The values of the roughness parameters σ_1 and σ_2 indicate that both the bulk-layer and layer-air interfaces are nominally smooth. This layer cannot be an ordinary oxide layer, amorphous GaAs, $GaCl_2$ or $AsCl_2$, since the difference in electron density is too great, and hence must have arisen from deposition of material from the vacuum chamber and/or electrodes.

When this second sample was wet etched by boiling in HCl for thirty minutes, the anomalous layer was entirely removed and a surface roughness of ~30 Å introduced to the GaAs wafer.

3.4.2 Surface Scattering Measurements

The analysis of the surface data collected near the (113) Bragg reflection for the samples was carried out using the theory developed by Andrews and Cowley (1985). According to their kinematical approach the intensity of scattering arising from a flat and sharp interface varies with wavevector $\mathbf{q}_y$ as q_y^{-2} (Bragg peak or Darwin 'tails' as discussed in chapter 2). There are two models for including the effects of surface roughness on this scattering. The simplest is to include a gaussian roughness

Table 3.1

Material	d	$\Delta\rho/\rho$	σ_1	σ_2
GaAs control	26 Å	-0.09	~5 Å	<1 Å
GaAs dry etched	208 Å	-0.22	5.9 Å	4.2 Å
GaAs wet etched	–	–	38 Å	–

Table 3.2

Material	χ^2	σ_3 / Å	n
GaAs control	0.81 1.55	– 14.0 ± 1.3	2.23 ± 0.03 –
GaAs dry etched	0.58 1.51	– 12.8 ± 0.09	2.20 ± 0.02 –
GaAs wet etched	1.83 5.48	– 214.0 ± 2.5	3.79 ± 0.03 –

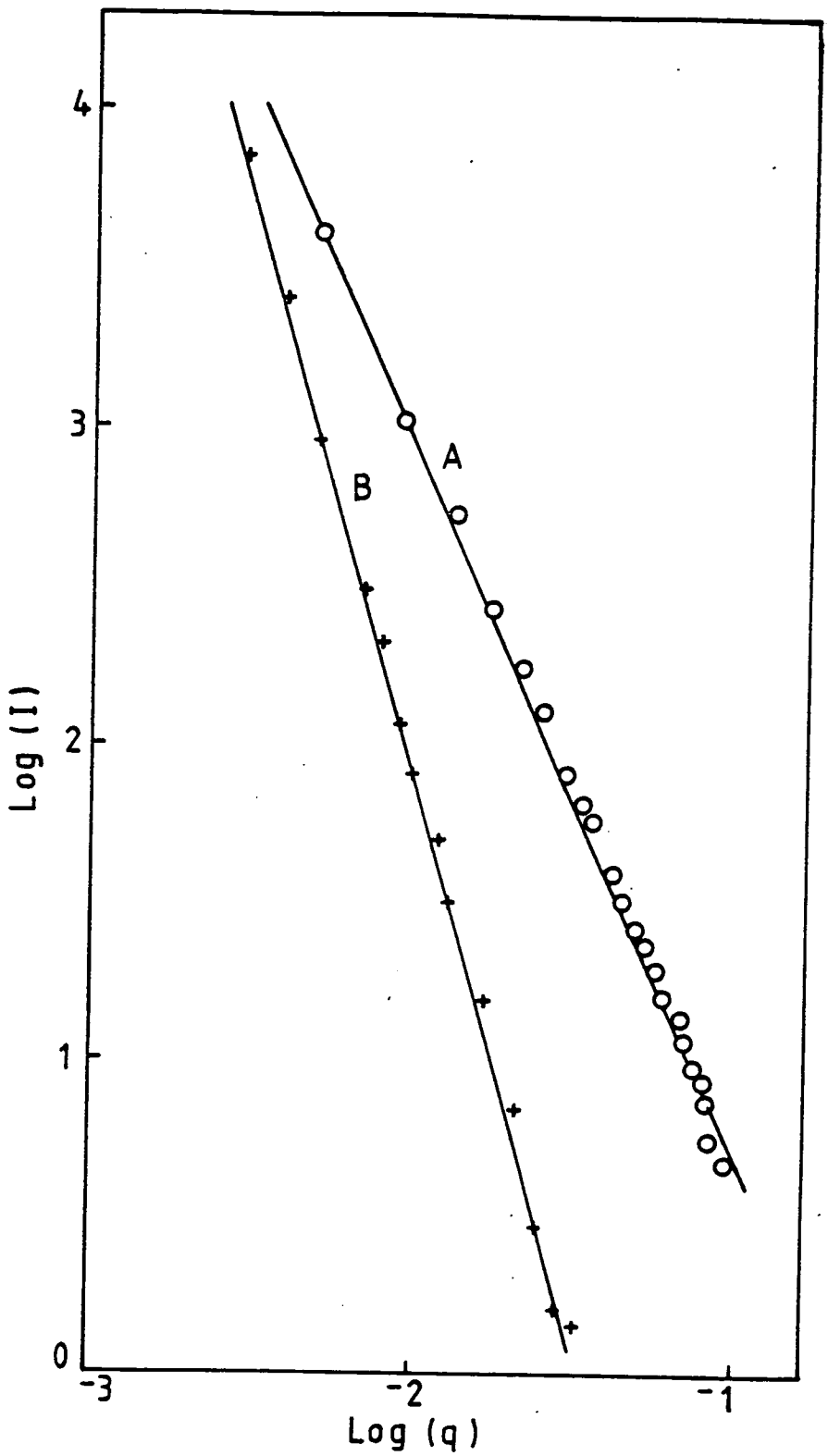

Figure 3.4

Surface scattering measurements for the (1 1 3) reciprocal lattice point for (a) the dry etched GaAs sample (b) the same sample after wet etching

$$I(q) = A/q_y^2 \exp(-(q_y\sigma_3)^2) \quad (7)$$

Alternatively, by introducing a fractal dimension to the surface

$$I(q) = A/q_y^n \quad (8)$$

where n is an exponent between 2 and 3. The data shown in figure 3.4 has been fitted to both these forms with the results shown in table 3.2. It should be noted that no oscillations are seen in the intensity as a function of q_y for curve a, figure 3.4, which suggests that the observed layer is not crystalline. The fits to the GaAs control wafer and the dry etched sample gives $n \sim 2.2$, which implies the surface in both cases is almost flat. This is further verified by the values of σ_3 obtained, $\sigma_3 = 14$ Å for the control wafer and $\sigma_3 = 13$ Å for the dry etched sample. The results for the second sample after wet etching in HCl give a value of $n = 3.8$ which is unreasonable and indicates that the surface is extremely rough; the value of σ_3 obtained is 214 Å. Since these measurements provide information about the termination of the GaAs lattice only, σ_3 is expected to equal σ_2 in table 3.1. It can be seen that the interface roughness found by the surface streak method is consistently greater than that found by the reflectivity technique. Both sets of results, however, indicate that the control GaAs wafer and dry etched samples are nominally smooth, and the effect of wet etching is to introduce a large surface roughness into the GaAs crystal.

CHAPTER 4

DETERMINATION OF THE CRITICAL EXPONENTS AT THE R-POINT INSTABILITY IN $KMnF_3$

4.1 Introduction

$KMnF_3$ belongs to the family of perovskite type crystals containing $SrTiO_3$ which undergo an antiferrodistortive phase transition from a cubic phase (with space group Pm3m) to a tetragonal phase (with space group I4/mcm): The transition in $SrTiO_3$ at T = 110K is that which has been most studied, and the theoretical results obtained in this case are expected to be generic. As discussed in chapter 1, it is generally accepted that such a phase transition is driven by an instability of the high temperature cubic phase against a three-fold degenerate zone corner (R_{25}) optic mode of vibration. The distorted phase, shown in figure 1.1, has a unit cell which is double that of the cubic phase, since the mode consists of alternate anti-phase rotations of the oxygen (or, in the case of $KMnF_3$, the fluorine) octahedra. The transition is characterized by a three component order parameter with wavevector $\mathbf{q}_s = 2\pi/a_o\,(1/2,1/2,1/2)$, and belongs to a universality class with n=3 cubic symmetry, and short range interactions, for which non-classical critical behaviour is expected. $KMnF_3$ undergoes this type of structural phase transition at a temperature of 186K as found by Minkiewicz et al (1970), and further investigated by Gesi et al (1972). The transition is slightly first order when compared with the almost continuous transition in $SrTiO_3$, and the critical fluctuations are strongly two-dimensional.

The research described in this chapter made use of a triple axis x-ray spectrometer to investigate the displacive phase transition near criticality in $KMnF_3$, and is an extention of work by Andrews (1986) on $SrTiO_3$ and by Ryan et al (1986) on $RbCaF_3$. As discussed in chapter 2, this technique enables a precise evaluation of the critical exponents associated with a structural phase transition, since the measured scattering cross section is an automatic integral over the energy and the wavevector resolution obtained is a considerable improvement over that of the best neutron triple axis spectrometers. The method provides a direct measurement of the static displacement-displacement correlation function in a system, and hence enables the effective lengthscale of the critical fluctuations at a structural phase transition

to be determined. The experimental investigations of the critical scattering in both $SrTiO_3$ and $RbCaF_3$ revealed behaviour which is not consistent with classical intrinsic theories since the scattering profile exhibited an anomalous second peak (corresponding to a long lengthscale) superimposed upon the expected phonon profile (corresponding to a shorter lengthscale) at temperatures close to T_c. It will be shown that this is also the case for $KMnF_3$. The work by Andrews suggested that the narrow component was resolution limited, but in the case of $RbCaF_3$ and $KMnF_3$ it transpires that both components can be resolved. An important question arises concerning the relationship between the central peak observed in neutron scattering experiments and the anomalous component observed here. Although the two features are not immediately comparable, they may be different manifestations of the same physical mechanism.

Two experiments were performed, the first using pyrolitic graphite monochromator and analyser crystals and the second using silicon monochromator and analyser crystals. As discussed in chapter 2, this produces two different resolution arrangements. The $KMnF_3$ crystal was grown by the Bridgeman method, and samples of approximate size 5x5x5mm were cleaved from the boule. The sample showed visible signs of growth strains and gave an x-ray rocking curve width of $\sim 0.0085(5)^\circ$(FWHM). The sample was attached in a strain free manner to the cold finger of a closed-cycle cryostat, and oriented with the face normal [001] and a cubic [110] axis in the horizontal plane of the diffractometer. The scattering plane which was investigated was therefore (1-10). The temperature stability of the cryostat was ±0.01K and temperatures were measured absolutely with an accuracy of ±0.02K.

The relevant soft-mode R_{25} corresponds to rotations of the MnF_6 octahedra about the three cubic axes, and hence has three components. It gives rise to scattering in the vicinity of the R-point in the cubic Brillouin zone, of wavevector $\boldsymbol{\tau}_R$. The wavevector dependence of the frequency of the soft mode can be expanded as a Taylor series in $\mathbf{q}$, there is no linear term in $\mathbf{q}$ when the order parameter has a high symmetry wavevector. In general the coefficients of the quadratic terms depend upon the direction of $\mathbf{q}$ and these may be reduced by symmetry for $KMnF_3$ (Cowley 1980) so that

$$\omega_{pq}^2(\mathbf{q}) = \left(\omega_o^2(0) + \lambda(\mathbf{q}^2 + f\mathbf{q}_p^2)\right)\delta_{pq} + h\,\mathbf{q}_p.\mathbf{q}_q(1-\delta_{pq}) \qquad (1)$$

The frequency is connected to the static dielectric susceptibility by the equation

$$\chi_{pq}^{-1}(\mathbf{q}) = \omega_{pq}^{2}(\mathbf{q}) \qquad (2)$$

The critical scattering (which is proportional to the static susceptibility) is hence Lorentzian in wavevector, the width depending upon the wavevector direction.

The dispersion in the scattering about the R-point in $KMnF_3$ has been measured using neutrons by Gesi et al (1972), and is shown in figure 4.1. The observed parameters are $\lambda = 42.0 \pm 0.5$ (THz Å)^2, $f = -0.99 \pm 0.01$ and $h = 0.14 \pm 0.04$. The diffuse scattering is therefore of rod-like streaks along the cubic <100> directions in the cubic phase (Comes et al 1971), since $f \sim -1$ and h is small. This can be understood qualitatively in terms of the rotations of the fluorine octahedra about a [100] axis. The fluctuations are highly correlated within the (100) plane due to a cogwheel motion between neighbouring octahedra. The inverse correlation length of these in-plane fluctuations is given by

$$\kappa = 2\pi/\xi = \sqrt{(\omega_o^2/\lambda)} \qquad (3)$$

There is no similar strong correlation between atoms along the [100] axis because the shared interplanar fluorine atoms are stationary.

The structure factors for the phonon modes corresponding to rotations of the fluorine octahedra about the three cubic axes x, y, and z for wavevectors in the (1-10) plane are found to be $F_x(\mathbf{Q}) = F_y(\mathbf{Q}) = F$, and $F_z(\mathbf{Q}) = 0$. The expectation is therefore of large and equal scattering in the <q00> and <0q0> directions (because f is close to -1), but little in the <00q> direction (because $F_z(\mathbf{Q}) = 0$).

The temperature dependence of the static susceptibility at $\mathbf{q} = 0$ is described by the equation

$$\chi_L = \chi_{pq}(0) = C_+ t^{-\gamma_L} \qquad (4)$$

where the subscript refers to a Lorentzian scattering model. The exponent γ is unity for classical theories, but is larger when critical effects are important.

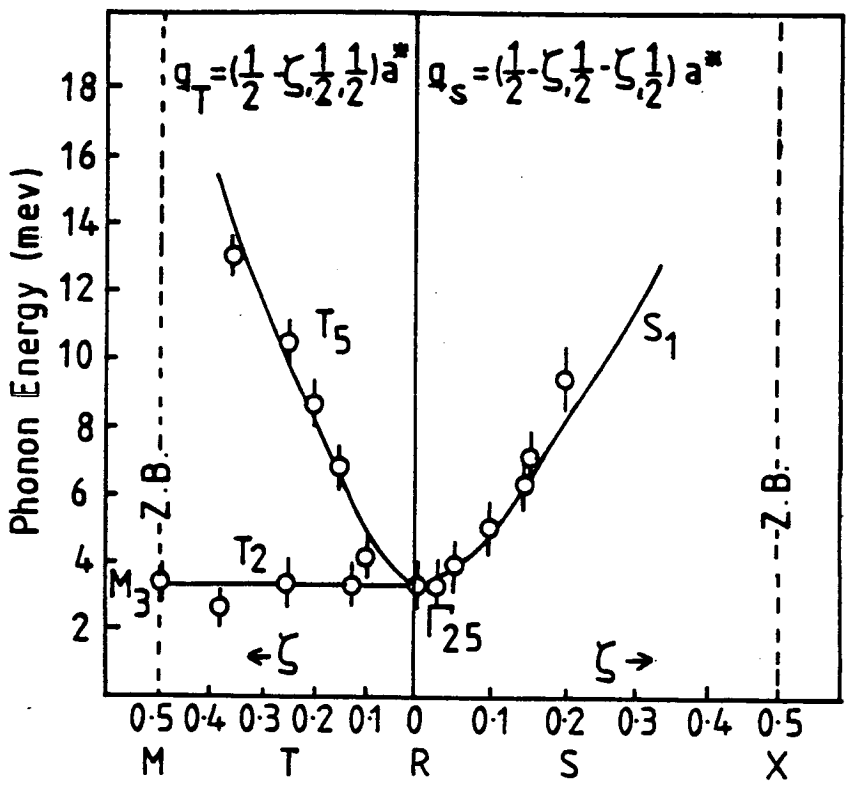

Figure 4.1

The phonon dispersion in the vicinity of the R-point in $KMnF_3$ at 295 K. The solid curves show the calculated dispersion. (After Gesi et al 1972).

Similarly the temperature dependence of the inverse correlation length of the fluctuations of the R_{25} normal mode can be characterized by the equations

$$\kappa_L = \kappa_o t^{\nu_L} \qquad \kappa_o = 2\pi/\xi_{Lo} \tag{5}$$

where ν_L is of the order of $1/2$ in classical theories and somewhat larger when critical effects are important.

When an antiferrodistortive phase transition such as in $KMnF_3$ occurs new Bragg peaks appear in the distorted phase as a result of cell doubling, the intensities of which are directly proportional to the square of the order parameter. The temperature dependence of the integrated intensity gives a measure of the exponent β used to describe the variation of the primary order parameter.

4.2 Scattering from Random Fields

Using a mean field approximation, the effect of symmetry breaking defects upon a perfect crystal is considered. The presence of isolated impurities frozen in symmetry breaking positions produces random static fields which couple linearly to the order parameter (Imry and Ma 1975) and produce a non-zero value of the local order parameter above T_c in the vicinity of the impurity. This gives rise to so called Huang scattering (Huang 1947). Specifically, the increase in potential energy due to this coupling is

$$V = \frac{1}{\sqrt{N}} \sum_{\mathbf{q}} U(\mathbf{q})\, Q(\mathbf{q}) \tag{6}$$

giving

$$\langle Q(\mathbf{q}) \rangle = \frac{1}{\sqrt{N}} \sum_{pq} U(\mathbf{q})\, \chi_{pq}(\mathbf{q}) \tag{7}$$

where $\chi_{pq}(\mathbf{q})$ is the static wavevector-dependent susceptibility of the host. Hence the observed scattering is given by

$$S(\mathbf{q}) = c \sum_{pq} \chi_{pq}^2(\mathbf{q}) \left|U(\mathbf{q})\right|^2 \tag{8}$$

where c is the concentration of impurities. We therefore expect to see a Lorentzian

squared component in the structure factor (Halperin and Varma 1976). This component is more significant close to T_c where the phonon frequency is small. The amplitude of the Lorentzian squared scattering has a temperature dependence

$$\chi_{L^2} = \chi_{pq}(0) = D_+ t^{-\gamma_{L^2}} \qquad (9)$$

4.3 Experimental Results

4.3.1 Measurement of T_c

The antiferrodistortive transition to a tetragonal phase occurs in $KMnF_3$ at 186K and is generally found to be slightly first order. In this experiment the transition temperature was measured by monitoring the intensity distribution of a Bragg peak as the temperature of the crystal was lowered, using high resolution. A typical example is shown in figure 4.2. On cooling, the (004) cubic reflection splits into a number of different peaks at T_c, caused by the domain structure of the crystal in the tetragonal phase. The transition temperature is $T_c = 187.5 \pm 0.08$ K.

Maetz et al (1978) predict that a cubic Bragg reflection will split into three tetragonal peaks below T_c, each corresponding to a rotation of fluorine octahedra about one cubic axis. At the symmetric (004) reflection the two domains with their c-axes in the plane of the crystal are superimposed, giving rise to only two peaks. However recent work on $RbCaF_3$ by Gibaud et al (1987a) shows this description to be inadequate because the domains are rotated with respect to each other. This analysis suggests that, around the (004) Bragg reflection, six peaks will be observed in a (1-10) projection below T_c.

In figure 4.2 only three peaks can be seen. It was found that the number of peaks detected corresponding to a given Bragg reflection and their relative intensities, varied as the x-ray beam was moved across the sample face. The intensities of the two major peaks of the (114) reflection below T_c were measured as a function of position across the sample, using low resolution and are shown in figure 4.3. At the -2mm position there are approximately equal proportions of both domains, while at the +1.5 mm position one of them dominates. The total intensity is roughly constant across

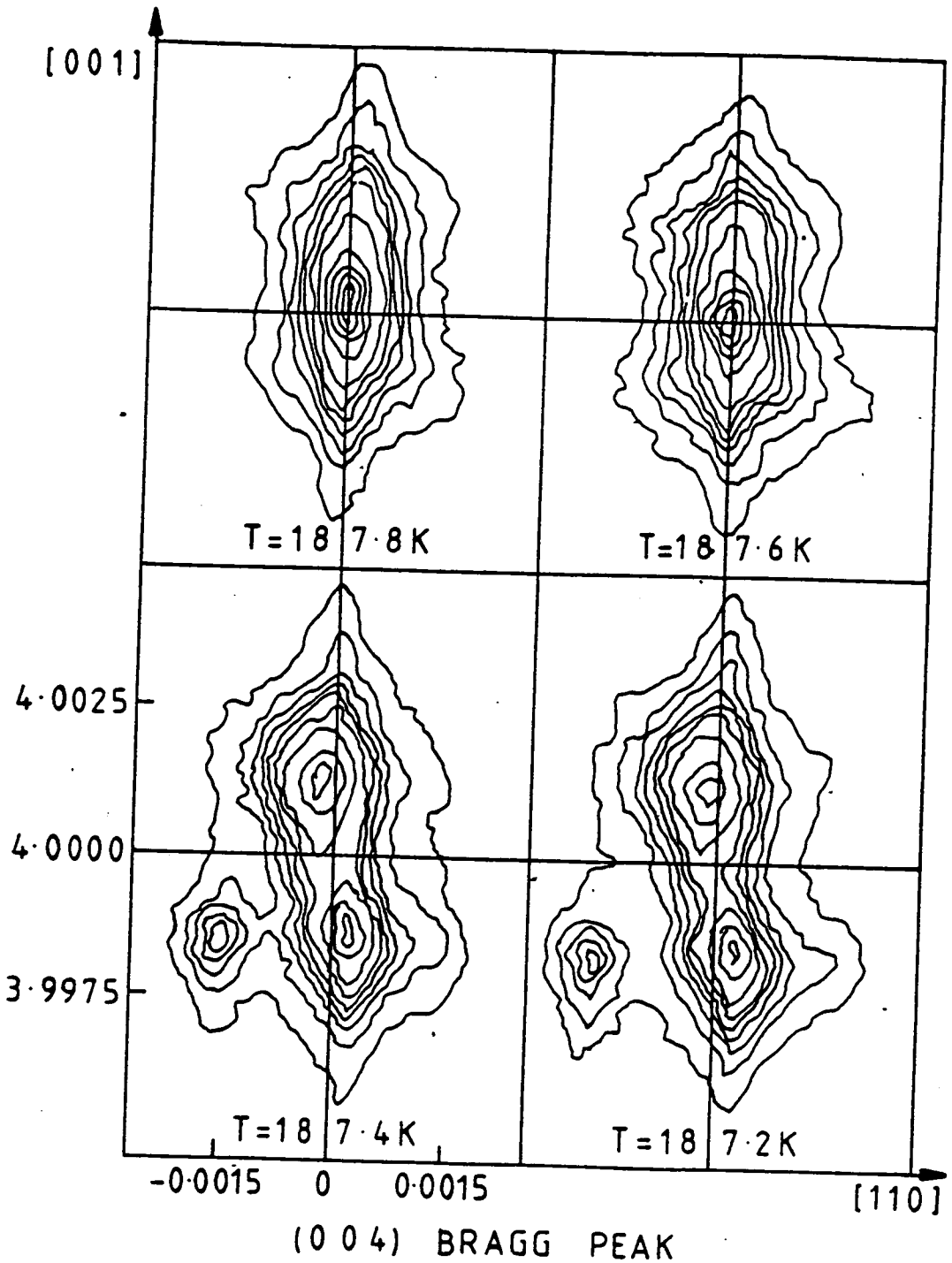

Figure 4.2

Intensity contour plot of the X-ray scattering from the Bragg peak (0 0 4) as the crystal is cooled through T_c, showing the abrupt splitting into domains at T_c. The reciprocal space axes are in units of $2\pi/a_o$.

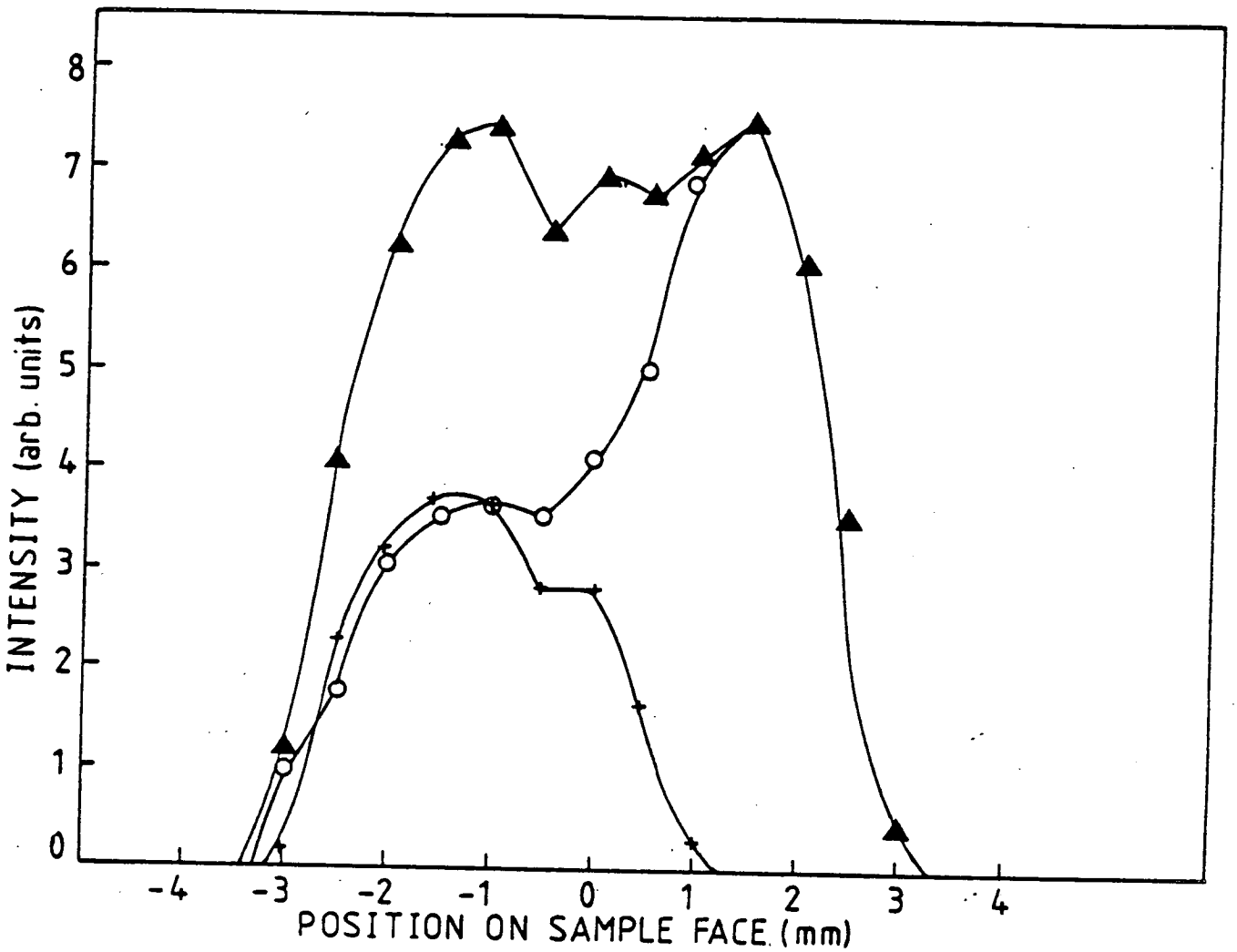

Figure 4.3

Peak X-ray scattering intensities (arbitrary units) of the two domains for the Bragg peak (1 1 4) at T = 160 K as a function of position across the sample face. The circles refer to domain 1, and the crosses to domain 2. The total peak intensity (the sum) is shown by the triangles.

the sample face and the integrated intensity did not alter significantly with temperature. This suggests that the domains are of macroscopic size.

A careful examination of a Bragg peak at a multi-domain point on the sample, using high resolution, shows five of the six peaks predicted by Gibaud and co-workers (figure 4.4). Their model can be tested by a measurement of the angle ϑ in figure 4.4, which should correspond to $\tan^{-1}(c_t/a_t\sqrt{2})$ (see appendix 1). At T = 150 K, c_t/a_t was measured as 1.0042 (1) from an analysis of the positions of the peaks in the <001> direction in figure 4.4. This predicts the angle to be $\vartheta = 35.15(1)^\circ$ which is in good agreement with the measured angle $\vartheta = 35(1)^\circ$.

4.3.2 Measurement of the exponent β

As described in section 4.1, the temperature dependence of the integrated intensity of the zone boundary scattering below the transition temperature is characterised by the critical exponent 2β. In a perovskite material such as $KMnF_3$ the method is complicated by the systematic absence of one of the tetragonal peaks, below T_c, at any superlattice reflection in the (1-10) plane . This means that if the relative proportions of the different domains are significantly temperature dependent the exponent β cannot be obtained. However, it is also possible to evaluate this critical exponent using x-ray scattering by a measurement of the tetragonal strain of the crystal as a function of temperature, since this is a secondary order parameter (see appendix 2).

Figure 4.5 shows the intensity of scattering at the (0.5 0.5 3.5) reflection, measured using the low resolution configuration, as a function of position and temperature. On approaching T_c, the dependence of the scattered intensity does appear to vary across the sample face. The extent to which this is significant is shown in figure 4.6. These curves display the integrated intensity of the zone boundary reflection , measured using low resolution (graphite monochromator and no analyser crystal), at positions -2 mm, -1 mm and +1.5 mm on the sample face. This intensity is obtained from a measurement of the rocking curve which is then integrated over the scan.

The data points for each curve were independently fitted over the range T = 150 - 190 K by a least squares procedure to the power law $I \sim t^{2\beta}$, $t = (T/T_c - 1)$.

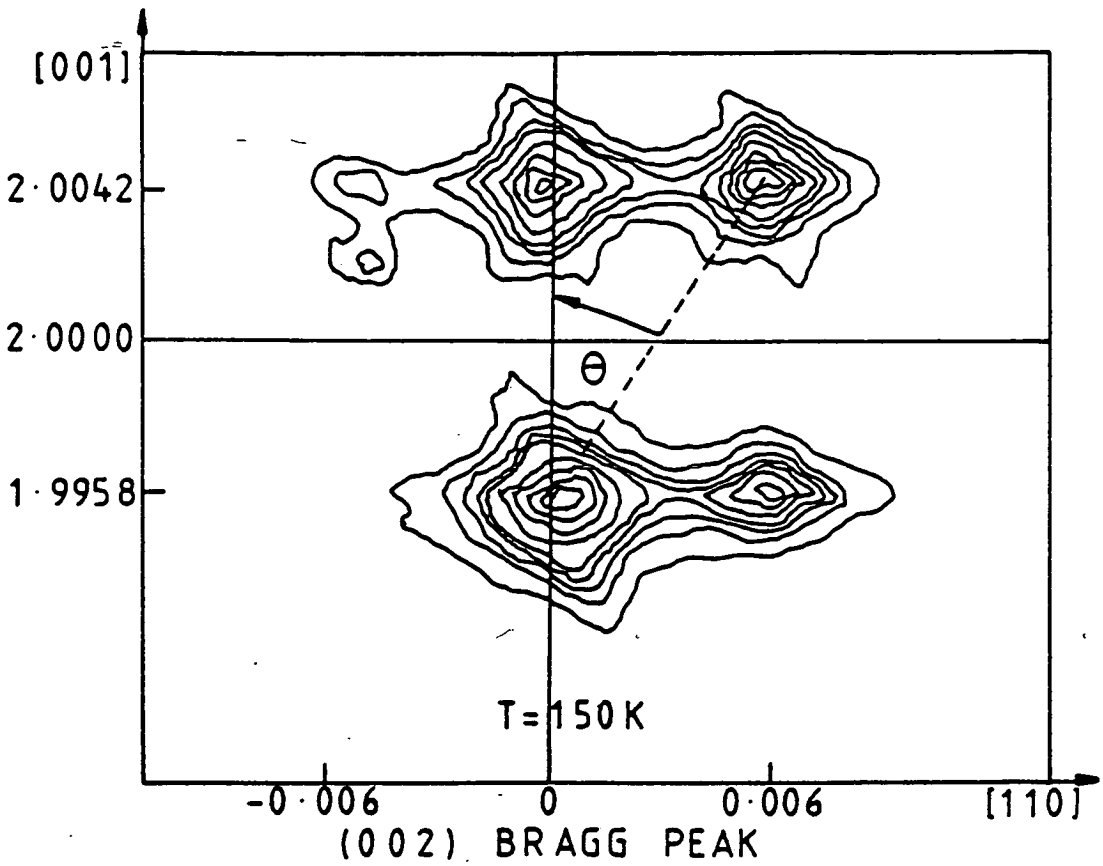

Figure 4.4

Intensity contour plot of the X-ray scattering from the Bragg peak (0 0 2) at T = 150K showing the domain structure pattern as described in the text. In the <0 0 1> direction the peaks lie at two wavevectors only; the wavevector furthest from the origin in reciprocal space corresponds to the lattice parameter a_t, and that nearer to the origin to the lattice parameter c_t. The angle ϑ measured on the figure is 35 (1)°. The reciprocal space axes are in units of $2\pi/a_o$.

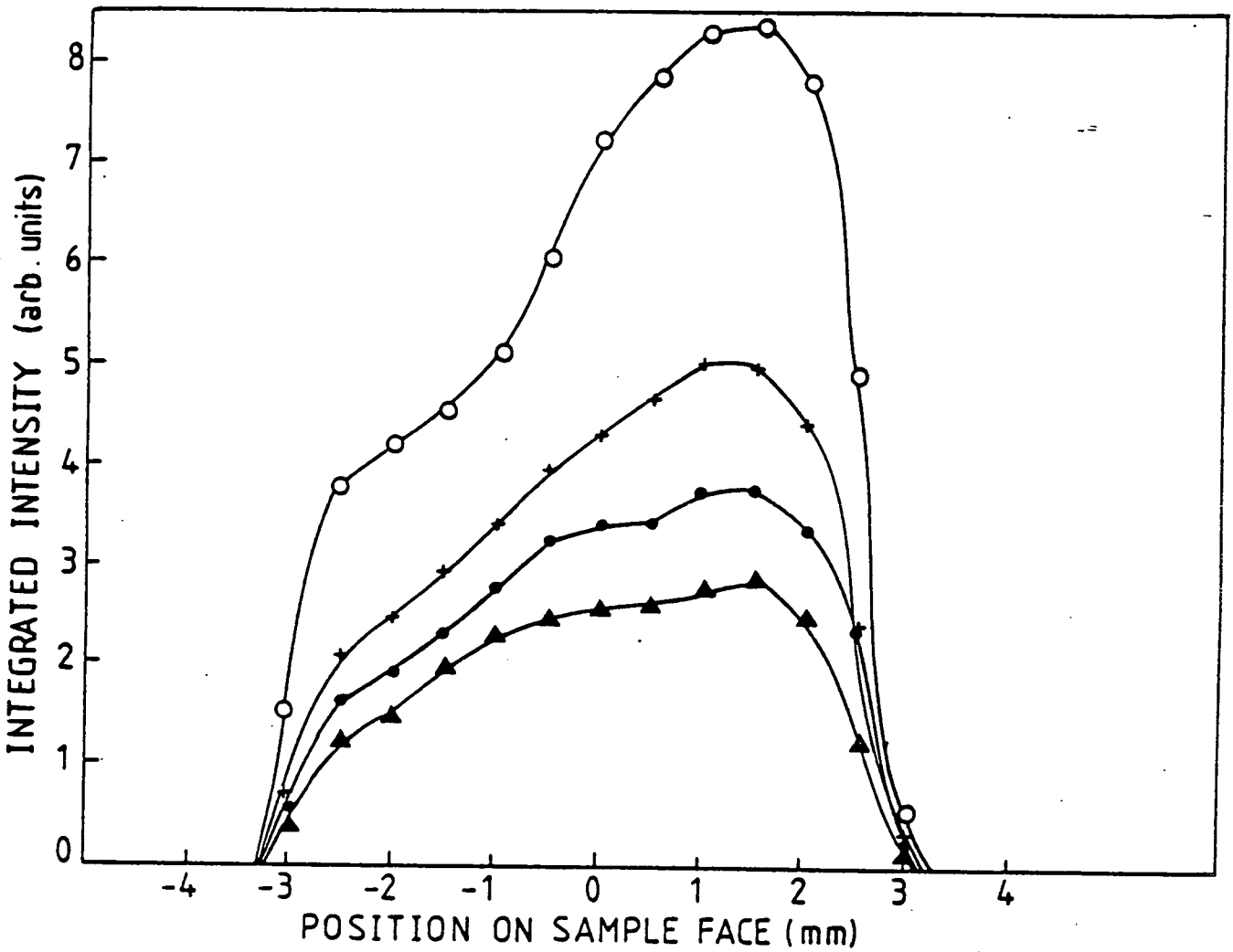

Figure 4.5

Integrated X-ray scattering intensity (arbitrary units) for the reciprocal lattice point (0.5 0.5 3.5), obtained in a measurement of the rocking curve, as a function both of position on the sample face and temperature. At this position in reciprocal space only two of the three domains contribute to the scattering. The different symbols refer to different temperatures -

open circles	T = 150K
crosses	T = 180K
closed circles	T = 185K
triangles	T = 187K.

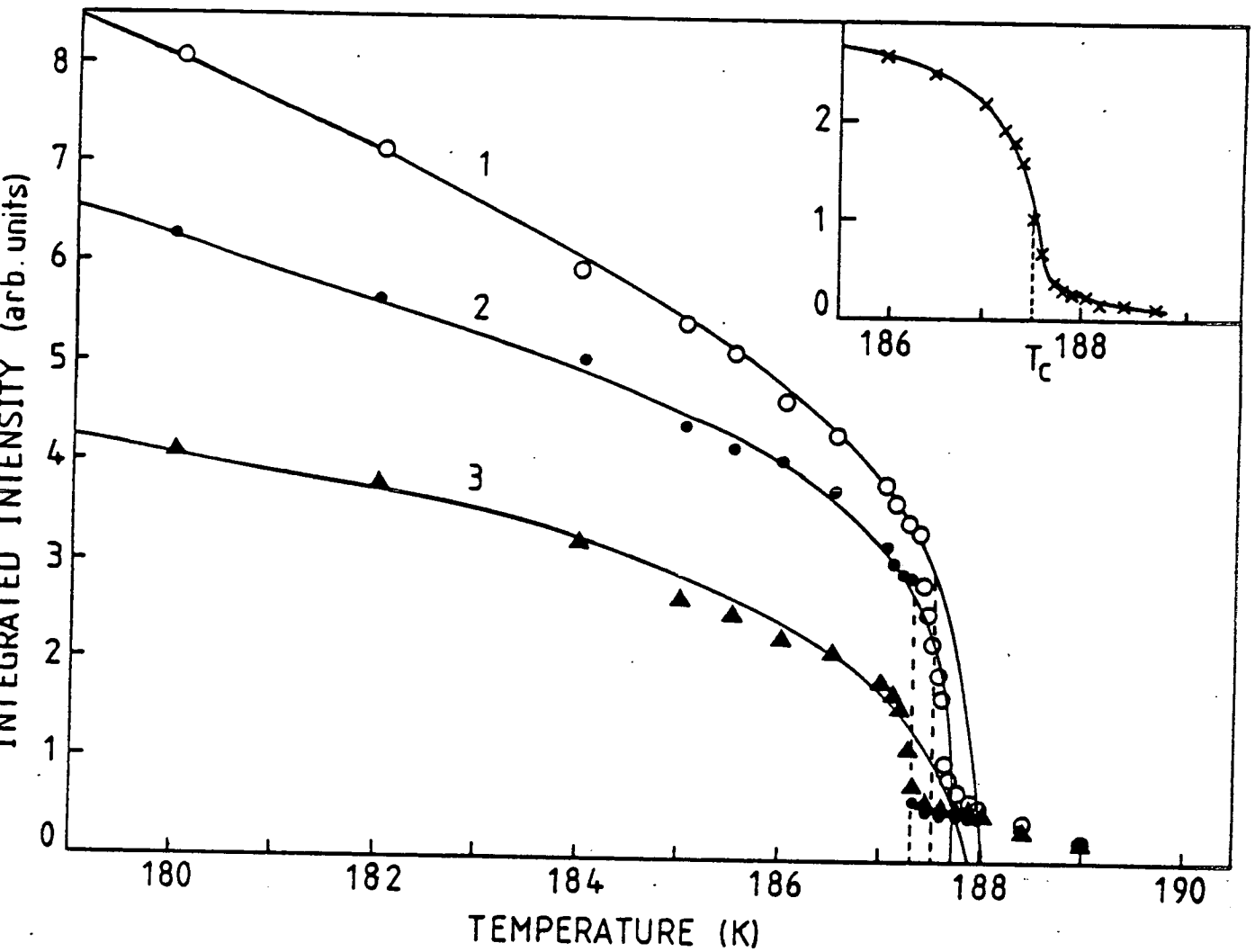

Figure 4.6

Integrated X-ray scattering intensity (arbitrary units) from the reciprocal lattice point (0.5 0.5 3.5), obtained in a measurement of the rocking curve on cooling through T_c. The three data sets were measured at different points on the sample face; set 1 at +2mm, set 2 at -1mm and set 3 at -2mm. The smooth curves are least squares fits to the power law $I \sim t^{2\beta}$ as described in the text. The inset shows the integrated intensity, obtained with higher resolution, as the crystal was cooled through T_c at position +1.5mm. The scale is also in arbitrary units.

Temperatures up to 187.3 K were included in all cases and the transition temperature allowed to vary (giving a value T_c'). The solid curves are the results of this fit and the dotted lines indicate the actual transition temperature for each set of data. Curve 1 shows an approximately continuous phase transition with $T_c \sim 187.5\,(1)$ K and exponent $\beta = 0.178$. Curve 2 displays a definite first order transition with an abrupt jump at $T_c \sim 187.3\,(1)$ K and $\beta = 0.135$. Curve 3 also shows a continuous transition with $T_c \sim 187.3\,(1)$ K and $\beta = 0.205$. This suggests that the character and the temperature of the transition are not consistent across the sample face.

The tetragonal strain in $KMnF_3$ was measured using high resolution by monitoring the ratio of the positions of the domain peaks for the (004) Bragg reflection in the <001> direction as a function of temperature. The results are shown in figure 4.7. The solid curve is a least squares fit to the power law $(c_t/a_t - 1) \sim t^{2\beta}$, with the transition temperature allowed to vary, while the dotted line is the actual transition temperature. The fit gives $T_c = 188.6$ K and $\beta = 0.26$. Table 4.1 contains a summary of the results for all measurements of the order parameter, which are discussed in section 4.4.

4.3.3 Critical Scattering

Introduction

The wavevector dependence of the critical scattering above T_c was measured around the reciprocal lattice point (0.5 0.5 3.5) using both low and high resolution. The measurements were made at the +1.5 mm position on the sample face where the scattering was most intense. Examples of low resolution scans parallel to [110] are shown in figure 4.8. The scattering profile was found to change as T_c was approached, with a temperature dependent width. Similarly, the scattering shown in figure 4.9, measured using high resolution, also has a temperature dependence. At this resolution it is only possible to detect extremely sharp components in the scattering profile, any broad part being indistinguishable from a uniform background.

X-ray scattering measurements of the R-point instability in $SrTiO_3$ and $RbCaF_3$ have been made by Andrews (1986), Ryan et al (1986), and Gibaud et al (1987a, b). These crystals showed an anomalous profile in the critical scattering at the R-point

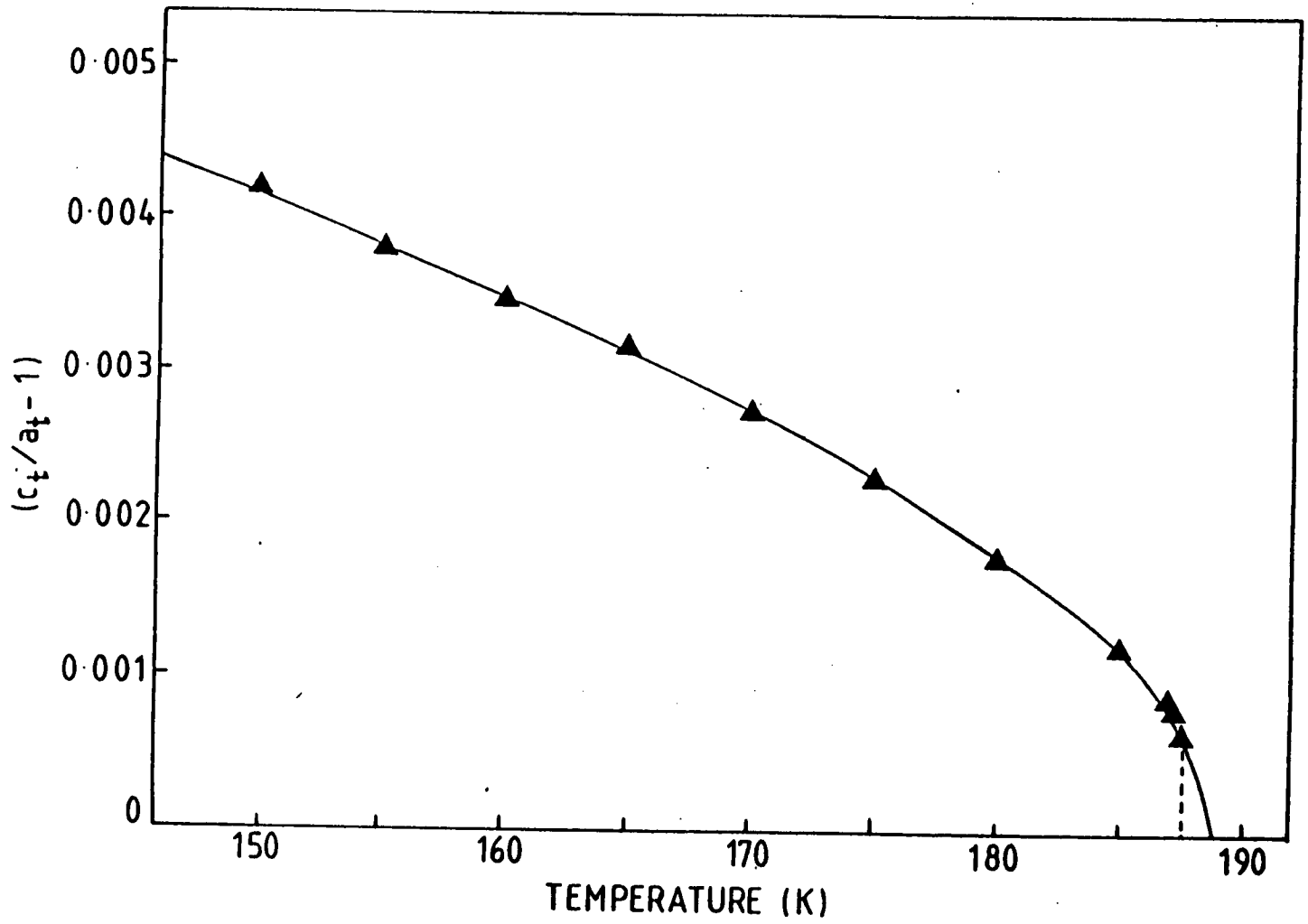

Figure 4.7

Measurement of the parameter $(c_t / a_t - 1)$ as a function of temperature below T_c for the Bragg peak (0 0 4).

Table 4.1 : The Critical Exponent β.
(Errors shown in brackets).

Curve	T_c' / K	β
1	188.0 (0.10)	0.178 (0.004)
2	187.7 (0.07)	0.135 (0.008)
3	187.9 (0.10)	0.205 (0.005)
$(c_t/a_t - 1)$	188.6 (0.07)	0.26 (0.02)
Theory for n=d=3 model	—	0.365 (0.002)

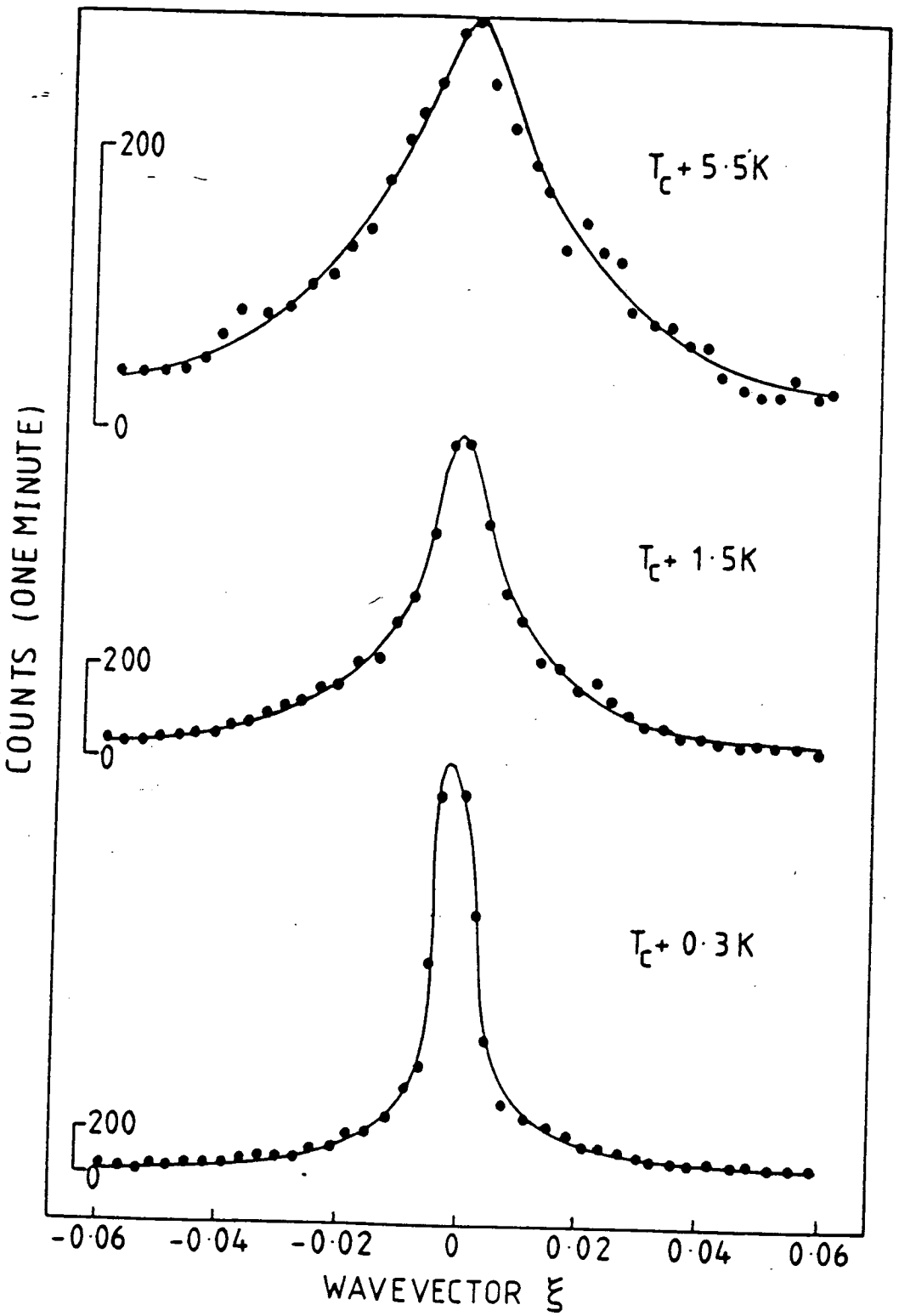

Figure 4.8

The diffuse X-ray scattering obtained using the low resolution configuration for wavevector $Q = (0.5+\zeta\ 0.5+\zeta\ 3.5)$ at various temperatures above T_c. The curves are least squares fits to a Lorentzian (anisotropic) plus a Lorentzian squared (isotropic) model convolved with the instrumental resolution function.

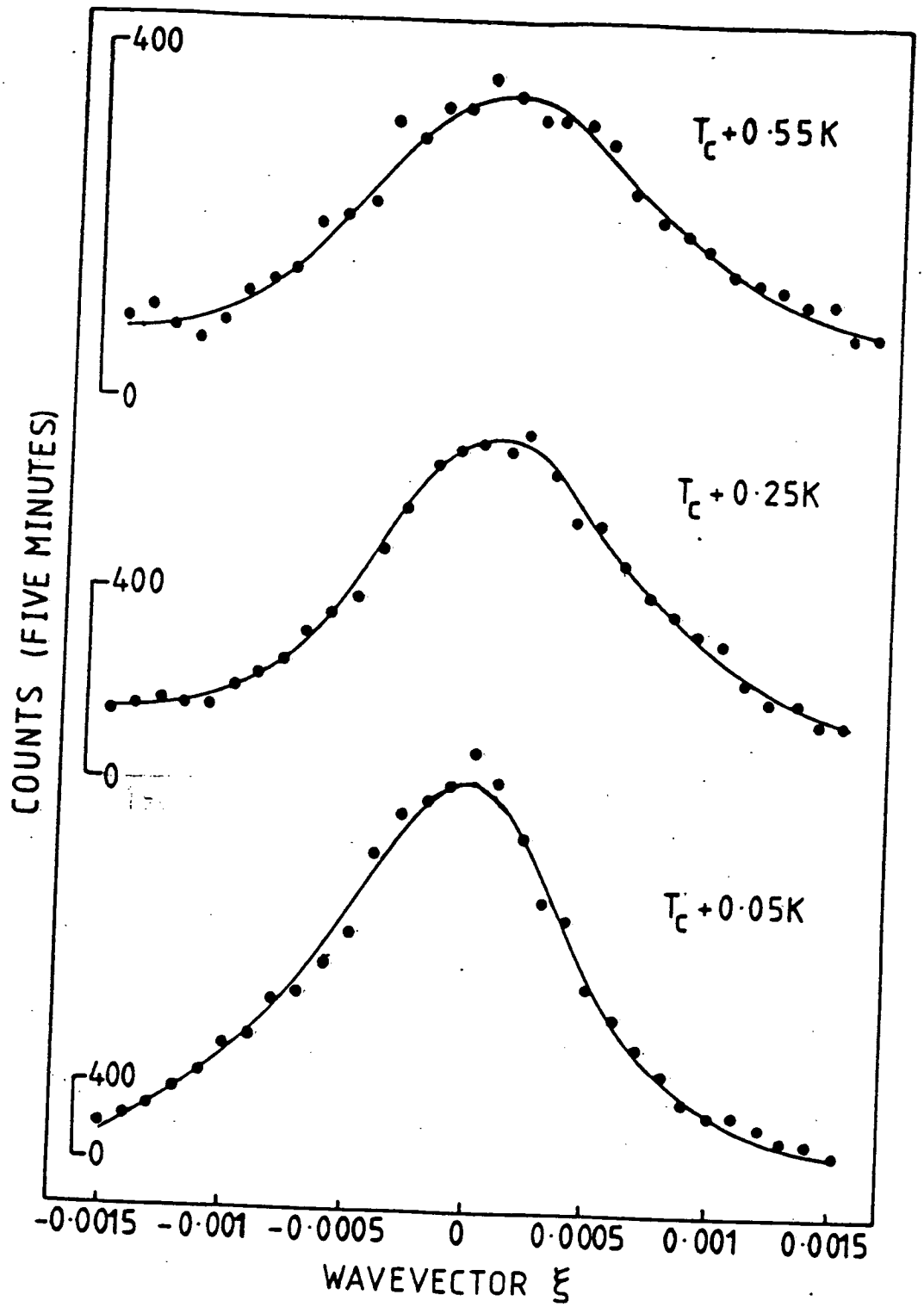

Figure 4.9

The diffuse X-ray scattering obtained using the high resolution configuration for wavevector Q = (0.5 0.5 2.5+ζ) at temperatures close to T_c. The curves are least squares fits to an isotropic Lorentzian squared model convolved with the instrumental resolution function.

above T_c which appeared to consist of two lengthscales. In $SrTiO_3$ the scattering was analysed in terms of a one-phonon component (Lorentzian) together with a resolution limited component. This second component first appeared some 10 K above T_c, and increased in intensity as T_c was approached. In $RbCaF_3$, a similar profile was measured using low resolution, but a closer investigation of the narrow component using higher resolution found it to be broader than the instrumental resolution, with a wavevector width which decreased continuously to the resolution limit at T_c. This component was observed in the temperature range T_c - T_c+8 K.

The next section describes the analysis of the critical scattering measurements made on $KMnF_3$ using x-ray diffraction.

Analysis of Results

The smooth curves through the data points in figures 4.8 and 4.9 are least squares fits to the trial function $I(\mathbf{q})$, where $I(\mathbf{q})$ consists of a model scattering function $S(\mathbf{q})$ convolved with the instrumental response function $R(\mathbf{q})$

$$I(\mathbf{q}) = \int_{\mathbf{q}_1} S(\mathbf{q})\, R(\mathbf{q}_1 - \mathbf{q})\, d\mathbf{q}_1 \qquad (10)$$

The fitting was performed on the Distributed Array Processor, (DAP) at the University of Edinburgh. The DAP consists of 4096 processing elements in a 64 by 64 array, each of which executes the same instruction on an independent data stream. The program used was written for investigation of neutron and x-ray scattering data (see Mitchell and Dove 1985). Use of the DAP facilitates numerical integration over all three cubic directions, alleviating the need to approximate the vertical resolution by a triangular function. Also, the anisotropy in the scattering function can be included without significantly increasing the computational time.

The theory of section 4.1 suggests that an appropriate model $S(\mathbf{q})$ for the one-phonon scattering above T_c is an anisotropic Lorentzian. Pairs of scans with wavevectors in the directions $\langle 0.5+\zeta\ 0.5+\zeta\ 3.5\rangle$ and $\langle 0.5\ 0.5\ 3.5+\zeta\rangle$ (obtained using low resolution) were fitted simultaneously to equation (10) with this model. The measured dispersion relation (Gesi et al 1972) gave $f=-1$ to reasonable accuracy, and h small. The data was fitted keeping $f=-1$, with $h=0$ and $h=0.14$, to

test the anisotropy in the dispersion (ie. the extent of coupling between rotations about different cube axes). In both cases, the amplitude χ_L and inverse correlation length $\varkappa_L$ were varied, with a fixed background. The fit was assessed in terms of the 'goodness of fit' parameter G = $\sqrt{(\chi^2/\text{degrees of freedom})}$. Contrary to the results of Andrews (1986) on $SrTiO_3$, the analysis of this data for the two different anisotropy parameters h produced identical values for both of the exponents ν_L and γ_L. This is probably because the scattering is more two-dimensional in $KMnF_3$.

Initially, data collected over the entire temperature range (T_c - T_c+50 K) was fitted to this model. The model was found to fit well for temperatures greater than T_c+8 K, with typical fits of G = 1.10 (T = 240 K) and G = 1.59 (T = 200 K). Closer to T_c the goodness of fit parameter was found to increase rapidly, for example, to G = 3.97 (T = 190 K) and G = 5.04 (T = 189 K). Section 4.2 gives a theoretical foundation for the inclusion of a Lorentzian squared component in the scattering cross section at temperatures close to T_c, of similar anisotropy and width to the Lorentzian component but different amplitude. However it was found this model did not significantly improve the fit (G = 3.95 (T = 190 K) and G = 5.03 (T = 189 K)). The recent work on $SrTiO_3$ and $RbCaF_3$ described above suggests that the inclusion of a second lengthscale in the scattering function would be appropriate, although the theoretical basis for this is still under discussion. Consequently the Lorentzian squared component was constrained to be isotropic, and of a different width to the Lorentzian part. The data was fitted to this model; the two amplitudes χ_L, χ_{L^2} and two widths $\varkappa_L$, $\varkappa_{L^2}$ were varied, again with a fixed background. Some examples of the goodness of fit are G = 1.61 (T = 190 K) and G = 1.74 (T = 189 K). The obtained values of the four parameters χ_L, χ_{L^2}, $\varkappa_L$, and $\varkappa_{L^2}$ as functions of the reduced temperature t = (T/T_c - 1) are shown in figures 4.10 and 4.11. The temperature dependence of these parameters is discussed below.

A second experiment using high resolution was performed on $KMnF_3$ to establish the presence of the second lengthscale $\varkappa_{L^2}$. As mentioned earlier, this component was unresolved in $SrTiO_3$ and $RbCaF_3$ (using graphite monochromator and analyser crystals), and found to be Lorentzian squared and isotropic with a temperature dependent width in $RbCaF_3$ (using silicon monochromator and analyser crystals). The scattering obtained for $KMnF_3$, examples of which are shown in figure 4.9, was found to vary in amplitude and width with temperature. Initially, pairs of scans with wavevectors in the directions $\langle 0.5+\zeta\ 0.5+\zeta\ 3.5 \rangle$ and

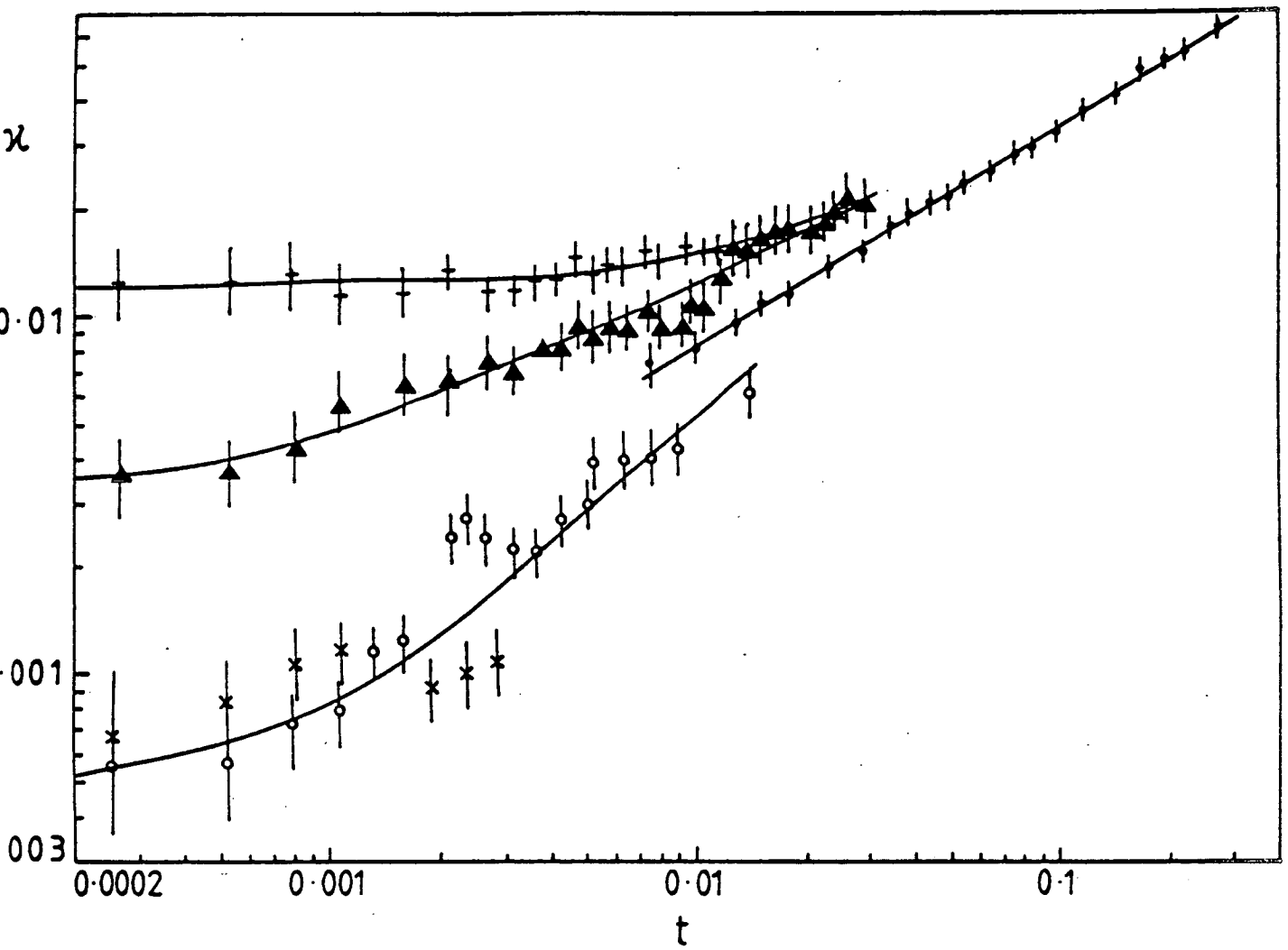

Figure 4.10

Inverse correlation lengths obtained from the analysis as described in the text of the diffuse X-ray scattering, in units of $2\pi/a_o$, for the reciprocal lattice points (0.5 0.5 3.5) and (0.5 0.5 2.5) (x's only). The closed circles correspond to data analysed using the anisotropic Lorentzian only model, with f = -1, h = 0. The crosses and triangles refer to data analysed using the Lorentzian (anisotropic) plus Lorentzian squared (isotropic) model, the crosses to the Lorentzian inverse correlation length and the triangles to the Lorentzian squared inverse correlation length. The open circles refer to the high resolution data, the model being Lorentzian squared only, with f = h = 0. In all cases the solid lines are least squares fits to the power law discussed in the text.

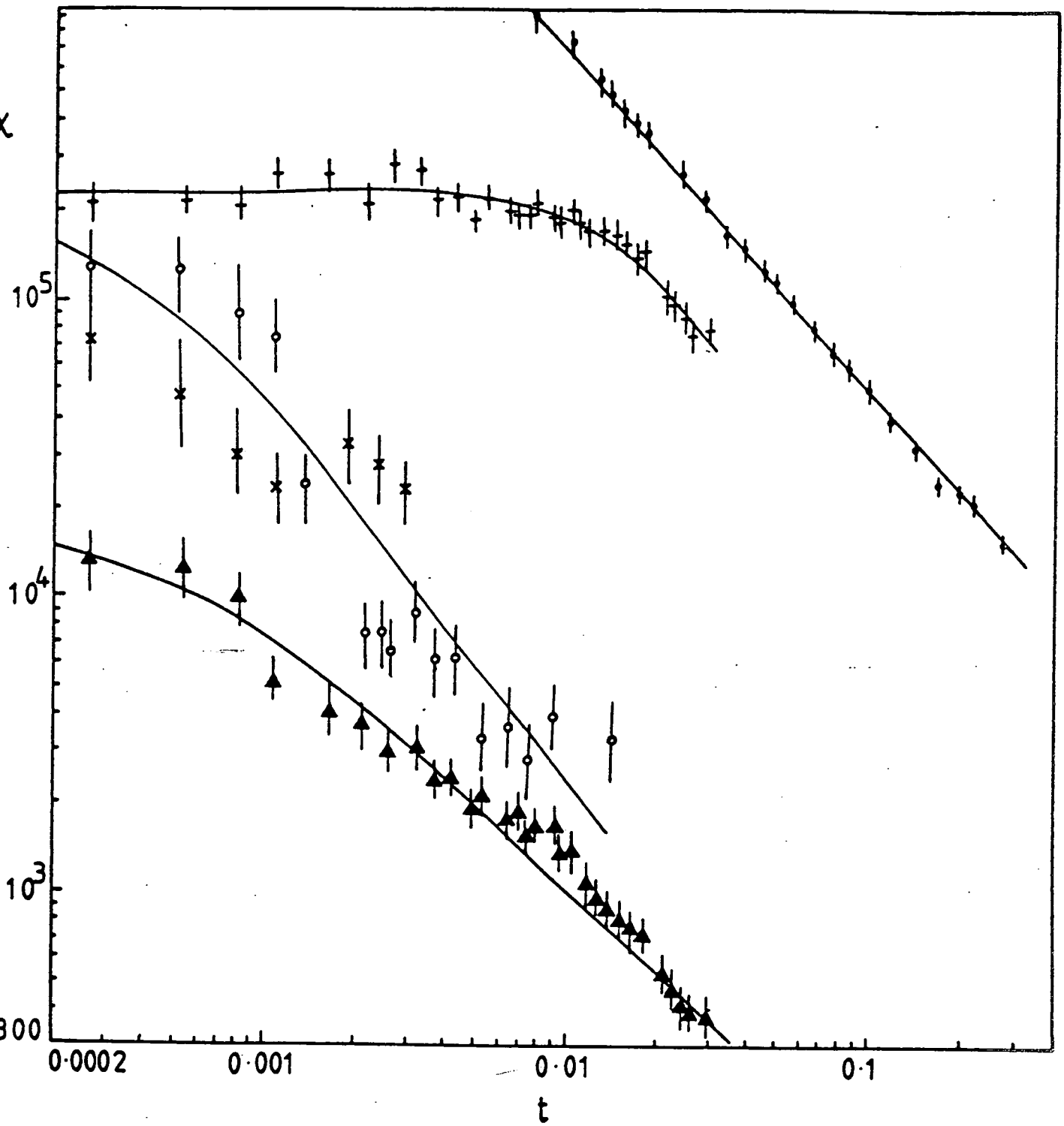

Figure 4.11

Amplitude (arbitrary units) obtained from the analysis as described in the text of the diffuse X-ray scattering for the reciprocal lattice points (0.5 0.5 3.5) and (0.5 0.5 2.5) (x's only). The solid lines are least squares fits to the power laws discussed in the text.

$\langle 0.5\ 0.5\ 3.5+\zeta \rangle$ were analysed simultaneously in terms of an anisotropic Lorentzian scattering model, as for the low resolution data, but the fitted curves did not describe the results. Because of this failure, the Lorentzian squared form was fitted to the data; it was found that the fit would not succeed unless the anisotropy was removed. An adequate fit was obtained using an isotropic Lorentzian squared model of amplitude $\chi_{L^2}^{(s)}$ and width $\kappa_{L^2}^{(s)}$. Some examples of fits obtained are G = 1.76 (T = 188 K) and G = 1.42 (T = 187.7 K). The obtained values of the parameters are shown in figures 4.10 and 4.11 as functions of t. As can be seen, there is little agreement between κ_{L^2} and $\kappa_{L^2}^{(s)}$; this is probably due to the limitations of the assumed model. The measurements made using silicon monochromator and analyser crystals were difficult because of the weak scattering involved. The results were not easily reproducible being sensitive to external factors such as small changes of position on the sample face between measurements.

Measurement of the Critical Exponents

The critical exponents ν_L and γ_L corresponding to the anisotropic Lorentzian model are given by equations (4) and (5). The data from the temperature range T = 189 - 240K was fitted by a least squares technique to these equations with the transition temperature, the amplitude, and the exponent allowed to vary. The effective transition temperature found from this analysis is T_c'. The results are shown in table 4.2 and are discussed below. Similarly, the critical exponents ν_{L^2} and γ_{L^2} corresponding to the isotropic Lorentzian squared component included in the analysis for T < 189K have been fitted to equations (5) (with κ_{L^2} and χ_{L^2}) and (9) for both the low and high resolution data. The results are shown in table 4.3 and are discussed below. In this temperature range the anisotropic Lorentzian component converged to a constant correlation length and amplitude at T_c as expected for a first order phase transition.

The Character of the Lorentzian Squared Component

The character of the narrow component shown in figure 4.9 was further investigated using high resolution. As shown in the inset of figure 4.6, a careful measurement of the integrated intensity of the critical scattering using silicon indicates a continuous phase transition. This was found to be consistent across the sample face. It was also found that, although the cubic Bragg reflection (004)

Table 4.2 : The Critical Exponent of the Lorentzian Component. (Errors shown in brackets).

	ν_L	ξ_{L_0} / Å	$(T_c' - T_c)$ /K	γ_L	$(T_c' - T_c)$ /K
$KMnF_3$	0.62 (0.07)	31 (6)	-0.12 (0.03)	1.19 (0.11)	-0.12 (0.03)
$SrTiO_3$	0.83 (0.05)	46 (5)	–	1.4 (0.1)	–
$RbCaF_3$	0.64 (0.07)	27 (5)	-0.54 (0.10)	1.34 (0.11)	-0.74 (0.10)
Theory for n=d=3 model	0.705 (0.003)	–	–	1.386 (0.004)	–

Table 4.3 : The Critical Exponent of the Lorentzian Squared Component. (Errors shown in brackets).

	ν_{L^2}	$\zeta_{L_0^2}$ / Å	$(T_c' - T_c)$ /K	γ_{L^2}	$(T_c' - T_c)$ /K
$KMnF_3$ Low Resolution data	0.49 (0.06)	38 (4)	-0.14 (0.03)	1.00 (0.08)	-0.15 (0.03)
$KMnF_3$ High Resolution data	0.84 (0.12)	20 (8)	-0.04 (0.05)	1.24 (0.16)	0.01 (0.06)
$RbCaF_3$ High Resolution data	0.60 (0.08)	66 (3)	-0.004(0.006)	–	–

jumps abruptly to its tetragonal phase positions at T_c (figure 4.12), as expected for a first order phase transition, the narrow component of the critical scattering does not undergo any discontinuous shift in position at T_c, and is already displaced from the cubic R-point above T_c. This suggests that the scattering is due to a tetragonal structure with a fixed strain (c_t/a_t ratio) just above T_c. A similar result was obtained in $RbCaF_3$ (Ryan et al 1986).

4.4 Discussion of Results

4.4.1 Temperature Dependence of the Order Parameter

The order parameter of the critical fluctuations below T_c at the R-point in $KMnF_3$ has been measured using x-ray scattering in two ways. Integrated intensity measurements of the R-point scattering below T_c (figure 4.6) were found to differ in temperature dependence across the sample face (see table 4.1) because domain proportions depend upon temperature. Close to T_c the influence of domains has particular importance since the character of the transition and the temperature at which it occurs vary. A quantitative measure of the temperature dependence of the domain volume distribution has been made for $KMnF_3$ by Tietze et al (1982) who found that the domain volumes are equally distributed at T_c and grow rapidly to a saturation ratio of 70:20:10 % at temperatures of $T_c - 10$ K and less. (In our experiment we see the first two domains superimposed). Although this can explain the differences in the integrated intensity measurements close to the transition, we found the saturation ratio was not constant across the sample face. In conclusion, it is not possible to attach much significance to the values of the critical exponent obtained by this technique; the low values however do indicate the importance of extinction in a large sample.

Measurement of the temperature dependence of the ratio of lattice parameters c_t and a_t (figure 4.7) gives an acceptable value for β since these quantities are insensitive to the domain structure; our result is $\beta = 0.26(2)$. The n=d=3 Heisenberg model predicts $\beta = 0.365(2)$ (Le Guillou and Zinn-Justin 1980). This exponent is appropriate asymptotically where the anisotropy parameter f is renormalised to zero at T_c (Bruce 1980), but is expected to be greater in systems with anisotropy f close to -1 (Natterman and Trimper 1975). It has also been shown (Fisher and Nelson 1974,

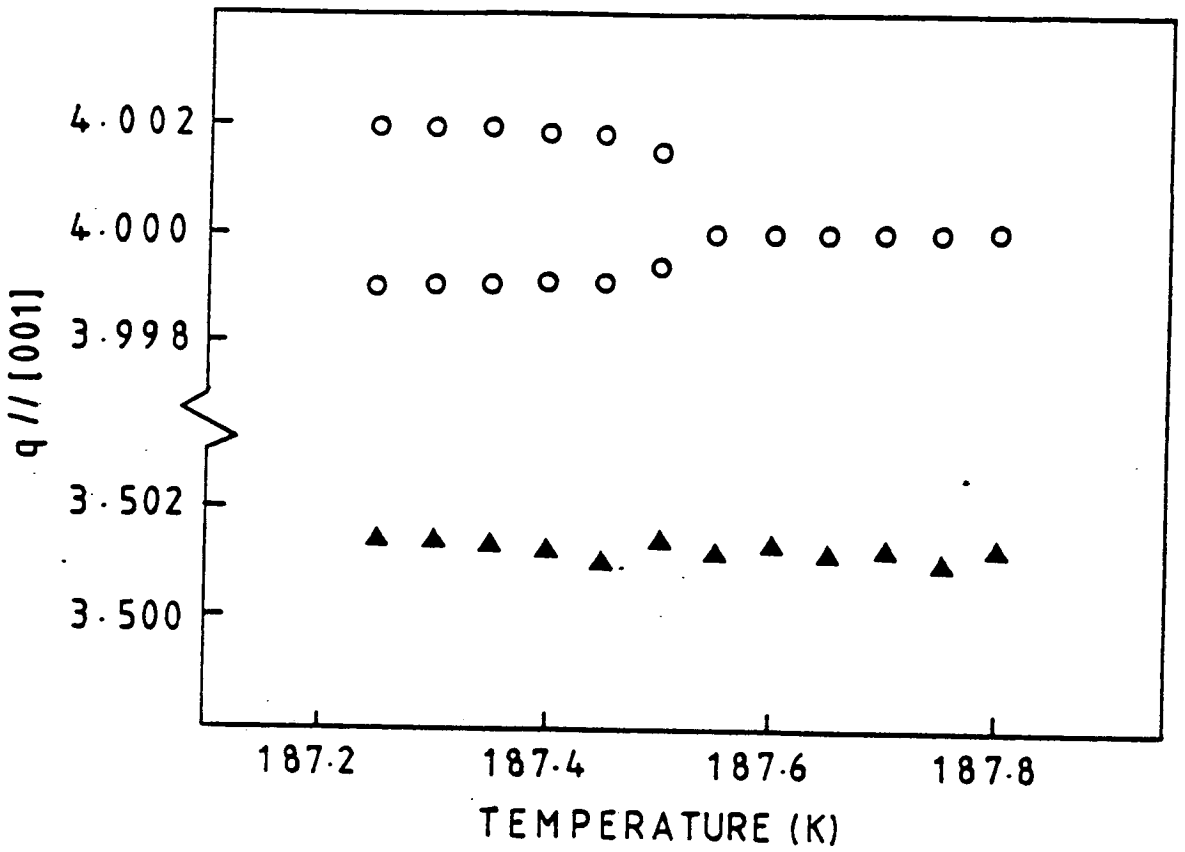

Figure 4.12

The positions of the peaks (0 0 4) (circles) and (0.5 0.5 3.5) (triangles) with respect to their cubic positions in the <0 0 1> direction as a function of temperature, all scans being measured using high resolution. The reciprocal space axis is in units of $2\pi/a_o$.

Aharony and Bruce 1974) that the tetragonal strain accompanying the phase transition has a temperature dependence described by $\tilde{\beta}$ where $\tilde{\beta} = 2-\alpha-\varphi$. Here φ is a crossover exponent reflecting the instability of the Heisenberg fixed point against a perturbation of uniaxial symmetry. For $n=d=3$, they find $\tilde{\beta} \sim 0.85$ which differs appreciably from the exponent $2\beta = 0.73$ predicted by Landau theory. Our result is considerably lower than either of these values and even than the $d=3$ Ising model of 0.315 (2) (Fisher 1974). Ising behaviour is possible if the sample is single domain with an orienting mechanism (strain field) which selects the monodomain axis (Courtens 1972, Aharony and Bruce 1974).

The critical exponent has been reported as $\frac{1}{3}$ by Borsa (1973) (from an analysis of the quadrupole coupling constant) and also by Hirotsu and Sawada (1973) and Benard and Walker (1976) (from measurements of the birefringence). A more recent measurement of the lattice parameter a_t by Sakahita et al (1981), using high-angle double crystal x-ray diffractometry, found the exponent to be $\beta=0.2875(6)$, in reasonable agreement with our result. Sakahita and co-workers suggest that the value of β is small because the weak first order phase transition occurs in the vicinity of a tricritical point (Aharony and Bruce 1979). Our results further substantiate this idea. Following the publication of the work by Sakahita and co-workers, the tricritical behaviour in $KMnF_3$ has been investigated by means of specific heat measurements (Stokka et al 1981). They found $KMnF_3$ to have two consecutive tricritical points joined by a second order line near $p=0.25$ Kbar and $T=188$ K for pressure applied along the <100> direction.

4.4.2 Critical Scattering

One Phonon Scattering Description

The one-phonon scattering from the R_{25} mode is adequate to describe the observed scattering cross section in the temperature range $0.01 < t < 0.3$. In the Ornstein-Zernike approximation (small $\mathbf{q}$ limit) the expected cross section for general wavevector transfer is described as the sum of two anisotropic Lorentzians of different widths, because the x-rays couple to fluctuations of two different R_{25} modes. At any given temperature the observed scattering profile closely agreed with the form of dispersion given by neutron scattering measurements (Gesi

et al 1972), showing $f=-1$ and h small. The cross section was found to be largely independent of the parameter h; the critical exponents are insensitive to the amount of anisotropy in the dispersion.

The critical exponents ν_L and γ_L obtained from the analysis are shown in table 4.2, together with the experimentally determined values for $SrTiO_3$ and $RbCaF_3$ measured using x-rays, and the theoretically predicted parameters of the $n=d=3$ Heisenberg model (Le Guillou and Zinn-Justin 1980). As mentioned above, the intrinsic critical behaviour of $KMnF_3$ is only expected to be close to that of the Heisenberg fixed point in the asymptotic limit, the effect of non-zero anisotropy is to raise the critical exponents by a few percent. However, the experimentally determined values of $\nu_L = 0.62\,(7)$ and $\gamma_L = 1.19\,(11)$ are actually smaller than predicted; this is attributed to changes in the scattering profile close to T_c causing κ_L to be artificially high.

The value for ν_L agrees favourably with that found in $RbCaF_3$ and is less than that measured in $SrTiO_3$. The reason for the anomalously high value in $SrTiO_3$ is unclear. It should be noted that the transition temperature was allowed to vary in the analysis of both the $KMnF_3$ and $RbCaF_3$ data producing an offset from the experimentally determined value which represents a measure of the first order character of the phase transition. In $SrTiO_3$ the width decreased rapidly close to T_c with a temperature dependence of $\nu_L \sim 2-3$ which is physically unreasonable: This change coincided with an alteration in the experimental configuration from low to high resolution and with the increasing importance of the quasi-Bragg component in the scattering cross section, and is probably due to an analysis in which a Lorentzian squared component was neglected. In the fit the transition temperature was constrained to equal the measured T_c. Another point to note is that the x-ray data for $KMnF_3$ was adequately described by the anisotropy parameters measured by Gesi et al (1972). In $SrTiO_3$ and $RbCaF_3$ it was necessary to reduce the anisotropy determined by neutron scattering techniques slightly in order to fit the x-ray data.

Anomalous Scattering Profile close to T_c

In this section the second component observed close to the transition temperature is discussed with reference to the x-ray experiments on $SrTiO_3$,

$RbCaF_3$ and $KMnF_3$. In all three materials it was necessary to introduce a second component into the analysis of the low resolution data. In $SrTiO_3$ and $RbCaF_3$ the component was unresolved, and in $KMnF_3$ it was isotropic and nominally Lorentzian squared in form with a temperature dependent width. Further measurements using the high resolution configuration showed the narrow component in $RbCaF_3$ to have a similar profile to that in $KMnF_3$ but in $SrTiO_3$ it remained unresolved with a width independent of temperature, the instrument-limited width being $\sim 0.001\,\text{Å}^{-1}$ (FWHM) in all cases. This difference may be an artifact of the Lorentzian squared model used for the analysis. No quasi-Bragg component was observed in $RbCaF_3$ and $KMnF_3$.

The high resolution measurements on several samples of $SrTiO_3$ with different surface preparations showed a variation in intensity of the quasi-Bragg peak. In particular the narrow component observed from sample II (polished and etched) initially increased in intensity with repeated temperature cycling through the transition but eventually saturated at a value some five times larger than the initial value, close to that measured in sample III (annealed and oxidised) which showed no evidence of history dependence. The intensity of the quasi-Bragg component in sample IV (reduced in vacuum) was roughly twice that in sample III at the same value of t. History dependent scattering at the R-point was observed in the high resolution measurements on $KMnF_3$, where no saturation occurred, but the results in $RbCaF_3$ were approximately reproducible. Of the three $RbCaF_3$ samples investigated, one showed no anomalous second component close to T_c: This sample differed from the others in its smaller mosaic spread, the surfaces of all samples being prepared in a similar manner. It should also be noted that at any particular temperature the intensity of the quasi-Bragg component in all samples of $SrTiO_3$ did not vary by more than ten per cent when the x-ray beam was scanned across the crystal surface. This differs from the measurements on $RbCaF_3$ and $KMnF_3$ which showed the critical scattering at the R-point to vary considerably with position of the x-ray beam on the sample face.

The isotropic Lorentzian squared scattering cross section measured in $RbCaF_3$ and $KMnF_3$ was found to have a temperature dependent width and to originate from a tetragonal structure. The results for the critical exponents ν_{L^2} and γ_{L^2} are shown in table 4.3. In the case of $RbCaF_3$, γ_{L^2} was constrained to be $2\nu_{L^2}$. The hysteresis in the high resolution critical scattering measurements in $KMnF_3$ is

reflected in the associated errors, but there is little agreement between the data collected using graphite monochromator and analyser crystals and that when graphite was replaced with silicon. It is therefore only possible to establish a qualitative temperature dependence for this component in $KMnF_3$. The analysis of the high resolution data in both $RbCaF_3$ and $KMnF_3$ showed the correlation length and amplitude of the Lorentzian squared component to diverge at or close to T_c. The correlated volume at $T_c+0.5K$ had a linear dimension of $\sim 4000 Å$ in $RbCaF_3$ and $\sim 2000 Å$ in $KMnF_3$: The quasi-Bragg component in $SrTiO_3$ corresponded to a correlated tetragonal volume of size $\sim 8000 Å$ which remained approximately unchanged over the temperature range $T_c - T_c + 3.5$ K.

Surface Effects

The influence of the surface upon the scattering profile has been considered in detail by Andrews (1986) who treats the surface as a macroscopic symmetry breaking defect. The model attributes the quasi-Bragg component to a surface layer in which the low temperature tetragonal phase is stabilized by the surface. It is possible for this model to explain the unresolved wavevector width in $SrTiO_3$ if the surface is rough or contains a compressive strain. However, the model also predicts the surface scattered intensity to be independent of the x-ray penetration depth μ, and consequently the ratio of surface to bulk scattering to be inversely proportional to μ. Measurements of this ratio at (0.5 0.5 2.5) and (0.5 0.5 4.5) in $SrTiO_3$ were found to vary by less than twenty percent compared with the difference in μ between the two wavevectors of a factor of 2.3 . In $KMnF_3$ the ratio of the integrated intensity at the two reciprocal lattice points (0.5 0.5 2.5) and (0.5 0.5 3.5) (measured using silicon monochromator and no analyser crystal) was independent of temperature on cooling through T_c at approximately the value predicted by the bulk (after the normal corrections to the intensity had been made). These results suggest that the scattering cannot be attributed to the surface. Further evidence is provided by the measurements on $RbCaF_3$, where the surfaces of all three samples were prepared in a similar way yet did not all display the same anomalous component in the scattering cross section close to the transition. Also, the correlation length measured in $RbCaF_3$ and $KMnF_3$ using high resolution was observed to be temperature dependent, which cannot be explained by the surface model.

Random Field Model

As discussed in section 4.2 the presence of isolated defects in symmetry breaking positions produce random static fields leading to a Lorentzian squared component in the structure factor. The range of distortion around each defect is controlled by the intrinsic correlation length of the fluctuations in the high temperature phase (Halperin and Varma 1976). These fluctuations are therefore expected to have the same degree of anisotropy in the dispersion as the one-phonon fluctuations described above. However the results in $RbCaF_3$ and $KMnF_3$ are quite different from this, showing isotropic scattering at a position displaced from the cubic R-point. The extent of the correlated volume close to T_c was found to differ substantially from the one-phonon correlation length in $RbCaF_3$ (at $T_c + 0.5\,K$, $\xi_{L^2} \sim 4000\,Å$ and $\xi_L \sim 300\,Å$). There is also a measurable difference in these values in $KMnF_3$, which suggests the critical scattering occurs on two lengthscales.

A plausible extension of the random field model to first order phase transitions has been made by Imry and Wortis (1979) who suppose that, in addition to the fluctuations of the phonon normal modes, there are defect mediated fluctuations from the cubic phase to the tetragonal phase close to the transition. These fluctuations occur when the free-energy lowering due to taking advantage of local variations in impurity density more than offsets the free-energy cost of the interface produced. The correlations between tetragonally distorted clusters centered on quenched impurities drive the transition and have a lengthscale which may or may not be equal to the correlation length ξ_L of the one-phonon fluctuations. The model explains the tetragonal structure of the narrow component and introduces a second lengthscale into the scattering. The isotropic dispersion of the Lorentzian squared component may arise because the tetragonal strain present in the distorted phase could cause the macroscopic elastic energy to favour a roughly spherical cluster. In this model the critical exponents ν_{L^2} and γ_{L^2} shown in table 4.3 refer to the degree of inter-cluster correlation.

As can be seen in figure 4.6 the phase transition in $KMnF_3$ as measured by the order parameter alters its character across the sample face, and is only slightly first order. The model of Imry and Wortis predicts a smearing of a first order phase transition because the size of the defect mediated fluctuations is determined by the free energy difference between the phases, which decreases

continuously to zero at T_c. Therefore if the Lorentzian squared component in $RbCaF_3$ and $KMnF_3$ corresponds to scattering from these fluctuations we would expect to see a continuous phase transition at the R-point when the high resolution configuration is used. This is in fact the case for both materials; the result for $KMnF_3$ can be seen in the inset of figure 4.6. The measurements of the one-phonon scattering imply that the fluctuations of the phonon normal modes have a non-divergent temperature dependence which is consistent with a first order phase transition.

4.5 Summary and Conclusions

1) Well above the transition temperature the critical scattering at the R-point has the expected Lorentzian form in the three perovskites $SrTiO_3$, $RbCaF_3$ and $KMnF_3$. The correlations in the order parameter fluctuations show considerable anisotropy, though this was found to be less in $SrTiO_3$ and $RbCaF_3$ than that predicted from the observed phonon dispersion relations (Stirling 1972 and Almairac et al 1977). The reason for this is probably because the x-ray scattering has contributions from the inelastic and central parts of the neutron scattering and the latter is less anisotropic than the former.

The temperature dependence of the scattering measured in the three materials is shown in table 4.2. The results for ν_L and γ_L in $RbCaF_3$ and $KMnF_3$ are consistent with the behaviour of the n=d=3 Heisenberg model with approximately the correct exponents, but with transition temperatures T_c' which are below the transition temperatures measured by monitoring the tetragonal strain. In $SrTiO_3$ the susceptibility has a temperature dependence which is in agreement with this model, but the experimental value of ν_L is significantly larger than that predicted by theory. The correlation length and amplitude converge to zero at the measured T_c.

2) Closer to the transition temperature a second component in the scattering cross section was observed in all three materials. The characteristics of this component are that

- it has a lineshape that is well described by a Lorentzian squared model in $RbCaF_3$ and $KMnF_3$ but is resolution limited in $SrTiO_3$. No quasi-Bragg component is observed in $RbCaF_3$ and $KMnF_3$

- it is isotropic in wavevector
- it is displaced from the cubic R-point position in $RbCaF_3$ and $KMnF_3$ suggesting that it can be attributed to clusters which have a tetragonal structure
- in $RbCaF_3$ and $KMnF_3$ it has an inverse correlation length which decreases continuously to zero at or close to the measured transition temperature with an amplitude different from the one- phonon scattering
- it has an amplitude which varies from sample to sample in $SrTiO_3$ and $RbCaF_3$

3) The explanation for these results is unclear, though the differing behaviour amongst the various samples of $RbCaF_3$ strongly suggest the importance of defects. Circumstantial evidence is provided in the lack of a viable alternative mechanism: The surface model, although it could explain the quasi-Bragg component in $SrTiO_3$, is untenable. The theoretical predictions of Imry and Wortis (1979) in their extension of the random field model describe many of the observed phenomena, and provide a basis for explaining the origin of a second scattering lengthscale. If the defects were extended, it is conceivable that coherently perturbed regions much larger than the intrinsic precursor clusters could occur. Consequently the $\mathbf{q}$ dependence of the x-ray scattering would reflect a distribution of lengthscales corresponding to spatial variations in crystal perfection. Imry and Wortis predict that the discontinuity at a first order transition will be reduced by the defect mediated fluctuations to the tetragonal phase which are continuously temperature dependent. This smearing of the transition is observed in $RbCaF_3$ and $KMnF_3$, but, unfortunately, the transition in $SrTiO_3$ is effectively continuous, suggesting their theory is inappropriate in this case.

The results can be compared with the central peak observed in neutron scattering measurements. In $RbCaF_3$ the anomalous x-ray peak persists over a temperature range which is much less than that over which the neutron central peak is seen in crystals grown by the Bridgeman-Stockbarger technique (Almairac et al 1977). In $SrTiO_3$ the neutron central peak assumes the bulk of the spectral weight at roughly the same temperature at which qualitative changes in the x-ray scattering occur (Shapiro et al 1972), and a strong temperature dependence of the scattering near T_c is observed in both instances. In the case of $KMnF_3$, analysis of

the neutron scattering data is complicated because the soft mode is overdamped at 40 K above T_c, and consequently the phonon and central component contributions to the observed intensities are not easily separated. In chapter 5 a more precise comparison between the two anomalous features is possible since x-ray and neutron scattering experiments are performed on the same samples. The following chapter thus contains the results of a series of x-ray and neutron scattering experiments on samples of $KMn_{1-x}Mg_xF_3$ with $x = 0.01$ and $x = 0.1$. It also attempts to correlate and quantify the effect of impurities on the structural phase transition.

Appendix 4.1

A simple theory of domain structure predicts three Bragg peaks in reciprocal space. In a (0 0 1) orientation the domains with the c-axis in the plane of the crystal give rise to a Bragg peak at ($a^*_t h$, $c^*_t k$, 0) and that with the c-axis perpendicular to the plane to a peak at ($c^*_t h$, $a^*_t k$, 0). Gibaud et al (1) (to be published) describe how these domains are rotated with respect to each other. In reciprocal space this causes satellite peaks which are distinguishable from the main peaks. For instance there is a peak at ($c^*_t h \cos\delta + a^*_t k \sin\delta$, $a^*_t k \cos\delta - c^*_t h \sin\delta$, 0) which is rotated by an angle δ from the reciprocal point ($c^*_t h$, $a^*_t k$, 0). The angle ϑ shown in figure 3 is therefore given by

$$\tan\vartheta = \frac{a^*_t h - c^*_t h \cos\delta - a^*_t k \sin\delta}{c^*_t k + c^*_t h \sin\delta - a^*_t k \cos\delta}$$

where

$$\delta = \pi/2 - 2\tan^{-1}(a_t/c_t)$$

and

$$a^*_t/c^*_t = c_t/a_t$$

This reduces to

$$\tan\vartheta = c_t/a_t$$

for all h, k.

For comparison with the obtained $KMnF_3$ data, a factor of $\sqrt{2}$ must be included in the value for the 'a_t' lattice parameter since the measurements were made in the (1-1 0) plane.

Appendix 4.2

The order parameter φ of the R-point critical scattering is the angle of rotation of the fluorine octahedra about a stationary potassium atom. Below T_c the effective unit cell has side $a_c \cos\varphi$ in the plane of rotation, and side a_c out of the plane. The ratio of lattice parameters is therefore

$$c_t / a_t = 1 / \cos\varphi$$

which reduces to

$$c_t / a_t = 1 + \tfrac{1}{2}\varphi^2$$

when φ is small. Hence $(c_t/a_t - 1)$ is proportional to the square of the order parameter.

CHAPTER 5

AN INVESTIGATION OF THE EFFECT OF POINT DEFECTS ON THE R-POINT INSTABILITY IN $KMnF_3$

5.1 Introduction

This chapter contains the results of a series of x-ray and neutron scattering experiments performed on two crystals of $KMnF_3$, containing known proportions of the compound $KMgF_3$ which had been introduced during the crystal growth procedure. The crystals had the chemical formulas $KMn_{0.99}Mg_{0.01}F_3$ and $KMn_{0.9}Mg_{0.1}F_3$ and were grown by the flux method. The size of the $KMn_{0.99}Mg_{0.01}F_3$ crystal was $\sim 8x8x9$ mm and of the $KMn_{0.9}Mg_{0.1}F_3$ crystal was $\sim 10x10x15$ mm; the samples used in the x-ray and neutron experiments were taken from these two crystals as described below. The aim of the experiments is two-fold. Firstly, to investigate the effects on the R-point structural phase transition in $KMnF_3$ when simple substitional impurities of known concentration have been added, and in particular to investigate if either or both of the anomalous components observed in the x-ray and neutron scattering cross sections at the R-point above T_c is enhanced by such an addition. Secondly, to perform x-ray and neutron experiments on the same crystals in an attempt to correlate the two anomalous features.

The series of x-ray experiments were performed in a similar manner to those described in chapter 4. The samples of $KMn_{0.99}Mg_{0.01}F_3$ and $KMn_{0.9}Mg_{0.1}F_3$ were cut perpendicular to a crystallographic $\langle 001 \rangle$ direction from the grown crystals and consisted in each case of a slice ~ 2 mm thick. The active surface of these slices was polished and then etched for ten minutes in ortho-phosporic acid to remove any surface damage. For each sample two experiments were performed on the triple axis x-ray spectrometer described in chapter 2, the first using pyrolitic graphite monochromator and analyser crystals and the second using silicon monochromator and analyser crystals. A measurement of the mosaic spread of the two x-ray samples was made in the high resolution configuration and found to be $\sim 0.019\,(3)^\circ$ in both cases. The samples were mounted in turn onto the cold finger of a closed-cycle cryostat, and oriented with the face normal [001] and a cubic [110] axis in the horizontal plane of the diffractometer, as in chapter 4.

The series of neutron scattering experiments were performed on the IN3 triple axis spectrometer situated on the guide tube of the nuclear reactor at the Institut Laue-Langevin, Grenoble, France. As in the x-ray experiments, two different resolution arrangements are possible (described in chapter 2). The lower resolution is achieved by inserting a pyrolitic graphite filter before the sample which fixes the incident energy to be 3.52 THz, and a considerably improved resolution is realized by replacing this filter with a cooled beryllium filter, to give an incident energy of 1.12 THz. The two samples consisted of the remainder of the grown crystals after removal of the slices for the x-ray work. The $KMn_{0.99}Mg_{0.01}F_3$ sample had a volume of $\sim 0.5 cm^3$ and a rather poor mosaic spread of 0.7 (1)°, and the $KMn_{0.9}Mg_{0.1}F_3$ sample a volume of $\sim 1.3 cm^3$ and a mosaic spread of 0.20 (5)°. Each sample was mounted in turn in a cryostat which had a temperature stability of ± 0.05° and was aligned with a [1-10] axis vertical.

5.2 Experimental Results

5.2.1 X-ray Scattering Experiments

Measurement of T_c and the Critical Exponent β

In both $KMn_{0.99}Mg_{0.01}F_3$ and $KMn_{0.9}Mg_{0.1}F_3$ the transition temperature was measured in a similar manner to that described in chapter 4 for pure $KMnF_3$; the intensity distribution of the (004) reciprocal lattice point was monitored as the temperature of the crystal was lowered, using the high resolution configuration. The results of such measurements are shown in figure 5.1 and 5.2 for the two samples. However, in both cases, the behaviour was less simple than for pure $KMnF_3$ where a single peak split into several smaller peaks within the temperature change T = (187.6 - 187.4) K. It was found that, for $KMn_{0.99}Mg_{0.01}F_3$ the single $T > T_c$ peak moved along the [001] axis at the shown transition temperature, and at a lower temperature of 182.4 (2) K began to develop several other peaks. A similar behaviour was observed in $KMn_{0.9}Mg_{0.1}F_3$ where the new peaks were first seen at a temperature of 159.0 (5) K. The transition temperatures are taken as $T_c^1 = 183.9$ (2) K for $KMn_{0.99}Mg_{0.01}F_3$ and $T_c^{10} = 161.7$ (2) K for $KMn_{0.9}Mg_{0.1}F_3$ since these temperatures correspond to the first movement of the peak. It can be seen that the difference between the transition temperature T_c^{10} for $KMn_{0.9}Mg_{0.1}F_3$ and T_c^0 for $KMnF_3$ is

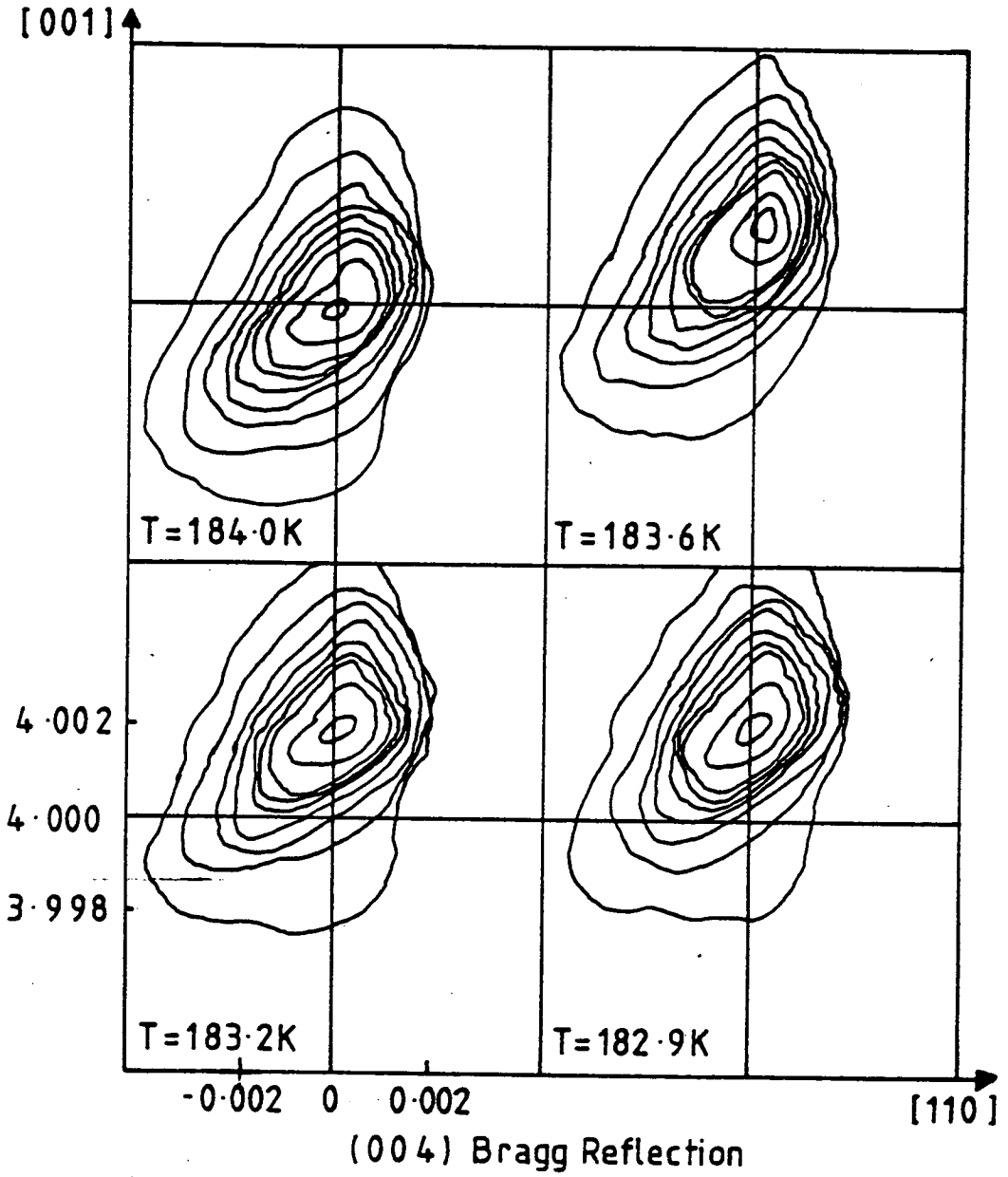

Figure 5.1

Intensity contour plot of the x-ray scattering from the reciprocal lattice point (004) for $KMn_{0.99}Mg_{0.01}F_3$ as the crystal is cooled through T_c; the peak shifts along the [001] direction at T_c. The reciprocal space axes are in units of $2\pi/a_o$.

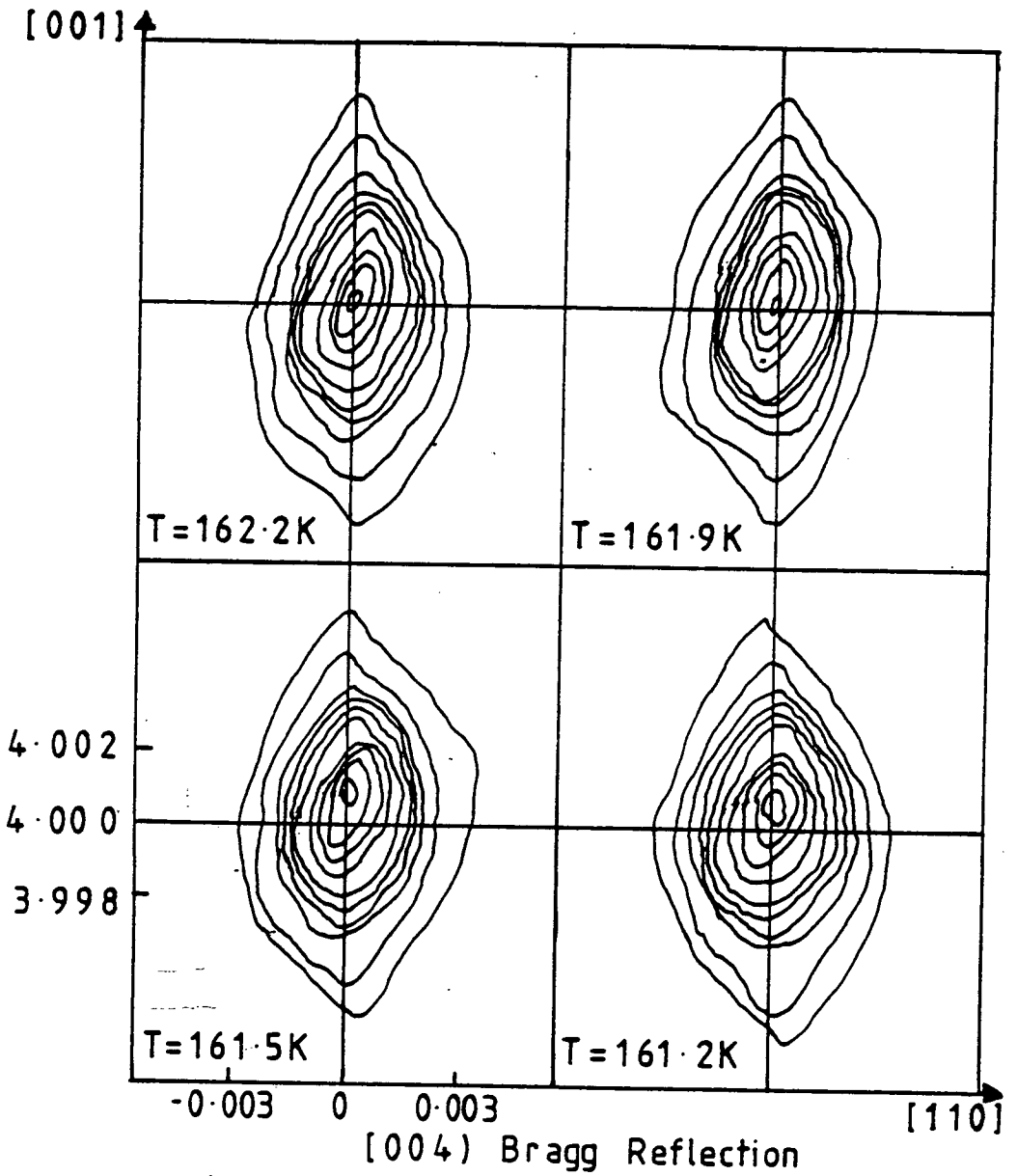

Figure 5.2

Intensity contour plot of the x-ray scattering from the reciprocal lattice point (0 0 4) for $KMn_{0.9}Mg_{0.1}F_3$ as the crystal is cooled through T_c; the peak shifts along the [001] direction at T_c. The reciprocal space axes are in units of $2\pi/a_o$.

approximately ten times the difference between the transition temperature T_c^1 for $KMn_{0.99}Mg_{0.01}F_3$ and T_c^0. Also, the observed 'jump' of the peak along the [001] axis is considerably smaller for the case of $KMn_{0.9}Mg_{0.1}F_3$ than for $KMn_{0.99}Mg_{0.01}F_3$ which suggests that the phase transition is more continuous.

The development and pattern of domains below the transition temperature has been discussed in the previous chapter. It was found (for pure $KMnF_3$) that the different domains exist on a macroscopic scale, and that the number of peaks detected corresponding to a given Bragg reflection, and their relative intensities, varied both as the x-ray beam was moved across the sample face and as the temperature was changed. The latter was of particular consequence when attempting to measure the critical exponent β by monitoring the integrated intensity of the scattering at the R-point below T_c, since at such a point in reciprocal space in the (1-10) plane, one of the tetragonal peaks is systematically absent. In the case of both $KMn_{0.99}Mg_{0.01}F_3$ and $KMn_{0.9}Mg_{0.1}F_3$, well below the transition the Bragg reflections were found to consist of the maximum number of peaks at all positions on the sample face. This suggests that the addition of impurities causes a sample to form many small domains in the tetragonal phase, which is plausible if point defects nucleate domain growth.

Figures 5.3 and 5.4 show the integrated intensity at the reciprocal lattice point (0.5 0.5 3.5) in $KMn_{0.99}Mg_{0.01}F_3$ and $KMn_{0.9}Mg_{0.1}F_3$ measured using the low resolution configuration (graphite monochromator and no analyser crystal) as a function of temperature, for two positions on each sample face. The difference in intensity of the two curves of each figure indicates that the relative proportions of the domains are contingent upon the position of the x-ray beam on the sample face, but the temperature dependence is less pronounced compared with pure $KMnF_3$ (see figure 4.6). The data points for each curve were fitted independently by a least squares fit to the power law $I \sim t^{2\beta}$, $t = (T/T_c - 1)$, with the transition temperature allowed to vary. The solid curves are the results of such fits and the dashed line indicates the actual transition temperature; the obtained values of β are shown in table 5.1. In the case of $KMn_{0.9}Mg_{0.1}F_3$ the transition is effectively continuous at both positions on the sample face.

The tetragonal strain below the transition in the three samples $KMnF_3$, $KMn_{0.99}Mg_{0.01}F_3$ and $KMn_{0.9}Mg_{0.1}F_3$ was measured using the high resolution

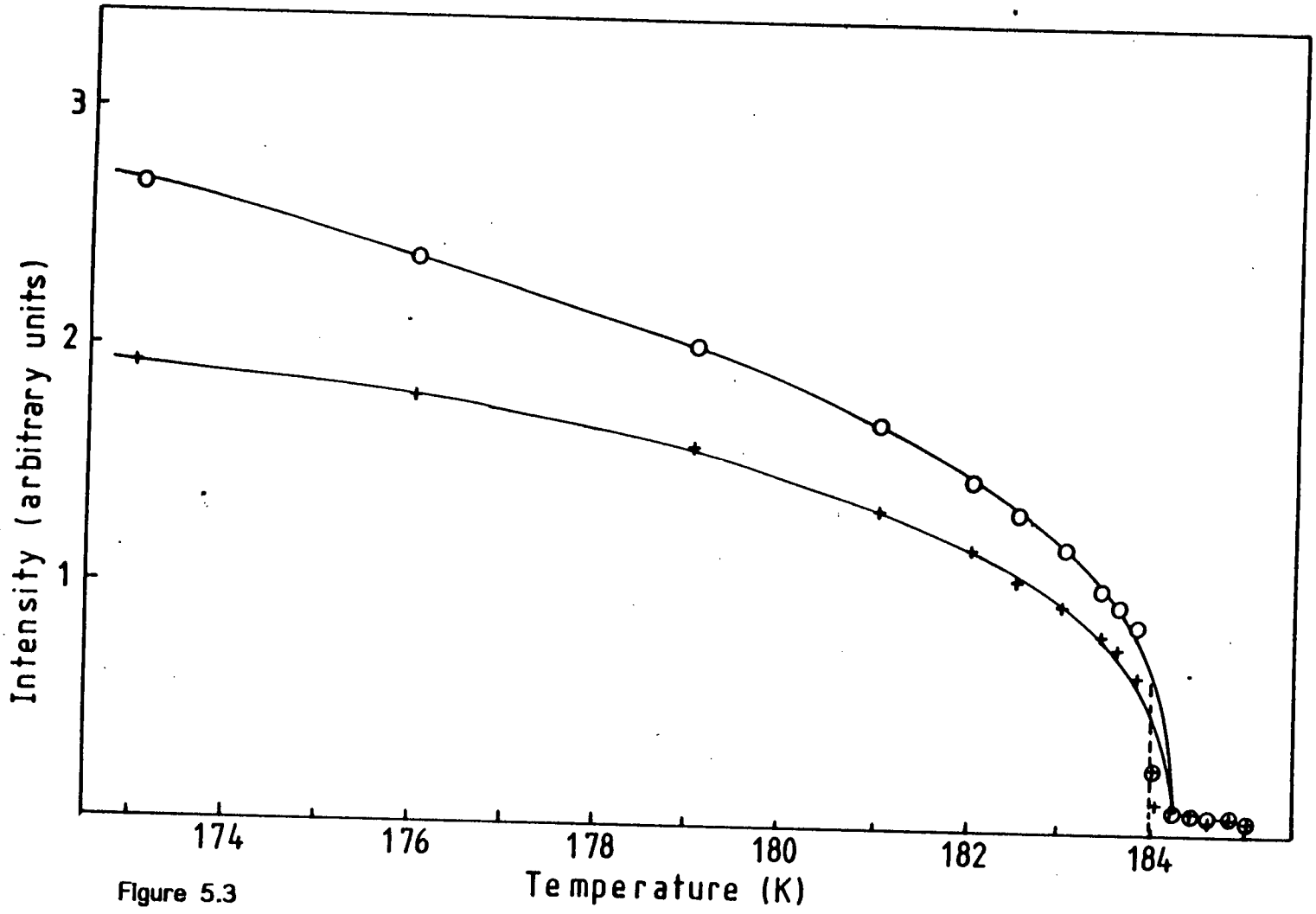

Figure 5.3

Integrated x-ray scattering intensity (arbitrary units) for the reciprocal lattice point (0.5 0.5 3.5) obtained in a measurement of the rocking curve, on cooling through T_c, for two different positions on the sample face for $KMn_{0.99}Mg_{0.01}F_3$. The open circles correspond to a position of -2mm on the sample face and the crosses to a position of +2mm. The smooth curves are least squares fits to the power law $I \sim t^{2\beta}$ as described in the text. The dotted line shows the actual transition temperature.

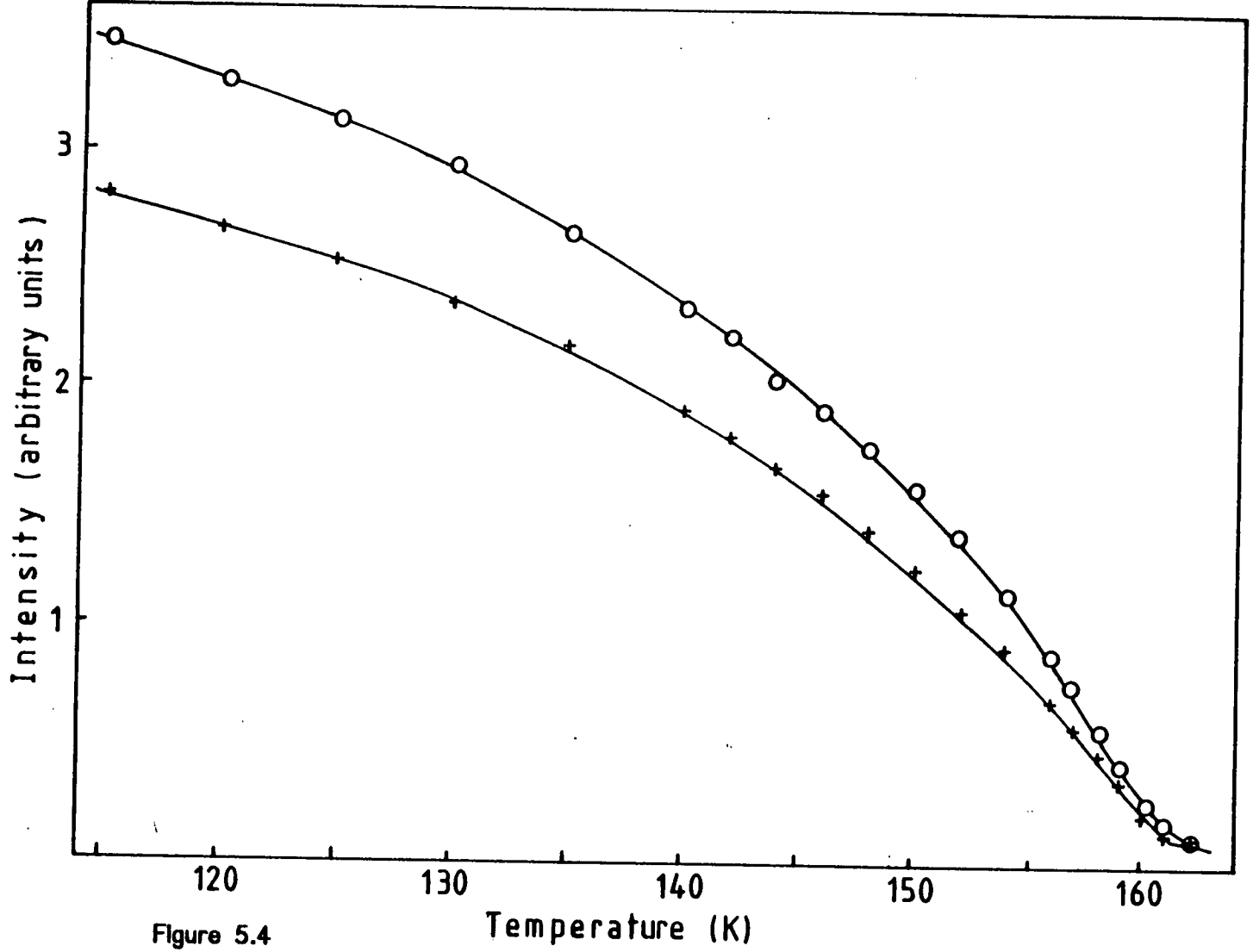

Figure 5.4

Integrated x-ray scattering intensity (arbitrary units) for the reciprocal lattice point (0.5 0.5 3.5) obtained in a measurement of the rocking curve on cooling through T_c for two different positions on the sample face for $KMn_{0.9}Mg_{0.1}F_3$. The open circles correspond to a position of -0.5mm on the sample face and the crosses to a position of +2mm. The smooth curves are least squares fits to the power law $I \sim t^{2\beta}$, as described in the text.

configuration by monitoring the ratio of the positions of the domain peaks at the (004) Bragg reflection in the <001> direction as a function of temperature. The results are shown in figure 5.5, where the solid curves are least squares fits to the power law $(c_t / a_t - 1) \sim t^{2\beta}$, with the transition temperature allowed to vary, and the dashed line is the actual transition temperature. The size of the first order step at T_c is $\sim 6.7 \times 10^{-4}$ for $KMnF_3$, $\sim 5.3 \times 10^{-4}$ for $KMn_{0.99}Mg_{0.01}F_3$ and ~ 0 for $KMn_{0.9}Mg_{0.1}F_3$. The results obtained for the critical exponent β for all three samples are shown in table 5.1, and will be discussed in section 3.

Critical Scattering Measurements

The wavevector dependence of the critical scattering above T_c was measured near the zone-boundary using both experimental resolution configurations for $KMn_{0.99}Mg_{0.01}F_3$ and $KMn_{0.9}Mg_{0.1}F_3$. Some examples of low resolution scans along the <110> direction offset from the reciprocal lattice point (0.5 0.5 3.5) are shown in figures 5.6 ($KMn_{0.99}Mg_{0.01}F_3$) and 5.7 ($KMn_{0.9}Mg_{0.1}F_3$). As in the case of pure $KMnF_3$ (see figure 4.8), the scattering profiles have temperature dependent widths and amplitudes. At $T=T_c+5.5$ K, the scattering profile of all three samples is very similar with comparable widths, the scattering being narrowest and weakest in the case of pure $KMnF_3$. By $T=T_c+0.3$ K, however, the scattering cross section has changed considerably in the case of $KMnF_3$, less so in the case of $KMn_{0.9}Mg_{0.1}F_3$ and hardly at all in the case of $KMn_{0.99}Mg_{0.01}F_3$. This is primarily reflected in the different values of the widths at this reduced temperature, which are ~ 0.008 rlu in $KMnF_3$, ~ 0.019 rlu in $KMn_{0.9}Mg_{0.1}F_3$ and ~ 0.037 rlu in $KMn_{0.99}Mg_{0.01}F_3$, the intensity of the scattering being nominally the same in all three samples.

Figures 5.8 and 5.9 show the scattering cross sections of $KMn_{0.99}Mg_{0.01}F_3$ and $KMn_{0.9}Mg_{0.1}F_3$ measured using the high resolution configuration along the <001> direction (offset from the reciprocal lattice point (0.5 0.5 2.5)). As mentioned in chapter 4, this resolution configuration can only detect the sharp anomalous component in the scattering cross section, the soft phonon being indistinguishable from a uniform background. Any temperature dependence of the widths of these peaks is less pronounced than in the case of pure $KMnF_3$ (see figure 4.9), though the scattering is narrower in $KMn_{0.99}Mg_{0.01}F_3$ than in $KMn_{0.9}Mg_{0.1}F_3$, and less intense by $T=T_c+0.5$ K. In both $KMn_{0.99}Mg_{0.01}F_3$ and $KMn_{0.9}Mg_{0.1}F_3$ the width of the scattering below the transition temperature at (0.5 0.5 2.5) in the <001> direction was measured as $\sim 0.0010(3)$ rlu.

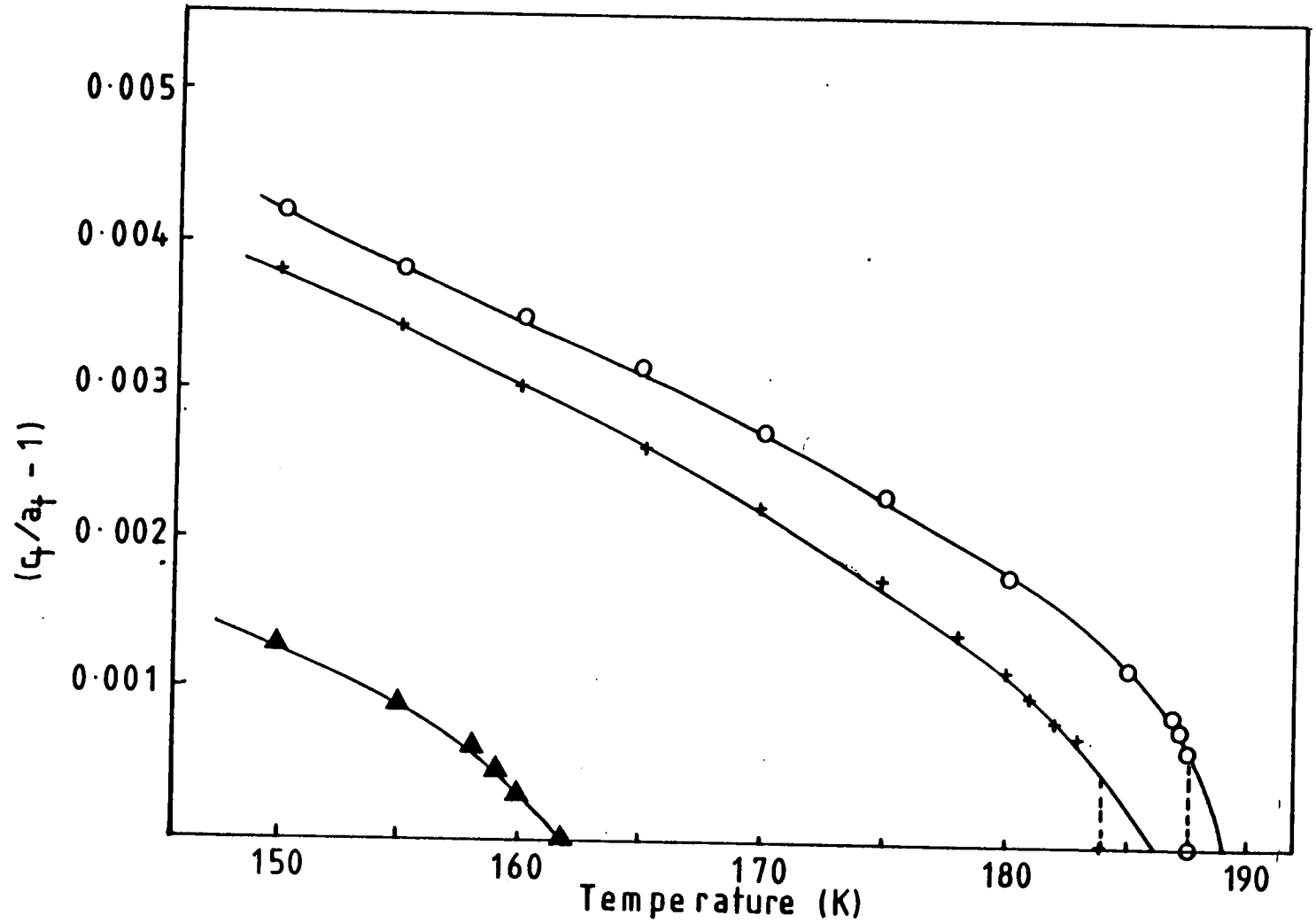

Figure 5.5

Measurement of the parameter $(c_t / a_t - 1)$ as a function of temperature below T_c for the reciprocal lattice point (0 0 4) for all three samples. The open circles correspond to $KMnF_3$, the crosses to $KMn_{0.99}Mg_{0.01}F_3$ and the triangles to $KMn_{0.9}Mg_{0.1}F_3$. In each case the smooth curves are least squares fits to the power law $I \sim t^{2\beta}$, and the dotted lines show the actual transition temperatures.

Table 5.1 : The Critical Exponent β.
(Errors shown in brackets).

	Curve	T_c' / K	β
$KMn_{0.99}Mg_{0.01}F_3$	- 2 mm	184.2 (0.12)	0.166 (0.005)
	+ 2 mm	184.2 (0.10)	0.123 (0.008)
	$(c_t/a_t - 1)$	186.5 (0.10)	0.336 (0.008)
$KMn_{0.9}Mg_{0.1}F_3$	- 0.5 mm	161.1 (0.05)	0.298 (0.010)
	+ 2 mm	161.2 (0.04)	0.305 (0.012)
	$(c_t/a_t - 1)$	161.5 (0.08)	0.332 (0.010)
$KMnF_3$	$(c_t/a_t - 1)$	188.6 (0.07)	0.26 (0.02)
Theory for n=d=3 model	—	—	0.365 (0.002)

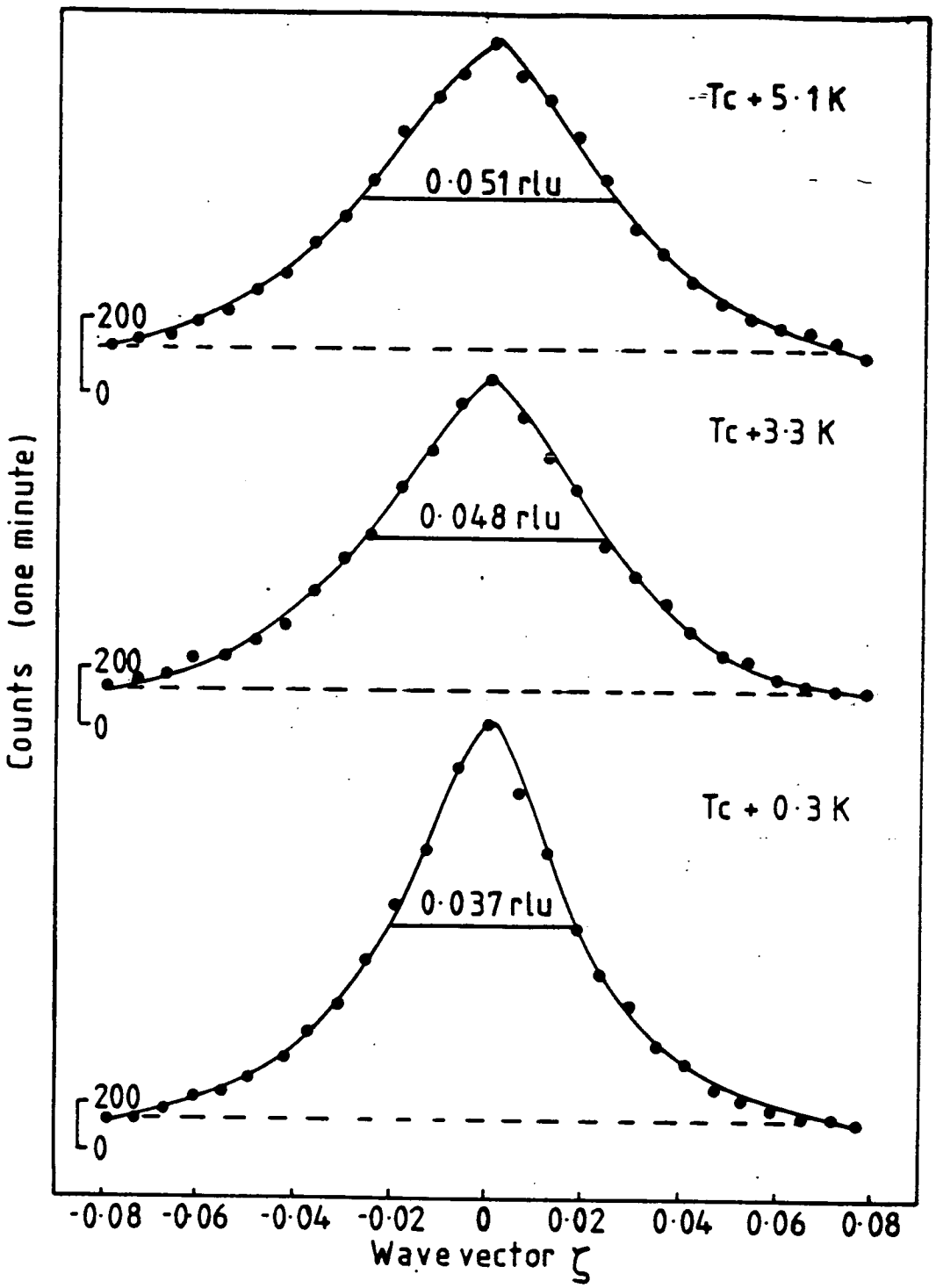

Figure 5.6

The diffuse x-ray scattering obtained using the low resolution configuration for wavevector Q = (0.5+ζ 0.5+ζ 3.5) at various temperatures above T_c for $KMn_{0.99}Mg_{0.01}F_3$. The curves are least squares fits to a Lorentzian (anisotropic) plus a Lorentzian squared (isotropic) model convolved with the instrumental resolution function.

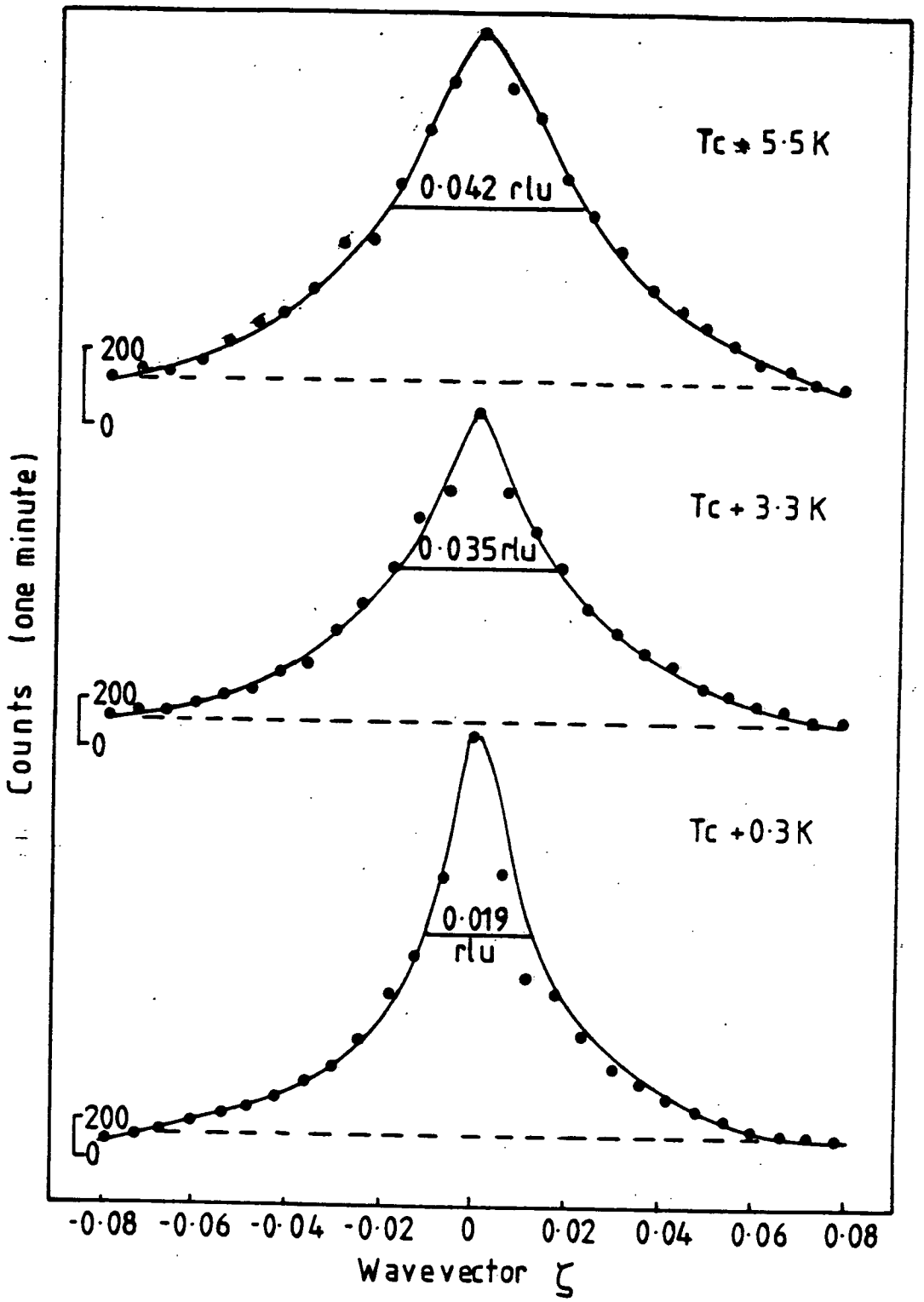

Figure 5.7

The diffuse x-ray scattering obtained using the low resolution configuration for wavevector **Q** = (0.5+ζ 0.5+ζ 3.5) at various temperatures above T_c for $KMn_{0.9}Mg_{0.1}F_3$. The curves are least squares fits to a Lorentzian (anisotropic) plus a Lorentzian squared (isotropic) model convolved with the instrumental resolution function.

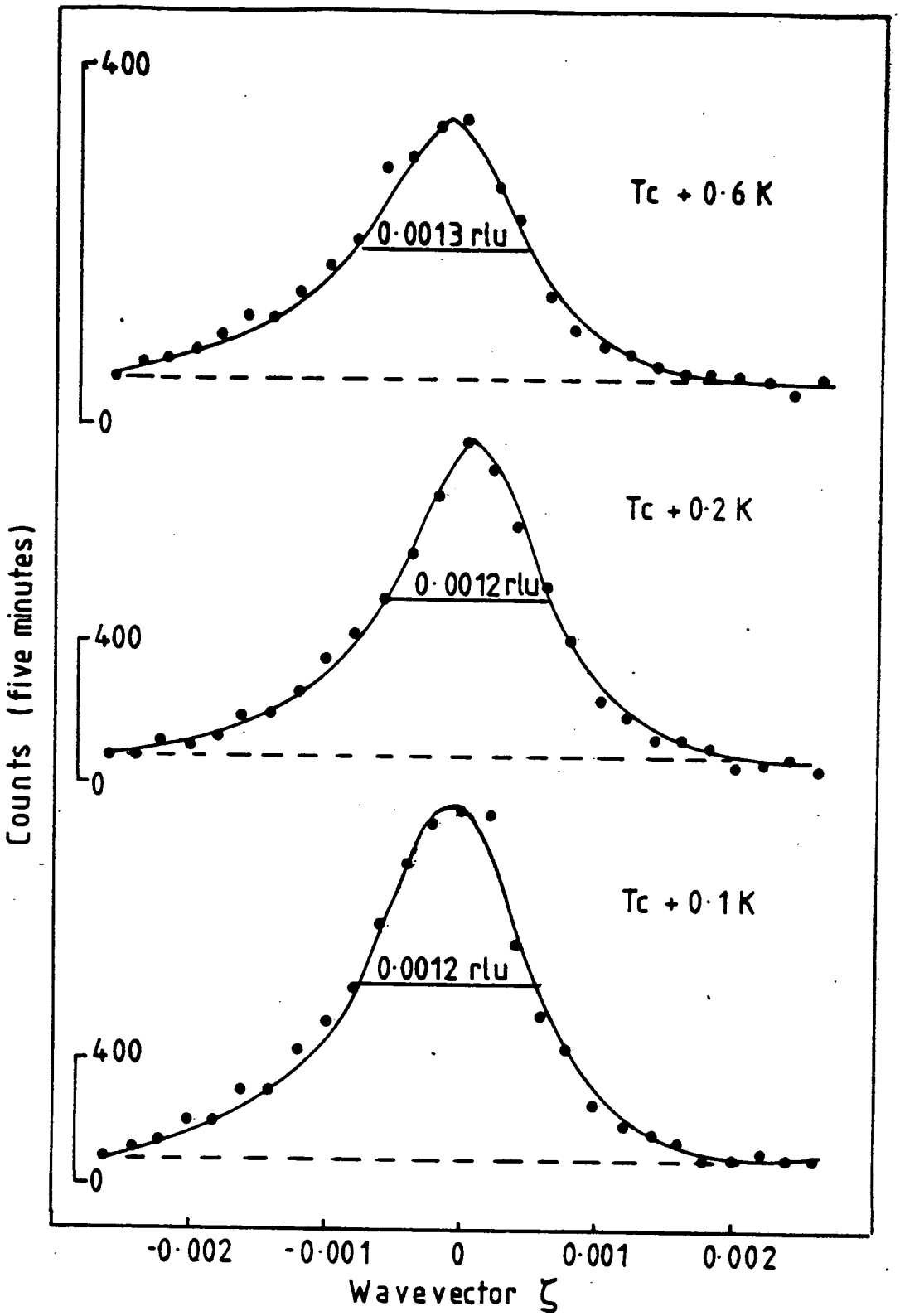

Figure 5.8

The diffuse x-ray scattering obtained using the high resolution configuration for wavevector **Q** = (0.5 0.5 2.5+ζ) at temperatures close to T_c for $KMn_{0.99}Mg_{0.01}F_3$. The curves are least squares fits to an isotropic Lorentzian squared model convolved with the instrumental resolution function.

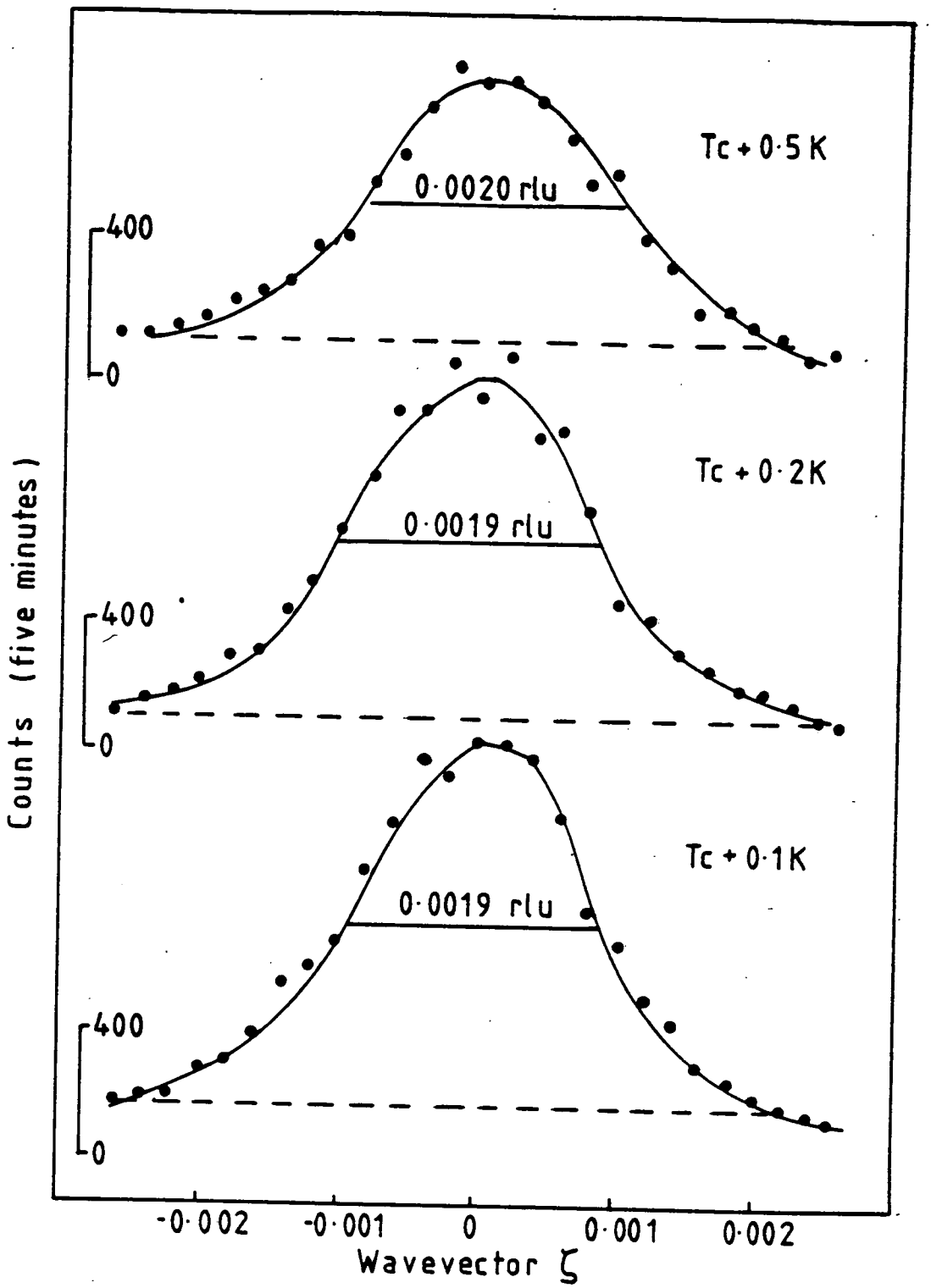

Figure 5.9

The diffuse x-ray scattering obtained using the high resolution configuration for wavevector **Q** = (0.5 0.5 2.5+ζ) at temperatures close to T_c for $KMn_{0.9}Mg_{0.1}F_3$. The curves are least squares fits to an isotropic Lorentzian squared model convolved with the instrumental resolution function.

Analysis of Critical Scattering

The analysis of the critical scattering data collected above T_c for $KMn_{0.99}Mg_{0.01}F_3$ and $KMn_{0.9}Mg_{0.1}F_3$ was conducted in a similar manner to that described in chapter 4. The data obtained with the low resolution configuration consisted, in both samples, of scans with wavevector in the directions $\langle 0.5+\zeta\ 0.5+\zeta\ 3.5\rangle$ and $\langle 0.5\ 0.5\ 3.5+\zeta\rangle$. These were fitted simultaneously to a model scattering function convolved with the instrumental response function. The data collected over the entire temperature ranges for $KMn_{0.99}Mg_{0.01}F_3$ and $KMn_{0.9}Mg_{0.1}F_3$ was fitted to an anisotropic Lorentzian model (with anisotropy parameters $f=-1$ and $h=0$ as for pure $KMnF_3$), the amplitude χ_L and inverse correlation length $\varkappa_L$ being varied with a fixed background. The fits gave the following typical values of G, the goodness of fit parameter: G=1.19 (T=230 K) and G=1.92 (T=186 K) for $KMn_{0.99}Mg_{0.01}F_3$, and G=1.13 (T=200 K) and G=1.93 (T=166 K) for $KMn_{0.9}Mg_{0.1}F_3$. In the case of $KMn_{0.99}Mg_{0.01}F_3$, this model continued to give reasonable values of G for the whole temperature range, though when a second isotropic Lorentzian squared component (with anisotropy parameters $f=h=0$, and amplitude χ_{L^2} and inverse correlation length $\varkappa_{L^2}$) was introduced into the model for temperatures very close to T_c, the fits did improve slightly. In the case of $KMn_{0.9}Mg_{0.1}F_3$, the values of G began to increase unreasonably at $\sim T_c+2$ K, and were improved with the addition of an isotropic Lorentzian squared component in the scattering model. The values of the four parameters χ_L, χ_{L^2}, $\varkappa_L$, and $\varkappa_{L^2}$ obtained from the fits are shown in figures 5.10 and 5.12 ($KMn_{0.99}Mg_{0.01}F_3$) and 5.11 and 5.13 ($KMn_{0.9}Mg_{0.1}F_3$) as functions of the reduced temperature $t=(T/T_c-1)$. The temperature dependence of these parameters, and those of pure $KMnF_3$ are discussed in section 3. In particular, the values of the critical exponents ν_L and γ_L obtained from least squares fits to the power laws describing the temperature variation of the inverse correlation length and static susceptibilty for the anisotropic Lorentzian model (for both $KMn_{0.99}Mg_{0.01}F_3$ and $KMn_{0.9}Mg_{0.1}F_3$) are shown in table 5.2. The solid curves in figures 5.10-5.13 are these least squares fits.

The data collected using the high resolution configuration for both $KMn_{0.99}Mg_{0.01}F_3$ and $KMn_{0.9}Mg_{0.1}F_3$ consisted of pairs of scans with wavevectors in the directions $\langle 0.5+\zeta\ 0.5+\zeta\ 2.5\rangle$ and $\langle 2.5\ 0.5+\zeta\ 0.5+\zeta\rangle$. These were fitted simultaneously to an isotropic Lorentzian squared model of amplitude $\chi_{L^2}^{(S)}$ and width $\varkappa_{L^2}^{(S)}$, and the results for these parameters for $KMn_{0.99}Mg_{0.01}F_3$ and $KMn_{0.9}Mg_{0.1}F_3$

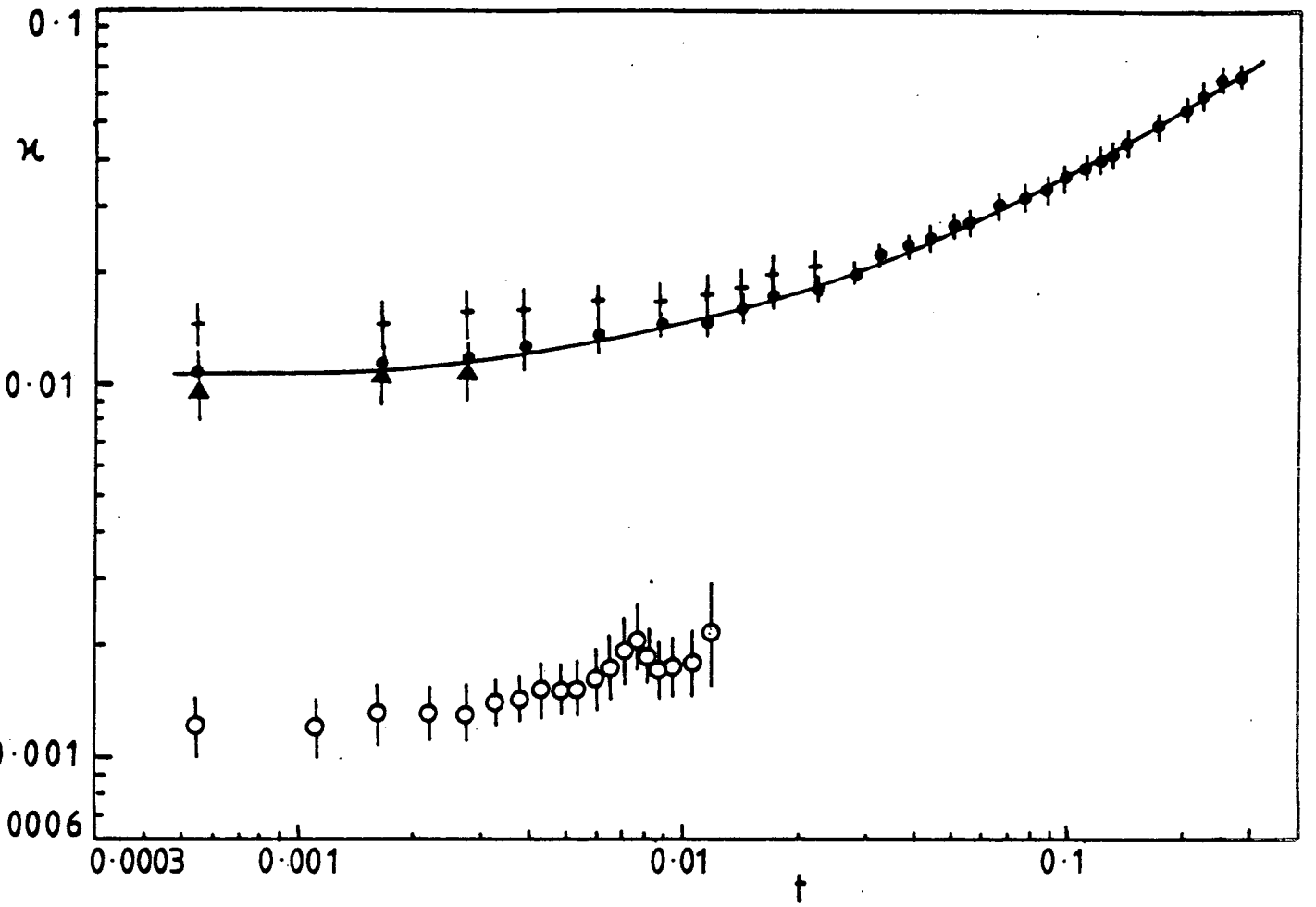

Figure 5.10

Inverse correlation lengths obtained from the analysis as described in the text of the diffuse x-ray scattering, in units of $2\pi/a_o$, for the reciprocal lattice points (0.5 0.5 3.5) and (0.5 0.5 2.5) [open circles] for $KMn_{0.99}Mg_{0.01}F_3$. The closed circles correspond to data analysed using the anisotropic Lorentzian only model, with f = -1, h = 0. The crosses and triangles refer to data analysed using the Lorentzian (anisotropic) plus Lorentzian squared (isotropic) model, the crosses to the Lorentzian inverse correlation length and the triangles to the Lorentzian squared inverse correlation length. The open circles refer to the high resolution data, the model being Lorentzian squared only, with f = h = 0. The solid line is a least squares fit to the power law discussed in the text.

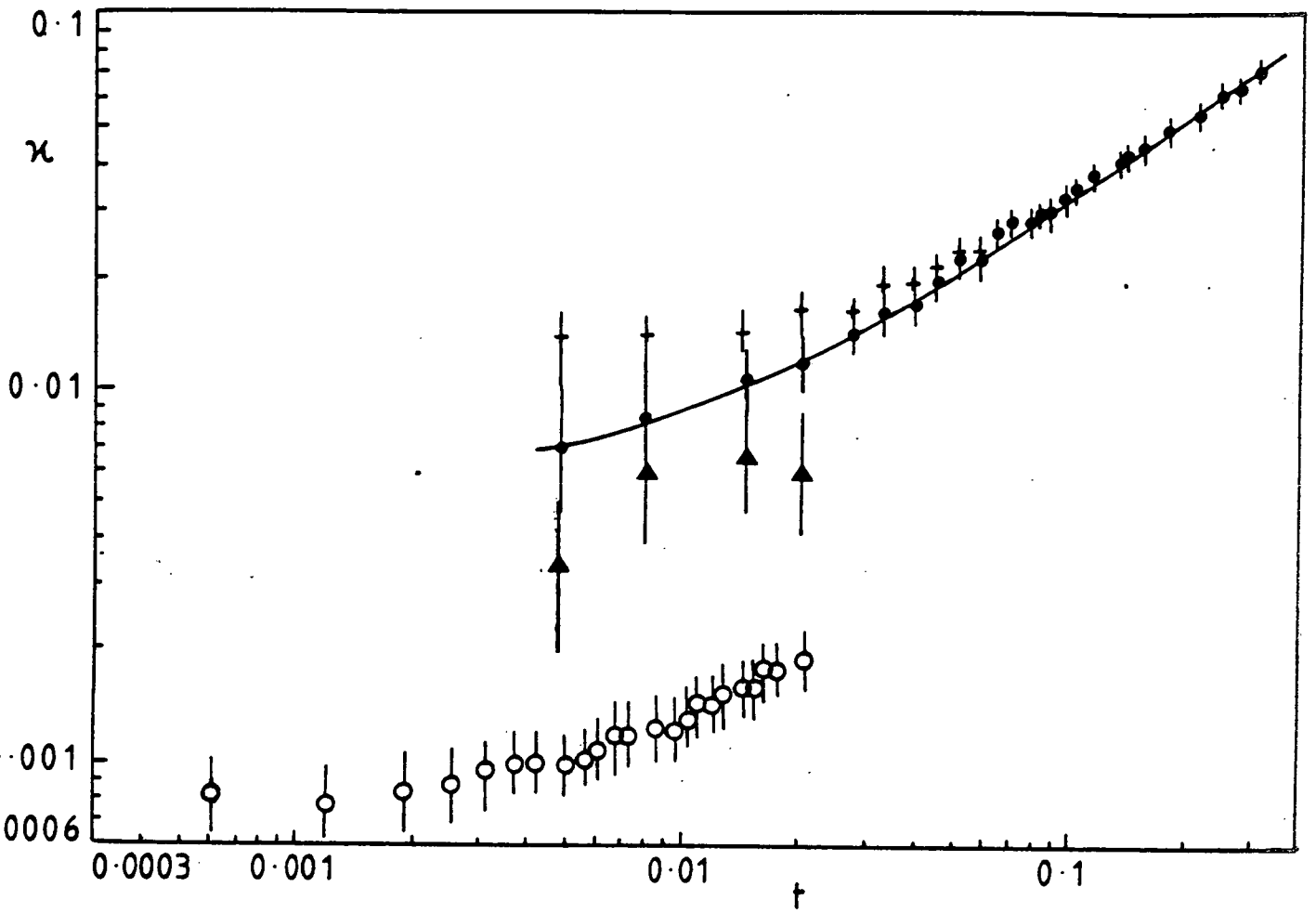

Figure 5.11

Inverse correlation lengths obtained from the analysis as described in the text of the diffuse x-ray scattering, in units of $2\pi/a_o$, for the reciprocal lattice points (0.5 0.5 3.5), and (0.5 0.5 2.5) [open circles] for $KMn_{0.9}Mg_{0.1}F_3$. The closed circles correspond to data analysed using the anisotropic Lorentzian only model, with f = -1, h = 0. The crosses and triangles refer to data analysed using the Lorentzian (anisotropic) plus Lorentzian squared (isotropic) model, the crosses to the Lorentzian inverse correlation length and the triangles to the Lorentzian squared inverse correlation length. The open circles refer to the high resolution data, the model being Lorentzian squared only, with f = h = 0. The solid line is a least squares fit to the power law discussed in the text.

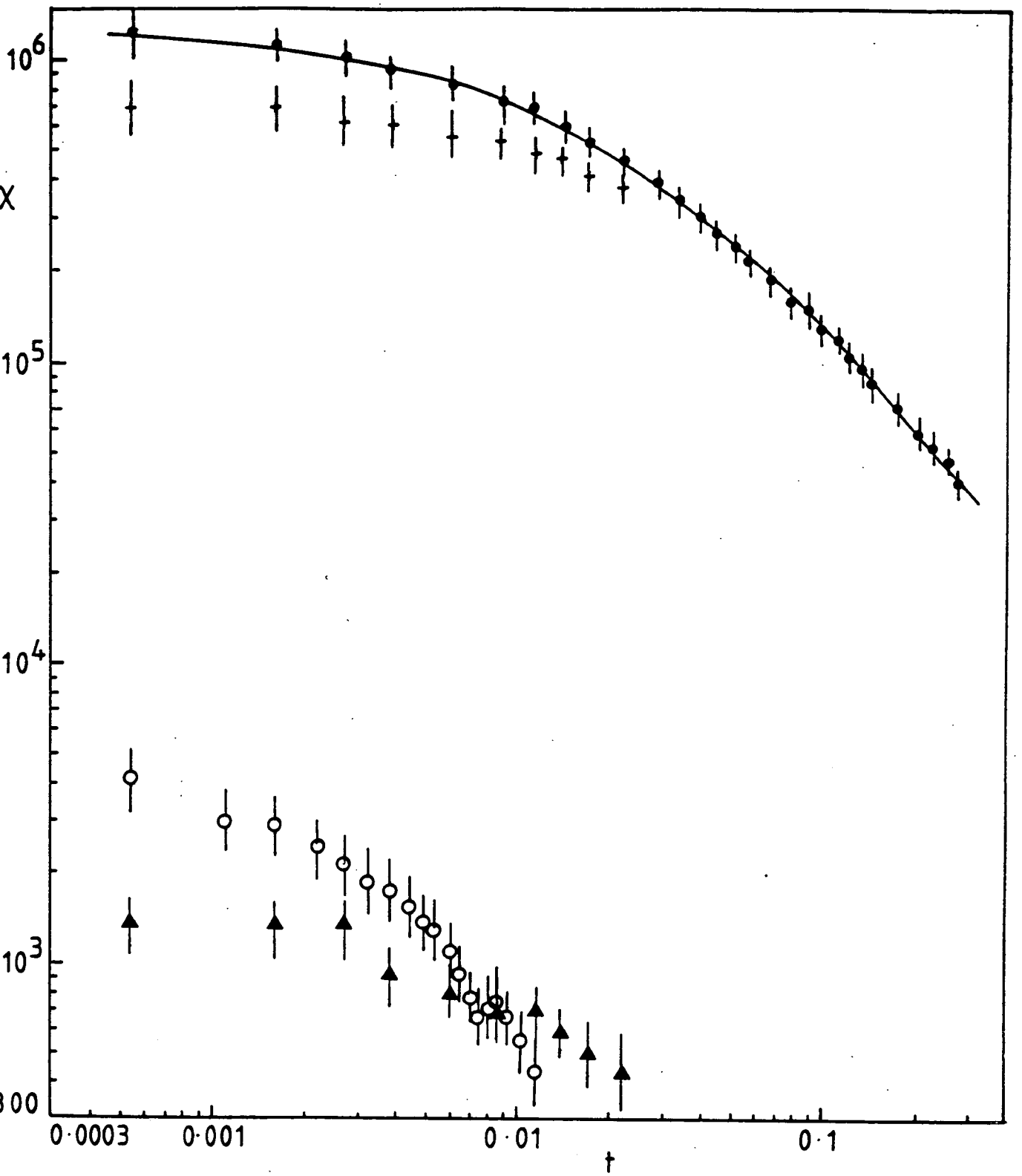

Figure 5.12

Amplitude (arbitrary units) obtained from the analysis as described in the text of the diffuse x-ray scattering for the reciprocal lattice points (0.5 0.5 3.5) and (0.5 0.5 2.5) [open circles] for $KMn_{0.99}Mg_{0.01}F_3$. The solid line is a least squares fit to the power law discussed in the text.

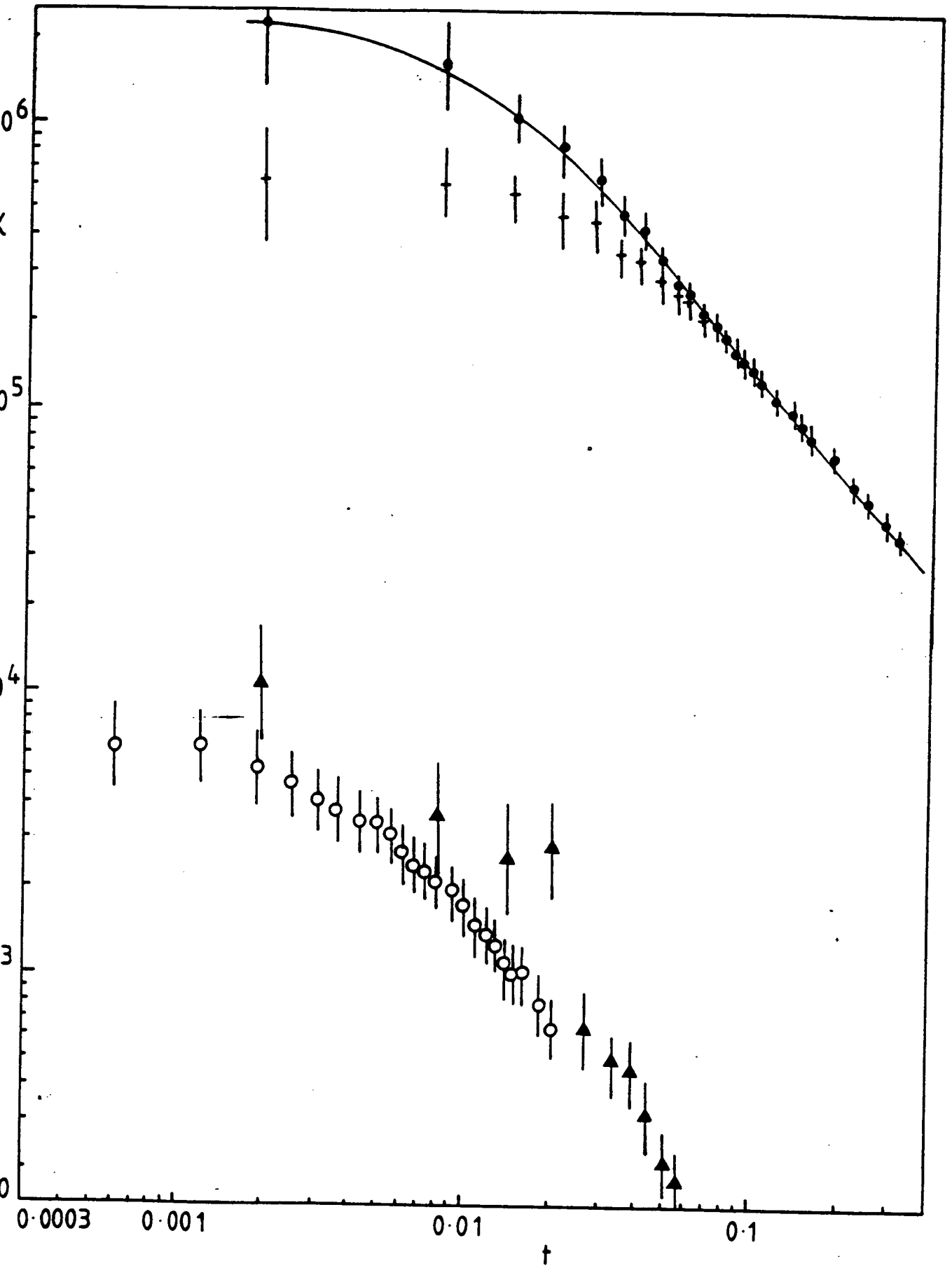

Figure 5.13

Amplitude (arbitrary units) obtained from the analysis as described in the text of the diffuse x-ray scattering for the reciprocal lattice points (0.5 0.5 3.5) and (0.5 0.5 2.5) [open circles] for $KMn_{0.9}Mg_{0.1}F_3$. The solid line is a least squares fit to the power law discussed in the text.

Table 5.2 : The Critical Exponent of the Lorentzian Component for $KMn_xMg_{1-x}F_3$ (Errors shown in brackets).

	ν_L	ξ_{L_0} / Å	$(T_c' - T_c)$ /K	γ_L	$(T_c' - T_c)$ /K
x = 0.99	0.65 (0.08)	43 (8)	-3.4 (1.0)	1.19 (0.15)	-3.1 (1.0)
x = 0.90	0.74 (0.05)	37 (7)	-1.4 (1.0)	1.59 (0.17)	-2.8 (0.7)
x = 1.00	0.62 (0.07)	31 (6)	-0.12 (0.03)	1.19 (0.11)	-0.12 (0.03)
Theory for n=d=3 model	0.705 (0.003)	—	—	1.386 (0.004)	—

are shown in figures 5.10 - 5.13. Their magnitude and temperature dependence will be discussed in conjunction with the results for $KMnF_3$ in section 3.

The Temperature Dependence and Amplitude of the Anomalous Component

The data close to the transition temperature in $KMnF_3$, $KMn_{0.99}Mg_{0.01}F_3$ and $KMn_{0.9}Mg_{0.1}F_3$ collected in the low resolution configuration, was fitted to a two part scattering model. The first, Lorentzian component, had the general form

$$S_1(q) = \frac{A}{(\kappa_L)^2 + q^2} \quad \text{and} \quad \chi_L = \frac{A}{(\kappa_L)^2} \qquad (1)$$

and the second, Lorentzian squared component, the form

$$S_2(q) = \frac{B}{((\kappa_{L^2})^2 + q^2)^2} \quad \text{and} \quad \chi_{L^2} = \frac{\sqrt{B}}{(\kappa_{L^2})^2} \qquad (2)$$

Consequently at zero wavevector, the weighting of the Lorentzian component is χ_L and equal to the amplitude, but the weighting of the Lorentzian squared component is $(\chi_{L^2})^2$. Figure 5.14 shows these two weightings obtained from the fits for all three samples, as a function of temperature. In the case of both $KMn_{0.99}Mg_{0.01}F_3$ and $KMn_{0.9}Mg_{0.1}F_3$ there is a clear cross-over temperature below which the Lorentzian squared component begins to carry most weight. This is $T \sim T_c + 2\,K$ for $KMn_{0.99}Mg_{0.01}F_3$ and $T \sim T_c + 5\,K$ in $KMn_{0.9}Mg_{0.1}F_3$. For pure $KMnF_3$, the two weightings converge at a temperature $T \sim T_c + 7\,K$.

Figure 5.15 is a plot of the peak intensity (unprocesssed data) of the R-point scattering collected at the reciprocal lattice point (0.5 0.5 2.5) in the high resolution configuration, for $KMn_{0.99}Mg_{0.01}F_3$ and $KMn_{0.9}Mg_{0.1}F_3$ above the transition. It is plotted on a log scale as a function of reduced temperature t (also on a log scale). The data is normalised to a counting time of one minute, and was collected with the x-ray spectrometer in identical configurations for both samples. Since the x-ray beam illuminates only a small part of the sample, and the width of the scattering was only slightly greater than the resolution width in both cases, this figure gives a reasonable estimate of the relative intensities of the anomalous component observed in the x-ray scattering cross section in $KMn_{0.99}Mg_{0.01}F_3$ and $KMn_{0.9}Mg_{0.1}F_3$. It can be seen that the scattering above T_c in $KMn_{0.9}Mg_{0.1}F_3$ is consistently greater than that observed in $KMn_{0.99}Mg_{0.01}F_3$, and that the temperature dependence is similar in both.

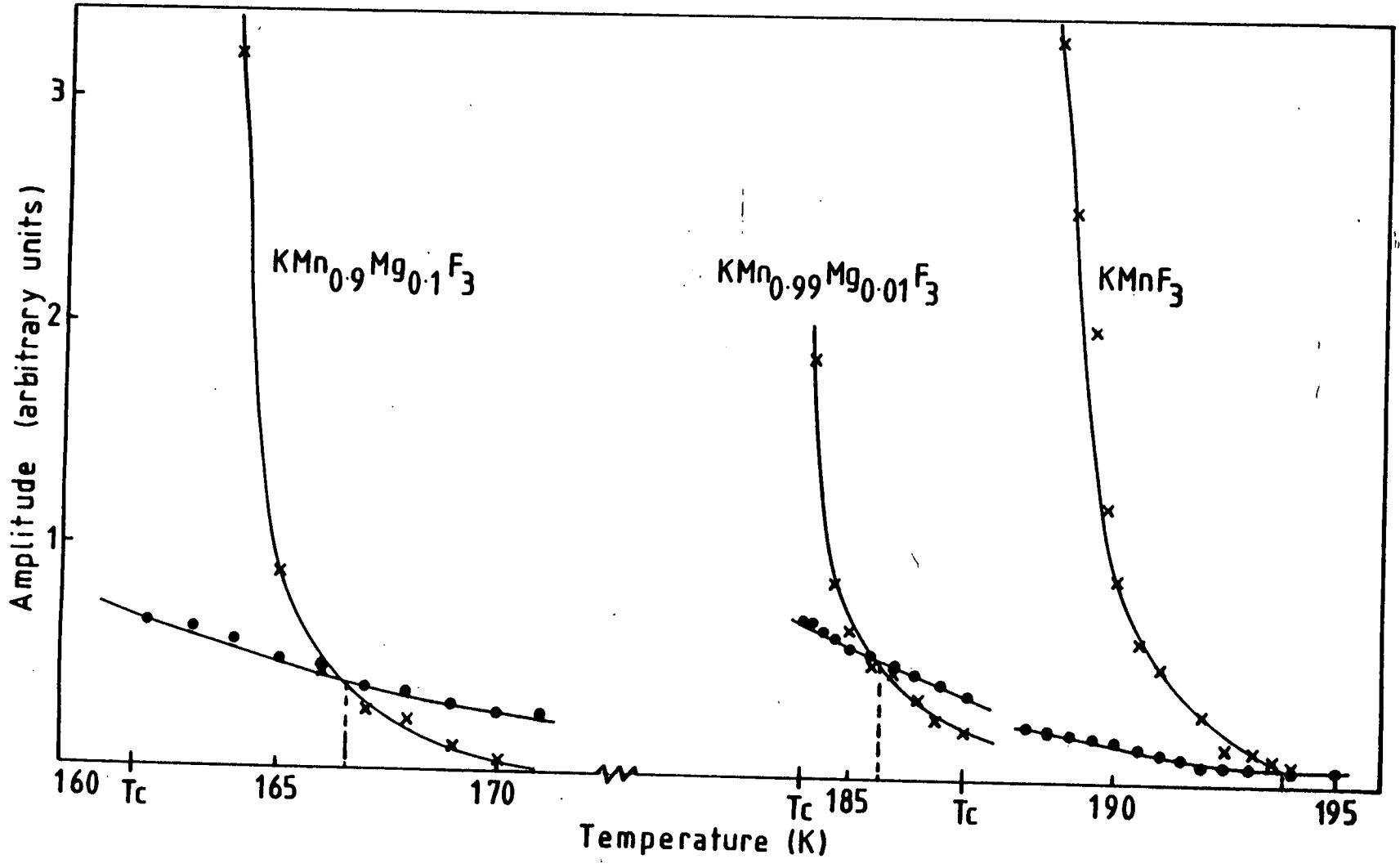

Figure 5.14

The relative weighting of the two components (anisotropic Lorentzian and isotropic Lorentzian squared) in the analysis of the x-ray data collected in the low resolution configuration for all three samples, as a function of temperature. In each case, the closed circles refer to the Lorentzian component and the crosses to the Lorentzian squared component. The dotted lines show the cross-over temperatures.

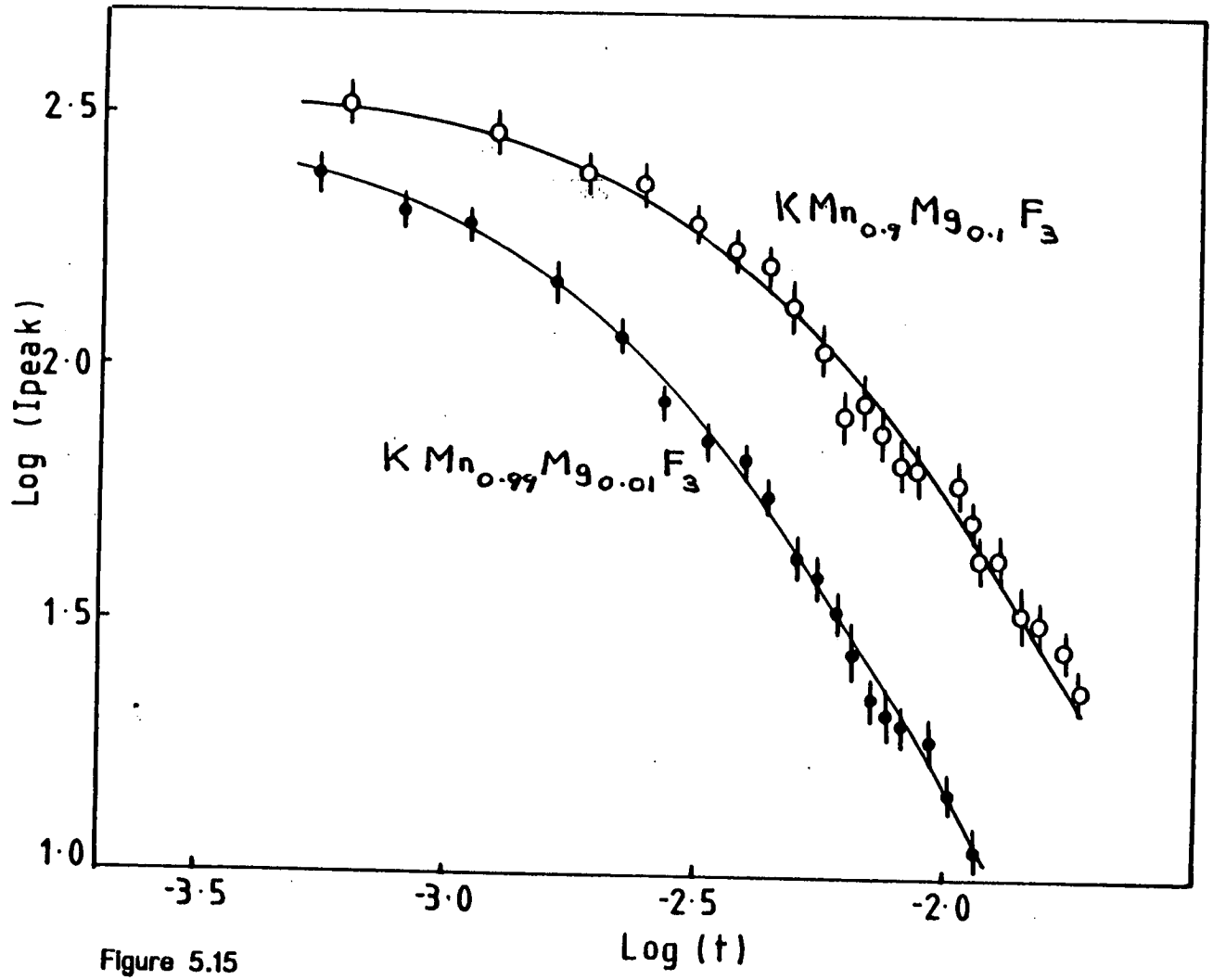

Figure 5.15

The peak intensity of the x-ray scattering (normalised to a counting time of 60 seconds) at the reciprocal lattice point (0.5 0.5 2.5) obtained with the high resolution configuration for the two samples $KMn_{0.99}Mg_{0.01}F_3$ and $KMn_{0.9}Mg_{0.1}F_3$, as a function of reduced temperature for temperatures above T_c.

The unprocessed scattering intensity observed in pure $KMnF_3$ is not included on the graph since the experiment was performed at an earlier date when the incident x-ray beam may have been of different amplitude.

5.2.2 Neutron Scattering Experiments

Measurement of the Transition Temperature

The transition temperature in $KMn_{0.99}Mg_{0.01}F_3$ and $KMn_{0.9}Mg_{0.1}F_3$ was measured using neutron scattering by monitoring the peak intensity at the reciprocal lattice point (0.5 0.5 1.5) as the temperature was lowered through the transition. The results for the two samples are shown in figure 5.16, and give values for T_c^1 and T_c^{10} which are in agreement with those determined using x-ray scattering.

Critical Scattering Measurements

The energy dependence of the critical scattering above T_c was measured at the zone-boundary reciprocal lattice point (0.5 0.5 1.5) using incident neutron energies of 3.53 and 1.12 THz for $KMn_{0.99}Mg_{0.01}F_3$ and $KMn_{0.9}Mg_{0.1}F_3$. Some high resolution measurements on pure $KMnF_3$ (the same sample as was used in the x-ray experiments described in chapter 4) were also made. Figures 5.17, 5.18, and 5.19 show the results for the three samples at approximately the same value of the reduced temperature $t = 0.033$, all collected with an incident energy of 1.12 THz and horizontal collimation 20' - 20' - 30'. The observed scattering cross section is clearly different in the three cases. In $KMnF_3$ the profile appears to consist of two components, a broad overdamped phonon centered on zero frequency, together with a narrow central peak sitting on top. This result is qualitatively similar to that found in pure $KMnF_3$ by Shapiro et al (1972). In $KMn_{0.99}Mg_{0.01}F_3$ an analogous division is possible, the scattering profile being consistent with a broad overdamped phonon and a small central peak, but in $KMn_{0.9}Mg_{0.1}F_3$ such a separation is less discernible, since the overdamped phonon is considerably narrower in energy (consistent with a larger damping constant) and the 'wings' of the measured cross section are correspondingly smaller. This behaviour is reflected in the results of the analysis and will be discussed in section 3.

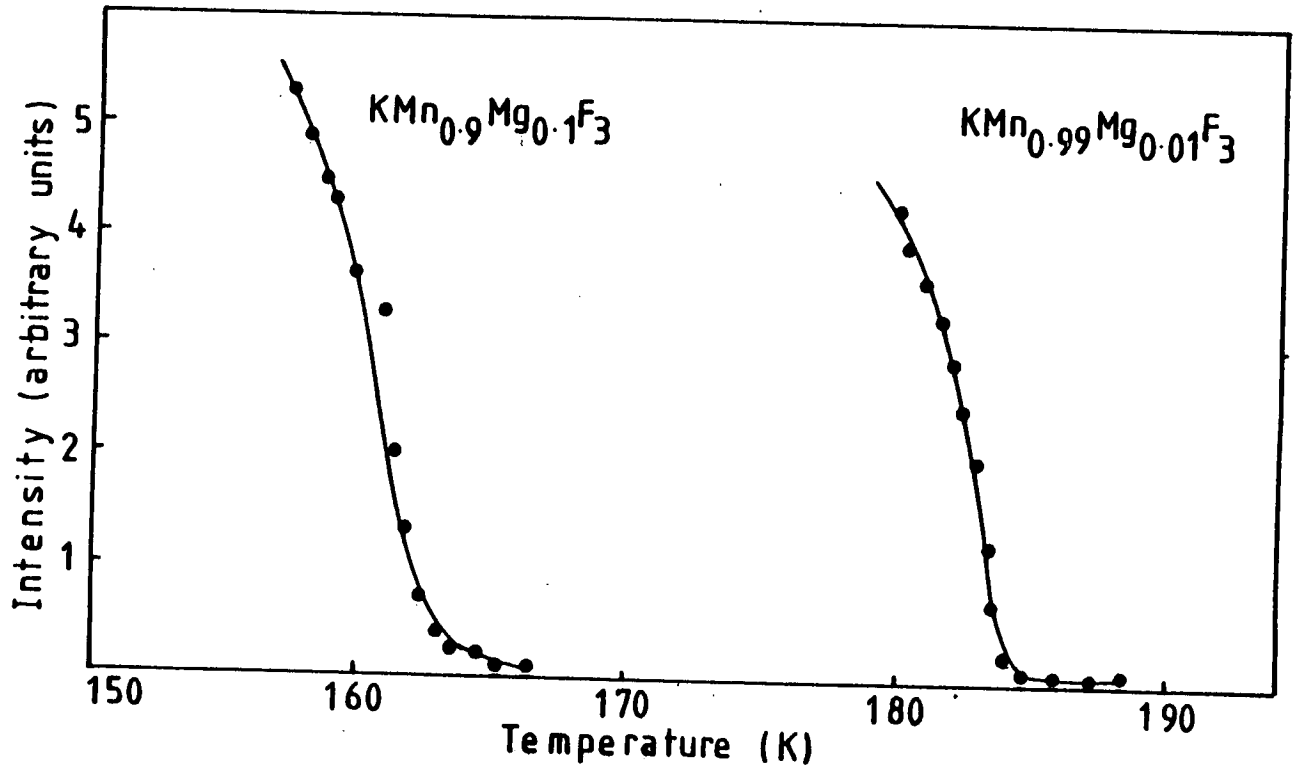

Figure 5.16

The peak intensity of the neutron scattering (normalised to a monitor count of 3) at the reciprocal lattice point (0.5 0.5 1.5) obtained with an incident energy of 1.12 THz for the two samples $KMn_{0.99}Mg_{0.01}F_3$ and $KMn_{0.9}Mg_{0.1}F_3$, as each sample was cooled through the transition.

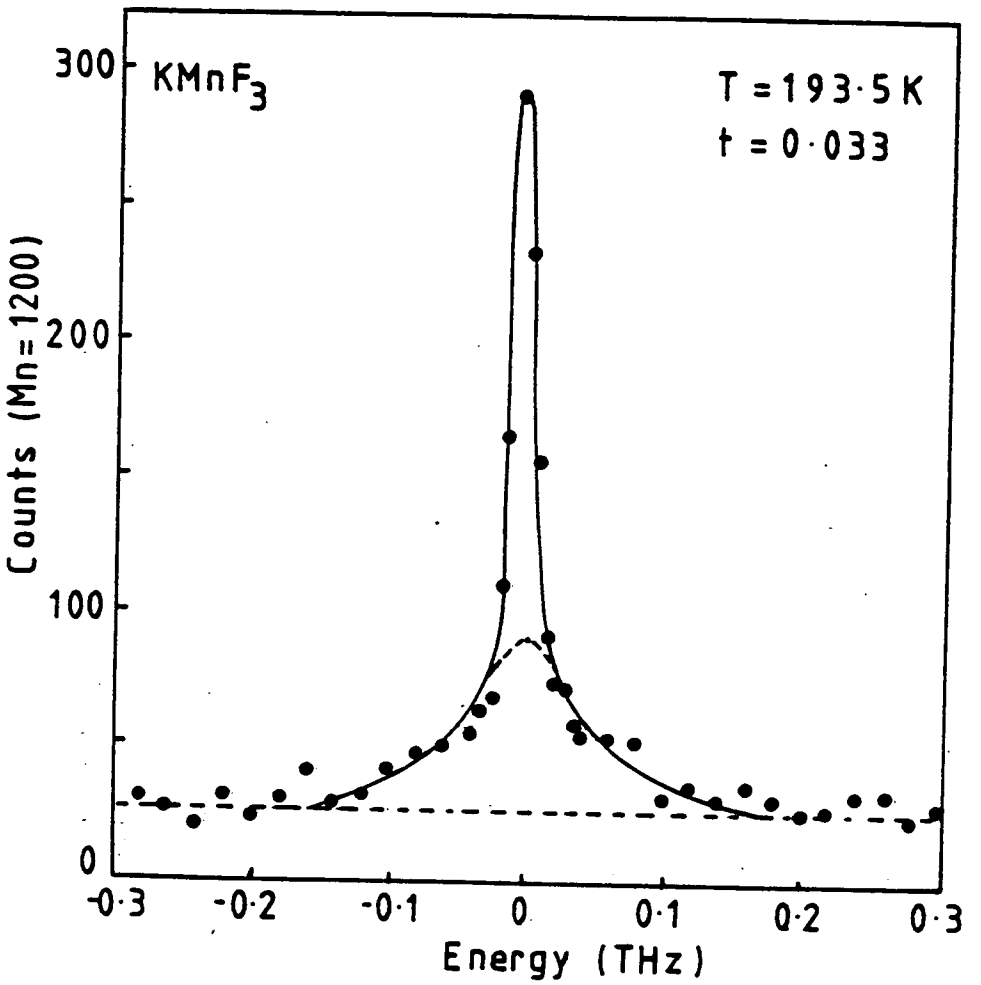

Figure 5.17

Scattered neutron intensity for pure $KMnF_3$ at the reciprocal lattice point (0.5 0.5 1.5) obtained with an incident energy of 1.12THz, as a function of energy at $T=T_c+6K$. The solid curve is a least squares fit to the model described in the text convolved with the instrumental resolution: The dotted curve corresponds to the contribution of the phonon peak.

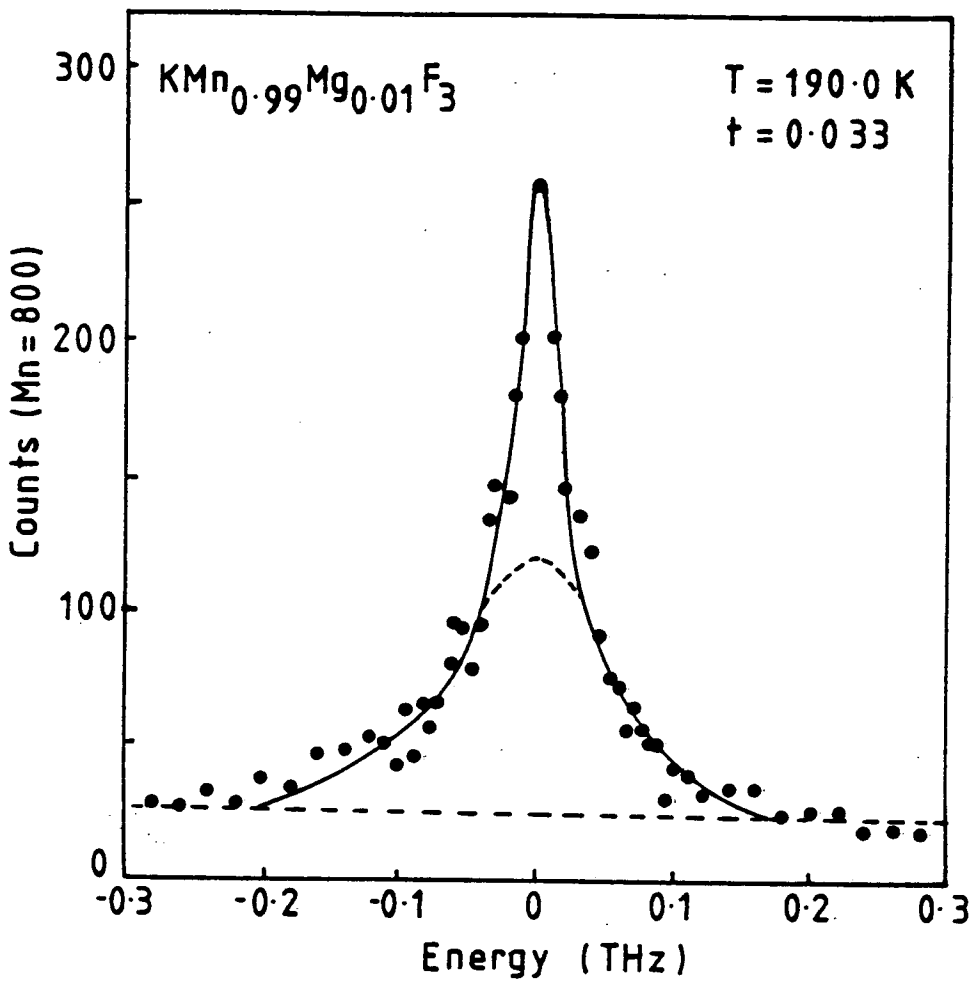

Figure 5.18

Scattered neutron intensity for $KMn_{0.99}Mg_{0.01}F_3$ at the reciprocal lattice point (0.5 0.5 1.5) obtained with an incident energy of 1.12THz, as a function of energy at $T=T_c+6.1K$. The solid curve is a least squares fit to the model described in the text convolved with the instrumental resolution: The dotted curve corresponds to the contribution of the phonon peak.

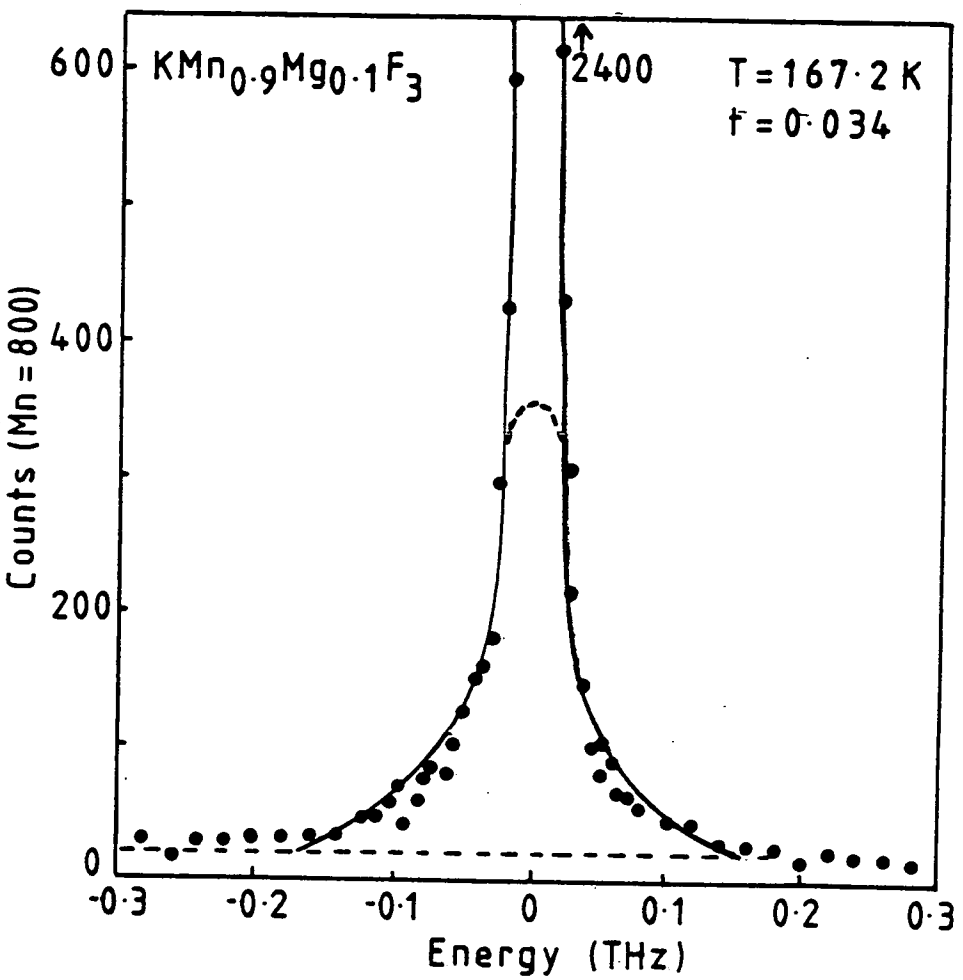

Figure 5.19

Scattered neutron intensity for $KMn_{0.9}Mg_{0.1}F_3$ at the reciprocal lattice point (0.5 0.5 1.5) obtained with an incident energy of 1.12THz, as a function of energy at $T=T_c+5.5K$. The solid curve is a least squares fit to the model with a non-zero central peak convolved with the instrumental resolution: The dotted curve corresponds to the contribution of the phonon peak.

The widths and peak heights of the critical scattering measured with an incident energy of 3.52THz are shown in figures 5.20-5.23 for the two samples $KMn_{0.99}Mg_{0.01}F_3$ and $KMn_{0.9}Mg_{0.1}F_3$ as functions of temperature (triangles). In all cases a small amount of incoherent scattering background was subtracted from the data. The solid curves are intended as guides to the eye. At this incident energy, it was not possible to distinguish between the phonon bands and the central peak in the scattering cross section at even the highest temperatures above the transition in either $KMn_{0.99}Mg_{0.01}F_3$ or $KMn_{0.9}Mg_{0.1}F_3$. It can be seen that in $KMn_{0.99}Mg_{0.01}F_3$ the width decreases approximately linearly with decreasing temperature, while the peak intensity increases exponentially. In $KMn_{0.9}Mg_{0.1}F_3$ the width of the scattering is considerably more narrow than in $KMn_{0.99}Mg_{0.01}F_3$ (N.B. the vertical axis is on a different scale), and less temperature dependent, beginning to saturate as T_c is approached. The amplitude of the scattering was more intense in $KMn_{0.9}Mg_{0.1}F_3$ since the sample was twice the volume in size, but it can be seen that the temperature dependence of the peak intensity is nominally the same in the two samples.

The widths of the scattering obtained in the two materials with an incident energy of 1.12THz are also shown as functions of temperature in figures 5.20 and 5.21 (crosses). The results show that the width of the scattering is temperature independent in both $KMn_{0.99}Mg_{0.01}F_3$ and $KMn_{0.9}Mg_{0.1}F_3$, at a value consistent with the energy width measured in a Vanadium scan (see figure 2.12) for this collimation, and is considerably less than the widths measured with an incident energy of 3.52THz. This suggests that the scattering observed in the higher resolution experiments is a resolution limited central peak: The phonon is indistinguishable from a uniform background that is above the level of incoherence unless the counting time is extremely long and the scan sufficiently wide.

The peak intensity of the scattering measured with an incident energy of 1.12THz (that is, the amplitude of the central peak) in the three samples $KMnF_3$, $KMn_{0.99}Mg_{0.01}F_3$ and $KMn_{0.9}Mg_{0.1}F_3$ is shown on a log scale as a function of reduced temperature (also plotted on a log scale) in figure 5.24. The figure shows that each curve (drawn as aids to the eye) flattens off to the phonon background level at high temperatures. It is not pragmatic to compare absolute intensities from sample to sample in a neutron scattering experiment since the scattered intensity is very dependent on the size of the crystal. However, the figure indicates that the temperature dependence of the central peak is similar in all three materials.

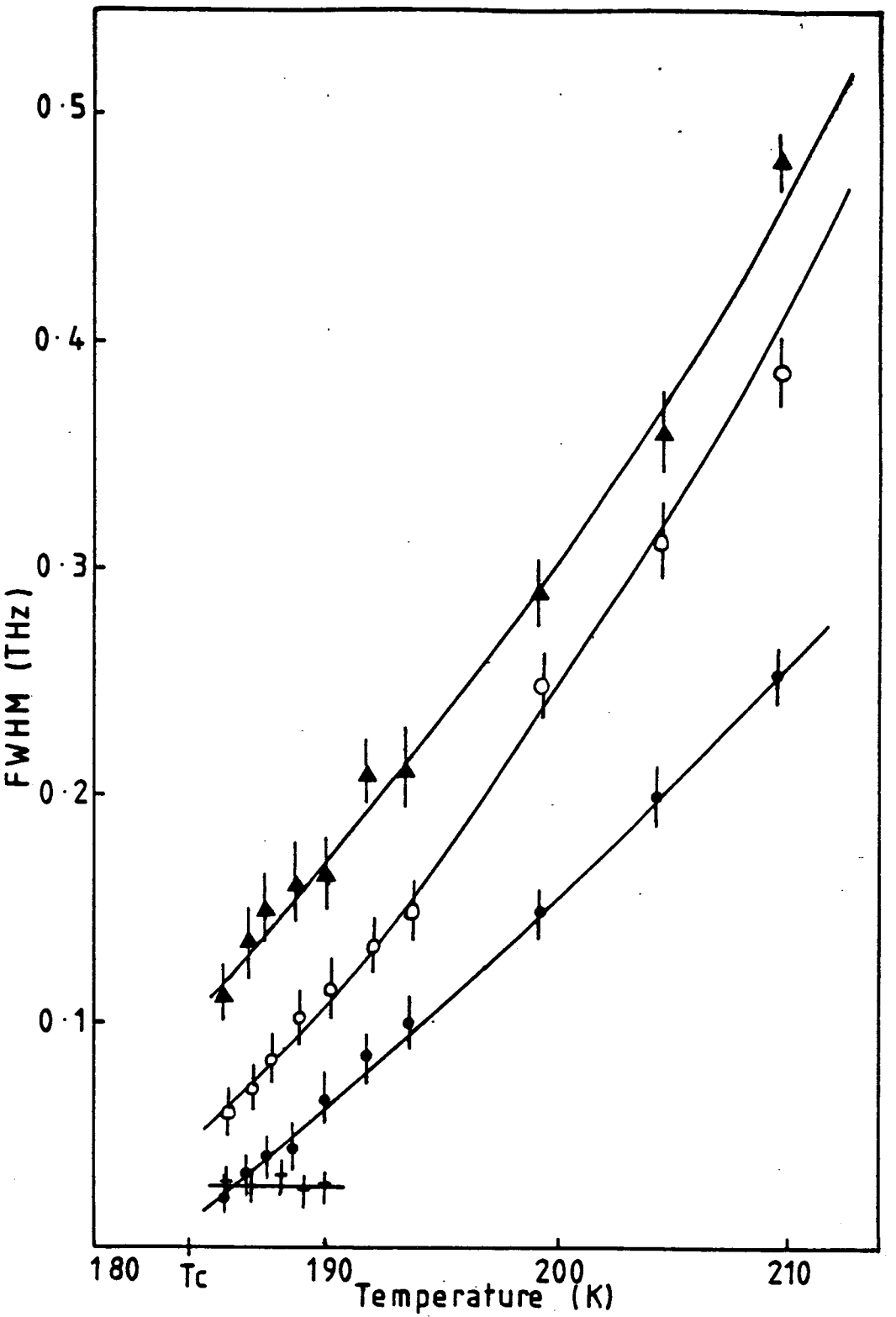

Figure 5.20

The energy width of the neutron scattering at the reciprocal lattice point (0.5 0.5 1.5) for $KMn_{0.99}Mg_{0.01}F_3$, as a function of temperature. The triangles and crosses refer to the widths of the unprocessed experimental data, the triangles to that collected with an incident energy of 3.52THz, and the crosses to an incident energy of 1.12THz. The open circles correspond to the width of the phonon obtained when the data was fitted to the model with a non-zero central peak, and the closed circles to the width of the phonon obtained when the central peak was constrained to be zero.

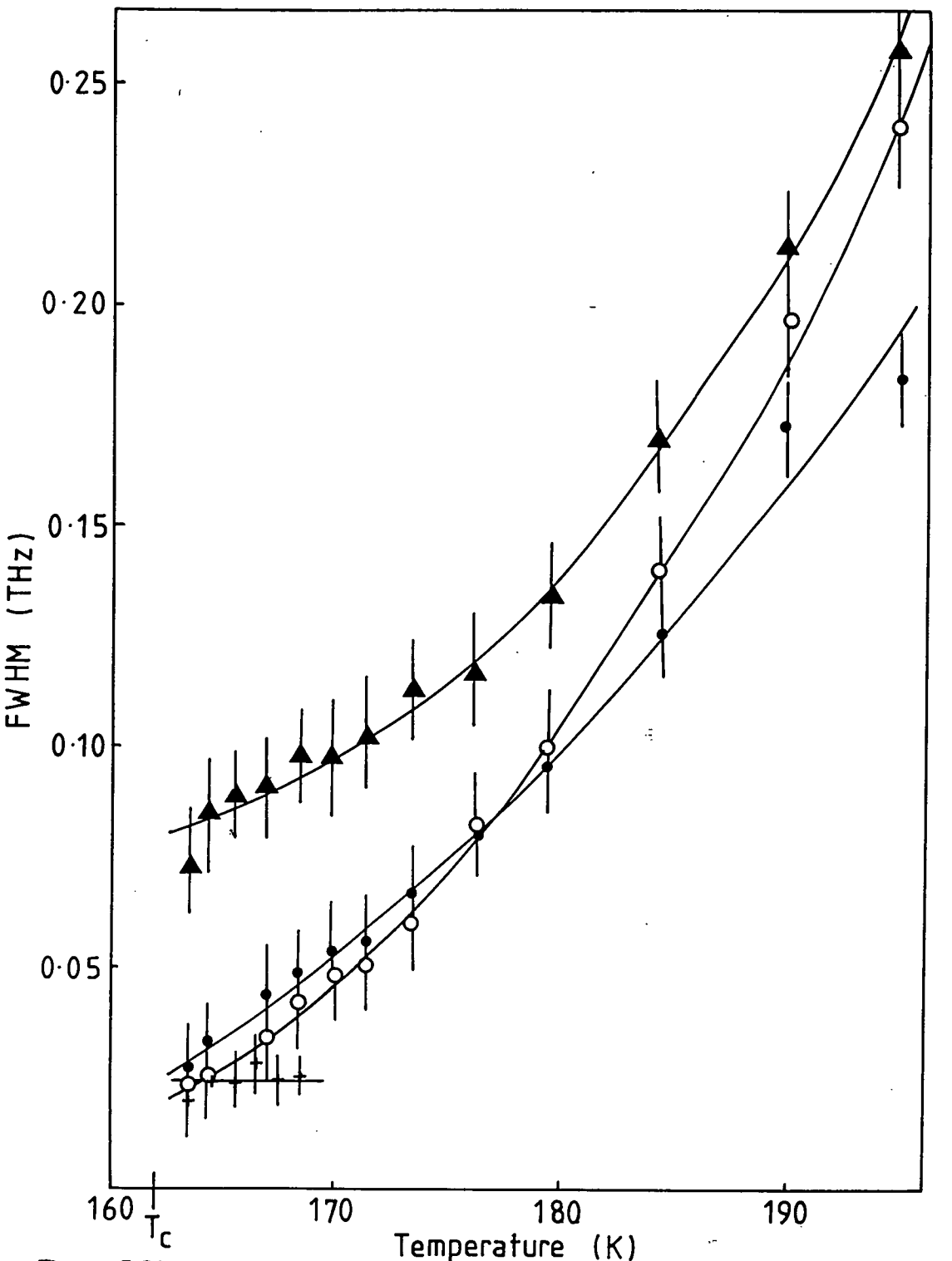

Figure 5.21

The energy width of the neutron scattering at the reciprocal lattice point (0.5 0.5 1.5) for $KMn_{0.9}Mg_{0.1}F_3$, as a function of temperature. The triangles and crosses refer to the widths of the unprocessed experimental data, the triangles to that collected with an incident energy of 3.52THz, and the crosses to an incident energy of 1.12THz. The open circles correspond to the width of the phonon obtained when the data was fitted to the model with a non-zero central peak, and the closed circles to the width of the phonon obtained when the central peak was constrained to be zero.

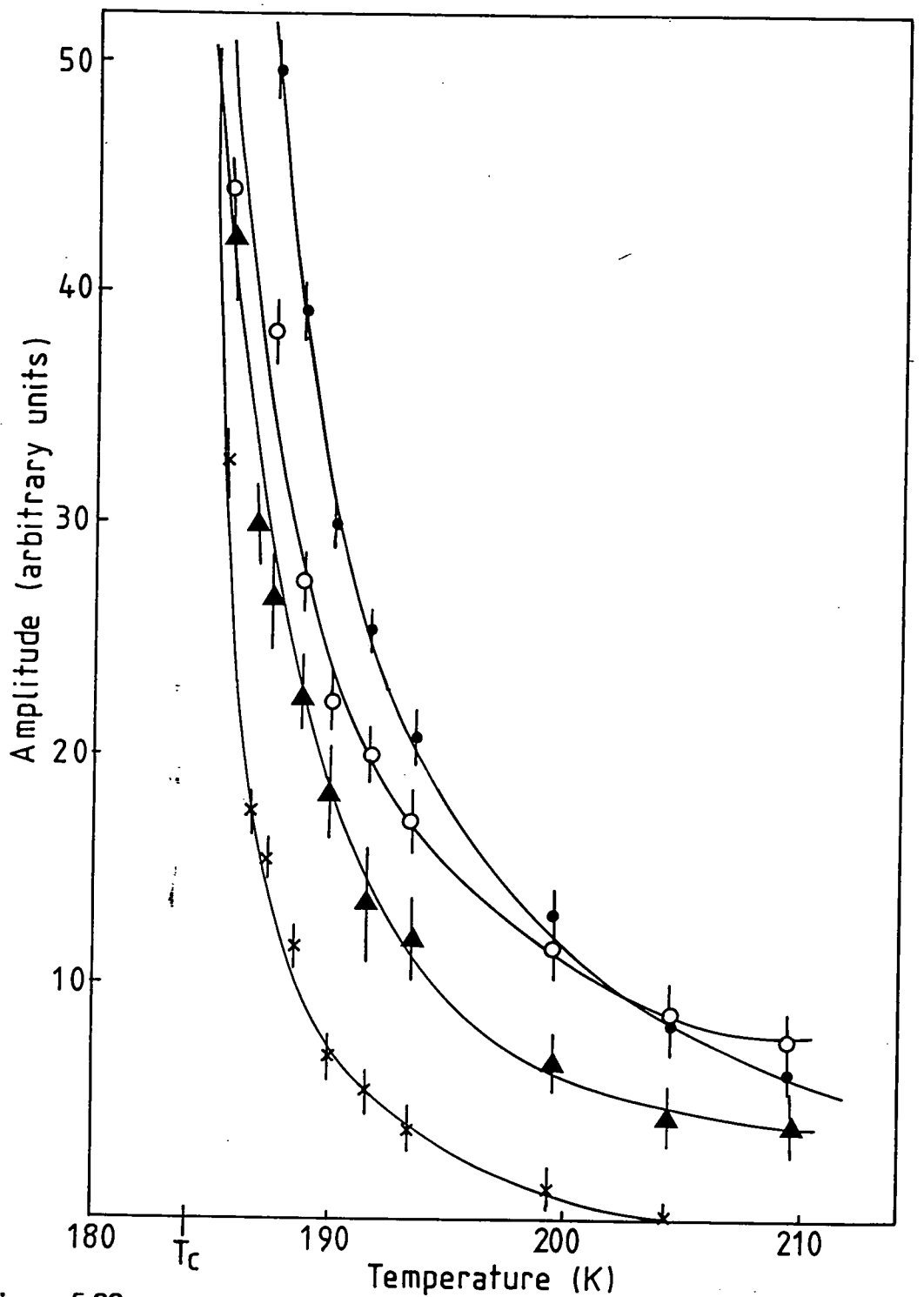

Figure 5.22

The amplitude of the neutron scattering at the reciprocal lattice point (0.5 0.5 1.5) for $KMn_{0.99}Mg_{0.01}F_3$ as a function of temperature. The triangles refer to the peak intensity of the unprocessed experimental data collected with an incident energy of 3.52THz and normalised to a monitor count of 12. The open circles and crosses correspond to the amplitudes of the phonon and central peak obtained when the data was fitted to the model with a non-zero central peak, the open circles to the amplitude of the phonon and the crosses to the amplitude of the central peak. The closed circles refer to the amplitude of the phonon obtained when the central peak was constrained to be zero.

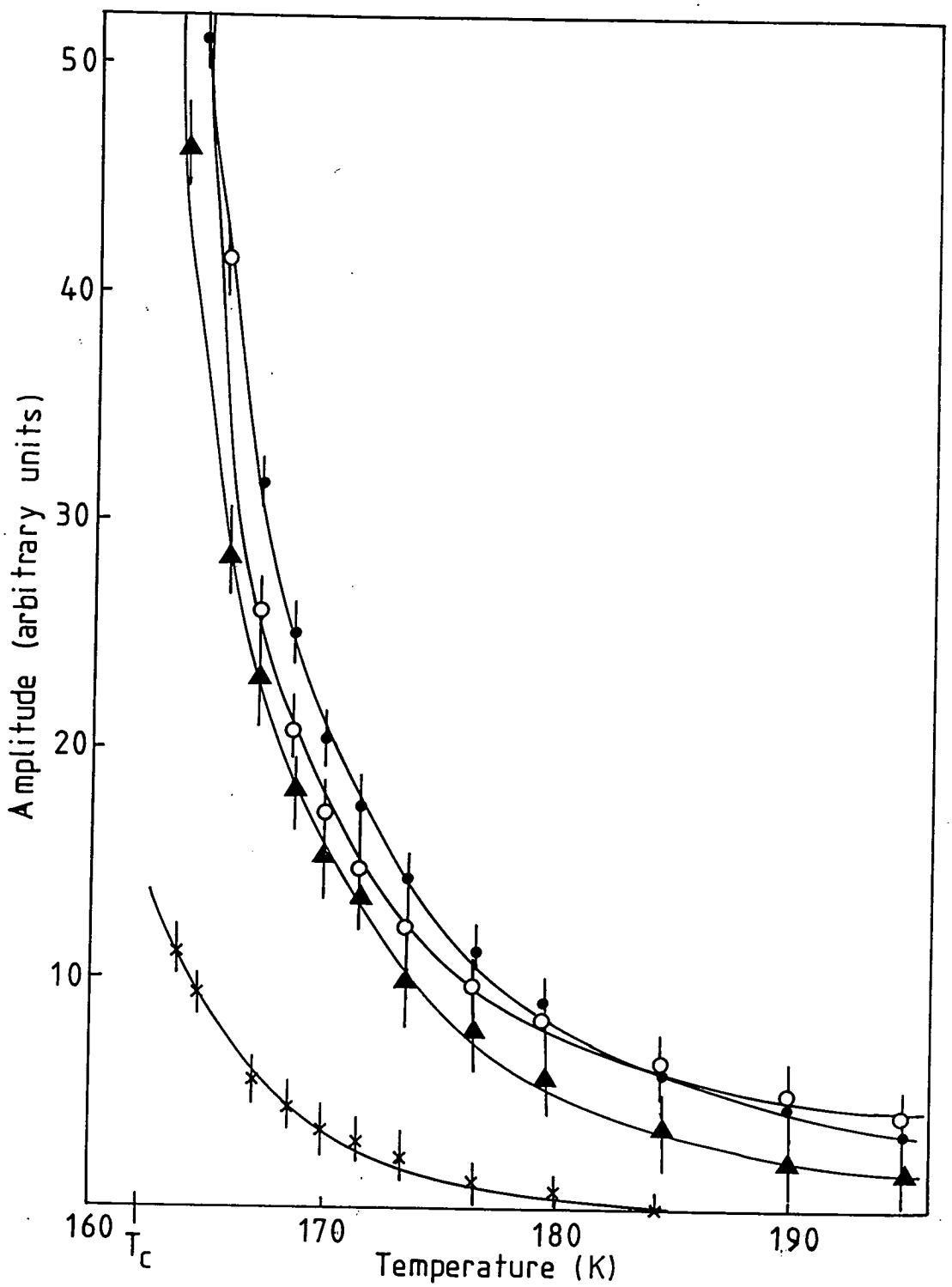

Figure 5.23

The amplitude of the neutron scattering at the reciprocal lattice point (0.5 0.5 1.5) for $KMn_{0.9}Mg_{0.1}F_3$, as a function of temperature. The triangles refer to the peak intensity of the unprocessed experimental data collected with an incident energy of 3.52THz and normalised to a monitor count of 4. The open circles and crosses correspond to the amplitudes of the phonon and central peak obtained when the data was fitted to the model with a non-zero central peak, the open circles to the amplitude of the phonon and the crosses to the amplitude of the central peak. The closed circles refer to the amplitude of the phonon obtained when the central peak was constrained to be zero.

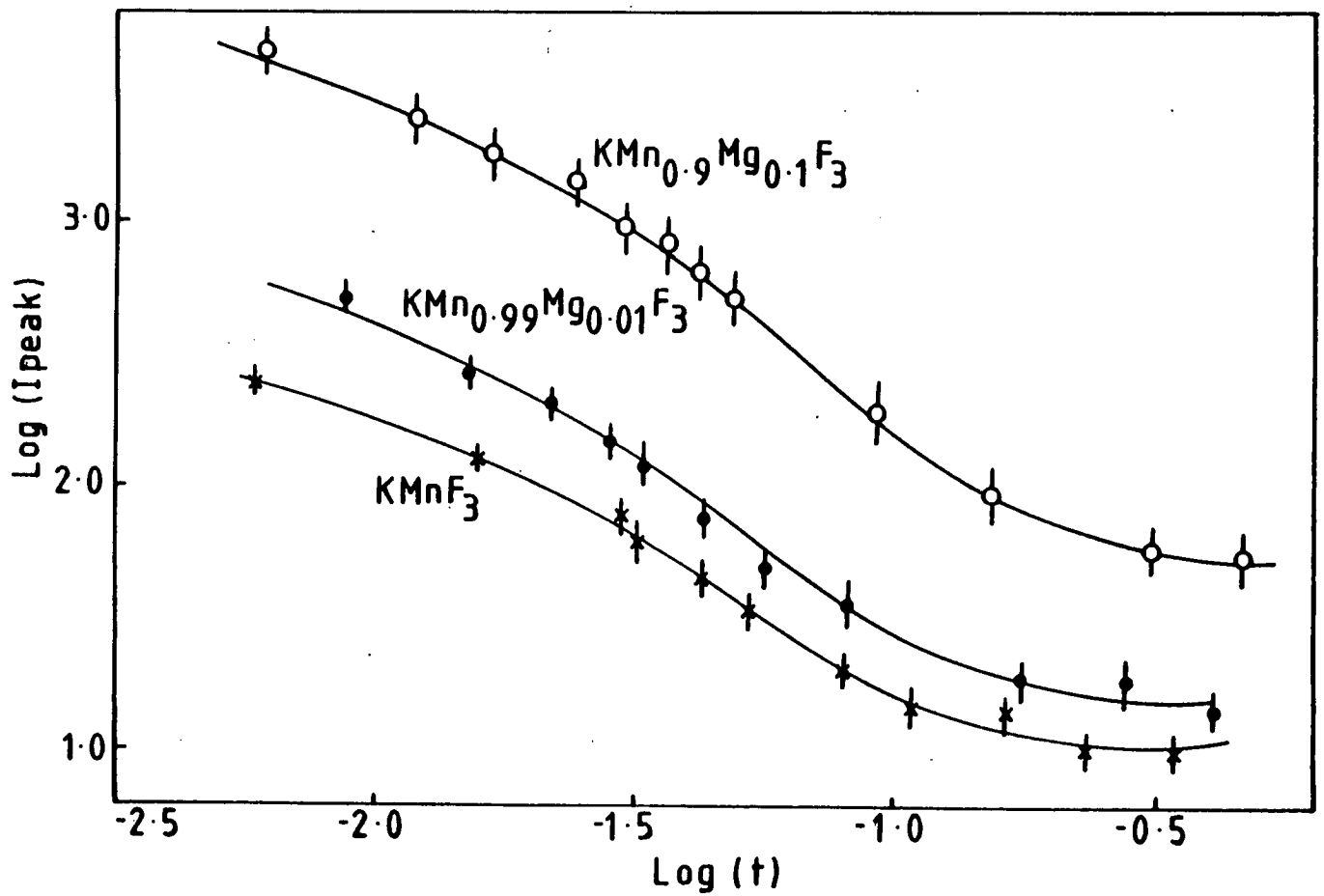

Figure 5.24

The peak intensity of the neutron scattering (normalised to a monitor count of 300) at the reciprocal lattice point (0.5 0.5 1.5) obtained with an incident energy of 1.12THz for the three samples, as a function of reduced temperature for temperatures above T_c.

Analysis of Critical Scattering

The critical scattering data collected using the low resolution configuration for $KMn_{0.99}Mg_{0.01}F_3$ and $KMn_{0.9}Mg_{0.1}F_3$ was analysed by a least squares fit to a trial function $I(\mathbf{q},\omega)$, where $I(\mathbf{q},\omega)$ is equal to the convolution of a model scattering function $S(\mathbf{q},\omega)$ with the instrumental response function

$$I(\mathbf{q},\omega) = \frac{k_f}{k_i} \iint S(\mathbf{q},\omega)\, R(\mathbf{q}'-\mathbf{q},\omega'-\omega)\, d\mathbf{q}'\, d\omega' \qquad (3)$$

The model $S(\mathbf{q},\omega)$ used here was the phenomenological model assumed by Shapiro et al (1972) in their analysis of the critical scattering measured above T_c in $SrTiO_3$ and which was introduced briefly in chapter 1. They supposed that the response function was that of a damped simple harmonic oscillator coupled, with a constant δ, to some unspecified internal degree of freedom. This provides an additional channel for decay for phonon fluctuations with frequencies ω less than some characteristic frequency γ. The scattering function could then be split into two terms if the damping constant $\Gamma_o \ll \delta^2/\gamma$ and the frequency $\omega_\infty^2 \gg \gamma^2$

$$S(\mathbf{q},\omega) = S_{ph}(\mathbf{q},\omega) + S_{ce}(\mathbf{q},\omega) \qquad (4)$$

where

$$S_{ph}(\mathbf{q},\omega) = \frac{|F(\mathbf{Q})|^2 k_B T}{\pi} \cdot \frac{\Gamma_o}{(\omega_\infty^2(\mathbf{q},T) - \omega^2)^2 + \omega^2 \Gamma_o^2} \qquad (5)$$

is the damped harmonic oscillator response with characteristic frequencies $\pm\omega_\infty(\mathbf{q},T)$ in the high temperature limit with $F(\mathbf{Q})$ the structure factor, and

$$S_{ce}(\mathbf{q},\omega) = \frac{|F(\mathbf{Q})|^2 k_B T}{\pi} \cdot \frac{\delta^2(T)}{\omega_o^2(\mathbf{q},T)\, \omega_\infty^2(\mathbf{q},T)} \cdot \frac{\gamma'}{(\omega^2+\gamma'^2)} \qquad (6)$$

is a narrow Lorentzian of width $\gamma' = \gamma.(\omega_o^2/\omega_\infty^2)$ centered about $\omega = 0$: The scattering function obeys the sum rule

$$\int_{-\infty}^{+\infty} S(\mathbf{q},\omega)\, d\omega = \frac{k_B T\ |F(\mathbf{Q})|^2}{\omega_o^2(\mathbf{q},T)} \qquad (7)$$

where $\omega_o^2(\mathbf{q},T) = \omega_\infty^2(\mathbf{q},T) - \delta^2(T)$ is the square of the renormalised mode frequency in the limit ω tends to 0. By integrating (5) and (6) it can be seen how they contribute separately to the sum rule:

$$\int S(\mathbf{q},\omega)\,d\omega = \int S_{ph}(\mathbf{q},\omega)\,d\omega + \int S_{ce}(\mathbf{q},\omega)\,d\omega$$

$$\frac{1}{\omega_o^2(\mathbf{q},T)} = \frac{1}{\omega_\infty^2(\mathbf{q},T)} + \frac{\delta^2(T)}{\omega_o^2(\mathbf{q},T).\,\omega_\infty^2(\mathbf{q},T)} \qquad (8)$$

Fitting Technique

The energy scans measured above T_c with an incident neutron energy of 3.52THz at the reciprocal lattice point (0.5 0.5 1.5) in $KMn_{0.99}Mg_{0.01}F_3$ and $KMn_{0.9}Mg_{0.1}F_3$ were fitted to the model scattering function $S(\mathbf{q},\omega)$ described above. In this fitting of this model it was assumed that Γ_o, γ' and δ were all independent of q, and that the entire q dependence of $S(\mathbf{q},\omega)$ was included in the phonon frequency $\omega_\infty(\mathbf{q},T)$. The phonon dispersion close to the R-point in $KMnF_3$ was discussed in chapter 4, and gave the following relationship for $\omega_\infty^2(\mathbf{q},T)$

$$\left(\omega_\infty^2(\mathbf{q},T)\right)_{pq} = \left(\omega_\infty^2(0,T) + \lambda(\mathbf{q}^2 + f q_p^2)\right)\delta_{pq} + h\,\mathbf{q}_p.\mathbf{q}_q(1-\delta_{pq}) \qquad (9)$$

In all fits for $KMn_{0.99}Mg_{0.01}F_3$ and $KMn_{0.9}Mg_{0.1}F_3$ the off-diagonal elements of the dynamical matrix were neglected (that is, h=0), and the anisotropy parameter f was fixed at -1 as in the analysis of the x-ray data: The parameter λ was constrained to equal 41$(THz\text{Å})^2$ (see Gesi et al 1972). The width γ' of the central peak was chosen to be such that it was always smaller than the energy resolution of the spectrometer.

As the soft-phonon in $KMnF_3$ is overdamped for $T \leq T_c$+40K, the data fitting is hindered by the difficulty in determining an unambiguous value for the overall scale. This problem was tackled for each sample in the following way: An energy scan collected at the R-point at a temperature well above the transition was chosen, and the frequency $\omega_\infty(0,T)$ and damping constant Γ_o were fixed at the values found by previous measurements (chiefly those by Gesi et al 1972); the central peak amplitude δ was held at zero. The scaling parameter was then allowed to converge to its optimum. This value was fixed for all scans, and the parameters $\omega_\infty(0,T)$, Γ_o and δ allowed to vary.

The fits were assessed in terms of the goodness of fit parameter G as in the x-ray analysis. In both $KMn_{0.99}Mg_{0.01}F_3$ and $KMn_{0.9}Mg_{0.1}F_3$ it was found that reasonable fits were achieved with either a zero or a non-zero value for δ, and so results for both cases are included in the figures. For an overdamped phonon $S_{ph}(\mathbf{q},\omega)$ is an anisotropic Lorentzian with an energy width $\omega_{ph}(\mathbf{q},T) = \omega_{\infty}^{2}(\mathbf{q},T)/\Gamma_o$ centered on zero frequency, and so this parameter is used to represent the analysed data. Figures 5.20 and 5.21 show the obtained values of $2.\omega_{ph}(0,T)$ as a function of temperature for $KMn_{0.99}Mg_{0.01}F_3$ and $KMn_{0.9}Mg_{0.1}F_3$, the solid lines being intended as guides to the eye. The contributions of the phonon and central peak to the scattering amplitude are given by the sum rule (equation (8)). Figures 5.22 and 5.23 show these contributions as a function of temperature for $KMn_{0.99}Mg_{0.01}F_3$ and $KMn_{0.9}Mg_{0.1}F_3$ respectively, again, the solid lines are intended as guides to the eye. The results shown in figures 5.20-5.23 will be discussed in section 3.

5.3 Discussion of Results

5.3.1 Temperature Dependence of the Order Parameter and the Character of the Phase Transition

The values of the critical exponent β obtained from the analyses of the temperature dependence of the tetragonal strain in the three materials $KMnF_3$, $KMn_{0.99}Mg_{0.01}F_3$ and $KMn_{0.9}Mg_{0.1}F_3$ are shown in table 5.1. It can be seen that the effect of adding point defects to pure $KMnF_3$ is to increase the value of β towards that predicted by the $n = d = 3$ Heisenberg model. In $KMn_{0.99}Mg_{0.01}F_3$, the value obtained is 0.336 (8), and in $KMn_{0.9}Mg_{0.1}F_3$ is 0.332 (8). These two values of β agree reasonably with the value of $\frac{1}{3}$ found by Borsa (1973), Hirotsu and Sawada (1973) and Benard and Walker (1976) in measurements on $KMnF_3$. The value of 0.26 (2) obtained by us in pure $KMnF_3$ (chapter 4) was considerably lower than this, and it was suggested that this is because the phase transition occurs at atmospheric pressure in the vicinity of an Ising-like tricritical point, where the critical exponent is predicted as $\frac{1}{4}$ (Chang et al 1974). The results for $KMn_{0.99}Mg_{0.01}F_3$ and $KMn_{0.9}Mg_{0.1}F_3$ indicate that the effect of point defects is to return the system to one adequately described by a three component order parameter. It should be mentioned that the values for β obtained from analysis of the integrated intensity measurements at the R-point below T_c in $KMn_{0.9}Mg_{0.1}F_3$ agree reasonably well with that found by monitoring

the tetragonal strain, but the corresponding results for $KMn_{0.99}Mg_{0.01}F_3$ are much smaller (see figures 5.3 and 5.4). This is probably because the temperature dependence of the domain proportions is greater in the latter.

In all fits to the tetragonal strain the transition temperature was allowed to vary, which enables the character of the phase transition to be deduced. In $KMnF_3$, the effective transition temperature T_c' obtained from the fit was 188.6 K and the first order step at $T_c^0 = 187.5$ K measured as $\sim 6.7(2) \times 10^{-4}$. This measurement was also made by Sakahita et al (1981) who found that at T_c $(c_t/a_t - 1) = 9.9(1) \times 10^{-4}$. In $KMn_{0.99}Mg_{0.01}F_3$, T_c' converged at 186.5 K, and the first order step at $T_c^1 = 183.9$K was $\sim 5.3(2) \times 10^{-4}$. In $KMn_{0.9}Mg_{0.1}F_3$, the fit gave a transition temperature in agreement with $T_c^{10} = 161.7$ K within the bounds of experimental error, so the phase transition can be considered continuous in this case.

Two conclusions about the effect of point defects on the R-point structural phase transition in $KMnF_3$ can be made: Firstly, that the replacement of manganese ions with magnesium ions causes the transition temperature to be lowered, and the size of the decrease appears to be linearly related to the concentration of impurity ions. Secondly, that this substitution causes the phase transition to become more continuous with increasing defect concentration. Renormalisation group calculations by Domany et al (1977) considered a variety of systems whose phase transitions, continuous within mean-field theory, are driven first order by critical fluctuations. They showed that in certain cases a continuous phase transition could be restored by the presence of symmetry-breaking fields. Imry and Wortis (1979) also showed that microscopic random quenched impurities may produce a smearing of a first order phase transition.

5.3.2 Critical Scattering

Evaluation of the Critical Exponents ν_L and γ_L

The wavevector dependence of the critical scattering obtained with the low resolution configuration in $KMn_{0.99}Mg_{0.01}F_3$ and $KMn_{0.9}Mg_{0.1}F_3$ was well described by an anisotropic Lorentzian function (with a $\mathbf{q}$ dependent width) over a large range of the temperatures investigated. The critical exponents γ_L and ν_L describing the

temperature dependence of the static susceptibilty χ_L and inverse correlation length κ_L in $KMn_{0.99}Mg_{0.01}F_3$ and $KMn_{0.9}Mg_{0.1}F_3$ are shown in table 5.2, together with the values found in pure $KMnF_3$ and the theoretically predicted parameters of the $n = d = 3$ Heisenberg model for the soft-mode (Le Guillou and Zinn-Justin 1980). The values obtained for $KMn_{0.99}Mg_{0.01}F_3$ are very similar to those of pure $KMnF_3$, slightly smaller than predicted by the Heisenberg model. The values in $KMn_{0.9}Mg_{0.1}F_3$ are considerably larger, implying that the phonon width and amplitude decreased more rapidly as T_c was approached than in the other two cases (as would be expected at a continuous phase transition). However, the presence of a second anomalous component in the scattering cross section close to T_c will affect the values for the critical exponents : Examination of the amplitude of the susceptibilty and inverse correlation length in the three samples for $t > 0.05$ shows them to be identical. In all fits the transition temperature was allowed to vary, producing an offset from the experimentally determined value. The offset is larger in $KMn_{0.99}Mg_{0.01}F_3$ than in $KMn_{0.9}Mg_{0.1}F_3$ for both the susceptibilty and the inverse correlation length which suggests that the transition is more first order for the former, and is consistent with the result found by monitoring the tetragonal strain. However the offsets in $KMn_{0.99}Mg_{0.01}F_3$ and $KMn_{0.9}Mg_{0.1}F_3$ should not be directly compared those shown for $KMnF_3$ because for the latter the data collected at temperatures close to the transition temperature could not be fitted unless an isotropic Lorentzian squared component was included in the model scattering function. When this was included the width and amplitude of the anisotropic Lorentzian component was found to be independent of temperature for $T < T_c + 1.5$ K, consistent with a first order phase transition.

The Spectral Response Function

The results obtained from the analysis of the neutron scattering cross section measured in $KMn_{0.99}Mg_{0.01}F_3$ and $KMn_{0.9}Mg_{0.1}F_3$ with an incident energy of 3.52 THz is shown in figures 5.20 - 5.23, together with the unprocessed data. As mentioned in the analysis section, reasonable fits were obtained in both samples with and without the inclusion of a central peak in the scattering model.

In $KMn_{0.99}Mg_{0.01}F_3$, when a non-zero value of δ was incorporated into the fit, the values of $\omega_{ph}(0,T)$ achieved were consistently greater than those obtained with $\delta = 0$, as would be expected. This was caused by a decrease in the damping constant Γ_o from 1.10 (15) THz to 0.75 (5) THz, which in both fits was independent of temperature.

As the value for the damping constant in $KMnF_3$ has been measured as 0.84 (2) THz by Gesi et al (1972), both these values are consistent, though it is expected that if impurities are added into a system the damping would increase rather than decrease. It can also be seen that when a central peak is included, the resulting temperature dependence of the phonon width mirrors more closely the temperature dependence of the unprocessed data. The inclusion of a central peak caused a reduction in the size of the phonon contribution to the scattering amplitude, shown in figure 5.22; the contribution of the central peak is seen to increase exponentially as the transition temperature is approached from above.

In $KMn_{0.9}Mg_{0.1}F_3$, the effect of a non-zero value of δ on the obtained values of $\omega_{ph}(0,T)$ is less pronounced. This is in part due to the difficulty of separating the observed cross section into two components when the phonon is very narrow, and suggests that any central peak is small. However, when a central peak was included the damping constant became less temperature dependent (with $\delta = 0$ the damping was found to decrease with decreasing values of reduced temperature) with an average of 2.2 (3) THz. As in $KMn_{0.99}Mg_{0.01}F_3$, the inclusion of a central peak reduced the phonon contribution to the scattering amplitude, though to a lesser extent. The central peak contribution increases as T_c is approached, but this contribution is not as large as in $KMn_{0.99}Mg_{0.01}F_3$.

Comparison of the Anomalous Components Observed in the Three Samples $KMnF_3$, $KMn_{0.99}Mg_{0.01}F_3$ and $KMn_{0.9}Mg_{0.1}F_3$

(1) The widths

The substitution of magnesium impurity ions for manganese in $KMnF_3$ influences the wavevector width of the anomalous component in the x-ray scattering. In the three samples $KMnF_3$, $KMn_{0.99}Mg_{0.01}F_3$ and $KMn_{0.9}Mg_{0.1}F_3$ investigated, the anomalous scattering measured with the high resolution configuration was found to be broader than the resolution limit of $\sim 0.001\,(2)\,\text{Å}^{-1}$, and to be well described by an isotropic Lorentzian squared model convoluted with the resolution function. The deconvolved values of the widths ($\varkappa_{L^2}^{(S)}$) obtained for $KMn_{0.99}Mg_{0.01}F_3$ and $KMn_{0.9}Mg_{0.1}F_3$ are shown in figures 5.10 and 5.11, and those for $KMnF_3$ in figure 4.10. At a reduced temperature $t = 0.001$ $\varkappa_{L^2}^{(S)}$ is nominally the same in $KMnF_3$ and $KMn_{0.9}Mg_{0.1}F_3$, but larger in $KMn_{0.99}Mg_{0.01}F_3$. This corresponds to a smaller correlated volume at this reduced temperature in $KMn_{0.99}Mg_{0.01}F_3$ than in the other two samples. A greater

contrast is seen in the temperature dependence of the inverse correlation length : In $KMnF_3$, $\kappa_{L^2}^{(S)}$ increases significantly as the temperature is raised, with a temperature dependence described by an exponent $\nu_{L^2}^{(S)} = 0.84\,(12)$ which converged to zero at the measured transition temperature (corresponding to a divergence of the correlation length). In $KMn_{0.9}Mg_{0.1}F_3$ the exponent was 0.72 (15) but the width saturated at a value of $\sim 0.0014\,(5)\,\text{Å}^{-1}$ at $T = T_c + 0.9\,K$, while in $KMn_{0.99}Mg_{0.01}F_3$ the width was nominally temperature independent at a value $\sim 0.0018\,(6)\,\text{Å}^{-1}$, only increasing slightly with increasing temperature. The results for $KMn_{0.99}Mg_{0.01}F_3$ and $KMn_{0.9}Mg_{0.1}F_3$ are not easily reconciled with the explanation of the anomalous component given at the end of chapter 4, where it was suggested that this scattering could be interpreted as large-scale fluctuations into the tetragonal phase mediated by defects, and should undergo a continuous phase transition.

To date, all measurements of the energy width of the central peak observed using neutron scattering at a displacive structural phase transition have found it to be resolution limited at all temperatures above the transition. Our results indicate that an upper resolution limit of 0.02 THz (FWHM) is appropriate for the central peak in $KMnF_3$ when magnesium impurity ions are substituted for manganese, and we conclude that the addition of impurities does not affect the energy width.

(2) The Amplitudes

The deconvolved amplitudes $\chi_{L^2}^{(S)}$ of the anomalous x-ray component observed in $KMnF_3$, $KMn_{0.99}Mg_{0.01}F_3$ and $KMn_{0.9}Mg_{0.1}F_3$ are shown in figures 4.11, 5.12 and 5.13. It is apparent that the scattering is the most intense in $KMnF_3$, especially close to the transition, and weakest in $KMn_{0.99}Mg_{0.01}F_3$. This result shows that a simple substitional impurity does not tend to enhance the component, but rather to reduce it. The temperature dependence of the component in $KMn_{0.99}Mg_{0.01}F_3$ and $KMn_{0.9}Mg_{0.1}F_3$ is quite similar (see figure 5.15 also), and tends to saturate within 0.5 K of the transition in both cases. In $KMnF_3$ the temperature dependence of the deconvolved amplitude is consistent with a continuous phase transition as it diverges at the measured T_c. The relative importance of the Lorentzian and Lorentzian squared components in the scattering model used to describe the data collected using the low resolution arrangement is shown in figure 5.14 for the three samples, as a function of temperature. This shows the temperature at which the anomalous isotropic Lorentzian squared component in the cross section begins to carry most weight. In $KMn_{0.99}Mg_{0.01}F_3$ and $KMn_{0.9}Mg_{0.1}F_3$ a distinct cross-over point can be discerned, ~ 4 K above the

transition temperature in $KMn_{0.9}Mg_{0.1}F_3$ and ~2 K in $KMn_{0.99}Mg_{0.01}F_3$. However, in $KMnF_3$ the anomalous scattering contribution constitutes the major part from ~8 K above T_c and is relatively more intense than in either $KMn_{0.99}Mg_{0.01}F_3$ or $KMn_{0.9}Mg_{0.1}F_3$.

The central peak intensity in $KMnF_3$ observed in the neutron scattering cross section is also reduced when substitutional impurities are present, though analysis of the data is complicated because the phonon is overdamped for all temperatures investigated so the two constituents are superimposed. In $KMnF_3$, the presence of a central peak is clearly evident from the high resolution energy scan shown in figure 5.17, which reveals a scattering cross section with two features. The scan shown in figure 5.18 for $KMn_{0.99}Mg_{0.01}F_3$ is consistent with such a division and indicates that the central peak is smaller than in pure $KMnF_3$. In $KMn_{0.9}Mg_{0.1}F_3$, the central peak cannot be distinguished from the overdamped phonon in figure 5.19 because of the large damping constant in this sample. However, narrow, low-monitor energy scans across the peak using high resolution resulted in scattering which was resolution limited in width for all temperatures investigated: This is taken as evidence for a central peak in this sample. The results of the analysis of the data collected using the low resolution configuration indicate that a central peak is present in both $KMn_{0.99}Mg_{0.01}F_3$ and $KMn_{0.9}Mg_{0.1}F_3$ and is weaker in the latter.

Comparison of the Anomalous Components Observed in the X-ray and Neutron Scattering Cross Sections

The above comparison shows that the substitution of magnesium ions for manganese in $KMnF_3$ does not tend to enhance either the anomalous component observed in the x-ray scattering cross section or the neutron central peak, but rather to decrease them. However, while the amplitude of the x-ray component was enhanced in $KMn_{0.9}Mg_{0.1}F_3$ over $KMn_{0.99}Mg_{0.01}F_3$, the amplitude of the neutron central peak was diminished: This suggests that the two components have a different origin. More conclusive evidence is found from a comparison of the temperature range over which they are visible. Figures 5.15 and 5.24 show the peak intensity of the anomalous scattering, measured using x-rays and neutrons respectively, as functions of temperature. The anomalous x-ray component has a very low intensity in both $KMn_{0.99}Mg_{0.01}F_3$ and $KMn_{0.9}Mg_{0.1}F_3$ at a reduced temperature of $t = 0.01$, which corresponds to one or two degrees above the transition temperature. In contrast, the neutron central peak persists over a temperature range which is a factor of ten

greater, to a reduced temperature of $t = 0.1$. This is further substantiated by the results of fits to the data collected using the low resolution configuration in both the x-ray and the neutron experiments. The cross-over temperatures shown in figure 5.14 all lie within ten degrees of the respective transition temperatures. Such a cross-over is not observed in the neutron results, but the central peak amplitude is first observed some twenty-five degrees above the transition in both $KMn_{0.99}Mg_{0.01}F_3$ and $KMn_{0.9}Mg_{0.1}F_3$.

5.4 Summary and Conclusions

1) The influence of point defects on the R-point structural instability in $KMnF_3$ has been studied using x-ray and neutron scattering. The x-ray scattering results indicate that for sufficiently high temperatures above the transitions the effect of the impurities is minimal, the wavevector dependence of the critical scattering in the three samples $KMnF_3$, $KMn_{0.99}Mg_{0.01}F_3$, and $KMn_{0.9}Mg_{0.1}F_3$ being well described by the anisotropic Lorentzian model as expected, with the same anisotropy parameters, and giving identical values for the inverse correlation length and static susceptibilty. The neutron scattering measurements of the spectral response shows that the effect of adding substitutional impurities to $KMnF_3$ is to increase the damping constant, and hence narrow the already overdamped phonon scattering. The same anisotropy parameters as used in the x-ray analysis were found to adequately describe the dynamic response.

2) Close to the transition temperature an anomalous component was observed in both the neutron and x-ray cross sections in addition to the scattering from the soft-phonon.

- The central peaks observed in the spectral response of the two doped materials $KMn_{0.99}Mg_{0.01}F_3$ and $KMn_{0.9}Mg_{0.1}F_3$ first appeared more than twenty degrees above the transition temperature, and increased in amplitude as the transition was approached. At all temperatures the width of this scattering was resolution limited at 0.02 THz. However, in the analysis of the data collected with an incident energy of 3.52 THz it was found that in both materials reasonable fits were achieved when the central peak amplitude was constrained to be zero. This suggested that the central peak in both cases was small. A comparison of the scattering at a reduced temperature of $t = 0.033$ in the three materials $KMnF_3$, $KMn_{0.99}Mg_{0.01}F_3$ and $KMn_{0.9}Mg_{0.1}F_3$

with an incident energy of 1.12 THz showed the central peak to be greater in pure $KMnF_3$ than in $KMnF_3$ containing isolated point defects. This indicates that the formation of a central peak is not directly related to the presence of simple substitutional impurities and may be an intrinsic phenomenon.

- The anomalous components observed in the x-ray scattering cross sections of $KMn_{0.99}Mg_{0.01}F_3$ and $KMn_{0.9}Mg_{0.1}F_3$ first appeared a few degrees above the transition temperature and increased in intensity as $T - T_c$ was reduced. The scattering was broader than the resolution width at all temperatures considered, and well described by an isotropic Lorentzian squared model. This latter result strongly suggests that this component is related to random fields in the system, such as occurs when isolated impurities are present. However, the intensity of this component does not increase with increasing impurity concentration, and in fact is strongest in the pure material. As discussed in chapter 4, the presence of a second type of fluctuation in the system at a first order phase transition could explain the anomalous scattering : The amplitude of the component would then be expected to decrease as the phase transition became more continuous.

REFERENCES

Aharony, A., 1976, Phase transitions and Critical Phenomena, Vol. 6, edited by C.Domb and M.S.Green, (New York : Academic Press), pg. 357

Aharony, A., and Bruce, A.D., 1974, Phys.Rev.Lett., **33** 427

- 1979, Phys.Rev.Lett., **42** 462

Almairac, R., Rosseau, M., Gesland, J.Y., Nouet, J., and Hennion, B., 1977, J. de Physique, **38** 1429

Anderson, P.W., 1960, Fisika Dielectrikov, edited by G.I.Skanavi, (Moscow : Acad.Nauk.SSR)

Andrews, S.R., 1986, J.Phys. C, **19** 3721

Andrews, S.R., and Cowley, R.A., 1985, J.Phys. C, **18** 6427

Aubry, S., 1975, J.Chem. Phys., **62** 3217

- 1976 a, J.Chem. Phys., **64** 3392
- 1976 b, Ferroelectrics, **12** 263

Axe, J.D., Keating, D.T., and Moss, S.C., 1975, Phys.Rev.Lett., **35** 30

Axe, J.D., Shapiro, S.M., and Shirane, G., 1974, Anharmonic Lattices, Structural Transitions and Melting, edited by T.Riste, (Leiden : Noordhoff) pg. 23

Axe, J.D., and Shirane, G., 1974, Phys.Rev. B, **8** 1965

Bausch, R., and Halperin, B.I., 1978, Phys.Rev. B, **18** 190

Benard, D.J., and Walker, W.C., 1976, Rev.Sci.Instrum., **47** 122

Birgeneau, R.J., Kjems, J.K., Shirane, G., and Van Uitert, L.G., 1974, Phys.Rev. B, **10** 2512

Bishop, A.R., and Krumhansl, J.A., 1975, Phys.Rev. B, **12** 2824

Bonse, U., and Hart, M., 1965, Z Phys., **189** 151

Borsa, E., 1973, Phys.Rev. B, **7** 917

Bruce, A.D., 1974, J.Phys. C,**7** 2089

- 1978, Solitons and Condensed Matter Physics, edited by A.R.Bishop and T.Schneider, (Berlin, Heidelberg : Springer-Verlag) pg. 116
- 1980, Adv.Phys., **29** 111

Bruce, A.D., and Cowley, R.A., 1973, J.Phys. C, **6** 2422

- 1980, Adv.Phys., **29** 219

Bruce, A.D., and Schneider, T., 1977, Phys.Rev. B, **16** 3991

Bruce, A.D., Schneider, T., and Stoll, E., 1979, Phys.Rev.Lett., **43** 1284

Bruce, A.D., Taylor, W., and Murray, A.F., 1980, J.Phys. C, **13** 483

Chang, T.S., Tuthill, G.F., and Stanley, H.E., 1974, Phys.Rev. B, **9** 4882

Chesser, N.J., and Axe, J.D., 1973, Acta Cryst., **A29** 160

Cochran, W., 1960, Adv.Phys., **9** 387

Comés, R., Denoyer, F., Deschamps, L., and Lambert, M., 1971, Phys. Lett., **34A** 65

Cooper, M.J., and Nathans, R., 1967, Acta Cryst., **23** 357

Courtens, E., 1972, Phys.Rev.Lett., **29** 1380

Cowley, R.A., 1963, Adv.Phys., **12** 421

- 1980, Adv.Phys., **29** 1
- 1987, accepted for publication in Acta Cryst.

Cowley, R.A., Axe, J.D., and Iizumi, M., 1976, Phys.Rev.Lett., **36** 806

Cowley, R.A., and Coombs, G.J., 1973, J.Phys. C, **6** 143

Cowley, R.A., and Ryan, T.W., 1987, J.Phys. D, **20** 61

Cowley, R.A., and Shirane, G., 1978, J.Phys. C, **11** L939

Cox, D.E., Shapiro, S.M., Cowley, R.A., Eibschutz, M., and Guggenheim, H.J., 1979, Phys.Rev. B, **19** 5754

Darlington, C.N.W., and O'Connor, D.A., 1976, J.Phys. C, **9** 3561

- 1978, Proceedings of the International Conference on Lattice Dynamics, edited by M.Balkaniski. (Paris : Flammarion) pg. 750

Darwin, C.G., 1914, Phil.Mag., **27** 315, 657

- 1922, Phil.Mag., **43** 800

Domany, E., Mukamel, D., and Fisher, M.E., 1977, Phys.Rev. B, **15** 5432

Dorner, B., 1972, Acta Cryst., **A28** 160

Doughty, G.F., Dargan, C.L., and Wilkinson, C.D.W., 1985, Proc.SPIE, **578** 82

Doughty, G.F., Thoms, S., Lau, V., and Wilkinson, C.D.W., 1986, Vacuum, **36** 803

Feder, J., 1971, Solid State Comm., **9** 2021

- 1976, Local Properties at Phase Transitions, edited by K.A.Muller and A.Rigamonti, (Amsterdam : North-Holland) pg.312

Fisher, M.E., 1974, Rev.Mod.Phys., **46** 597

Fisher, M.E., and Nelson, D.R., 1974, Phys.Rev.Lett., **32** 1350

Gesi, K., Axe, J.D., Shirane, G., and Linz, A., 1972, Phys.Rev. B, **5** 1933

Gibaud, A., Ryan, T.W., and Nelmes, R.J., 1987, J.Phys. C, **20** in press

Gibaud, A., Cowley, R.A., and Mitchell, P.W., 1987, J.Phys. C, **20** in press

Halperin, B.I., Hohenberg, P.C., and Ma, S.K., 1972, Phys.Rev.Lett., **29** 1548
- 1974, Phys.Rev. B, **10** 139
- 1976, Phys.Rev. B, **13** 4119

Halperin, B.I., and Varma, C.M., 1976, Phys.Rev. B, **14** 4030

Harada, J., Pedersen, T., and Barnea, Z., 1970, Acta Cryst. A, **26** 336

Hastings, J.B., Shapiro, S.M., and Frazer, B.C., 1978, Phys.Rev.Lett., **40** 237

Heller, P., 1970, Int.J.Mag., **1** 53

Hirotsu, S., and Sawada, S., 1973, Solid State Comm., **12** 1002

Hohenberg, P.C., and Halperin, B.I., 1977, Rev.Mod.Phys., **49** 435

Hoshino, S., and Motegi, H., 1967, Jap.J.Appl.Phys., **6** 708

Huang, K., 1947, Proc.Roy.Soc., **A190** 122

Imry, Y., and Ma, S.K., 1975, Phys.Rev.Lett., **35** 1399

Imry, Y., and Wortis, M., 1979, Phys.Rev. B, **19** 3580

Johann, H.H., 1931, Z Phys., **69** 185

Kadanoff, L.P., 1971, Critical Phenomena, Proc.Int.School of Physics 'Enrico Fermi', edited by M.S.Green, (New York : Academic Press) pg. 100

Kanzig, W., 1951, Helv.Phys.Acta, **24** 175

Kjems, J.K., Shirane, S.M., Muller, K.A., and Scheel, H.J., 1973, Phys.Rev. B, **8** 1119

Krumhansl, J.A., and Schrieffer, J.R., 1975, Phys.Rev. B, **11** 3535

Landau, L.D., 1937, Phys.Z.Sowjlln, **11** 26

Le Guillou, J.C., and Zinn-Justin, J., 1980, Phys.Rev. B, **21** 3976

Maetz, J., M llner, M., Jex, H., and Peters, K., 1978, Solid State Comm., **28** 555

Megaw, H.D., 1947, Proc.R.Soc., **189** 261

Mezei, F., and Heyter, J., 1974, EPS Conf. Budapest (unpublished)

Minkiewicz, V.J., Fujii, Y., and Yamada, Y., 1970, J.Phys.Japan, **28** 443

Mitchell, P.W., and Dove, M.T., 1985, J.Appl.Cryst., **18** 493

Moss, S.C., Keating, D.T., and Axe, J.D., 1973, Phase Transitions, edited by C.E.Cross, (New York : Pergamon) pg. 179

Murata, K.K., 1975, Phys.Rev. B, **11** 462

Natterman, T., 1976, J.Phys. C, **9** 3337

Natterman, T., and Trimper, S., 1975, J.Phys. A, **8** 2000

Ohnari, I., and Takada, S., 1979, Prog.Theo.Phys., **61** 11

Riste, T., Samuelsen, E.J., Otnes, K., and Feder, J., 1971, Solid State Comm., **9** 1455

Robinson, I.K., 1986, Phys.Rev. B, **33** 3830

Ryan, T.W., Nelmes, R.J., Cowley, R.A., and Gibaud, A.,
1986, Phys. Rev.Lett., **56** 2704

Sakahita, H., Ohama, N., and Okazaki, A., 1981, J.Phys.Japan, **50** 4021

Schneider, T., and Stoll, E., 1973, Phys.Rev.Lett., **31** 1254

- 1975, Phys.Rev.Lett., **35** 296

- 1976, Phys.Rev. B, **13** 1216

Schulhof, M.P., Nathans, R., Heller, P., and Linz, A., 1971, Phys.Rev. B, **4** 2254

Scott, L.J., 1974, Rev.Mod.Phys., **46** 83

Shapiro, S.M., Axe, J.D., Shirane, G., and Riste, T., 1972, Phys.Rev. B, **6** 4332

- 1974, Anharmonic Lattices, Structural Transitions and Melting, edited by T.Riste, (Leiden : Noordhoff) pg. 135

Shirane, G., 1974, Rev.Mod.Phys., **46** 437

Shirane, G., Jona, F., and Pepinsky, R., 1955, Proc.Inst.Radio.Engrs., **43** 738

Shirane, G., and Yamada, Y., 1969, Phys.Rev., **177** 858

Silberglitt, R., 1972, Solid State Comm., **11** 247

Stirling, W.G., 1972, J.Phys. C, **5** 2711

Stokka, S., Fossheim, K., and Samulionis, V., 1981, Phys.Rev.Lett., **47** 1740

Thoms, S., Beaumont, S.P., Wilkinson, C.D.W., Frost, J., and Stanley, C.R.,
1986, Microelectronics Eng., **5** 249

Tietze, H., M Ilner, M., and Jex, H., 1982, J.Phys. C, **16** 2209

Topler, J., Alefeld, B., and Kollmar, A., 1975, Phys.Lett. A, **51** 297

Topler, J., Alefeld, B., and Heidemann, A., 1977, J.Phys. C, **10** 635

Unoki, H., and Sakudo, T., 1967, J.Phys.Soc.Japan, **23** 546

Varma, C.M., 1976, Rev.Mod.Phys., **48** 219

Wegner, F.J., and Houghton, A., 1973, Phys.Rev. A, **8** 401

Werner, S.A., and Pynn, R., 1971, J.Appl.Phys., **42** 4736

Wilson, K.G., 1971, Phys.Rev. B, **4** 3174, 3184

- 1972, Phys.Rev.Lett., **28** 548

Wilson, K.G., and Kogut, J., 1974, Phys.Rev. C, **12** 77

Zachariasen, W.H., 1945, Theory of X-ray Diffraction in Crystals,
(New York : Wiley)

J. Phys. C: Solid State Phys. 20 (1987) 3417–3437. Printed in the UK

Determination of the critical exponents at the R-point instability in $KMnF_3$

U J Nicholls and R A Cowley
Department of Physics, University of Edinburgh, Mayfield Road, Edinburgh EH9 3JZ, UK

Received 30 December 1986

Abstract. X-ray scattering measurements have been performed on the perovskite $KMnF_3$ to investigate the critical behaviour at the cubic-to-tetragonal structural phase transition at 186 K. The critical exponents describing the temperature dependence of the order parameter, the correlation length and the susceptibility have been determined. An anomalous second component was observed in the scattering cross section close to the transition temperature, in addition to the anisotroic diffuse scattering from the softening R_{25} normal mode. The anomalous component was well described by an isotropic Lorentzian-squared lineshape.

1. Introduction

$KMnF_3$ is one of a family of perovskite-type crystals (space group Pm3m) which undergo an antiferrodistortive-phase transition to a tetragonal structure (space group I4/mcm). It is generally accepted that the phase transition is driven by an instability of the high-temperature cubic phase against a threefold degenerate zone corner, R_{25}, mode of vibration. The transition is characterised by a three component order parameter with wave-vector $\boldsymbol{q}_s = 2\pi/a_0(\frac{1}{2}, \frac{1}{2}, \frac{1}{2})$, and belongs to a universality class with $n = 3$, cubic symmetry, and short-range interactions, for which non-classical critical behaviour is expected. It has been shown that $KMnF_3$ undergoes such a phase transition at a temperature $T_c = 186$ K (see, for example, Minkiewicz *et al* 1970 and Gesi *et al* 1972). The transition is found to be slightly first order and the critical fluctuations are nearly two-dimensional.

The soft-mode theory of displacive phase transitions (Cochran 1960) suggests that as the critical temperature is approached from above the frequency of the R_{25} normal mode decreases to zero. This behaviour, and that given by more detailed theories, would suggest that the dynamic critical behaviour of the crystal is characterised by a single timescale. However neutron scattering studies by Riste *et al* (1971) on $SrTiO_3$ and later Shapiro *et al* (1972) on $SrTiO_3$ and $KMnF_3$, have shown this characterisation to be inadequate. They observed a central component in the scattering profile in addition to the phonon-like response. The overdamped phonon peak initially softened in accord with the classical soft-mode theory but saturated a few degrees above T_c, while the narrow component, centred on zero frequency, first appeared at ~50 K above T_c and its intensity diverged as T_c was approached. These results mean that the near critical behaviour of the order-parameter degrees of freedom in displacive phase transitions

0022-3719/87/233417 + 21 $02.50

must be characterised by two distinct timescales. The first of these is a short timescale whose magnitude is set by the soft-mode sideband and the second a longer timescale associated with the narrow central peak.

Many attempts have been made to understand the frequency-response function near criticality in terms of both intrinsic and extrinsic crystal behaviour. These have been reviewed in detail by Bruce and Cowley (1980) and so are only mentioned here. One approach is to explain the longer timescale through anharmonic phonon perturbation theories (Silberglitt 1972, Cowley and Coombs 1973 and others). Another approach provides a more conceptually appealing explanation of the second timescale but is not analytically explicit: It associates the central peak with the existence of precursor clusters of local order, which introduce an order–disorder component into the collective motion (Schneider and Stoll 1973, Krumhansl and Schrieffer 1975 and others). A third approach, described in detail by Halperin and Varma (1976), considers the influence of crystal imperfections and has the advantage of explaining the two timescales as arising from the intrinsic and defect behaviour respectively.

In the present paper we extended the work of Andrews (1986) on $SrTiO_3$ and of Ryan *et al* (1986) on $RbCaF_3$ by using the same experimental techniques to investigate the displacive phase transition near criticality in $KMnF_3$. Measurements of the x-ray scattering profile for all three materials show behaviour which is not consistent with classical intrinsic theories since they show a central peak (corresponding to a long length scale) superimposed upon the expected phonon profile (corresponding to a shorter length scale). The work by Andrews suggested that the narrow component was resolution limited but in the case of $RbCaF_3$ and $KMnF_3$ both components can be resolved. We find that both components are temperature dependent and that the long length scale diverges at the transition temperature whereas the short length scale remains finite at this temperature.

2. Experimental arrangement

The x-ray scattering measurements were performed on a two-circle, triple-crystal diffractometer. The function of the third (analyser) crystal in front of the detector is to control the angular divergence of the x-ray beam scattered from the sample. Cu $K\alpha_1$ radiation was produced by a rotating anode generator operating at 3 kW with a focal spot size of $3 \times 0.03\ mm^2$. The incident and scattered radiation were collimated by reflection from either pyrolitic graphite (0 0 0 2) or silicon (1 1 1) planes. When flat pyrolitic graphite monochromator and analyser were used the wave-vector resolution produced in the scattering plane was $\sim 0.02(2)\ Å^{-1}$ and $0.007(2)\ Å^{-1}$ (FWHM) perpendicular and parallel to the scattered wave-vector respectively. When graphite was replaced with single-crystal silicon, the wave-vector resolution was decreased to a FWHM of $\sim 0.001(2)\ Å^{-1}$ in both directions in the plane. This difference arises because the mosaic spread of the pyrolitic graphite is considerably greater than that of the single-crystal silicon, the latter giving rise to a highly monochromated beam. In both cases the out-of-plane resolution was $\sim 0.07(1)\ Å^{-1}$. This is relatively poor in comparison with the in-plane resolution and arises largely from the height of the monochromator, sample and analyser crystals.

The $KMnF_3$ crystal was grown by the Bridgman method, and samples of approximate size $5 \times 5 \times 5$ mm were cleaved from the boule. The sample showed visible signs of growth strains and gave an x-ray rocking curve width of $\sim 0.0085(5)°$ (FWHM).

The sample was attached in a strain free manner to the cold finger of a closed-cycle cryostat, and oriented with the face normal [0 0 1] and a cubic [1 1 0] axis in the horizontal plane of the diffractometer. The scattering plane which was investigated was therefore (1 −1 0). The temperature stability of the cryostat was ±0.01 K and temperatures were measured absolutely with an accuracy of ±0.02 K.

3. Theory of critical scattering

X-ray scattering measures the differential scattering cross section integrated over all energy transfers. The one-phonon scattering cross section in a perfect crystal approximation is given by

$$S(\boldsymbol{Q}) = \sum_{ij} \Delta(\boldsymbol{Q} + \boldsymbol{q}) F_i(\boldsymbol{Q}) F_j(-\boldsymbol{Q}) \xi_{ij}(\boldsymbol{q}) \tag{1}$$

where

(i) $\xi_{ij}(\boldsymbol{q})$ is the static displacement–displacement correlation function, related in the classical approximation to the generalised susceptibility $\chi_{ij}(\boldsymbol{q})$ by a factor of $1/k_B T$ (Cowley 1980).

(ii) $\Delta(\boldsymbol{Q} + \boldsymbol{q})$ ensures wave-vector conservation, $\boldsymbol{Q} + \boldsymbol{q} = \boldsymbol{\tau}$, a reciprocal-lattice vector.

(iii) $$F_i(\boldsymbol{Q}) = \sum_k f_k(\boldsymbol{Q}) \exp(-Wk) \boldsymbol{Q} \cdot \boldsymbol{e}(k, \boldsymbol{q}_i) \exp[\mathrm{i}(\boldsymbol{Q} + \boldsymbol{q}) \cdot \boldsymbol{R}_k] \tag{2}$$

is the one-phonon structure factor, a measure of the interaction between initial and final states of the system. The sum runs over all atomic sites $\boldsymbol{R}_k$ in the unit cell, f_k being the form factor and $\exp(-Wk)$ the Debye–Waller factor for the kth atom in the unit cell. The eigenvectors of the normal modes of the system are given by $\boldsymbol{e}(k, \boldsymbol{q}_i)$. We are interested in scattering in the vicinity of the R point in the cubic Brillouin zone, of wave-vector τ_R, which corresponds to rotations of the MnF_6 octahedra about the three cubic axes. Any scattering from other modes varies only slowly with $\boldsymbol{Q}$ close to the R point, τ_R, and is assumed to contribute only to the constant background. The important eigenvectors in equation (2) are therefore $\boldsymbol{e}(k, \boldsymbol{\tau}_R, i)$, where i refers to the three components of the R_{25} mode. Any variation with $\boldsymbol{q}$ in the structure factors has been neglected.

The soft-mode concept, introduced independently by Anderson (1960) and Cochran (1960) for a harmonic crystal, views the phase transition as an instability against a particular normal mode whose frequency decreases to zero at T_c. The wave-vector dependence of the frequency of these normal modes can be expanded as a Taylor series in q. There is no linear term in q when the order parameter has a high symmetry wave-vector. In general the coefficients of the quadratic terms depend upon the direction of $\boldsymbol{q}$ and these may be reduced by symmetry (Cowley 1980) so that

$$w_{ij}^2(\boldsymbol{q}) = [\omega_0^2(\boldsymbol{q} = 0) + \lambda(q^2 + f q_i^2)]\delta_{ij} + h q_i q_j (1 - \delta_{ij}). \tag{3}$$

The frequency is connected to the static susceptibility by the equation

$$\chi_{ij}^{-1}(\boldsymbol{q}) = \omega_{ij}^2(\boldsymbol{q}). \tag{4}$$

Hence the critical scattering will be Lorentzian in wave-vector, with width depending upon the wave-vector direction.

The dispersion in the scattering about the R point in $KMnF_3$ has been measured using neutrons by Gesi *et al* (1972). The observed parameters are $\lambda = 42.0 \pm 0.5$ THz^2 Å^2, $f = -0.99 \pm 0.01$ and $h = 0.14 \pm 0.04$. The diffuse scattering is therefore of rod-like streaks along the cubic $\langle 1\,0\,0 \rangle$ directions in the cubic phase (Comès *et al* 1971), since $f \sim -1$ and h is small. This can be understood qualitatively in terms of the rotations of the fluorine octahedra about a [1 0 0] axis. The fluctuations are highly correlated within the (1 0 0) plane due to a cogwheel motion between neighbouring octahedra. The inverse correlation length of these in-plane fluctuations is given by

$$\kappa = 2\pi/\xi = (\omega_0^2/\lambda)^{1/2} \tag{5}$$

where ξ is the correlation length. There is no similar strong correlation between atoms along the [1 0 0] axis because the shared inter-planar fluorine atoms are stationary.

The structure factors for the phonon modes corresponding to rotations of the fluorine octahedra about the three cubic axes x, y, and z for wave-vectors in the $(1\,-1\,0)$ plane are found to be $F_x(\boldsymbol{Q}) = F_y(\boldsymbol{Q}) = F$, and $F_z(\boldsymbol{Q}) = 0$. The expectation is therefore of large and equal scattering in the $\langle q\,0\,0 \rangle$ and $\langle 0\,q\,0 \rangle$ directions (because f is close to -1), but little in the $\langle 0\,0\,q \rangle$ direction (because $F_z(\boldsymbol{Q}) = 0$).

The temperature dependence of the static susceptibility at $\boldsymbol{q} = 0$ is described by the equation

$$\chi_L = \chi_{ij}(\boldsymbol{q} = 0) = C_+ t^{-\gamma_L} \tag{6}$$

where $t = (T/T_c - 1)$ and the superscript refers to a Lorentzian scattering model. This exponent is unity for classical theories, but is larger when critical effects are important.

Similarly the temperature dependence of the inverse correlation length of the fluctuations of the R_{25} normal mode can be characterised by the equations

$$\kappa_L = \kappa_0 t^{\nu_L} \qquad \kappa_0 = 2\pi/\xi_{Lo} \tag{7}$$

where ν_L is of the order $\frac{1}{2}$ in classical theories and somewhat larger when critical effects are important.

When an antiferrodistortive phase transition such as in $KMnF_3$ occurs new Bragg peaks appear in the distorted phase as a result of cell doubling, the intensities of which are directly proportional to the square of the order parameter. The temperature dependence of the integrated intensity gives a measure of the exponent β used to describe the variation of the primary order parameter.

In this section the theory has been based thus far upon the assumption that the sample is a perfect crystal. Using a mean-field approximation we now relax this assumption and consider the effect of symmetry breaking defects. The presence of isolated impurities frozen in symmetry breaking positions produces random static fields which couple linearly to the order parameter (Imry and Ma 1975) and produce a non-zero value of the local order parameter above T_c in the vicinity of the impurity. This gives rise to so-called Huang scattering (Huang 1947). Specifically, the increase in potential energy due to this coupling is

$$V = N^{-1/2} \sum_{\boldsymbol{q}} U(\boldsymbol{q}) Q(\boldsymbol{q}) \tag{8}$$

giving

$$\langle Q(\boldsymbol{q}) \rangle = N^{-1/2} \sum_{ij} U(\boldsymbol{q}) \chi_{ij}(\boldsymbol{q}) \tag{9}$$

where $\chi_{ij}(q)$ is the static wave-vector-dependent susceptibility of the host. Hence the observed scattering is given by

$$S(q) = c \sum_{ij} \chi_{ij}^2(q)|U(q)|^2 \tag{10}$$

where c is the concentration of impurities. We therefore expect to see a Lorentzian-squared component in the structure factor (Halperin and Varma 1976). This component is more significant close to T_c where the phonon frequency is small. The amplitude of the Lorentzian-squared scattering has a temperature dependence

$$\chi_{L2} = \chi_{ij}(q = 0) = C_+^{(2)} t^{-\gamma_{L2}}. \tag{11}$$

4. Experimental results

4.1. Measurement of T_c

The antiferrodistortive transition to a tetragonal phase occurs in $KMnF_3$ at 186 K and is generally found to be slightly first order. In this experiment the transition temperature was measured by monitoring the intensity distribution of a Bragg peak as the temperature of the crystal was lowered, using high resolution (silicon monochromator and analyser crystals). A typical example is shown in figure 1. On cooling, the (0 0 4) cubic reflection splits into a number of different peaks at T_c, caused by the domain structure of the crystal in the tetragonal phase. The transition temperature is $T_c = 187.5 \pm 0.08$ K.

Maetz *et al* (1978) predict that a cubic Bragg reflection will split into three tetragonal peaks below T_c, each corresponding to a rotation of fluorine octahedra about one cubic axis. At the symmetric (0 0 4) reflection the two domains with their c axes in the plane of the crystal are superimposed, giving rise to only two peaks. However recent work on $RbCaF_3$ by Gibaud *et al* (1987a) shows this description to be inadequate because the domains are rotated with respect to each other. This analysis suggests that, around the (0 0 4) Bragg reflection, six peaks will be observed in a (1 −1 0) projection below T_c.

In figure 1 only three peaks can be seen. It was found that the number of peaks detected corresponding to a given Bragg reflection and their relative intensities, varied as the x-ray beam was moved across the sample face. The intensities of the two major peaks of the (1 1 4) reflection below T_c were measured as a function of position across the sample, using low resolution (graphite monochromator and analyser crystals), and are shown in figure 2. At the −2 mm position there are approximately equal proportions of both domains, while at the +1.5 mm position one of them dominates. The total intensity is roughly constant across the sample face and the integrated intensity did not alter significantly with temperature. This suggests that the domains are of macroscopic size.

A careful examination of a Bragg peak at a multi-domain point on the sample, using high resolution, shows five of the six peaks predicted by Gibaud and co-workers (figure 3). Their model can be tested by a measurement of the angle θ in figure 3, which should correspond to $\tan^{-1}(c_t/a_t\sqrt{2})$ (see the Appendix). At $T = 150$ K, c_t/a_t was measured as 1.0042(1) from an analysis of the positions of the peaks in the ⟨0 0 1⟩ direction in figure 3. This predicts the angle to be $\theta = 35.15(1)$ which is in good agreement with the measured angle $\theta = 35(1)$.

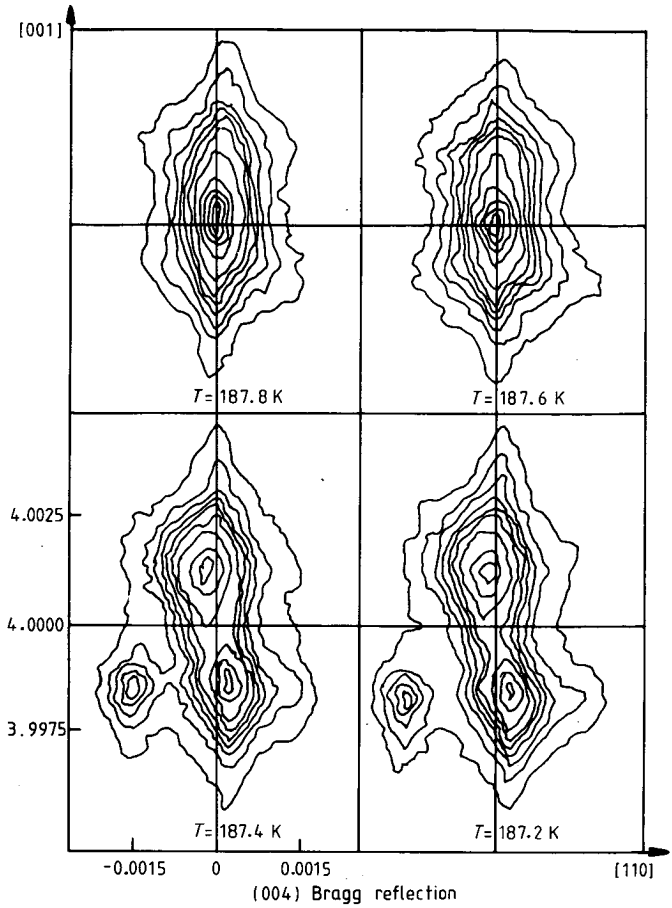

Figure 1. Intensity contour plot of the x-ray scattering from the Bragg reflection (0 0 4) as the crystal is cooled through T_c, showing the abrupt splitting into domains at T_c. The reciprocal-space axes are in units of $2\pi/a_0$.

4.2. Measurement of the exponent β

As described in § 3, the temperature dependence of the integrated intensity of the zone-boundary scattering below the transition temperature is characterised by the critical exponent 2β. In a perovskite material such as $KMnF_3$ the method is complicated by the systematic absence of one of the tetragonal peaks, below T_c, at any superlattice reflection in the (1 −1 0) plane. This means that if the relative proportions of the different domains are significantly temperature dependent the exponent β cannot be obtained. However, it is also possible to evaluate this critical exponent using x-ray scattering by a measurement of the tetragonal strain of the crystal as a function of temperature, since it is a secondary-order parameter.

Figure 4 shows the intensity of scattering at the (0.5 0.5 3.5) reflection, measured using the low-resolution configuration, as a function of position and temperature. On approaching T_c, the dependence of the scattered intensity does appear to vary across the sample face. The extent to which this is significant is shown in figure 5. These curves display the integrated intensity of the zone-boundary reflection, measured using low

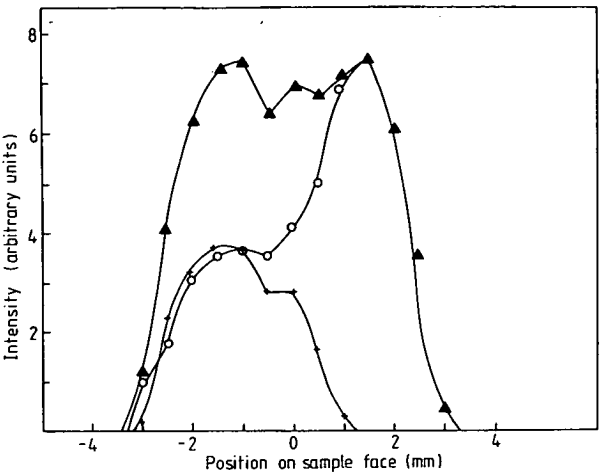

Figure 2. Peak x-ray scattering intensities (arbitrary units) of the two domains for the Bragg reflection (1 1 4) at $T = 160$ K as a function of position across the sample face. The circles refer to the first domain, and the crosses to the second domain. The total peak intensity (the sum) is shown by the triangles.

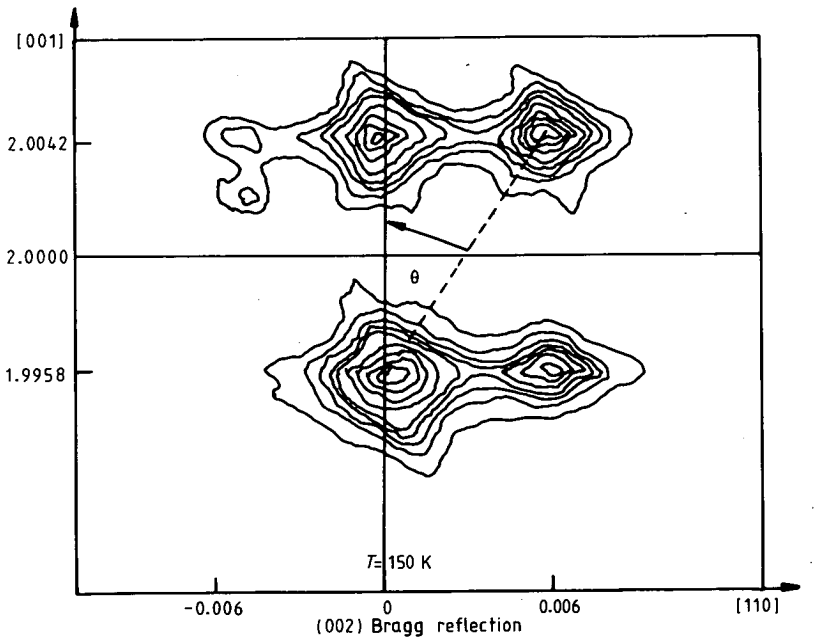

Figure 3. Intensity contour plot of the x-ray scattering from the Bragg peak (0 0 2) at $T =$ 150 K showing the domain structure pattern as described in the text. In the ⟨0 0 1⟩ direction the peaks lie at two wave-vectors only; the wave-vector furthest from the origin in reciprocal space corresponds to the lattice parameter a_t, and that nearer to the origin to the lattice parameter c_t. The angle θ measured on the figure is 35(1)°. The reciprocal-space axes are in units of $2\pi/a_0$.

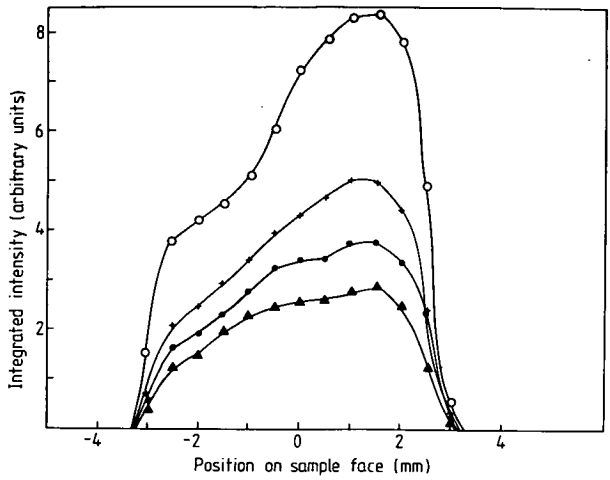

Figure 4. Integrated x-ray scattering intensity (arbitrary units) for the reciprocal-lattice point (0.5 0.5 3.5), obtained in a measurement of the rocking curve, as a function both of position on the sample face and temperature. At this position in reciprocal space only two of the three domains contribute to the scattering. The different symbols refer to different temperatures: open circles, 150 K; crosses, 180 K; closed circles, 195 K; triangles, 187 K.

resolution (graphite monochromator and no analyser crystal), at positions −2 mm, −1 mm and +1.5 mm on the sample face. This intensity is obtained from a measurement of the rocking curve which is then integrated over the scan.

The data points for each curve were independently fitted over the range $T = 150 \rightarrow 190$ K by a least-squares procedure to the power law $I \sim t^{2\beta}$, $t = (T/T_c - 1)$.

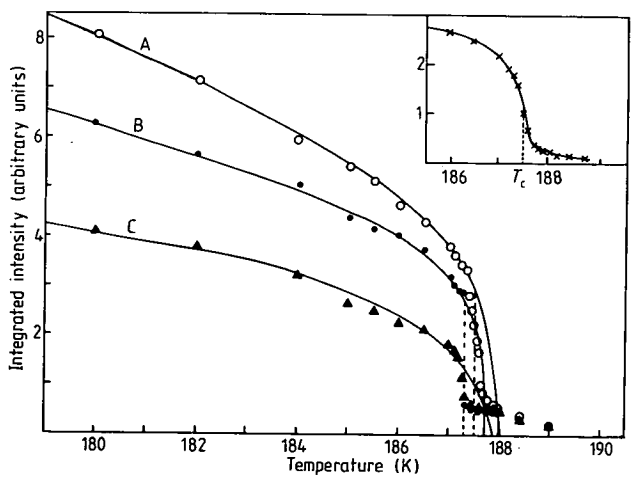

Figure 5. Integrated x-ray scattering intensity (arbitrary units) from the reciprocal-lattice point (0.5 0.5 3.5), obtained in a measurement of the rocking curve on cooling through T_c. The three data sets were measured at different points on the sample face; set A at +2 mm, set B at −1 mm and set C at −2 mm. The smooth curves are least-squares fits to the power law $I \sim t^{2\beta}$ as described in § 4. The inset shows the integrated intensity, obtained with higher resolution, as the crystal was cooled through T_c at position +1.5 mm. The scale is also in arbitrary units.

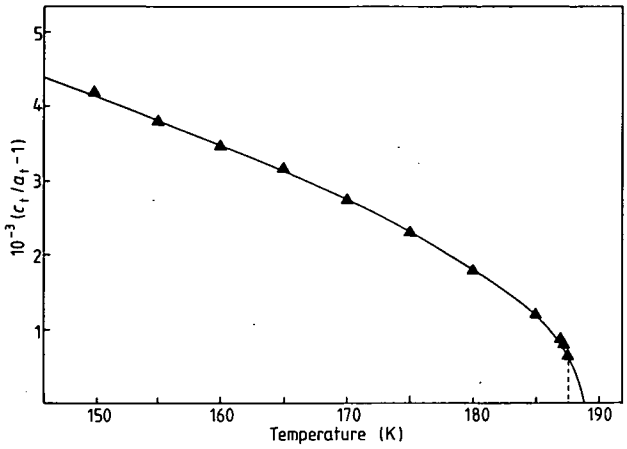

Figure 6. Measurement of the parameter $(c_t/a_t - 1)$ as a function of temperature below T_c for the Bragg peak (0 0 4).

Temperatures up to 187.3 K were included in all cases and the transition temperature allowed to vary (giving a value T_c'). The full curves are the results of this fit and the broken lines indicate the actual transition temperature for each set of data. Curve A shows an approximately continuous phase transition with $T_c \sim 187.5(1)$ K and exponent $\beta = 0{\cdot}178$. Curve B displays a definite first-order transition with an abrupt jump at $T_c \sim 187.3(1)$ K and $\beta = 0.135$. Curve C also shows a continuous transition with $T_c \sim 187.3(1)$ K and $\beta = 0.205$. This suggests that the character and the temperature of the transition are not consistent across the sample face.

The tetragonal strain in $KMnF_3$ was measured using high resolution by monitoring the ratio of the positions of the domain peaks for the (0 0 4) Bragg reflection in the [0 0 1] direction as a function of temperature. The results are shown in figure 6. The full curve is a least-squares fit to the power law $(c_t/a_t - 1) \sim t^{2\beta}$, with the transition temperature allowed to vary, while the broken line is the actual transition temperature. The fit gives $T_c = 188.6$ K and $\beta = 0.26$. Table 1 contains a summary of the results for all enlarged measurements of the order parameter, which are discussed in § 5.

4.3. Critical scattering

4.3.1. Introduction. The wave-vector dependence of the critical scattering above T_c was measured around the reciprocal-lattice point (0.5 0.5 3.5) using both low and high resolution arrangements. The measurements were made at the +1.5 mm position on the

Table 1. The critical exponent β (errors in brackets).

Curve	T_c' (K)	β
A	188.0 (0.1)	0.178 (0.004)
B	187.7 (0.07)	0.135 (0.008)
C	187.9 (0.1)	0.205 (0.005)
$(c_t/a_t - 1)$	188.6 (0.07)	0.26 (0.02)
Theory for $n = d = 3$ Heisenberg	—	0.365 (0.002)

sample face where the scattering was most intense. Examples of low-resolution scans parallel to [1 1 0] are shown in figure 7. The scattering profile was found to change as T_c was approached, with a temperature dependent width. Similarly, the scattering shown in figure 8, measured using high resolution, also has a temperature dependence. At this resolution it is only possible to detect extremely sharp components in the scattering profile, any broad part being indistinguishable from a uniform background.

X-ray scattering measurements of the R-point instability in $SrTiO_3$ and $RbCaF_3$ have been made by Andrews (1986), Ryan *et al* (1986), and Gibaud *et al* (1987a, b). These crystals showed an anomalous profile in the critical scattering at the R-point above T_c which appeared to consist of two length scales. In $SrTiO_3$ the scattering was analysed in terms of a one-phonon component (Lorentzian) together with a resolution limited component. This second component first appeared some 10 K above T_c, and increased in intensity as T_c was approached. In $RbCaF_3$, a similar profile was measured using low resolution, but a closer investigation of the narrow component using higher resolution found it to be broader than the instrumental resolution, with a wave-vector width which decreased continuously to the resolution limit at T_c. This component was observed in the temperature range $T_c \rightarrow T_c + 8$ K.

The next section describes the analysis of the critical-scattering measurements made on $KMnF_3$ using x-ray diffraction.

4.3.2. Analysis of results. The smooth curves through the data points in figures 7 and 8

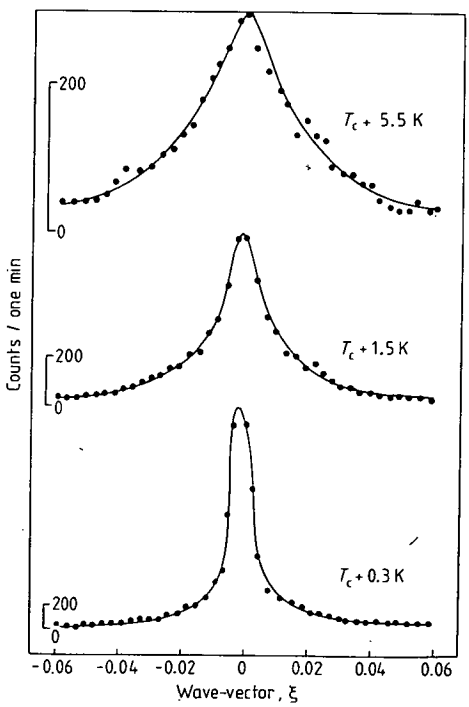

Figure 7. The diffuse x-ray scattering obtained using the low-resolution configuration for wave-vector $Q = (0.5 + \xi, 0.5 + \xi, 3.5)$ at various temperatures above T_c. The curves are least-squares fits to a Lorentzian (anisotropic) plus a Lorentzian-squared (isotropic) model convolved with the instrumental resolution function.

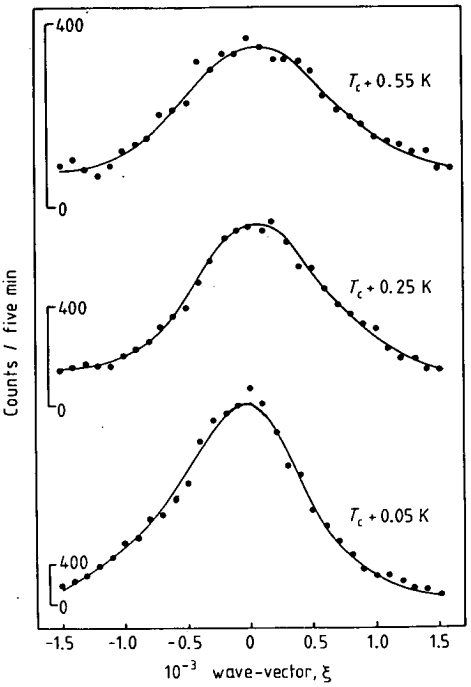

Figure 8. The diffuse x-ray scattering obtained using the high-resolution configuration for wave-vector $Q = (0.5, 0.5, 2.5 + \xi)$ at temperatures close to T_c. The curves are least-squares fits to an isotropic Lorentzian-squared model convolved with the instrumental resolution function.

are least-squares fits to the trial function $I(q)$, where $I(q)$ consists of a model scattering function $S(q)$ convolved with the instrumental response function $R(q)$

$$I(q) = \int_{q_1} S(q)R(q_1 - q)\,\mathrm{d}q_1. \tag{12}$$

The fitting was performed on the distributed array processor, (DAP) at the University of Edinburgh. The DAP consists of 4096 processing elements in a 64 by 64 array, each of which executes the same instruction on an independent data stream. The program used was written for investigation of neutron and x-ray scattering data (see Mitchell and Dove 1985). Use of the DAP facilitates numerical integration over all three cubic directions, alleviating the need to approximate the vertical resolution by a triangular function. Also, the anisotropy in the scattering function can be included without significantly increasing the computational time.

The theory of § 3 suggests that an appropriate model $S(q)$ for the one-phonon scattering above T_c is an anisotropic Lorentzian (see equations (1–4)). Pairs of scans with wave-vectors in the directions $\langle 0.5 + \xi\ 0.5 + \xi\ 3.5\rangle$ and $\langle 0.5\ 0.5\ 3.5 + \xi\rangle$ (obtained using low resolution) were fitted simultaneously to equation (12) with this model. The measured dispersion relation (Gesi *et al* 1972) gave $f = -1$ to reasonable accuracy, and h small. The data was fitted keeping $f = -1$, with $h = 0$ and $h = 0.14$, to test the anistropy in the dispersion (i.e. the extent of coupling between rotations about different cube axes). In both cases, the amplitude χ_L and inverse correlation length κ_L

were varied, with a fixed background. The fit was assessed in terms of the 'goodness of fit' parameter $G = (\chi^2/\text{degrees of freedom})^{1/2}$. Contrary to the results of Andrews (1986) on $SrTiO_3$, the analysis of the data for the two different anisotropy parameters h produced identical values for both of the exponents ν_L and γ_L. This is probably because the scattering is more two-dimensional in $KMnF_3$.

Initially, data collected over the entire temperature range ($T_c \rightarrow T_c + 50$ K) was fitted to this model. The model was found to fit well for temperatures greater than $T_c + 8$ K, with typical fits of $G = 1.10$ ($T = 240$ K) and $G = 1.59$ ($T = 200$ K). Closer to T_c the goodness of fit parameter was found to increase rapidly, for example, to $G = 3.97$ ($T = 190$ K) and $G = 5.04$ ($T = 189$ K). The last part of § 3 gives a theoretical foundation for the inclusion of a Lorentzian-squared component in the scattering cross section at temperatures close to T_c, of similar anisotropy and width to the Lorentzian component but different amplitude. However it was found this model did not significantly improve the fit ($G = 3.95$ ($T = 190$ K) and $G = 5.03$ ($T = 189$ K)). The recent work on $SrTiO_3$ and $RbCaF_3$ described above suggests that the inclusion of a second length scale in the scattering function would be appropriate, although the theoretical basis for this is still under discussion. Consequently the Lorentzian-squared component was constrained to be isotropic, and of a different width to the Lorentzian part. The data was fitted to this model; the two amplitudes χ_L, χ_{L2} and two widths κ_L, κ_{L2} were varied, again with a fixed background. Some examples of the goodness of fit are $G = 1.61$ ($T = 190$ K) and $G = 1.74$ ($T = 189$ K). The obtained values of the four parameters χ_L, χ_{L2}, κ_L and κ_{L2} as functions of the reduced temperature $t = (T/T_c - 1)$ are shown in figures 9 and 10. The temperature dependence of these parameters is discussed below.

A second experiment using high resolution was performed on $KMnF_3$ to establish

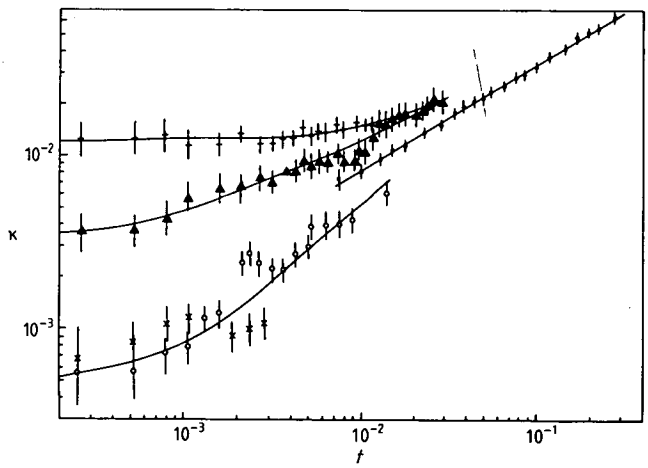

Figure 9. Inverse correlation lengths obtained from the analysis as described in the text of the diffuse x-ray scattering, in units of $2\pi/a_0$, for the reciprocal-lattice points (0.5 0.5 3.5) and (0.5 0.5 2.5) (crosses only). The full circles correspond to data analysed using the anisotropic Lorentzian-only model, with $f = -1$, $h = 0$. The crosses and triangles refer to data analysed using the Lorentzian (anisotropic) + Lorentzian-squared (isotropic) model, the crosses to the Lorentzian inverse correlation length and the triangles to the Lorentzian squared inverse correlation length. The open circles refer to the high-resolution data, the model being Lorentzian-squared only, with $f = h = 0$. In all cases the full curves are least-squares fits to the power law discussed in the text.

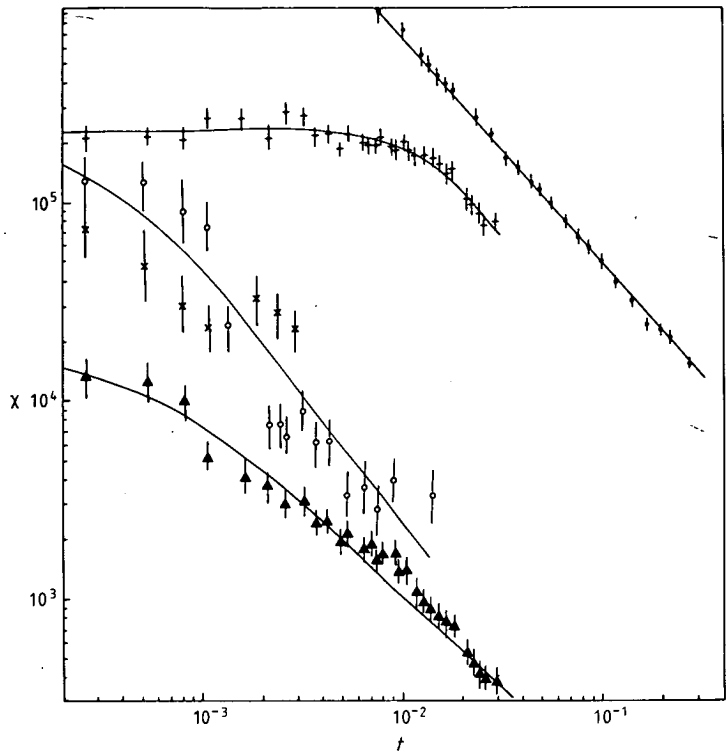

Figure 10. Amplitude (arbitrary units) obtained from the analysis as described in the text of the diffuse x-ray scattering for the reciprocal-lattice points (0.5 0.5 3.5) and (0.5 0.5 2.5) (crosses only). The full curves are least-squares fits to the power laws discussed in the text.

the presence of the second length scale κ_{L2}. As mentioned earlier, this component was unresolved in $SrTiO_3$ and $RbCaF_3$ (using graphite monochromator and analyser crystals), and found to be Lorentzian squared and isotropic with a temperature dependent width in $RbCaF_3$ (using silicon monochromator and analyser crystals). The scattering obtained for $KMnF_3$, examples of which are shown in figure 8, was found to vary in amplitude and width with temperature. Initially, pairs of scans with wave-vectors in the directions $\langle 0.5 + \xi \; 0.5 + \xi \; 3.5 \rangle$ and $\langle 0.5 \; 0.5 \; 3.5 + \xi \rangle$ were analysed simultaneously in terms of an anisotropic Lorentzian scattering model, as for the low-resolution data, but the fitted curves did not describe the results. Because of this failure, the Lorentzian-squared form was fitted to the data; it was found that the fit would not succeed unless the anisotropy was removed. An adequate fit was obtained using an isotropic Lorentzian-squared model of amplitude $\chi_{L2}^{(s)}$ and width $\kappa_{L2}^{(s)}$. Some examples of fits obtained are $G = 1.76$ ($T = 188$ K) and $G = 1.42$ ($T = 187.7$ K). The obtained values of the parameters are shown in figures 9 and 10 as functions of t. As can be seen, there is little agreement between κ_{L2} and $\kappa_{L2}^{(s)}$; this is probably due to the limitations of the assumed model. The measurements made using silicon monochromator and analyser crystals were difficult because of the weak scattering involved. The results were not easily reproducible being sensitive to external factors such as small changes of position on the sample face between measurements.

Table 2. Critical exponents of the Lorentzian component (errors in brackets).

	ν_L	ξ_{Lo} (Å)	$(T_c' - T_c)$ (K)	γ_L	$(T_c' - T_c)$ (K)
$KMnF_3$	0.62 (0.07)	31 (6)	−0.12 (0.03)	1.19 (0.11)	−0.12 (0.03)
$SrTiO_3$	0.83 (0.05)	46 (5)	—	1.4 (0.1)	—
$RbCaF_3$	0.64 (0.07)	27 (5)	−0.54 (0.1)	1.34 (0.11)	−0.74 (0.1)
Theory for $n = d = 3$ Heisenberg	0.705 (0.003)	—	—	1.386 (0.004)	—

4.3.3. Measurement of the critical exponents. The critical exponents ν_L and γ_L corresponding to the anisotropic Lorentzian model described in § 3 are given by equations (6) and (7). The data from the temperature range $T = 189 \rightarrow 240$ K was fitted by a least-squares technique to these equations with the transition temperature, the amplitude, and the exponent allowed to vary. The effective transition temperature found from this anslysis is T_c'. The results are shown in table 2 and will be discussed in § 5. Similarly, the critical exponents ν_{L2} and γ_{L2} corresponding to the isotropic Lorentzian-squared component included in the analysis for $T < 189$ K have been fitted to equations (7) (with χ_{L2} and ν_{L2}) and (11) for both the low and high resolution data. The results are shown in table 3 and will also be discussed in § 5. In this temperature range the anisotropic Lorentzian component converged to a constant correlation length and amplitude at T_c as expected for a first-order phase transition.

4.4. The character of the Lorentzian-squared component

The character of the narrow component shown in figure 8, was further investigated using high resolution. As shown in the inset of figure 5, a careful measurement of the integrated intensity of the critical scattering using silicon indicates a continuous phase transition. This was found to be consistent across the sample face. It was also found that, although the cubic Bragg reflection (0 0 4) jumps abruptly to its tetragonal phase positions at T_c (figure 11), as expected for a first-order phase transition, the narrow component of the critical scattering does not undergo any discontinuous shift in position at T_c, and is already displaced from the cubic R point above T_c. This suggests that the scattering is due to a tetragonal structure with a fixed strain (c_t/a_t ratio) just above T_c. A similar result was obtained in $RbCaF_3$ (Ryan *et al* 1986).

Table 3. Critical exponents of the Lorentzian-squared component (errors in brackets).

	ν_{L2}	ξ_{L2o} (Å)	$(T_c' - T_c)$ (K)	γ_{L2}	$(T_c' - T_c)$ (K)
$KMnF_3$ low-resolution data	0.49 (0.06)	38 (4)	−0.14 (0.03)	1.00 (0.08)	−0.15 (0.03)
$KMnF_3$ high-resolution data	0.84 (0.12)	20 (8)	−0.04 (0.05)	1.24 (0.16)	0.01 (0.06)
$RbCaF_3$ high-resolution data	0.60 (0.08)	66 (3)	−0.004 (0.006)	—	—

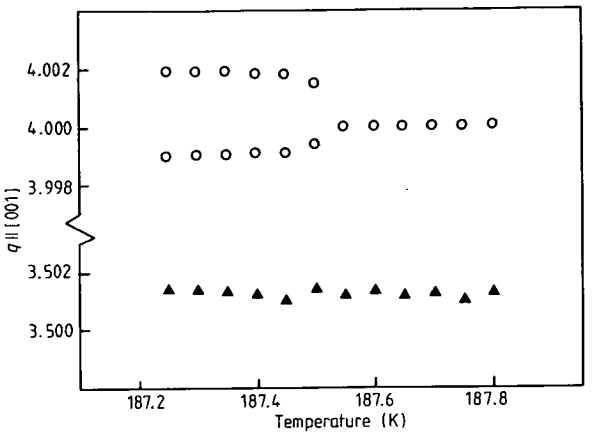

Figure 11. The position of the peaks (0 0 4) (circles) and (0.5 0.5 3.5) (triangles) with respect to their cubic positions in the ⟨0 0 1⟩ direction as a function of temperature, all scans being measured using high resolution. The reciprocal-space axis is in units of $2\pi/a_0$.

5. Discussion of results

5.1. Temperature dependence of the order parameter

The order parameter of the critical fluctuations below T_c at the R point in $KMnF_3$ has been measured using x-ray scattering in two ways. Integrated intensity measurements of the R-point scattering below T_c (figure 5) were found to differ in temperature dependence across the sample face (see table 1) because domain proportions depend upon temperature. Close to T_c the influence of domains has particular importance since the character of the transition and the temperature at which it occurs vary. A quantitative measure of the temperature dependence of the domain volume distribution has been made for $KMnF_3$ by Tietze *et al* (1982) who found that the domain volumes are equally distributed at T_c and grow rapidly to a saturation ratio of 70:20:10% at temperatures of $T_c - 10$ K and less. (In our experiment we see the first two domains superimposed.) Although this can explain the differences in the integrated intensity measurements close to the transition, we found the saturation ratio was not constant across the sample face. In conclusion, it is not possible to attach much significance to the values of the critical exponent β obtained by this technique; the low values however do indicate the importance of extinction in a large sample.

Measurement of the temperature dependence of the ratio of lattice parameters c_t and a_t (figure 6) gives an acceptable value for β since these quantities are insensitive to the domain structure; our result is $\beta = 0.26(2)$. The $n = d = 3$ Heisenberg model predicts $\beta = 0.365(2)$ (Le Guillou and Zinn-Justin 1980). This exponent is appropriate asymptotically where the anisotropy parameter f is renormalised to zero at T_c (Bruce (1980), but expected to be greater in systems with anisotropy f close to -1 (Natterman and Trimper 1975). It has also been shown (Fisher and Nelson 1974, Aharony and Bruce 1974) that the tetragonal strain accompanying the phase transition has a temperature dependence described by $\tilde{\beta}$ where $\tilde{\beta} = 2 - \alpha - \varphi$. Here φ is a crossover exponent reflecting the instability of the Heisenberg fixed point against a 'perturbation' of uniaxial symmetry. For $n = d = 3$, they find $\tilde{\beta} \sim 0.85$ which differs appreciably from the exponent $2\beta = 0.73$ predicted by Landau theory. Our result is considerably lower than either of these values

and even than the $d = 3$ Ising model of 0.315(2) (Fisher 1974). Ising behaviour is possible if the sample is single domain with an orienting mechanism (strain field) which selects the mono-domain axis (Courtens 1972, Aharony and Bruce 1974).

The critical exponent has been reported as $\frac{1}{3}$ by Borsa (1973) (from an analysis of the quadrupole coupling constant) and also by Hirotsu and Sawada (1973) and Benard and Walker (1976) (from measurements of the birefringence). A more recent measurement of the lattice parameter a_t by Sakahita *et al* (1981), using high-angle double crystal x-ray diffractometry, found the exponent to be $\beta = 0.2857(6)$, in reasonable agreement with our result. Sakahita and co-workers suggest that the value of β is small because the weak first-order phase transition occurs in the vicinity of a tricritical point (Aharony and Bruce 1979). Our results further substantiate this idea. Following the publication of the work by Sakahita and co-workers, the tricritical behaviour in $KMnF_3$ has been investigated by means of specific heat measurements (Stokka *et al* 1981). They found $KMnF_3$ to have two consecutive tricritical points joined by a second-order line near $p = 0.25$ kbar and $T = 188$ K for pressure applied along the $\langle 1\,0\,0 \rangle$ direction.

5.2. *Critical scattering*

5.2.1. One-phonon scattering description. The one-phonon scattering from the R_{25} mode discussed in § 3 is adequate to describe the observed scattering cross section in the temperature range $0.01 < t < 0.3$. In the Ornstein–Zernike approximation (small q limit) the expected cross section for general wave-vector transfer is described as the sum of two anisotropic Lorentzians of different widths because the x-rays couple to fluctuations of two different R_{25} modes. At any given temperature the observed scattering profile closely agreed with the form of dispersion given by neutron scattering measurements (Gesi *et al* 1972), showing $f = -1$ and h small. The cross section was found to be largely independent of the parameter h; the critical exponents are insensitive to the amount of anistropy in the dispersion.

The critical exponents ν_L and γ_L obtained from the analysis are shown in table 2, together with the experimentally determined values for $SrTiO_3$ and $RbCaF_3$ measured using x-rays, and the theoretically predicted parameters of the $n = d = 3$ Heisenberg model (Le Guillou and Zinn-Justin 1980). As mentioned above the intrinsic critical behaviour of $KMnF_3$ is only expected to be close to that of the Heisenberg fixed point in the asymptotic limit, the effect of non-zero anisotropy is to raise the critical exponents by a few per cent. However, the experimentally determined values of $\nu_L = 0.62(7)$ and $\gamma_L = 1.19(11)$ are actually smaller than predicted; this is attributed to changes in the scattering profile close to T_c causing κ_L to be artificially high.

The value for ν_L agrees favourably with that found in $RbCaF_3$ and is less than that measured in $SrTiO_3$. The reason for the anomalously high value in $SrTiO_3$ is unclear. The correlation length ξ_{Lo} at $2T_c$ is of the same order of magnitude in all three materials. It should be noted that the transition temperature was allowed to vary in the analysis of both the $KMnF_3$ and $RbCaF_3$ data producing an offset from the experimentally determined value, which represents a measure of the first-order character of the phase transition. In $SrTiO_3$ the width decreased rapidly close to T_c with a temperature dependence of $\nu_L \sim 2$–3 which is physically unreasonable: This change coincided with an alteration in the experimental configuration from low to high resolution and with the increasing importance of the quasi-Bragg component in the scattering cross section, and is probably due to an analysis in which a Lorentzian squared component was neglected. In the fit the transition temperature was constrained to equal the measured T_c. Another

point to note is that the x-ray data for $KMnF_3$ was adequately described by the anisotropy parameters measured by Gesi *et al* (1972). In $SrTiO_3$ and $RbCaF_3$ it was necessary to reduce the anisotropy determined by neutron scattering techniques slightly in order to fit the x-ray data.

5.2.2. Anomalous scattering profile close to T_c. In this section the second component observed close to the transition temperature is discussed with reference to the x-ray experiments on $SrTiO_3$, $RbCaF_3$ and $KMnF_3$. In all three materials it was necessary to introduce a second component into the analysis of the low-resolution data close to T_c. In $SrTiO_3$ and $RbCaF_3$ the component was unresolved, and in $KMnF_3$ it was isotropic and nominally Lorentzian squared in form with a temperature-dependent width. Further measurements using the high-resolution configuration showed the narrow component in $RbCaF_3$ to have a similar profile to that in $KMnF_3$, but in $SrTiO_3$ it remained unresolved with a width independent of temperature, the instrument-limited width being ~ 0.001 Å^{-1} (FWHM) in all cases. This difference may be an artefact of the Lorentzian squared model used for the analysis. No quasi-Bragg component was observed in $RbCaF_3$ and $KMnF_3$.

The high-resolution measurements on several samples of $SrTiO_3$ with different surface preparations showed a variation in intensity of the quasi-Bragg peak. In particular the narrow component observed from sample II (polished and etched) initially increased in intensity with repeated temperature cycling through the transition but eventually saturated at a value some five times larger than the initial value, close to that measured in sample III (annealed and oxidised) which showed no evidence of history dependence. The intensity of the quasi-Bragg component in sample IV (reduced in vacuum) was roughly twice that in sample III at the same value of t. History-dependent scattering at the R point was observed in the high-resolution measurements on $KMnF_3$, where no saturation occurred (§ 4.3.2.), but the results in $RbCaF_3$ were approximately reproducible. Of the three $RbCaF_3$ samples investigated, one showed no anomalous second component close to T_c: This sample differed from the others only in its smaller mosaic spread, the surfaces of all samples being prepared in a similar manner. It should also be noted that at any particular temperature the intensity of the quasi-Bragg component in all samples of $SrTiO_3$ did not vary by more than 10 per cent when the x-ray beam was scanned across the crystal surface. This differs from the measurements on $RbCaF_3$ and $KMnF_3$ which showed the critical scattering at the R point to vary considerably with position of the x-ray beam on the sample face.

The isotropic Lorentzian-squared scattering cross section measured in $RbCaF_3$ and $KMnF_3$ was found to have a temperature dependent width and to originate from a tetragonal structure. The results for the critical exponents ν_{L2} and γ_{L2} are shown in table 3. In the case of $RbCaF_3$ γ_{L2} was constrained to be $2\nu_{L2}$. The hysteresis in the high-resolution critical scattering measurements in $KMnF_3$ is reflected in the associated errors, but there is little agreement between the data collected using graphite monochromator and analyser crystals and that when graphite was replaced with silicon. It is therefore only possible to establish a qualitative temperature dependence for this component in $KMnF_3$. The analysis of the high-resolution data in both $RbCaF_3$ and $KMnF_3$ showed the correlation length and amplitude of the Lorentzian-squared component to diverge at or close to T_c. The correlated volume at $T_c + 0.5$ K had a linear dimension of ~ 4000 Å in $RbCaF_3$ and ~ 2000 Å in $KMnF_3$: The quasi-Bragg component in $SrTiO_3$ corresponded to a correlated tetragonal volume of size ~ 8000 Å which remained approximately unchanged over the temperature range $T_c \rightarrow T_c + 3.5$ K.

5.2.3. Surface effects. The influence of the surface upon the scattering profile has been considered in detail by Andrews (1986) who treats the surface as a macroscopic symmetry breaking defect. The model attributes the quasi-Bragg component to a surface layer in which the low-temperature tetragonal phase is stabilised by the surface. It is possible for this model to explain the unresolved wave-vector width in $SrTiO_3$ if the surface is rough or contains a compressive strain. However, the model also predicts the surface scattered intensity to be independent of the x-ray penetration depth μ, and consequently the ratio of surface to bulk scattering to be inversely proportional to μ. Measurements of this ratio at (0.5 0.5 2.5) and (0.5 0.5 4.5) in $SrTiO_3$ were found to vary by less than twenty percent compared with the difference in μ between the two wave-vectors of a factor of 2.3. In $KMnF_3$ the ratio of the integrated intensity at the two reciprocal-lattice points (0.5 0.5 2.5) and (0.5 0.5 3.5) (measured using silicon monochromator and no analyser crystal) was independent of temperature on cooling through T_c at approximately the value predicted by the bulk (after the normal corrections to the intensity had been made). These results suggest that the scattering cannot be attributed to the surface. Further evidence is provided by the measurements on $RbCaF_3$, where the surfaces of all three samples were prepared in a similar way yet did not all display the same anomalous component in the scattering cross section close to the transition. Also, the correlation length measured in $RbCaF_3$ and $KMnF_3$ using high resolution was observed to be temperature dependent, which cannot be explained by the surface model.

5.2.4. Random field model. As discussed in § 3 the presence of isolated defects in a symmetry breaking positions produce random static fields leading to a Lorentzian-squared component in the structure factor. The range of distortion around each defect is controlled by the intrinsic correlation length of the fluctuations in the high-temperature phase (Halperin and Varma 1976). These fluctuations are therefore expected to have the same degree of anisotropy in the dispersion as the one-phonon fluctuations described above. However the results in $RbCaF_3$ and $KMnF_3$ are quite different from this, showing isotropic scattering at a position displaced from the cubic R point. The extent of the correlated volume close to T_c was found to differ substantially from the one-phonon correlation length in $RbCaF_3$ (at $T_c + 0.5$ K, $\xi_{L2} \sim 4000$ Å and $\xi_L \sim 300$ Å). There is also a measurable difference in these values in $KMnF_3$, which suggests the critical scattering occurs on two length scales.

A plausible extension of the random field model to first-order phase transitions has been made by Imry and Wortis (1979) who suppose that, in addition to the fluctuations of the phonon normal modes, there are defect mediated fluctuations from the cubic phase to the tetragonal phase close to the transition. These fluctuations occur when the free-energy lowering due to taking advantage of local variations in impurity density more than offsets the free-energy cost of the interface produced. The correlations between tetragonally distorted clusters centred on quenched impurities drive the transition and have a length scale which may or may not be equal to the correlation length ξ_L of the one-phonon fluctuations. The model explains the tetragonal structure of the narrow component and introduces a second length scale into the scattering. The isotropic dispersion of the Lorentzian-squared component may arise because the tetragonal strain present in the distorted phase could cause the macroscopic elastic energy to favour a roughly spherical cluster. In this model the critical exponents ν_{L2} and γ_{L2} shown in table 3 refer to the degree of inter-cluster correlation.

As can be seen in figure 5 the phase transition in $KMnF_3$ as measured by the order parameter alters its character across the sample face, and is only slightly first order. The

model of Imry and Wortis predicts a smearing of a first-order phase transition because the size of the defect mediated fluctuations is determined by the free-energy difference between the phases, which decreases continuously to zero at T_c. Therefore if the Lorentzian-squared component in $RbCaF_3$ and $KMnF_3$ corresponds to scattering from these fluctuations we would expect to see a continuous phase transition at the R point when the high-resolution configuration is used. This is in fact the case for both materials; the result for $KMnF_3$ can be seen in the inset of figure 5. The measurements of the one-phonon scattering discussed in § 5.2.1. imply that the fluctuations of the phonon normal modes have a non-divergent temperature dependence which is consistent with a first-order phase transition.

6. Summary and conclusions

(i) Well above the transition temperature the critical scattering at the R point has the expected Lorentzian form in the three perovskites $SrTiO_3$, $RbCaF_3$ and $KMnF_3$. The correlations in the order-parameter fluctuations show considerable anisotropy, though this was found to be less in $SrTiO_3$ and $RbCaF_3$ than that predicted from the observed phonon dispersion relations (Stirling 1972 and Almairac *et al* 1977). The reason for this is probably because the x-ray scattering has contributions from the inelastic and central parts of the neutron scattering and the latter is less anisotropic than the former.

The temperature dependence of the scattering measured in the three materials is shown in table 2. The results for ν_L and γ_L in $RbCaF_3$ and $KMnF_3$ are consistent with the behaviour of the $n = d = 3$ Heisenberg model with approximately the correct exponents, but with transition temperatures T_c' which are below the transition temperatures measured by monitoring the tetragonal strain. In $SrTiO_3$ the susceptibility has a temperature dependence which is in agreement with this model, but the experimental value of ν_L is significantly larger than that predicted by theory. The correlation length and amplitude converge to zero at the measured T_c.

(ii) Closer to the transition temperature a second component in the scattering cross section was observed in all three materials. The characteristics of this component are that:

(a) It has a lineshape that is well described by a Lorentzian-squared model in $RbCaF_3$ and $KMnF_3$ but is resolution limited in $SrTiO_3$. No quasi-Bragg component is observed in $RbCaF_3$ and $KMnF_3$.

(b) It is isotropic in wave-vector.

(c) It is displaced from the cubic R-point position in $RbCaF_3$ and $KMnF_3$ suggesting that it can be attributed to clusters which have a tetragonal structure.

(d) In $RbCaF_3$ and $KMnF_3$ it has an inverse correlation length which decreases continuously to zero at or close to the measured transition temperature with an amplitude different from the one-phonon scattering.

(e) It has an amplitude which varies from sample to sample in $SrTiO_3$ and $RbCaF_3$.

(iii) The explanation for these results is unclear, though the differing behaviour amongst the various samples of $RbCaF_3$ strongly suggest the importance of defects. Circumstantial evidence is provided in the lack of a viable alternative mechanism: The surface model, although it could explain the quasi-Bragg component in $SrTiO_3$, is untenable. The theoretical predictions of Imry and Wortis (1979) in their extension of the random field model describe many of the observed phenomena, and provide a basis for explaining the origin of a second scattering length scale. If the defects were extended,

it is conceivable that coherently perturbed regions much larger than the intrinsic precursor clusters could occur. Consequently the q dependence of the x-ray scattering would reflect a distribution of length scales corresponding to spatial variations in crystal perfection. Imry and Wortis predict that the discontinuity at a first-order transition will be reduced by the defect mediated fluctuations to the tetragonal phase which are continuously temperature dependent. This smearing of the transition is observed in $RbCaF_3$ and $KMnF_3$, but, unfortunately, the transition in $SrTiO_3$ is effectively continuous, suggesting their theory is inappropriate in this case.

The results can be compared with the central peak observed in neutron scattering measurements. In $RbCaF_3$ the anomalous x-ray peak persists over a temperature range which is much less than that over which the neutron central peak is seen in crystals grown by the Bridgman–Stockbarger technique (Almairac *et al* 1977). In $SrTiO_3$ the neutron central peak assumes the bulk of the spectral weight at roughly the same temperature at which qualitative changes in the x-ray scattering occur (Shapiro *et al* 1972), and a strong temperature dependence of the scattering near T_c is observed in both instances. In the case of $KMnF_3$, analysis of the neutron-scattering data is complicated because the soft mode is overdamped at 40 K above T_c, and consequently the phonon and central component contributions to the observed intensities are not easily separated.

(iv) Further experiments are necessary on crystals with controlled defect concentrations in order to understand the anomalous scattering cross secton. It is also important to establish the effect of the surface on the phase transition in more perfect samples of $RbCaF_3$ and $KMnF_3$. To date experiments have only been performed on perovskites with very anisotropic R_{25} mode dispersion and it might be instructive to investigate $LaAlO_3$ which has a nearly isotropic dispersion.

Acknowledgments

We are grateful for the technical assistance of T W Ryan. Financial support for this work was provided by the Science and Engineering Research Council.

Appendix

A simple theory of domain structure predicts three Bragg peaks in reciprocal space. In a (0 0 1) orientation the domains with the c axis in the plane of the crystal give rise to a Bragg peak at $(a_t^* h \;\; c_t^* k \;\; 0)$ and that with the c axis perpendicular to the plane to a peak at $(c_t^* h \;\; a_t^* k \;\; 0)$. Gibaud *et al* (1987a) describe how these domains are rotated with respect to each other. In reciprocal space this causes satellite peaks which are distinguishable from the main peaks. For instance there is a peak at $(c_t^* h \cos\delta + a_t^* k \sin\delta, a_t^* k \cos\delta - c_t^* h \sin\delta, 0)$ which is rotated by an angle δ from the reciprocal point $(c_t^* h, a_t^* k, 0)$. The angle θ shown in figure 3 is therefore given by

$$\tan\theta = \frac{a_t^* h - c_t^* h\cos\delta - a_t^* k \sin\delta}{c_t^* k + c_t^* h \sin\delta - a_t^* k \cos\delta}$$

where $\delta = \pi/2 - 2\tan^{-1}(a_t/c_t)$ and $a_t^*/c_t^* = c_t/a_t$. This reduces to $\tan\theta = c_t/a_t$ for all h, k.

For comparison with the obtained $KMnF_3$ data, a factor of $\sqrt{2}$ must be included in

the value for the 'a_t' lattice parameter since the measurements were made in the (1 −1 0) plane.

References

Aharony A and Bruce A D 1974 *Phys. Rev. Lett.* **33** 427
—— 1979 *Phys. Rev. Lett.* **42** 462
Almairac R, Rosseau M, Gesland J Y, Nouet J and Hennion B 1977 *J. Physique* **38** 1429
Anderson P W 1960 *Fisika Dielectrikov* ed. G I Skanavi (Moscow: Acad. Nauk. SSR)
Andrews S R 1986 *J. Phys. C: Solid State Phys.* **19** 3721
Benard D J and Walker W C 1976 *Rev. Sci. Instrum.* **47** 122
Borsa E 1973 *Phys. Rev.* B **7** 917
Bruce A D 1980 *Adv. Phys.* **29** 111
Bruce A D and Cowley R A 1980 *Adv. Phys.* **29** 219
Cochran W 1960 *Adv. Phys.* **9** 387
Comès R, Denoyer F, Deschamps L and Lambert M 1971 *Phys. Lett.* **34A** 65
Courtens E 1972 *Phys. Rev. Lett.* **29** 1380
Cowley R A 1980 *Adv. Phys.* **29** 1
Cowley R A and Coombs G J 1973 *J. Phys. C: Solid State Phys.* **6** 143
Gibaud A, Cowley R A and Mitchell P W 1987a *J. Phys. C: Solid State Phys.* **20** at press
Gibaud A, Ryan T W and Nelmes R J 1987b *J. Phys. C: Solid State Phys.* **20** at press
Gesi K, Axe J D, Shirane G and Linz A 1972 *Phys. Rev.* B **5** 1933
Fisher M E 1974 *Rev. Mod. Phys.* **46** 597
Fisher M E and Nelson D R 1974 *Phys. Rev. Lett.* **32** 1350
Halperin B I and Varma C M 1976 *Phys. Rev.* B **14** 4030
Hirotsu S and Sawada S 1973 *Solid State Commun.* **12** 1002
Huang K 1947 *Proc. R. Soc.* A **190** 122
Imry Y and Ma S K 1975 *Phys. Rev. Lett.* **35** 1399
Imry Y and Wortis M 1979 *Phys. Rev.* B **19** 3580
Krumhansl J A and Schrieffer J R 1975 *Phys. Rev.* B **11** 3535
Le Guillou J C and Zinn-Justin J 1980 *Phys. Rev.* B **21** 3976
Maetz J, Müllner M, Jex H and Peters K 1978 *Solid State Commun.* **28** 555
Mitchell P W and Dove M T 1985 *J. Appl. Crystallogr.* **18** 493
Minkiewicz V J, Fujii Y and Yamada Y 1970 *J. Phys. Japan* **28** 443
Natterman T and Trimper S 1975 *J. Phys. A: Math. Gen.* **8** 2000
Riste T, Samuelsen E J, Otnes K and Feder J 1971 *Solid State Commun.* **9** 1455
Ryan T W, Nelmes R J, Cowley R A and Gibaud A 1986 *Phys. Rev. Lett.* **56** 2704
Sakahita H, Ohama N and Okazaki A 1981 *J. Phys. Japan* **50** 4021
Schneider T and Stoll E 1973 *Phys. Rev. Lett.* **31** 1254
Shapiro S M, Axe J D, Shirane G and Riste T 1972 *Phys. Rev.* B **6** 4332
Silberglitt R 1972 *Solid State Commun.* **11** 247
Stirling W G 1972 *J. Phys. C: Solid State Phys.* **5** 2711
Stokka S, Fossheim K and Samulionis V 1981 *Phys. Rev. Lett.* **47** 1740
Tietze H, Müllner M and Jex H 1982 *J. Phys. C: Solid State Phys.* **16** 2209